Elucidation of the Behavior of Covalent Chalcogen-Chalcogen Bonds and the Related Noncovalent Interactions: Theoretical and Experimental Investigations

March 2018

Graduate School of Systems Engineering

Wakayama University

Yutaka Tsubomoto

カルコゲン–カルコゲン共有結合および関連する非結合相互作用の挙動解明：理論的および実験的研究

平成 30 年　3 月

和歌山大学大学院システム工学研究科

坪本　裕

Abstract

Chemical science is based on classical covalent bonds and non-covalent interactions. The classical covalent interactions set up the skeleton of molecules. Diamond and graphite are consisted of same carbon atom, but both of physical and chemical properties are completely different. It is meant that the structural features have relation to the physical and chemical properties, and classical covalent interactions have important rolls for occurrence of the difference. The most important non-bonded interactions are van der Waals forces, hydrogen bonding and charge transfer interaction, which are also called weak interactions. One of the most attractive examples of resulting from such weak interactions is the helix structure of DNA and RNA. These interactions play a very important role in physical, chemical, and biological sciences, such as in the crystal engineering for material development.

Therefore, it is important to understand nature of weak and strong interactions, so that these bonds and interactions are key to determine the structures and the properties of compounds. It is also necessary to search for the theoretical method to evaluate and classify these interactions for achievement of green sustainable chemistry. The quantum theory of atoms-in-molecules (QTAIM) approach, proposed by Bader, is one of the fine concept for such the aim.

Based on the conception, he elucidated the nature of the interactions related to chalcogen atoms in various compounds with QTAIM dual functional analysis (QTAIM-DFA) and high-resolution measurements of X-ray diffraction. His research group has proposed QTAIM-DFA recently, which will enable us to analyze, evaluate and clarify the nature of classical chemical bonds and non-covalent interactions. In the method, bonds and interactions are evaluated on the point of view from not only static nature but also dynamic nature of them.

In this work, he succeeded in the following two points. These results would be very important to develop of the chalcogen chemistry.

1. The nature of the E–E′(E, E′ = S, Se) in the five stable conformations of cysteine and glutathione disulfide together with their derivatives of them was clarified by QTAIM-DFA. Every conformer are generated with conformation research by Spartan02 program and each structures are optimized and performed frequency analysis by Gaussian 09 program. (Chapter 3-4)
2. The nature of σ(4c–6e), which is the σ type liner interactions, was estimated and clarified from the points of view with theoretical and experimental methods. (Chapter 5-7)

概　要

全ての物質は、物質を構成する原子間に化学結合や非結合相互作用が形成し、原子が結びつくことでその構造を構築している。また、物質の構造は物性と大きな関連性がある。例えば、ダイヤモンドとグラファイトは炭素原子からなる単体であるが、それらは三次元構造が全く異なるため、その物性も異なる。炭素原子間に働く化学結合がそれらの母骨格を形成している。非結合相互作用においては、物質の微細構造を決定する因子となる。例えばDNAやRNAは、それらを構成する核酸塩基間に非結合相互作用が形成されることで、らせん構造を構築していることが知られている。よって、高い機能を有する新規物質の創生には、化学結合や非結合相互作用への理解を深めることが大切であり、それらの発現を予測し、定量的に評価する方法を確立することが出来れば、研究開発の効率化および活性化が期待できる。その実現に向けた研究は、化学の発展に加え、グリーンケミストリーおよびサステイナブルな社会の実現のために必要である。

以上の考えに基づき、本研究では所属研究室が提案するQTAIM2元関数解析法(QTAIM-DFA)やX線回折の精密測定による電子密度解析を用い、カルコゲン原子が関与した結合や非結合相互作用を理論的および実験的に解析し、その性質を静的および動的挙動の観点から明らかにした。カルコゲン原子が関与した結合および非結合相互作用は、近年では化学のみならず生化学においても大きな注目を集めている。QTAIM-DFAでは、最適化構造および摂動構造に対してAIM2000プログラムを用いて電子密度解析することにより得られた種々の関数値を用いて相互作用を定量的に解析する。今後、QTAIM-DFAの適用範囲を広げ、研究における様々な場面で応用することで、より効率的で高次元な研究開発の実現が期待できる。

本研究では、以下に示した研究成果を得た。下記の成果は、カルコゲン化学の今後の発展のための基盤になると期待される。

1. 生体内で活性酸素種を無害な物質に変える重要な役割を果たしているシスチンやグルタチオンジスルフィドや、それらのセレン代替物の最適化構造および安定な配座を求めた。さらに、それぞれの構造中のE–E′ (E, E′ = S, Se)結合に対してQTAIM-DFAを適用し、それらの性質を静的および動的挙動の観点から明らかにした。また、それぞれの構造中に働く分子内相互作用と配座の安定性との関連性についても追究した (3, 4章)。
2. 直線状に並ぶ4つのカルコゲンおよびハロゲン原子間で軌道の重なりによる引力相互作用が働き、構造の安定化をもたらすことで物性の発現に関与する4中心6電子結合の性質を理論的および実験的手法により明らかにした (5, 6, 7章)。

Contents

Chapter 1. General Introduction 1

Chapter 2. Methodological Details for Quantum Theory Atoms-in-Molecules Dual Functional Analysis (QTAIM-DFA) 9

Chapter 3. Dynamic and Static Behavior of the E–E′ Bonds (E, E′ = S and Se) in *R*-Cystine and Derivatives, Elucidated by AIM Dual Functional Analysis 23

Chapter 4. Behavior of the E–E′ Bonds (E, E′ = S and Se) in Glutathione Disulfide and Derivatives, Elucidated by QC Calculations with QTAIM Approach 37

Chapter 5. Nature of E_2X_2 σ(4c–6e) of the X---E–E---X Type at Naphthalene 1,8-positions and Model, Elucidated by X-ray Crystallographic Analysis and QC Calculations with QTAIM Approach 75

Chapter 6. Nature of S_2Se_2 σ(4c–6e) at Naphthalene 1,8-positions and Models, Elucidated by QTAIM Dual Functional Analysis 103

Chapter 7. High Resolution X-Ray Diffraction Determination of Electron Densities for 1-(8-$PhSC_{10}H_6SSC_{10}H_6SPh$-8')-1' with QTAIM Approach: Evidence for S_4 σ(4c–6e) at Naphthalene *peri*-positions 135

Conclusions 157

List of Publications 160

Other Publication 160

List of International Conferences 161

Acknowledgement 162

Chapter 1

General Introduction

The E–E′ bonds (E, E′ = S and Se) are of current and continuous interest due to the indispensable role in biological, chemical and physical sciences.[1–7] The E–E′ bonds in chalcogenides are characterized by the high energy levels of HOMO and low energy levels of LUMO. HOMO and LUMO of E–E′ would correspond to np(E/E′) and σ*(E–E′), respectively, where np(E/E′) denote the p-type lone pair orbitals of E and/or E′, while σ*(E–E′) corresponds to the σ*-orbital of E–E′. Figure 1-1 shows ε_{HOMO} and ε_{LUMO} of MeEMe and MeEEMe (E = O, S, Se, and Te), together with $MeCH_2Me$ and $MeCH_2CH_2Me$. The energy profile of E–E′ must be the driving force for the high reactivity in the redox processes and the E–E′ bonds play a crucial role in the redox process in the biological processes.[8] It is challenging to clarify the nature of the E–E′ bonds (E, E′ = S and Se) and the related interactions, in greater detail. The quantum theory of atoms-in-molecules dual functional analysis (QTAIM-DFA) is employed for the purpose.[9-12]

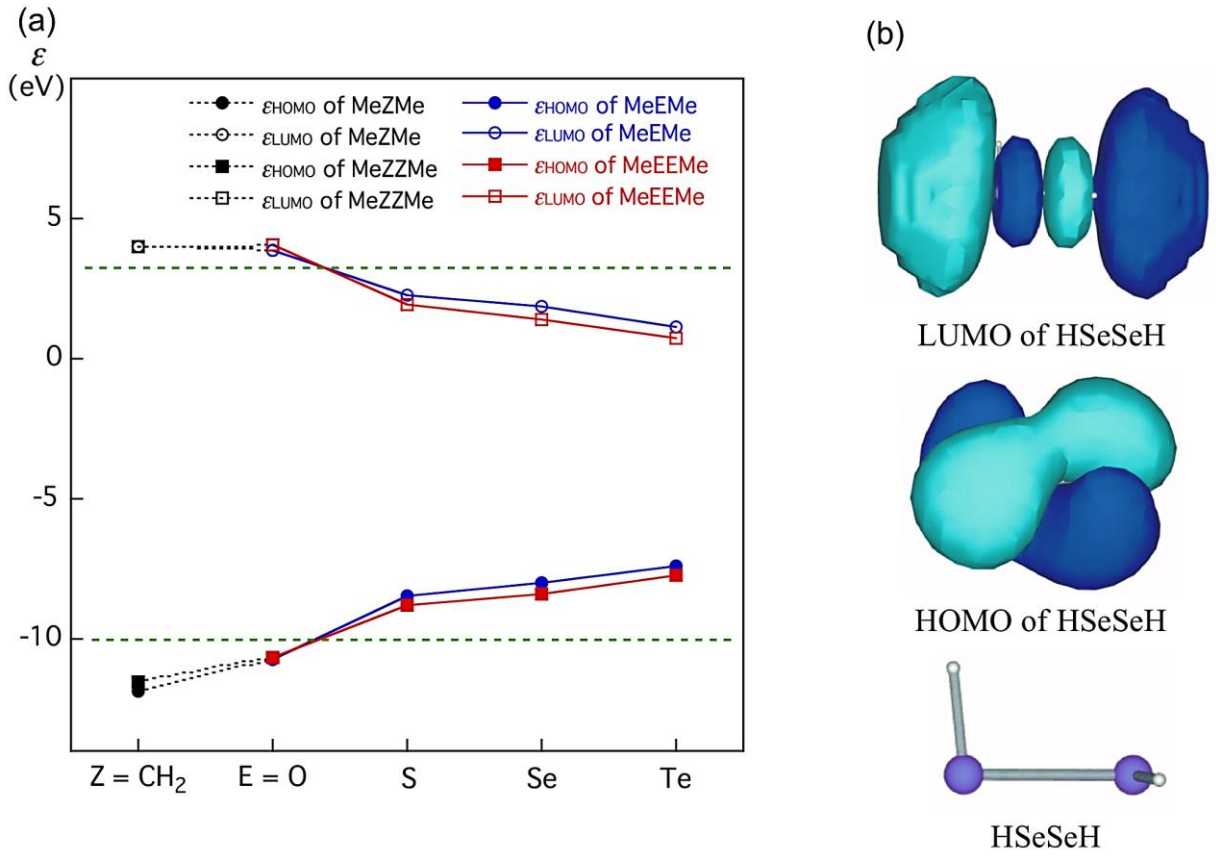

Figure 1-1. (a) Plot of ε_{HOMO} and ε_{LUMO} for MeEMe and MeEEMe (E = O, S, Se, and Te, together with CH_2). (b) HOMO and LUMO are also illustrated exemplified by HSeSeH.

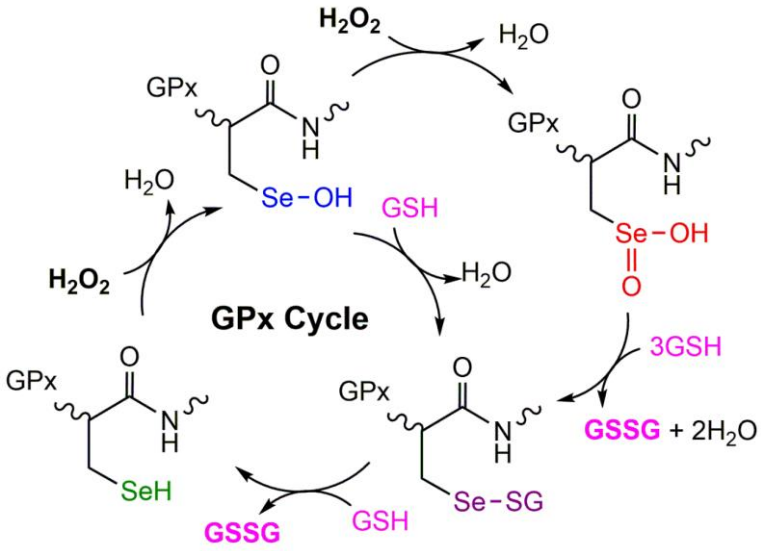

Figure 1-2. A catalytic mechanism, proposed for the antioxidant activity of GPx.

Nakanishi and his co-workers proposed the dynamic nature of interactions based on QTAIM-DFA, recently, by employing the data from the perturbed structures around the fully optimized structures. The nature of the E–E′ bonds (E, E′ = S and Se) and the related interactions will be discussed separately by the static and dynamic nature. Normal coordinates of internal vibrations are mainly employed to generate the perturbed interactions, necessary for QTAIM-DFA. The method to generate the perturbed structures is called NIV.[11] The methodological details, containing QTAIM-DFA, are explained in Chapter 2.

Among the redox process in biology, detoxification of hydroperoxide in the glutathione peroxidase (GPx) process must be one of most important biological activities.[13-25] Figure 1-2 summarizes a catalytic mechanism proposed for the antioxidant activity of GPx, which is a typical example of the intervention of E–E′ (E, E' = S, Se) in biological reactions. Two equivalent of GSH is oxidized to the corresponding oxidized disulfide in the overall process according to the mechanism, while the hydroperoxide is reduced to water.[26, 27]

The behavior of the S–S bond is to be clarified, together with the S–Se and Se–Se bonds, with the role of the bonds in the mechanism bearing in mind. The S–S bond in glutathione disulfide (**1-1**) must be a very important candidate for the behavior to be elucidated, together with S–Se and Se–Se in the derivatives of **1-1** (**1-2** and **1-3**, respectively). Chart 1-1 illustrates the structures of **1-1**–**1-3**. There are a lot of possibilities for the formation of intramolecular hydrogen bonds (HBs) in **1-1**–**1-3**, although the intermolecular HBs of the solute-solute and solute-solvent interactions must also be important in the real system. HBs in **1-1**–**1-3** must be considered, if the basic properties of **1-1**–**1-3** are discussed based on the calculated results, where the usual calculations correspond to the conditions for a single molecule in vacuum. Chart 1-1 also shows the structures of *R*-cystine and derivatives (**1-4**–**1-6**) and MeEE′Me (**1-7**–**1-9**).

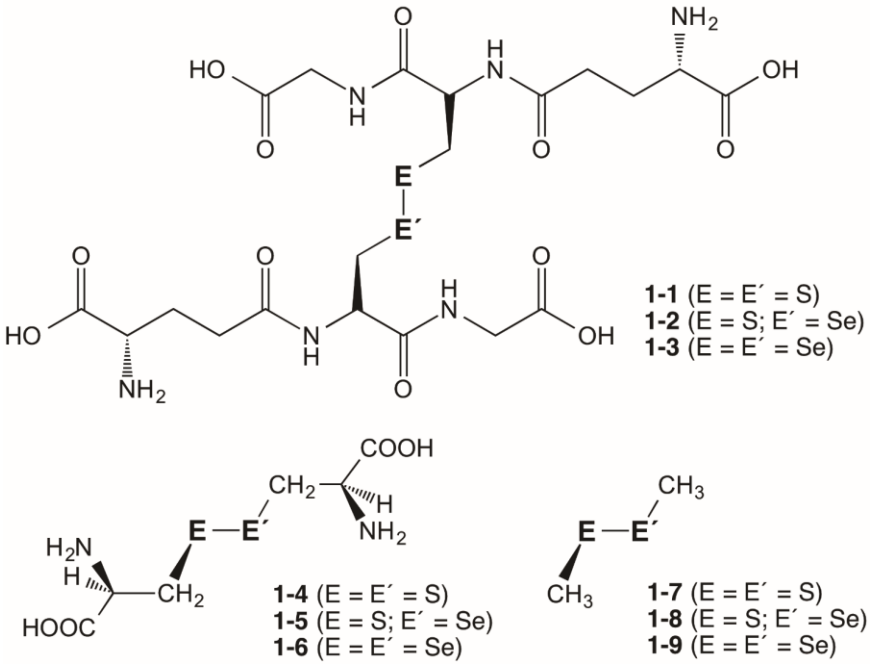

Chart 1-1. Structures of glutathione disulfide (**1-1**) and derivatives (**1-2** and **1-3**) and *R*-cystine (**1-4**) and derivatives (**1-5** and **1-6**), together with MeEE′Me (**1-7**–**1-9**).

Before detailed discussion on the behavior of E–E′ (E, E' = S, Se) in **1-1**–**1-3**, the nature of E–E′ (E, E′ = S, Se) in **1-4**–**1-6** is discussed in Chapter 3,[28] together with that in **1-7**–**1-9** as the reference. Then the nature of E–E' (E, E' = S, Se) in **1-1**–**1-3** is discussed in Chapter 4,[29] with the behavior of E–E′(E, E′ = S, Se) in **1-4**–**1-6** and **1-7**–**1-9** as the reference.

As mentioned above (see, Figure 1-1), the σ*-orbitals of E–E′ (E, E′ = S and Se) are able to accept rather easily electron pairs of atoms belonging to the groups 15–17 elements (A), due to the low energy levels of σ*(E–E′) with the reasonably high energy levels of n_p(A). If the interaction occurs at one side of E–E′, the interaction can be described by the CT (charge-transfer) interactions of the n_p(A)→σ*(E–E') form. The interaction can be analyzed by the σ(3c-4e) model (the three center-four electron model of the σ bond).[30] What happens, if the CT interactions occur at both sides of E–E′? The process can be described by CT of the n_p(A)→σ*(E–E′)←n_p(A) form. The CT interaction could be described by the double σ(3c-4e) occurred at the both sides of σ*(E–E′). However, Nakanishi and Hayashi have proposed that the CT interaction is analyzed by the extended hypervalent interactions of the E_2A_2 σ(4c-6e) model.[6b-c, 7, 31] Figure 1-3 shows molecular orbital approximation of σ(4c–6e), exemplified by Cl_4^{2-}.

How are the nature of the X---E–E---X interactions in E_2X_2 σ(4c-6e), where the halogen atoms X interact with σ*(E–E)? The results of the investigations for E_2X_2 σ*(4c-6e), mainly based on QTAIM-DFA, are discussed in Chapter 5, together with the structural feature of **1-10**–**1-13** and model **1-A**.[32] Chart 1-2 also shows the structures of **1-10**–**1-13** and model **1-A**.

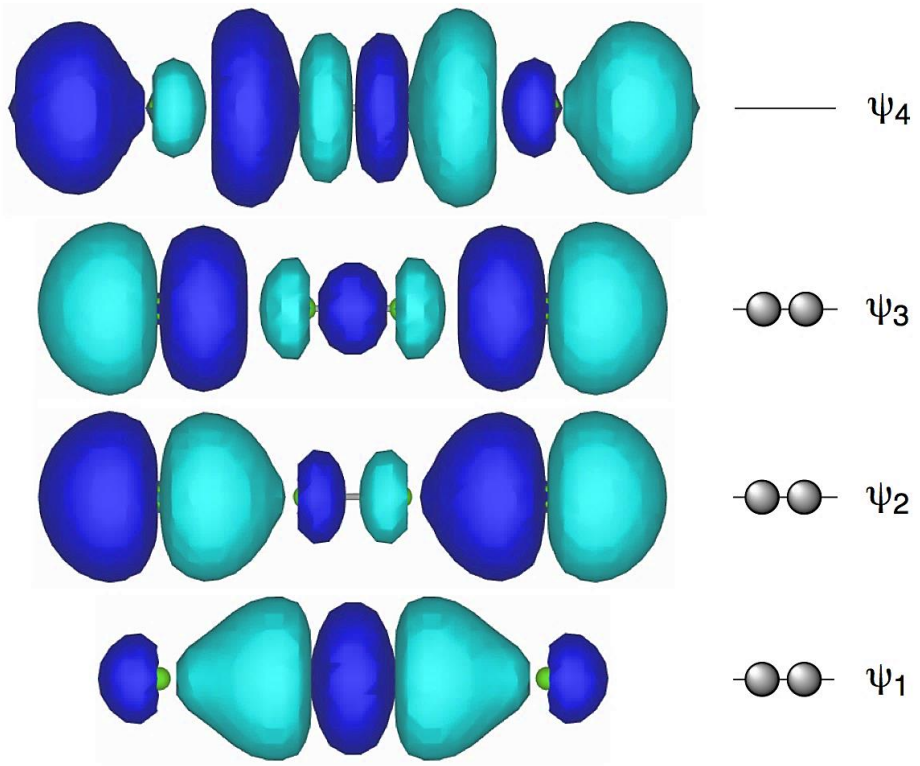

Figure 1-3. Approximate MO model for E_4 σ(4c–6e), exemplified by Cl_4 σ(4c–6e).

Similarly to the case of E_2X_2 σ(4c-6e), σ*(E–E) (E = S and Se) must accept easily electron pairs of chalcogen atoms. The process will forms E_4 σ*(4c-6e). The behavior of ^{B}E---^{A}E–^{A}E---^{B}E in E_4 σ*(4c-6e) is elucidated, together with the structural feature, exemplified by 1-(8-Me$^{B}EC_{10}H_6$)^{A}E–^{A}E($C_{10}H_6$$^{B}E$Me-8')-1': **1-14** ($^{A}E$, ^{B}E) = (S, S), **1-15** (S, Se), **1-16** (Se, S) and **1-17** (Se, Se). E_4 σ(4c-6e) is also elucidated for models **1-B**–**1-E**, $^{B}R_2$$^{B}E$---($^{A}R$)$^{A}E$–$^{A}E$($^{A}R$)---$^{B}E$$^{B}R_2$ (^{A}R, ^{B}R = H and/or Me). The results of the investigations are discussed in Chapter 6.[33]

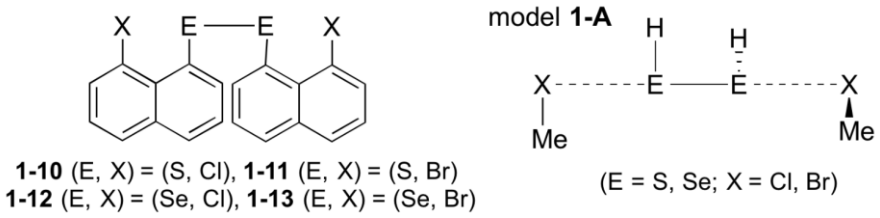

1-10 (E, X) = (S, Cl), **1-11** (E, X) = (S, Br)
1-12 (E, X) = (Se, Cl), **1-13** (E, X) = (Se, Br)

Chart 1-2. Structures of **1-10**–**1-13** and model **1-A**.

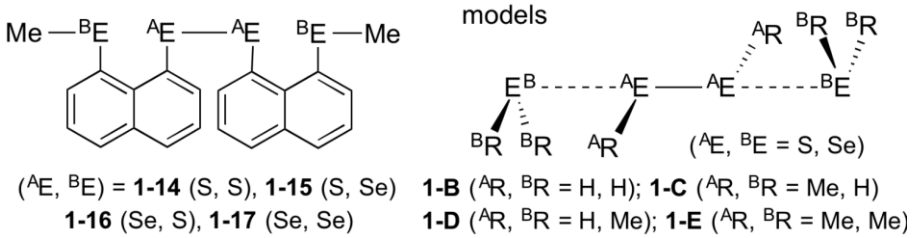

Chart 1-3. Structures of **1-14**–**1-17** and models **1-B**–**1-E**.

How is the real nature of E---E–E---E in E_4 σ*(4c-6e)? It must be very instructive and of highly importance, if the nature of E---E–E---E in E_4 σ*(4c-6e) can be experimentally analyzed. On the basis of such motif, the high-resolution X-ray diffraction determination of electron densities is performed on E---E–E---E in E4 σ*(4c-6e), exemplified by 1-(8-$Ph^BSC_{10}H_6$)^{A}S–^{A}S($C_{10}H_6{}^B$SPh-8')-1' (**1-18**), which consists of S_4 σ(4c-6e) of the linear ^{B}S-∗-^{A}S-∗-^{A}S-∗-^{B}S interaction. The results of the investigations are discussed in Chapter 7, [34] where the nature of E---E–E---E in E_4 σ(4c-6e) (E = S) is experimentally clarified and the experimental results are well in according to the theoretical prediction with QTAIM-DFA.

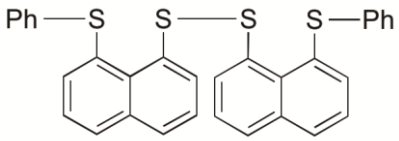

1-18

Chart 1-3. Compound of **1-18**

References

1 a) *Organic Selenium Compounds: Their Chemistry and Biology*, ed. by D. L. Klayman, W. H. H. Gu¨nther, Wiley, New York, **1973**; b) *The Chemistry of Organic Selenium and Tellurium Compounds*, eds. S. Patai, Z. Rappoport, John-Wiley, Sons, New York, **1986**, Vols. 1 and 2; c) *Organic Selenium Chemistry*, ed. D. Liotta, Wiley-Interscience, New York, **1987**; d) *Organoselenium Chemistry, A practical Approach*, ed. T. G. Back, Oxford University Press, Oxford, **1999**; e) *Organoselenium Chemistry Modern Developments in Organic Synthesis*, *Topics in Current Chemistry*, eds. T. Wirth, Springer, Berlin, Heidelberg, New York, London, Paris, Tokyo, **2000**.

2 *Chemistry of Hypervalent Compounds*, ed. K.-y. Akiba, Wiley- VCH, New York, **1999**.

3 a) W. Nakanishi, In *Handbook of Chalcogen Chemistry: New Perspectives in Sulfur, Selenium and Tellurium*: ed. F. A. Devillanova, Royal Society of Chemistry, Cambridge, **2006**, Chap. 10.3, pp. 644–668; b) W. Nakanishi, S. Hayashi, In *Handbook of Chalcogen Chemistry: New Perspectives in Sulfur, Selenium and Tellurium: 2nd Edition*, eds. F. A. Devillanova, W.-W. du Mont, Royal Society of Chemistry, Cambridge, **2013**, Vol. 2, Chap. 12.3, pp. 335–372. c) W. Nakanishi, S. Hayashi, M. Hashimoto, M. Arca, M. C. Aragoni, V. Lippolis, in *The Chemistry of Organic Selenium and Tellurium Compounds*, ed. Z. Rappoport, Wiley, New York, 2013, vol. 4, ch. 11, pp. 885–972.

4 A. J. Mukherjee, S. S. Zade, H. B. Singh, R. B. Sunoj, *Chem. Rev.* **2010**, 110, 4357–4416.

5 a) M. Kulcsar, A. Beleaga, C. Silvestru, A. Nicolescu, C. Deleanu, C. Todasca, A. Silvestru, *Dalton Trans.* **2007**, 2187–2196; b) A. Beleaga, M. Kulcsar, C. Deleanu, A. Nicolescu, C. Silvestru, A. Silvestru, *J. Organomet. Chem.* **2009**, *694*, 1308–1316.

6 a) S. Hayashi and W. Nakanishi, *J. Org. Chem.* **1999**, *64*, 6688–6696; b) W. Nakanishi, S. Hayashi and S. Toyota, *J. Org. Chem*. **1998**, *63*, 8790–8800; c) W. Nakanishi, S. Hayashi and S. Toyota, *Chem. Commun*. **1996**, 371–372; d) W. Nakanishi, S. Hayashi and H. Yamaguchi, *Chem. Lett.* **1996**, 947–948; W. Nakanishi, *Chem. Lett*. **1993**, 2121–2122.

7 W. Nakanishi, S. Hayashi and T. Arai, *Chem. Commun.* **2002**, 2416-2417.

8 W. Brandt, and L. A. Wessjohann, *Chem. Bio. Chem*. **2005**, *6*, 386–394.

9 a) W. Nakanishi, S. Hayashi, K. Narahara, *J. Phys. Chem. A* **2009**, *113*, 10050–10057; b) W. Nakanishi, S. Hayashi, K. Narahara, *J. Phys. Chem. A* **2008**, *112*, 13593–13599.

10 W. Nakanishi, S. Hayashi, *Curr. Org. Chem*. **2010**, *14*, 181–197.

11 W. Nakanishi, S. Hayashi, *J. Phys. Chem*. A **2010**, *114,* 7423–7430.

12 W. Nakanishi, S. Hayashi, K. Matsuiwa, M. Kitamoto, *Bull. Chem. Soc. Jpn*. **2012**, *85*, 1293–1305.

13 a) W. Brandt, L. A. Wessjohann, *Chem Bio Chem*. **2005**, *6*, 386-394; b) S. Gromer, L. A. Wessjohann, J. Eubel, W. Brandt, *Chem Bio Chem*. **2006**, *7*, 1649-1652; c) L. A. Wessjohann, A. Schneider, M. Abbas, W. Brandt, *Biol. Chem*. **2007**, *388*, 997-1006; d) B. M. Lacey, B. E. Eckenroth, S. Flemer Jr, R. J. Hondal, *Biochemistry* **2008**, *47*, 12810-12821; (e) L. A. Wessjohann, A. Schneider, *Chem. Biodiversity* **2008**, *5*, 375-388.

14 B. Ren, W. Huang, B. Åkesson, R. Ladenstein, *J. Mol. Biol*. **1997**, *268*, 869-885.

15 W. A. Hendrickson, *Science* **1991**, *254*, 51-58.

16 A. Ishii, S. Matsubayashi, T. Takahashi, J. Nakayama, *J. Org. Chem*. **1999**, *64*, 1084-1085.

17 a) T. Saiki, K. Goto, R. Okazaki, *Angew. Chem*. *Int. Ed*. **1997**, *36*, 2223-2224.; b) K. Goto, D. Sonoda, K. Shimada, S. Sase, T. Kawashima, *Angew. Chem*., *Int. Ed*. **2010**, *49*, 545-547.

18 G. Mugesh, H. B. Singh, *Chem. Soc. Rev.* **2000**, *29*, 347-357.

19 a) K. P. Bhabak, G. Mugesh, *Chem. Asian. J*. **2009**, *4*, 974-983.; b) B. K. Sarma, G. Mugesh, *Chem. Eur. J*. **2008**, *14*, 10603-10614.

20 a) K. P. Bhabak, G. Mugesh, *Chem. Eur. J*. **2009**, *15*, 9846-9845; b) K. P. Bhabak, G. Mugesh, *Chem. Eur. J*. **2008**, *14*, 8640-8651; c) K. P. Bhabak, G. Mugesh, *Chem. Eur. J*. **2007**, *13*, 4594-4601; d) B. K. Sarma, G. Mugesh, *Inorg. Chem*. **2006**, *45*, 5307-5314; e) P. P. Phadnis, G. Mugesh, *Org. Biomol. Chem*. **2005**, *3*, 2476-2481.

21 M. Iwaoka, R. Ooka, T. Nakazato, S. Yoshida, S. Oishi, *Chem. Biodiversity* **2008**, *5*, 359-374.

22 F. Kumakura, B. Mishra, K. I. Priyadarsini, M. Iwaoka, *Eur. J. Org. Chem*. **2010**, 440-445.

23 K. Arai, K. Dedachi, M. Iwaoka, *Chem.Eur. J*. **2011**, *17*, 481-485.

24 S. Yoshida, F. Kumakura, I. Komatsu, K. Arai, Y. Onuma, H. Hojo, B. G. Singh, K. I. Priyadarsini, M. Iwaoka, Angew. *Chem., Int. Ed*. **2011**, *50*, 2125-2128.

25 D. Manna, G. Mugesh, *J. Am. Chem. Soc.* **2012**, *134*, 4269-4279.

26 L. Flohe, W. A. Günzler, H. H. Schock, *FEBS Lett*. **1973**, *32*, 132-134.

27 L. Flohé, *Glutathione peroxidase brought into focus, in Free radicals in biology*, ed. W. A. Pryor, Academic Press, New York, **1982**, vol. 5, pp. 223-253.

28 Y. Tsubomoto, S. Hayashi, W. Nakanishi, *RSC Adv*. **2015**, *5*, 11534-11540.

29 Y. Tsubomoto, S. Hayashi, W. Nakanishi, in preparation.

30 a) G. C. Pimentel, *J. Chem. Phys*. **1951**, *19*, 446-448; b) J. I. Musher, *Angew. Chem., Int. Ed. Engl.* **1969**, *8*, 54-68.

31 W. Nakanishi, S. Hayashi, S. Morinaka, T. Sasamori, N. Tokitoh, *New J. Chem*. **2008**, *32*, 1881-1889.

32 Y. Tsuomoto, S. Hayashi, W. Nakanishi, T. Sasamori, N. Tokitoh, *Acta Cryst.* **2017**, *B73*, 265-275.

33 W. Nakanishi, Y. Tsubomoto, S. Hayashi, *RSC Adv.* **2016**, *6*, 93195-93204.

34 Y. Tsubomoto, S. Hayashi, W. Nakanishi, L. A. Mapp, S. J. Coles, in preparation.

Chapter 2

Methodological Details for Quantum Theory Atoms-in-Molecules Dual Functional Analysis (QTAIM-DFA)

QTAIM Approach

QTAIM (the quantum theory of atoms-in-molecules) approach, proposed by Bader,[1,2] enables us to analyze, evaluate, and classify the nature of chemical bonds and interactions.[3–7] The bond critical point (BCPs: $\boldsymbol{r}_c$, ∗) is an important concept in QTAIM. BCP of $(\omega, \sigma) = (3, -1)^1$ is a point along the bond path (BP) at the interatomic surface, where charge density $\rho(\boldsymbol{r})$ reaches a minimum. A chemical bond or an interaction between A and B is usually denoted by A–B, which corresponds to BP between A and B in QTAIM. A-∗-B emphasizes the existence of BCP in A–B, in our treatment. As shown in Figure 2-1, the first derivatives of $\rho(\boldsymbol{r})$ will be zero at BCP for each direction of *x*, *y*, and *z* ($\partial\rho_b(\boldsymbol{r}_c)/\partial r_i = 0$ for $r_i = x, y,$ and *z*), where $\rho(\boldsymbol{r})$ at BCP is denoted by $\rho_b(\boldsymbol{r}_c)$ (Figure 2-1a). The behavior of $\rho(\boldsymbol{r})$ around BCP can be understood by the image of the three dimensional saddle point (Figure 2-1b). Therefore, the second derivative of $\rho_b(\boldsymbol{r}_c)$ will be positive in the bond direction ($\partial^2\rho_b(\boldsymbol{r}_c)/\partial z^2 > 0$, where *z* is defined as the bond direction), whereas they will be negative for the directions perpendicular to *z* ($\partial^2\rho_b(\boldsymbol{r}_c)/\partial x^2 < 0$ and $\partial^2\rho_b(\boldsymbol{r}_c)/\partial y^2 < 0$). $\rho_b(\boldsymbol{r}_c)$ are strongly related to the binding energies[8–14] and bond orders.[15]

The sign of the Laplacian $\rho_b(\boldsymbol{r}_c)$ ($\nabla^2\rho_b(\boldsymbol{r}_c) = \partial^2\rho_b(\boldsymbol{r}_c)/\partial x^2 + \partial^2\rho_b(\boldsymbol{r}_c)/\partial y^2 + \partial^2\rho_b(\boldsymbol{r}_c)/\partial z^2$) indicates that $\rho_b(\boldsymbol{r}_c)$ is depleted or concentrated with respect to its surrounding. While $\rho_b(\boldsymbol{r}_c)$ is locally concentrated relative to the average distribution around BCP if $\nabla^2\rho_b(\boldsymbol{r}_c) < 0$, it is depleted when $\nabla^2\rho_b(\boldsymbol{r}_c) > 0$. On the other hand, total electron energy densities at BCPs ($H_b(\boldsymbol{r}_c)$) must be a more appropriate measure for weak interactions on the energy basis.[1,2,16–20] $H_b(\boldsymbol{r}_c)$ are the sum of kinetic energy densities ($G_b(\boldsymbol{r}_c)$) and potential energy densities ($V_b(\boldsymbol{r}_c)$) at BCPs, as shown by eq (2-1). Electrons at BCPs are stabilized when $H_b(\boldsymbol{r}_c) < 0$, therefore, interactions exhibit the covalent nature in this region, whereas they exhibit no covalency if $H_b(\boldsymbol{r}_c) > 0$, due to the destabilization of electrons at BCPs under the conditions. Eq (2-2) represents the relation between $\nabla^2\rho_b(\boldsymbol{r}_c)$ and $H_b(\boldsymbol{r}_c)$, together with $G_b(\boldsymbol{r}_c)$ and $V_b(\boldsymbol{r}_c)$, which is closely related to the Virial theorem.

$$H_b(\boldsymbol{r}_c) = G_b(\boldsymbol{r}_c) + V_b(\boldsymbol{r}_c) \tag{2-1}$$

$$(\hbar^2/8m)\nabla^2\rho_b(\boldsymbol{r}_c) = H_b(\boldsymbol{r}_c) - V_b(\boldsymbol{r}_c)/2 = G_b(\boldsymbol{r}_c) + V_b(\boldsymbol{r}_c)/2 \tag{2-2}$$

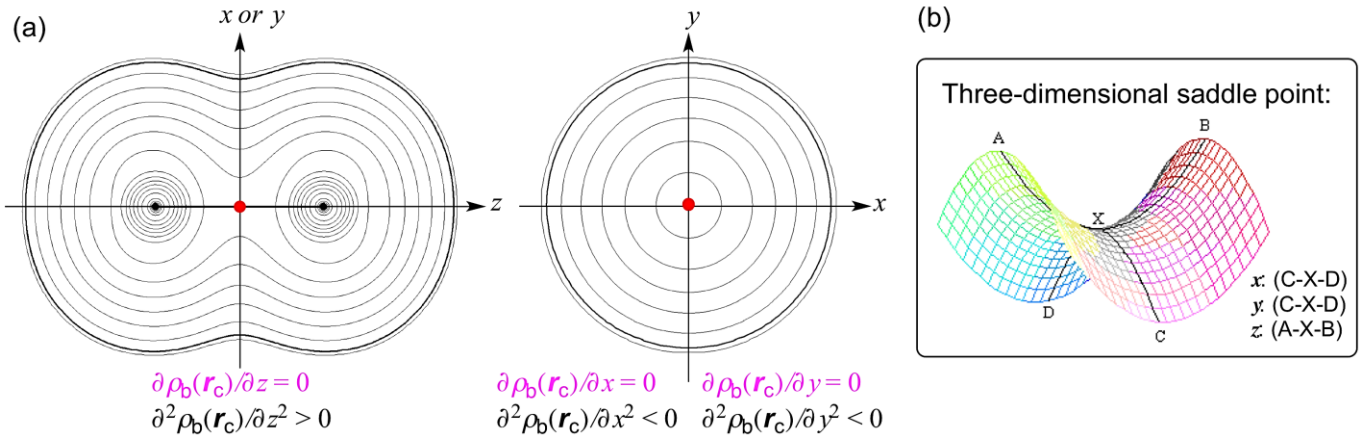

Figure 2-1. Behavior of $\rho(\boldsymbol{r})$ at around BCP. (a) Counter Map of $\rho(\boldsymbol{r})$, exemplified by Cl-∗-Cl and (b) three dimensional saddle point of $\rho(\boldsymbol{r})$ illustrated as a model of BCP.

Chemical bonds and interactions are classified by the signs of $\nabla^2\rho_b(\boldsymbol{r}_c)$ and $H_b(\boldsymbol{r}_c)$. Scheme 2-1 summarizes the classification. Interactions in the region of $\nabla^2\rho_b(\boldsymbol{r}_c) < 0$ are called shared-shell (SS) interactions and they are closed-shell (CS) interactions for $\nabla^2\rho_b(\boldsymbol{r}_c) > 0$. $H_b(\boldsymbol{r}_c)$ must be negative when $\nabla^2\rho_b(\boldsymbol{r}_c) < 0$, since $H_b(\boldsymbol{r}_c)$ are larger than $(\hbar^2/8m)\nabla^2\rho_b(\boldsymbol{r}_c)$ by $V_b(\boldsymbol{r}_c)/2$ where $V_b(\boldsymbol{r}_c)$ are negative at all BCPs eq (2-2). Consequently, $\nabla^2\rho_b(\boldsymbol{r}_c) < 0$ and $H_b(\boldsymbol{r}_c) < 0$ for the SS interactions. The CS interactions are especially called *pure* CS interactions for $H_b(\boldsymbol{r}_c) > 0$ and $\nabla^2\rho_b(\boldsymbol{r}_c) > 0$, since electrons at BCPs are depleted and destabilized under the conditions.[1] Electrons in the intermediate region between SS and *pure* CS, which belong to CS, are locally depleted but stabilized at BCPs, since $\nabla^2\rho_b(\boldsymbol{r}_c) > 0$ but $H_b(\boldsymbol{r}_c) < 0$.[11] The redistribution of $\rho_b(\boldsymbol{r}_c)$ occurs between the electronic states in this region. Nakanishi and Hayashi called the interactions in this intermediate region *regular* CS, since it is necessary to distinguish from *pure* CS. In this thesis, he will call the interactions *regular* CS. The role of $\nabla^2\rho_b(\boldsymbol{r}_c)$ in the classification of interactions can be replaced by $H_b(\boldsymbol{r}_c) - V_b(\boldsymbol{r}_c)/2$, since $(\hbar^2/8m)\nabla^2\rho_b(\boldsymbol{r}_c) = H_b(\boldsymbol{r}_c) - V_b(\boldsymbol{r}_c)/2$ (eq (2-2)). The classification by the signs of $\nabla^2\rho_b(\boldsymbol{r}_c)$ and $H_b(\boldsymbol{r}_c)$ can be achieved by one parameter of θ, as shown in Scheme 2-1.

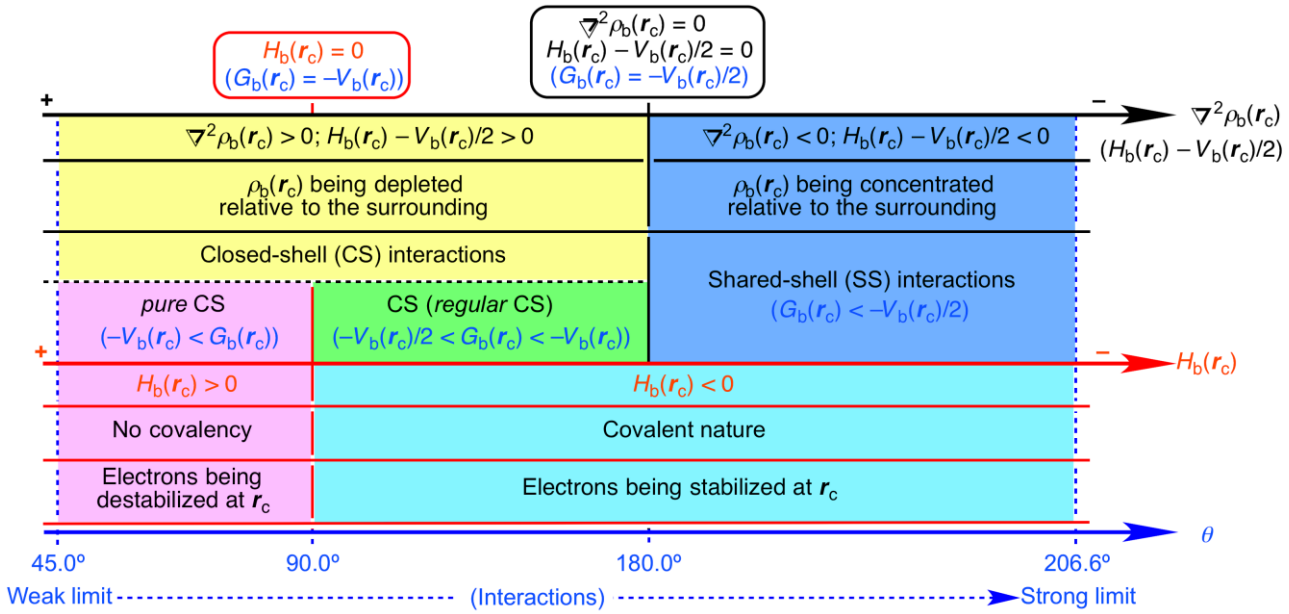

Scheme 2-1. Classification of interactions by the signs of $\nabla^2\rho_b(\boldsymbol{r}_c)$ and $H_b(\boldsymbol{r}_c)$, where $H_b(\boldsymbol{r}_c) - V_b(\boldsymbol{r}_c)/2 = (\hbar^2/8m)\nabla^2\rho_b(\boldsymbol{r}_c)$.

Survey of QTAIM-DFA

QTAIM-DFA: Plots of $H_b(r_c)$ versus $H_b(r_c) - V_b(r_c)/2$

Nakanishi and Hayashi proposed QTAIM-dual functional analysis (QTAIM-DFA) by plotting $H_b(\boldsymbol{r}_c)$ versus $H_b(\boldsymbol{r}_c) - V_b(\boldsymbol{r}_c)/2$ [$= (\hbar^2/8m)\nabla^2\rho_b(\boldsymbol{r}_c)$], after proposal of the plot of $H_b(\boldsymbol{r}_c)$ versus $\nabla^2\rho_b(\boldsymbol{r}_c)$.[17,18] Two treatments are essentially the same, which incorporate the classification shown in Scheme 2-1. The former is obtained by reducing the *x*-axis of the latter by 1/8 in atomic unit according to eq (2-2). Scheme 2-2 summarizes the proposal. Interactions of *pure* CS appear in the first quadrant, those of *regular* CS in the fourth quadrant and data of SS drop in the third quadrant. No interactions appear in the second one. Both axes in Scheme 2-2 are given in energy unit, therefore, distances on the $(x, y) = (H_b(\boldsymbol{r}_c) - V_b(\boldsymbol{r}_c)/2, H_b(\boldsymbol{r}_c))$ plane can be expressed in energy units, which provides an analytical development.

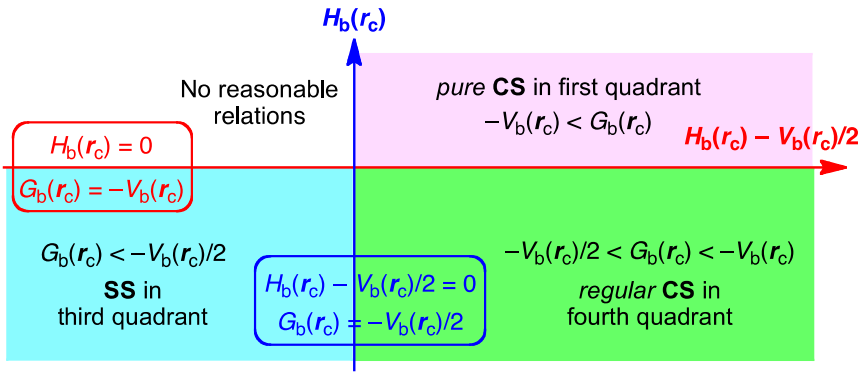

Scheme 2-2. Requirements for data to appear in certain quadrant in the plots of $H_b(\boldsymbol{r}_c)$ versus $H_b(\boldsymbol{r}_c) - V_b(\boldsymbol{r}_c)/2$, where $H_b(\boldsymbol{r}_c) - V_b(\boldsymbol{r}_c)/2 = (\hbar^2/8m)\nabla^2\rho_b(\boldsymbol{r}_c)$.

Analysis of the Plots

Plots of $H_b(\boldsymbol{r}_c)$ versus $H_b(\boldsymbol{r}_c) - V_b(\boldsymbol{r}_c)/2$ are analyzed employing the polar coordinate (R, θ) representation with the (θ_p, κ_p) parameters.[18,19,21] Figure 2-2 explains the treatment. R in (R, θ) is defined by eq (2-3) and given in the energy unit. R corresponds to the energy for an interaction at BCP. The plots show a spiral stream, as a whole. θ is defined by eq (2-4) and measured from the y-axis, which controls the spiral stream of the plot and classifies the interactions. The acceptable range of θ is limited to $45.0^o < \theta < 206.6^o$.[18,19] The range is sub-divided into $45.0^o < \theta < 90.0^o$ for *pure* CS ($0 < H_b(\boldsymbol{r}_c)$; $0 < H_b(\boldsymbol{r}_c) - V_b(\boldsymbol{r}_c)/2$), $90.0^o < \theta < 180.0°$ for *regular* CS ($H_b(\boldsymbol{r}_c) < 0$; $0 < H_b(\boldsymbol{r}_c) - V_b(\boldsymbol{r}_c)/2$) and $180.0° < \theta < 206.6^o$ for SS interactions ($H_b(\boldsymbol{r}_c) < 0$; $H_b(\boldsymbol{r}_c) - V_b(\boldsymbol{r}_c)/2 < 0$). This is the reason for the interactions classified by the sings of $H_b(\boldsymbol{r}_c)$ and $\nabla^2\rho_b(\boldsymbol{r}_c)$ (Scheme 2-2) can be classified only by θ.[18] Each plot for an interaction gives a specific curve with the data from the perturbed structures and the fully-optimized one, which provides important information for the interaction. The curve is expressed by (θ_p, κ_p). θ_p is defined by eq (2-5) and measured from the y-direction, which corresponds to the tangent line of the plot. θ_p specifies the character of the interaction. κ_p is the curvature of the plot (eq (2-6)).[21] Rough criteria are obtained, after analysis of the plots, according to eqs (2-3)–(2-6).[18,19,21] Scheme 2-3 shows the rough criteria for the typical interactions.

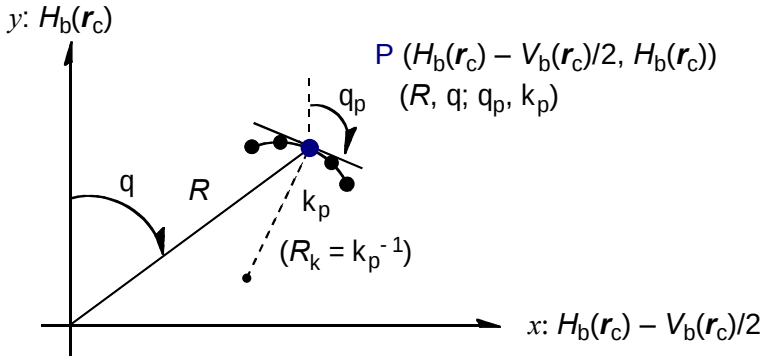

Figure 2-2. Application of QTAIM-DFA. Polar (R, θ) coordinate representation with (θ_p, κ_p) for the plot of $H_b(\boldsymbol{r}_c)$ versus $H_b(\boldsymbol{r}_c) - V_b(\boldsymbol{r}_c)/2$.

$$R = (x^2 + y^2)^{1/2} \tag{2-3}$$

$$\theta = 90^o - \tan^{-1}(y/x) \tag{2-4}$$

$$\theta_p = 90^o - \tan^{-1}(dy/dx) \tag{2-5}$$

$$\kappa_p = |d^2y/dx^2| /[1 + (dy/dx)^2]^{3/2} \tag{2-6}$$

$$k_b(\boldsymbol{r}_c) = V_b(\boldsymbol{r}_c)/G_b(\boldsymbol{r}_c) \tag{2-7}$$

where $(x, y) = (H_b(\boldsymbol{r}_c) - V_b(\boldsymbol{r}_c)/2, H_b(\boldsymbol{r}_c))$

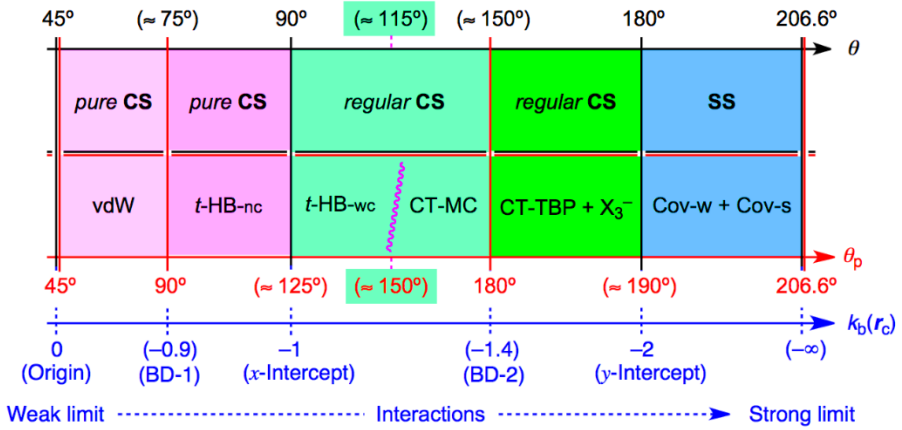

Scheme 2-3. Rough criteria to classify and characterize interactions by θ and θ_p. Values for $\kappa_b(\boldsymbol{r}_c)$ are also given.

To Generate Perturbed Structures-1: POM

How can the perturbed structures be generated, necessary to evaluate the dynamic behavior of interactions? Nakanishi and Hayashi proposed that the perturbed structures can be obtained by the partial optimization method with the length of an interaction in question being fixed suitably. This primitive method is called POM.[18,19,21] A perturbed structure by POM must exist on the potential energy surface, therefore, POM should be closely related to the thermal process. In POM, a molecule or an adduct will be optimized with an interaction in question (r) being fixed to satisfy eq (2-8), where r_o shows the distance in the fully optimized structure with a_o of Bohr radius (0.52918 Å). Therefore, r in the perturbed structures must be fixed longer and shorter than r_o by $0.05a_o$ and $0.1a_o$ with other structural parameters being at the minimum values.

$$r = r_o + wa_o \qquad (2\text{-}8)$$

(w = (0), ±0.05 and ±0.1; a_o = 0.52918 Å)

To Generate Perturbed Structures-2: NIV

Nakanishi and Hayashi also proposed a method to generate the perturbed structures. Normal coordinates of internal vibrations (NIV), obtained by the frequency analysis, were employed to generate the perturbed structures.[21] Nakanishi and his co-workers call this method to generate the perturbed structures NIV. The method is explained in eq (2-9). A k-th perturbed structure in question ($\mathbf{S}_{kw}$) is generated by the addition of the normal coordinates of the k-th internal vibration ($\mathbf{N}_k$) to the standard orientation of a fully-optimized structure ($\mathbf{S}_o$) in the matrix representation.[21] The coefficient f_{kw} in eq (2-9) controls the

difference in the structures between $\mathbf{S}_{kw}$ and $\mathbf{S}_o$: f_{kw} is determined to satisfy eq (2-8) for the interaction distance in question (r) in a perturbed structure.[22] $\mathbf{N}_k$ of five digits are used to predict $\mathbf{S}_{kw}$, although only two digits are usually printed out.[23] Perturbed structures generated with NIV correspond to those with r in question being elongated or shortened by $0.05a_o$ or $0.1a_o$, relative to r_o, (eq (2-8)). NIV may also correspond to the photographic survey of the structures over the instantaneous ones of the selected motion in the zero-point internal vibrations by amplifying them to the extent where r in question satisfies eq (2-9). The selected motion must be most effectively located on the interaction in question among the zero-point internal vibrations.

$$\mathbf{S}_{kw} = \mathbf{S}_o + f_{kw} \bullet \mathbf{N}_k \quad (2\text{-}9)$$

$$y = a_o + a_1 x + a_2 x^2 + a_3 x^3 \ (R_c^2\text{: square of correlation coefficient}) \quad (2\text{-}10)$$

In QTAIM-DFA, each plot of $H_b(r_c)$ versus $H_b(r_c) - V_b(r_c)/2$ for data of five points (w = 0, ±0.05 and ±0.1 in eq (2-9)) is analyzed using a regression curve assuming the cubic function as shown in eq (2-10), where $(x, y) = (H_b(r_c) - V_b(r_c)/2, H_b(r_c))$ ($R_c^2 > 0.99999$ in usual).[19, 24]

Application of QTAIM-DFA to Typical Interactions: Criteria to Classify and Characterize Interactions

QTAIM-DFA had been applied to typical interactions shown in Table 2-1, which are van der Waals forces (vdW)[25,26], hydrogen bonds (HBs), [27,28] molecular complexes formed through Charge transfer (CT-MC), [29] trihalide ions (X_3^-),[29] trigonal bipyramidal adducts formed through CT (CT-TBP), [29] weak covalent bonds (Cov-w) and strong covalent bonds (Cov-s). Figure 2-3 shows the plots of $H_b(\boldsymbol{r}_c)$ versus $H_b(\boldsymbol{r}_c) - V_b(\boldsymbol{r}_c)/2$ for the data of the typical interactions shown in Table 2-1. Data for the perturbed structures around the fully optimized structures are plotted in Figure 2-3, together with data for the fully optimized structures, which are shown by red stars. The static and dynamic nature of the interactions and chemical bonds are evaluated with NIV. Table 2-1 also collects the calculated values for θ_p and κ_p of the interactions in question with NIV (denoted by $\theta_{p;NIV}$ and $\kappa_{p;NIV}$, respectively), together with the frequencies (ν) and force constants (k_f). The criteria to classify and characterize interactions, which is summarized in Schemes 2-2 and 2-3, are obtained from the results. The criteria tell us that $45° < \theta < 90°$ for *pure* CS interactions. The θ_p value predicts the character of the interactions. In the *pure* CS region, the character of the interactions will be the vdW type for $45° < \theta_p < 90°$, whereas it will be the t-HB (typical hydrogen bonds) type with no covalency (t-HBnc) for $90° < \theta_p \leq 125°$, where $\theta_p = 125°$ tentatively corresponds to $\theta = 90°$.

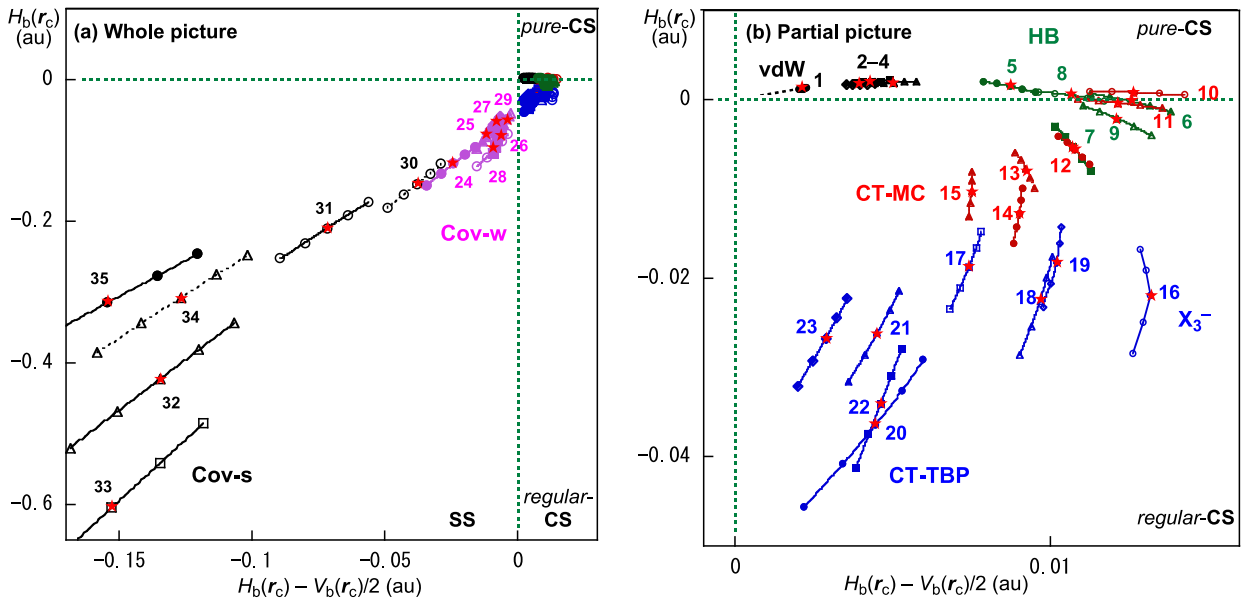

Figure 2-3. Plots of $H_b(\boldsymbol{r}_c)$ versus $H_b(\boldsymbol{r}_c) - V_b(\boldsymbol{r}_c)/2$ of data for the fully optimized structures (shown by red stars), together with the perturbed structures around the fully optimized ones, for the typical interactions (see Table 2-1). (a) Whole picture and (b) partial one for $H_b(\boldsymbol{r}_c) - V_b(\boldsymbol{r}_c)/2 > 0$.

Table 2-1 QTAIM functions and parameters evaluated for weak to strong interactions calculated with NIV.

No.	Species[c] (X-*-Y)	$\rho_b(r_c)$ (ea_o^{-3})	$c\nabla^2\rho_b(r_c)$[d] (au)	$H_b(\boldsymbol{r}_c)$ (au)	$k_b(\boldsymbol{r}_c)$[e]	R (au)	θ (°)
1	He--*--HF[g]	2.2454	0.0022	0.0013	–0.591	0.0025	59.9
2	Ne--*--HF[g]	2.1982	0.0050	0.0019	–0.765	0.0054	69.2
3	Ar--*--HF[g]	2.5142	0.0043	0.0020	–0.696	0.0048	65.0
4	Kr--*--HF[g]	2.6423	0.0040	0.0017	–0.722	0.0043	66.5
5	NN--*--HF[g]	2.0293	0.0087	0.0015	–0.903	0.0088	80.0
6	HF-*-HF	1.8196	0.0125	–0.0002	–1.007	0.0125	90.8
7	HCN-*-HF	1.8238	0.0107	–0.0053	–1.197	0.0120	116.1
8	H_2O-*-HOH	1.9427	0.0106	0.0005	–0.976	0.0107	87.3
9	Me_2O-*-HOH	1.8636	0.0121	–0.0021	–1.079	0.0123	99.8
10	Me_2O-*-Cl_2[g,h]	2.5513	0.0128	0.0007	–0.971	0.0128	86.8
11	Me_2O-*-Br_2[h]	2.5913	0.0123	–0.0004	–1.015	0.0123	91.8
12	Me_2S-*-Cl_2[h]	2.6331	0.0108	–0.0057	–1.207	0.0122	117.6
13	Me_2S-*-Br_2[h]	2.6923	0.0093	–0.0078	–1.296	0.0122	130.0
14	Me_2Se-*-Cl_2[h]	2.5700	0.0093	–0.0125	–1.402	0.0156	143.3
15	Me_2Se-*-Br_2[h]	2.7286	0.0078	–0.0102	–1.396	0.0128	142.7
16	[Cl-*-Cl_2]$^-$	2.2956	0.0133	–0.0220	–1.454	0.0257	149.0
17	[Br-*-Br_2]$^-$	2.5474	0.0078	–0.0185	–1.543	0.0201	157.2
18	[Cl-*-BrCl]$^-$	2.4022	0.0100	–0.0225	–1.530	0.0246	156.1
19	[Br-*-ClBr]$^-$	2.4392	0.0104	–0.0182	–1.465	0.0210	150.1
20	Me_2ClS-*-Cl[h]	2.2650	0.0046	–0.0364	–1.798	0.0367	172.8
21	Me_2BrS-*-Br[h]	2.4387	0.0048	–0.0258	–1.728	0.0262	169.4
22	Me_2ClSe-*-Cl[h]	2.3547	0.0053	–0.0335	–1.759	0.0339	171.0
23	Me_2BrSe-*-Br[h]	2.5196	0.0035	–0.0262	–1.787	0.0264	172.3
24	Me_2S^+-*-Cl[h]	1.9791	–0.0241	–0.1197	–2.673	0.1221	191.4
25	Me_2S^+-*-Br[h]	2.1433	–0.0110	–0.0798	–2.380	0.0806	187.8
26	Me_2Se^+-*-Cl[h]	2.1089	–0.0070	–0.0849	–2.197	0.0852	184.7
27	Me_2Se^+-*-Br[h]	2.2636	–0.0075	–0.0636	–2.308	0.0640	186.7
28	Cl-*-Cl	1.9845	–0.0087	–0.0985	–2.213	0.0988	185.0
29	Br-*-Br	2.2690	–0.0040	–0.0586	–2.158	0.0588	183.9
30	H_3C-*-Cl	1.7713	–0.0376	–0.1468	–3.052	0.1516	194.4
31	H_3C-*-CH_3	1.5236	–0.0718	–0.2097	–4.170	0.2216	198.9
32	H_2C-*-CH_2	1.3349	–0.1335	–0.4195	–3.754	0.4402	197.7
33	HC-*-CH	1.2107	–0.1529	–0.6048	–3.022	0.6238	194.2
34	H_3C-*-H	1.0854	–0.1265	–0.3075	–6.631	0.3325	202.4
35	H-*-H	0.7366	–0.1544	–0.3154	–49.261	0.3512	206.1

(Table 2-1 continued)

No.	Species[c] (X-*-Y)	ν_n (cm^{-1})	k_f[e] (mDyn Å^{-1})	θ_p (°)	κ_p (au^{-1})	coments
1	He--*--HF[g]	69.1	0.013	57.2	8.13	vdW
2	Ne--*--HF[g]	77.6	0.047	84.3	84.79	vdW
3	Ar--*--HF[g]	70.6	0.039	76.4	161.94	vdW
4	Kr--*--HF[g]	64.0	0.029	80.3	219.23	vdW
5	NN--*--HF[g]	130.6	0.114	126.3	235.13	*t*-HB-wc
6	HF-*-HF	166.9	0.081	128.5	103.33	*t*-HB-wc
7	HCN-*-HF	191.5	0.203	167.7	21.60	*t*-HB-wc
8	H_2O-*-HOH	188.1	0.043	116.7	158.13	*t*-HB-nc
9	Me_2O-*-HOH	176.6	0.052	146.4	89.37	*t*-HB-wc
10	Me_2O-*-Cl_2[g,h]	118.0	0.070	98.6	35.54	CT-MC
11	Me_2O-*-Br_2[h]	100.5	0.037	111.7	59.42	CT-MC
12	Me_2S-*-Cl_2[h]	104.4	0.044	162.8	51.24	CT-MC
13	Me_2S-*-Br_2[h]	114.9	0.059	171.5	33.00	CT-MC
14	Me_2Se-*-Cl_2[h]	123.5	0.058	182.3	14.47	CT-MC
15	Me_2Se-*-Br_2[h]	108.8	0.078	181.0	13.82	CT-MC
16	[Cl-*-Cl_2]$^-$	292.5	1.763	180.2	23.75	X_3^-
17	[Br-*-Br_2]$^-$	198.9	1.840	186.5	6.33	X_3^-
18	[Cl-*-BrCl]$^-$	248.3	1.721	185.2	5.58	X_3^-
19	[Br-*-ClBr]$^-$	271.5	1.689	183.4	10.74	X_3^-
20	Me_2ClS-*-Cl[h]	334.6	0.389	192.8	4.84	CT-TBP
21	Me_2BrS-*-Br[h]	358.5	0.294	188.9	2.89	CT-TBP
22	Me_2ClSe-*-Cl[h]	307.8	0.366	186.3	0.57	CT-TBP
23	Me_2BrSe-*-Br[h]	233.4	0.946	189.0	1.95	CT-TBP
24	Me_2S^+-*-Cl[h]	565.4	2.456	198.2	0.16	Cov-w
25	Me_2S^+-*-Br[h]	450.9	1.450	193.7	0.31	Cov-w
26	Me_2Se^+-*-Cl[h]	465.8	4.625	185.6	1.14	Cov-w
27	Me_2Se^+-*-Br[h]	337.8	2.952	190.0	0.37	Cov-w
28	Cl-*-Cl	577.8	6.878	194.2	0.64	Cov-w
29	Br-*-Br	342.7	5.460	190.9	0.27	Cov-w
30	H_3C-*-Cl	779.0	2.509	198.3	0.19	Cov-s
31	H_3C-*-CH_3	1435.0	1.540	202.6	0.54	Cov-s
32	H_2C-*-CH_2	1680.2	4.708	199.4	0.05	Cov-s
33	HC-*-CH	1968.5	9.214	195.9	0.06	Cov-s
34	H_3C-*-H	3203.6	6.660	202.5	0.12	Cov-s
35	H-*-H	4517.6	12.119	206.4	0.01	Cov-s

[a] Calculated with the 6-311++G(3df,3pd) basis sets at the MP2 level. [b] See also ref. 18. [c] Data are given for interaction at BCP, which is shown by * as in He--*--HF ($C_{\infty v}$). [d] $c = \hbar^2/8m$. [e] $k_b(\boldsymbol{r}_c) = V_b(\boldsymbol{r}_c)/G_b(\boldsymbol{r}_c)$. [f] mDyne Å^{-1}. [g] An interaction with a BCP denoted by --*-- stands for the *pure* CS interaction, while -*- for the regular CS or SS interaction. [h] The 6-311+G(3d,2p) basis sets being employed only for C and H in CH_3. See also ref. 21.

Application of NIV, Explained and Exemplified by N≡N-∗-H–F.

The process to generate the perturbed structures with NIV is explained, exemplified by N≡N---H–F ($C_{\infty v}$). Seven internal vibrations belong to N≡N---H–F ($C_{\infty v}$). They are three stretching vibrations of ν_3 (ν_{SG}: 130.6 cm^{-1}), ν_6 (ν_{SG}: 2203.5 cm^{-1}), and ν_7 (ν_{SG}: 4091.2 cm^{-1}), if evaluated with the 6-311++G(3df,3pd) basis sets at the MP2 level. Angular deformations were reported to affect a little the dynamic behavior of interactions,[21] therefore, two sets of doubly degenerate angular deformations of ν_1 and ν_2 (ν_{PI}: 99.5 cm^{-1}) and ν_4 and ν_5 (ν_{PI}: 505.7 cm^{-1}) are neglected form the discussion. Internal frequency motions of ν_3, ν_6, and ν_7 locate mainly on N-∗-H, N≡N, and H–F in N≡N-∗-H–F. $\mathbf{N}_3$ (corresponding to ν_3), $\mathbf{N}_6$ (ν_6), and $\mathbf{N}_7$ (ν_7) were employed for NIV. For $\mathbf{N}_3$, $f_3 = -0.05373$ satisfied $w = 0.1$ in eq (2-9). In this case, $wa_o = 0.052918$ Å for H-∗-N with $w'a_o = 0.000204$ Å for N≡N and $w'a_o = -0.000043$ Å for H–F, where $r = r_o + wa_o$ for H---N and $r' = r_o' + w'a_o$ for N≡N and H–F. Consequently, $w'/w = 0.004$ for N≡N and –0.001 for H–F, when $w/w = 1.000$ for H---N at $w = 0.1$. The largest displacement in H-∗-N is confirmed for $\mathbf{N}_3$ (ν_3), which should be employed for H-∗-N with NIV. The H-∗-N interaction is called major and others minor with respect to $\mathbf{N}_3$. In the process of NIV, the major interaction for NIV must correspond to that in question.

Figure 2-4 shows the plots of $H_b(\boldsymbol{r}_c)$ versus $H_b(\boldsymbol{r}_c) - V_b(\boldsymbol{r}_c)/2$ at the *pure* CS region of N-∗-N--∗--H-∗-F for the data obtained with NIV employing $\mathbf{N}_3$, $\mathbf{N}_6$, and $\mathbf{N}_7$, which correspond to major, minor, and minor interactions for N--∗--H, respectively. The QTAIM-DFA parameters of (θ_p, κ_p) for N--∗--H obtained with NIV employing $\mathbf{N}_3$, $\mathbf{N}_6$, and $\mathbf{N}_7$ are given in the figure. The dynamic behavior of the N--∗--H interaction is characterized by (θ_p, κ_p) of (126.3°, 235 au^{-1}).

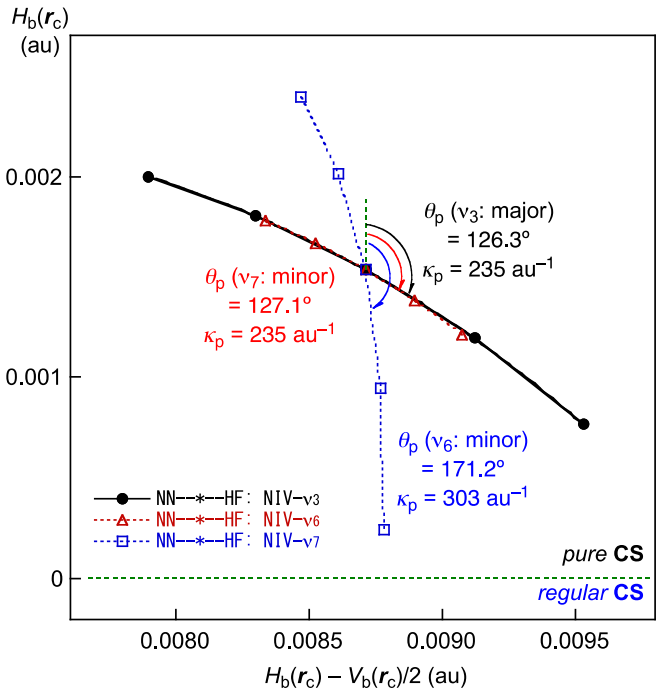

Figure 2-4. Plots of $H_b(\boldsymbol{r}_c)$ versus $H_b(\boldsymbol{r}_c) - V_b(\boldsymbol{r}_c)/2$ for the H-∗-F interaction in N≡N---H–F. Perturbed structures are generated with NIV employing $\mathbf{N}_3$ (●), $\mathbf{N}_6$ (△), and $\mathbf{N}_7$ (□), which correspond to the major, minor, and minor interactions, respectively.

Appendix

Abbreviated Words

QTAIM-DFA・・・・Quantum theory of Atoms-in-Molecules dual functional analysis

POM ・・・・・・・・Partial optimization method

NIV ・・・・・・・・Normal coordinates of internal vibrations

BCP ・・・・・・・・Bond critical point

RCP ・・・・・・・・Ring critical point

CCP ・・・・・・・・Cage critical point

BP ・・・・・・・・Bond Path

$\rho_b(\boldsymbol{r}_c)$ ・・・・・・・・Electron densities at BCPs

$\nabla^2\rho_b(\boldsymbol{r}_c)$ ・・・・・・・・Laplacian $\rho_b(\boldsymbol{r}_c)$; second derivative of $\rho_b(\boldsymbol{r}_c)$;

$(\hbar^2/8m)\nabla^2\rho_b(\boldsymbol{r}_c) = H_b(\boldsymbol{r}_c) - V_b(\boldsymbol{r}_c)/2$

$H_b(\boldsymbol{r}_c)$ ・・・・・・・・Total electron energy densities at BCPs; $G_b(\boldsymbol{r}_c) + V_b(\boldsymbol{r}_c)$

$G_b(\boldsymbol{r}_c)$ ・・・・・・・・Kinetic energy densities at BCPs

$V_b(\boldsymbol{r}_c)$ ・・・・・・・・Potential energy densities at BCPs

SS interaction・・・・Shared-shell interaction; $\nabla^2\rho_b(\boldsymbol{r}_c) < 0$

CS interaction・・・・Closed-shell interaction; $\nabla^2\rho_b(\boldsymbol{r}_c) > 0$

Pure CS・・・・・・ CS interaction for $H_b(\boldsymbol{r}_c) > 0$

Regular CS・・・・・CS interaction for $\nabla^2\rho_b(\boldsymbol{r}_c) > 0$ and $H_b(\boldsymbol{r}_c) < 0$

vdW ・・・・・・・・Van der Waals

HB ・・・・・・・・Hydrogen bond

t-HB-nc ・・・・・・Typical hydrogen bond no covalency

t-HB-wc ・・・・・ Typical hydrogen bond with covalency

CT-MC ・・・・・・Molecular complexes through charge transfer

X_3^- ・・・・・・・・・Trihalide ions

CT-TBP・・・・・・ Trigonal bipyramidal adducts through charge transfer

Cov-w・・・・・・・Classical chemical bonds of weak cases

Cov-s ・・・・・・・Classical chemical bonds of strong cases

Reference

1 a) *Atoms in Molecules. A Quantum Theory*, ed. by R. F. W. Bader, Oxford University Press, Oxford, UK, **1990**; b) *An Introduction to the Quantum Theory of Atoms in Molecules In The Quantum Theory of Atoms in Molecules: From Solid State to DNA and Drug Design*, eds. C. F. Matta, R. J. Boyd, WILEY-VCH, Weinheim, Germany, **2007**.

2 a) R. F. W. Bader, T. S. Slee. D. Cremer, E. Kraka, *J. Am. Chem. Soc.* **1983**, *105*, 5061–5068; b) R. F. W. Bader, *Chem. Res.* **1991**, *91*, 893–926; c) R. F. W. Bader, *J. Phys. Chem. A* **1998**, *102*, 7314–7323; d) F. Biegler-König, R. F. W. Bader, T. H. Tang, *J. Comput. Chem.* **1982**, *3*, 317–328; e) R. F. W. Bader, *Acc. Chem. Res.* **1985**, *18*, 9–15; f) T. H. Tang, R. F. W. Bader, P. MacDougall, *Inorg. Chem.* **1985**, *24*, 2047–2053; g) F. Biegler-König, J. Schönbohm, D. Bayles, *J. Comput. Chem*. **2001**, *22*, 545–559; h) F. Biegler-König, J. Schönbohm, *J. Comput. Chem.* **2002**, *23*, 1489–1494.

3 J. Molina, J. A. Dobado, *Theor. Chem. Acc.* **2001**, *105*, 328–337.

4 J. A. Dobado, H. Martinez-Garcia, J. Molina, M. R. Sundberg, *J. Am. Chem. Soc.* **2000**, *122*, 1144–1149.

5 S. K. Ignatov, N. H. Rees, B. R. Tyrrell, S. R. Dubberley, A. G. Razuvaev, P. Mountford, G. I. Nikonov, *Chem. Eur. J.* **2004**, *10*, 4991–4999.

6 S. K. Tripathi, U. Patel, D. Roy, R. B. Sunoj, H. B. Singh, G. Wolmershäuser, R. J. Butcher, *J. Org. Chem.* **2005**, *70*, 9237–9247.

7 R. J. Boyd, S. C. Choi, *Chem. Phys. Lett.* **1986**, *129*, 62–65.

8 M. T. Carroll, R. F. W. Bader, *Mol. Phys.* **1988**, *65*, 695–722.

9 E. Espinosa, E. Molins, C. Lecomte, *Chem. Phys. Lett.* **1998**, *285*, 170–173.

10 S. J. Grabowski, *J. Phys. Chem. A* **2001**, *105*, 10739–10746.

11 a) E. Espinosa, I. Alkorta, J. Elguero, E. Molins, *J. Chem. Phys.* **2002**, *117*, 5529–5542; b) I. Rozas, I. Alkorta, J. Elguero, *J. Am. Chem. Soc.* **2000**, *122*, 11154–11161.

12 M. Domagała, S. Grabowski, K. Urbaniak, G. Mloston, *J. Phys. Chem. A* **2003**, *107*, 2730–2736.

13 S. Grabowski, W. A. Sokalski, J. Leszczynski, *J. Phys. Chem. A* **2005**, *109*, 4331–4341.

14 M. Domagala, S. Grabowski, *J. Phys. Chem. A* **2005**, *109*, 5683–5688.

15 The bond order (BO), which corresponds to the strength of a chemical bond, is correlated to $\rho_b(\boldsymbol{r}_c)$ by the form shown below, where A and B are constants which depend on the nature of the bonded atoms.[1b] $BO = \exp[A\rho_b(\boldsymbol{r}_c) - B]$.

16 W. Nakanishi, T. Nakamoto, S. Hayashi, T. Sasamori, N. Tokitoh, *Chem. Eur. J.* **2007**, *13*, 255–268.

17 W. Nakanishi, S. Hayashi, K. Narahara, *J. Phys. Chem. A* **2008**, *112*, 13593–13599.

18 W. Nakanishi, S. Hayashi, K. Narahara, *J. Phys. Chem. A* **2009**, *113*, 10050–10057.

19 W. Nakanishi, S. Hayashi, *Curr. Org. Chem.* **2010**, *14*, 181–197.

20 K. T. Potts, J. Kane, *J. Org. Chem.* **1974**, *39*, 3783–3785.

21 W. Nakanishi, S. Hayashi, *J. Phys. Chem. A* **2010**, *114*, 7423–7430.

22 The values of w = (0), ±0.1, and ±0.2 in $r = r_o + wa_o$ were employed for the perturbed structures in POM in refs. 18, 19, since the bond orders becomes 2/3 and 3/2 times larger at w = +0.2 and –0.2 relative to the original values at w = 0, respectively. However, it seems better to employ the perturbed structures as close as possible to the fully optimized ones in NIV. The perturbed structures closer to the fully optimized one will reduce the errors in the QTAIM functions with the perturbed structures generated by NIV and/or POM. Therefore, w = (0), ±0.05, and ±0.1 for $r = r_o + wa_o$ are employed for the analysis in this chapter. Similarly, it is recommended that w = (0), ±0.025, and ±0.05 for $\theta_s = \theta_{so} + wb_o$ are applied to the perturbed structures when the effect from the angular deformations are discussed, since $\pm 0.1b_o$ ($\approx \pm 5.73^o$ with $b_o = 180^o/\pi \approx 57.30^o$) would be too large as the perturbations of angles.

23 It is achieved by changing the corresponding parameters in Gaussian 03 from the default values to print out the normal coordinates of five digits for the purpose.

24 Indeed, fourth functions can be applied to the five points in a plot, but fourth functions may show an irregular behavior with five points in some cases. Therefore, a regression curve of cubic functions would be more suitable as applied in the text, since the calculation errors in the data will be processed suitably.

25 *Molecular Interactions. From van der Waals to Strongly Bound Complexes*, ed. by S. Scheiner, Wiley, New York, **1997**. For example, A. van der Avoird, P. E. S. Wormer, R. Moszynski, *Theory and Computation of Vibration, Rotation and Tunneling Motions of Van der Waals Complexes and their Spectra*, in Chapter 4; J. E. Del Bene, L. Shavitt, *The Quest for Reliability in Calculated Properties of Hydrogen-bonded Complexes*, in Chapter 5; and T. A. Ford, *Ab Initio Predictions of the Vibrational Spectra of Some Molecular Complexes: Comparison with Experiment*, in Chapter 6. See also other chapters.

26 For van der Waals interactions, see C. E. H. Dessent, K. Müller-Dethlefs, *Chem. Rev.* **2000**, *100*, 3999–4021; P. E. S. Wormer, A. van der Avoird, *Chem. Rev.* **2000**, *100*, 4109–4143.

27 E. Espinosa, E. Molins, C. Lecomte, *Chem. Phys. Lett.* **1998**, *285*, 170–173.

28 a) *Hydrogen Bonding – A Theoretical Perspective*, ed. S. Scheiner, Oxford University. Press, New York, **1997**; b) *The Weak Hydrogen Bond in Structural Chemistry and Biology; International Union of Crystallography Monographs on Crystallography*, eds. G. R. Desiraju, T. Steiner, Oxford University Press, New York, **1999**; c) M. Nishio, *Cryst. Eng. Commun.* **2004**, *6*, 130–158; d) E. Espinosa, M. Souhassou, H. Lachekar, C. Lecomte. *Acta Crystallogr. B*, **1999**, *55*, 563–572; e) E. Espinosa, C. Lecomte, E. Molins. *Chem. Phys. Lett.* **1999**, *300*, 745–748; f) E. Espinosa, I. Alkorta, I. Rozas, J. Elguero, E. Molins, *Chem. Phys. Lett.* **2001**, *336*, 457–461; g) C. Gatti, L. Bertini, *Acta Crystallogr A* **2004**, *60*, 438–449.

29 a) *Chemistry of Hypervalent Compounds*, ed. K.-y. Akiba, Wiley-VCH, New York, **1999**; b) W. Nakanishi, *Hypervalent Chalcogen Compounds In Handbook of Chalcogen Chemistry: New Perspectives in Sulfur, Selenium and Tellurium*, ed. by F. A. Devillanova, Royal Society of Chemistry, Cambridge, **2006**, Chap. 10.3, pp. 644–668.

Chapter 3

Dynamic and Static behavior of the E–E′ Bonds (E, E′ = S and Se) in Cystine and Derivatives, Elucidated by QTAIM Dual Functional Analysis

Abstract

Quantum theory atoms-in-molecules dual functional analysis (QTAIM-DFA) is applied to the E–E′ bonds (E, E′ = S and Se) in *R*-cystine (**3-1**) and the derivatives of **3-1**, together with MeEE′Me. $H_b(\boldsymbol{r}_c)$ are plotted versus $H_b(\boldsymbol{r}_c) - V_b(\boldsymbol{r}_c)/2$ at bond critical points (BCPs), where $H_b(\boldsymbol{r}_c) - V_b(\boldsymbol{r}_c)/2 = (\hbar^2/8m)\nabla^2\rho_b(\boldsymbol{r}_c)$. The plots are analyzed by the polar coordinate (R, θ) representation. Data of perturbed structures around the fully optimized structures are also plotted in this treatment. Perturbed structures are generated using NIV (normal coordinates of internal vibrations). Each plot for an interaction with data of a fully optimized and four perturbed structures gives a curve, which supplies important information. It is expressed by (θ_p, κ_p): θ_p corresponds to the tangent line for the plot measured from the y-direction and κ_p is the curvature. While (R, θ) correspond to the static nature of interactions, (θ_p, κ_p) represent the dynamic nature. The behavior of the E–E′ bonds is well described by (R, θ) and (θ_p, κ_p).

Introduction

The E–E′ bonds (E, E' = S and Se) are of current and continuous interest due to the indispensable role in biological, chemical and physical sciences.[1–7] The S–S bond plays a crucial role to maintain the three dimensional structures of peptides. On the other hand, the E–E′ bonds show typical behavior in the redox process,[8] which must be responsible for the highly important biological activities such as detoxification of hydroperoxides in the glutathione peroxidase (GPx) process.[9–21]

Scheme 3-1 summarizes the proposed catalytic mechanism for the antioxidant activity of GPx, which is one of typical examples of the intervention of E–E′ in biological activities. The mechanism involves the initial oxidation of selenol (R_1-SeH) to produce the corresponding selenenic acid (R_1-SeOH), which reacts with glutathione (GSH) to produce selenenyl sulfide (R_1-SeSG). Then a second molecule of GSH attacks at the sulfur center of R_1-SeSG to regenerate the active form of the enzyme (R_1-SeH) (GPx cycle in Scheme 3-1). In the overall process, 2 equivalent of GSH is oxidized to the corresponding disulfide (GSSG), while the hydroperoxide is reduced to water.[22,23] When the peroxide concentration is higher than that of the thiol, the selenium center in the selenenic acid (R_1-SeOH) may undergo further oxidation to produce the seleninic acid (R_1-SeO_2H) (another cycle in Scheme 3-1).

The behavior of the E–E′ bonds seems well described at first glance, however, it is still of highly importance to clarify the causality in the phenomena of the bonds, with physical necessity. Here, he clarified the dynamic and static behavior of the S–S bond in *R*-cystine (**3-1**), of which structures were determined by the X-ray crystallographic analysis, although the derivatives.[24] Similar behavior of the S–Se and Se–Se bonds in the derivatives of **3-1** (**3-2** and **3-3**, respectively) was also investigated, together with the E–E′ bonds in MeEE'Me (E, E' = S and Se) (**3-4**–**3-6**, respectively) (Chart 3-1). The effect of the hydrogen bonds (HBs) in **3-1**–**3-3** on the dynamic and static nature of the E–E' bonds must also be of interest. Quantum theory atoms-in-molecules dual functional analysis (QTAIM-DFA),[25–28] which his research group proposed recently, is applied to the E–E′ bonds in **3-1**–**3-6**. QTAIM-DFA is surveyed next, together with the basic concept of the QTAIM approach introduced by Bader, enables us to analyze and evaluate the nature of chemical bonds and interactions, together with the classification.[30–37]

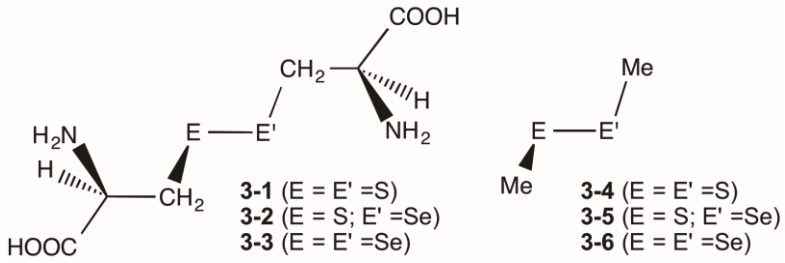

Chart 3-1. Chalcogen–chalcogen bonds in **3-1**–**3-6**, examined.

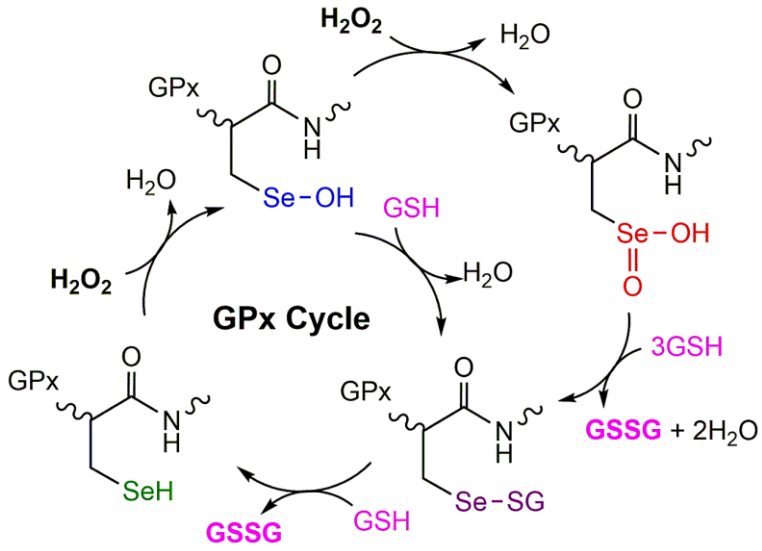

Scheme 3-1. Proposed Catalytic Mechanism for the Antioxidant Activity of GPx.

Methodological details in calculations

Structures of **3-1**–**3-6** were optimized using the Gaussian 09 program package,[38] after the conformation research with the Monte-Carlo method[39] in the Spartan 02[40] for **3-1**–**3-3**. Seven hundred and twenty two conformers were generated for each with the PM3 method.[41] Thirty of most stable conformers by the Monte-Carlo method were re-optimized using the 6-311+G(3d) basis sets[42] for S and Se and the 6-311++G(d, p) basis sets for O, N, C and H at the M06-2X level.[43] The basis set system is called BSS-A in this chapter. Frequency analysis was performed on three of most stable conformers at the same method for each of **3-1a**–**3-3c**, where **a** represents the most stable conformer with the second and third ones by **b** and **c**, respectively. The global minima for **3-4**–**3-6** were determined by usual optimizations with the frequency analysis.

QTAIM functions were calculated using the Gaussian 09 program package[38] with the same method of the optimizations. The results were analyzed with the AIM2000 program.[44] Normal coordinates of internal vibrations (NIV) obtained by the frequency analysis were employed to generate the perturbed structures.[28,29,45] The details of NIV and QTAIM-DFA are explained in Chapter 2.

Results and Discussion

Figure 3-1 draws the three of most stable conformers for **3-1a**–**3-3c**. Figure 3-1 also shows the stretching modes of **3-1a**–**3-3c**, necessary to evaluate the dynamic nature of the E–E′ bonds with NIV. Conformers **3-1a**–**3-3c** are stabilized by intramolecular HBs, as shown in Figure 3-1. Table 3-1 collects the optimized E–E′ distances and torsional angles (ϕ(CEE'C)) for **3-1**–**3-6**, together with the distances and angles for the intramolecular HBs formed between the different moieties of the E–E′ bonds in **3-1a**–**3-3c**.

Figure 3-2 shows contour maps of $\rho_b(\boldsymbol{r}_c)$ drawn on an EE'C plane of **3-1a**–**3-3c**. All BCPs expected are clearly detected, containing those on the E–E′, E–C (E′–C) and C–H bonds. QTAIM-DFA is applied to clarify the static and dynamic behavior of E–E′ in **3-1**–**3-6**. Figure 3-3 shows the plots of $H_b(\boldsymbol{r}_c)$ versus $H_b(\boldsymbol{r}_c) - V_b(\boldsymbol{r}_c)/2$ for **3-1**–**3-6**. The magnified picture around the data of the fully optimized structures for **3-2a**–**3-2c** and **3-5** is also shown in Figure 3-3. QTAIM parameters corresponding to the static and dynamic behavior of E–E′ are obtained for **3-1**–**3-6**, through analysis of the plots in Figure 3-3, according to eqs (2-3)–(2-6) in Chapter 2. Table 3-2 collects the QTAIM functions and parameters of the static and dynamic behavior evaluated for **3-1**–**3-6**.

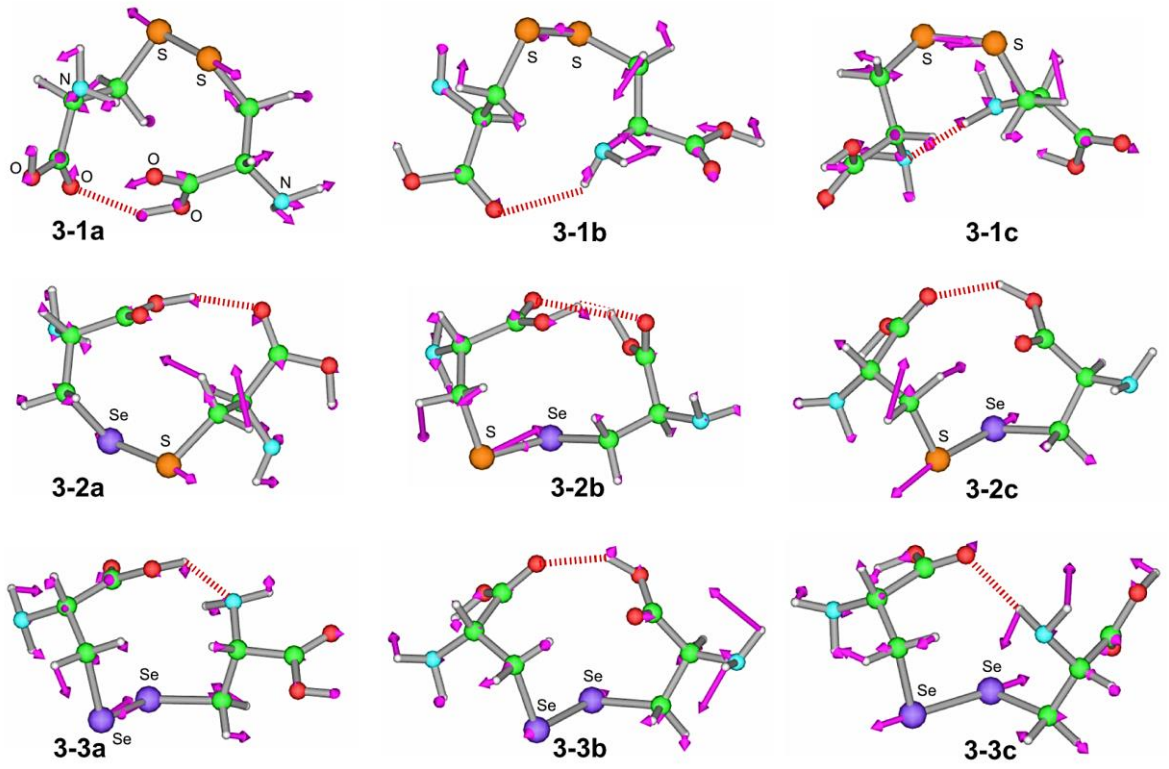

Figure 3-1. Optimized structures for **3-1a**–**3-3c**. Directions of the motions, corresponding to NIV used to generate the perturbed structures, are shown (purple arrows), together with the intramolecular hydrogen bonds (red heavy dotted lines).

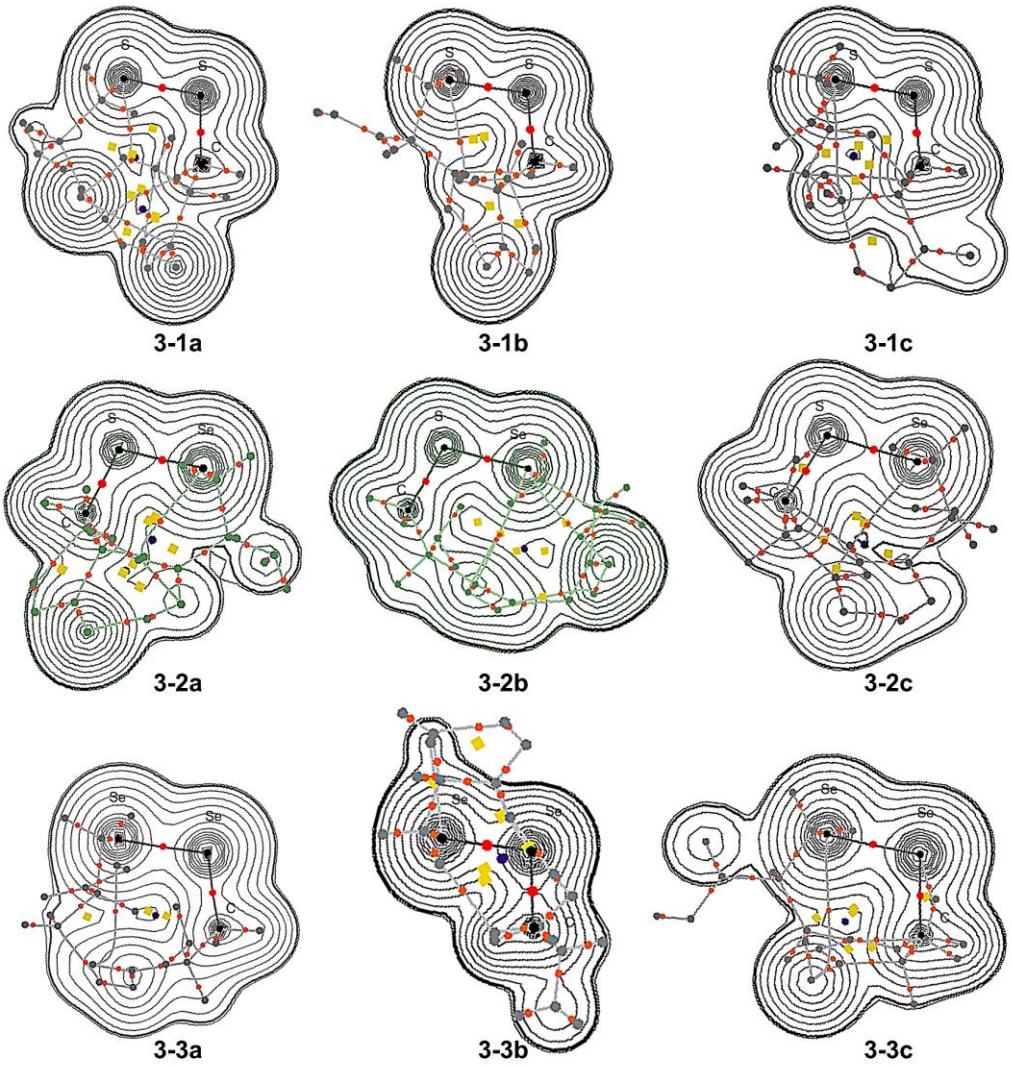

Figure 3-2. Contour maps of $\rho_b(\boldsymbol{r}_c)$ drawn on the EE′C planes of **3-1a**–**3-3c**, together with BCPs (red solid circles), RCPs (ring critical points: lime green solid squares), and bond paths (solid lines). The counters (ea_o^{-3}) are at 2^l ($l = \pm 8, \pm 7$, ---, 0) and 0.0047, which corresponds to the molecular surface (heavy line).

The behavior of E–E′ in **3-1**–**3-6** is examined by comparing the (θ, θ_p, R) values with those of the standard ones. The standard values are roughly determined to classify the interactions in question, employing typical weak to strong interactions. Scheme 2-3 illustrates the standard values for the typical interactions. The results tell us that θ are larger than 180º for SS interactions, which correspond to $H_b(\boldsymbol{r}_c) - V_b(\boldsymbol{r}_c)/2 < 0$. The θ_p value will play an important role to discuss the characters of CS interactions with $\theta <$ 180º ($H_b(\boldsymbol{r}_c) - V_b(\boldsymbol{r}_c)/2 > 0$). While the character of interactions will be that of CT-TBP (trigonal bipyramidal adducts formed through charge-transfer) such as in $Me_2Se(-*-Cl)_2$, if $\theta_p > 180º$, it will be that of CT-MC (molecular complexes formed through CT) such as in $Me_2S-*-Br_2$, when $\theta_p < 180º$, for example. The R values also contribute to classify SS. Classical chemical bonds of SS are strong for $R > 0.15$ au but they would be weak when $R < 0.15$ au.[26]

Table 3-1 Optimized E–E' distances and torsional angles for **3-1**–**3-6**, together with the distances and angles for the intramolecular hydrogen bonds in **3-1a**–**3-3c**[a]

Species (symmetry)	ΔE_{rel} (kJ mol^{-1})	r_o(E, E´) (Å)	ϕ(CEE´C) (°)	(A–H---B)	r_o(A, H) (Å)	r_o(A, H) (Å)	∠AHB (°)
3-1a (C_1)	0.0	2.0625	67.7	(O–H---O)	0.9780	1.9828	149.8
3-1b (C_1)	0.3	2.0471	–82.2	(N–H---O)	1.0155	2.4136	134.4
3-1c (C_1)	0.7	2.0529	88.5	(N–H---N)	1.0210	2.2551	172.3
3-2a (C_1)	0.0	2.1984	–83.9	(O–H---O)	0.9850	1.8025	156.4
3-2b (C_1)	15.7	2.1890	84.3	(O–H---O)	0.9748	1.8996	142.6
				(O–H---O)	0.9743	2.1631	126.4
3-2c (C_1)	17.5	2.2011	94.0	(O–H---O)	0.9771	1.8581	142.9
3-3a (C_1)	0.0	2.3275	88.5	(O–H---N)	0.9863	1.8955	137.7
3-3b (C_1)	1,4	2.3303	93.4	(O–H---O)	0.9773	1.8335	145.1
3-3c (C_1)	3.3	2.3309	90.2	(N–H---O)	1.0193	2.0185	167.6
3-4 (C_2)		2.0491	85.0				
3-5 (C_2)		2.1923	85.6				
3-6 (C_3)		2.3236	86.1				

[a] The 6-311+G(3d) basis sets being employed for S and Se with the 6-311++G(d,p) basis sets for O, N, C and H at the DFT level of M06-2X.

Table 3-2 QTAIM functions and QTAIM-DFA parameters for E-∗-E´ at BCPs of **3-1**–**3-6**.[a]

Species[b] (symmetry)	$\rho_b(\boldsymbol{r}_c)$ (ea_o^{-3})	$c\nabla^2\rho_b(\boldsymbol{r}_c)$[c] (au)	$H_b(\boldsymbol{r}_c)$ (au)	R (au)	θ (°)	$k_b(\boldsymbol{r}_c)$[d]
RS-∗-SR (**3-1a**: C_1)	0.1409	–0.0117	–0.0710	0.0719	189.4	–2.495
RS-∗-SR (**3-1b**: C_1)	0.1443	–0.0126	–0.0749	0.0759	189.6	–2.509
RS-∗-SR (**3-1c**: C_1)	0.1432	–0.0124	–0.0737	0.0747	189.6	–2.508
RS-∗-SeR (**3-2a**: C_1)	0.1171	–0.0041	–0.0529	0.0531	184.4	–2.183
RS-∗-SeR (**3-2b**: C_1)	0.1188	–0.0045	–0.0547	0.0548	184.7	–2.195
RS-∗-SeR (**3-2c**: C_1)	0.1166	–0.0040	–0.0525	0.0527	184.4	–2.180
RSe-∗-SeR (**3-3a**: C_1)	0.1020	–0.0042	–0.0431	0.0433	185.6	–2.242
RSe-∗-SeR (**3-3b**: C_1)	0.1021	–0.0046	–0.0432	0.0434	186.0	–2.268
RSe-∗-SeR (**3-3c**: C_1)	0.1023	–0.0046	–0.0435	0.0437	186.1	–2.269
MeS-∗-SMe (**3-4**: C_2)	0.1446	–0.0131	–0.0751	0.0763	189.9	–2.535
MeS-∗-SeMe (**3-5**: C_2)	0.1189	–0.0048	–0.0544	0.0547	185.0	–2.213
MeSe-∗-SeMe (**3-6**: C_3)	0.1036	–0.0050	–0.0445	0.0448	186.4	–2.291

[a] BSS-A; the 6-311+G(3df) basis sets being employed for S and Se with the 6-311G(d) basis sets for C and H. [b] RSH = *R*-cysteine. [c] $c\nabla^2\rho_b(\boldsymbol{r}_c) = H_b(\boldsymbol{r}_c) - V_b(\boldsymbol{r}_c)/2$, where $c = \hbar^2/8m$. [d] $k_b(\boldsymbol{r}_c) = V_b(\boldsymbol{r}_c)/G_b(\boldsymbol{r}_c)$.

(Table 3-2 continued)

Species[b] (symmetry)	ν_n (n)[e] (cm^{-1})	k_f[f] (mDyn $Å^{-1}$)	θ_p (°)	κ_p (au^{-1})	Classification/ characterization
RS-∗-SR (**3-1a**: C_1)	511.3 (20)	2.060	197.5	0.75	SS/Cov-w
RS-∗-SR (**3-1b**: C_1)	522.5 (21)	1.118	197.4	0.67	SS/Cov-w
RS-∗-SR (**3-1c**: C_1)	506.8 (20)	1.947	197.5	0.69	SS/Cov-w
RS-∗-SeR (**3-2a**: C_1)	414.4 (18)	0.551	188.0	0.34	SS/Cov-w
RS-∗-SeR (**3-2b**: C_1)	423.6 (19)	1.896	188.4	0.33	SS/Cov-w
RS-∗-SeR (**3-2c**: C_1)	414.7 (19)	1.440	188.2	0.40	SS/Cov-w
RSe-∗-SeR (**3-3a**: C_1)	301.9 (15)	1.875	188.9	0.71	SS/Cov-w
RSe-∗-SeR (**3-3b**: C_1)	308.0 (16)	0.174	189.3	0.77	SS/Cov-w
RSe-∗-SeR (**3-3c**: C_1)	298.7 (13)	0.938	189.4	0.68	SS/Cov-w
MeS-∗-SMe (**3-4**: C_2)	513.7 (6)	2.645	197.6	0.66	SS/Cov-w
MeS-∗-SeMe (**3-5**: C_2)	419.7 (6)	2.072	188.6	0.38	SS/Cov-w
MeSe-∗-SeMe (**3-6**: C_3)	307.7 (6)	2.730	189.1	0.77	SS/Cov-w

[e] Corresponding to the interaction in question. [f] Force constant for ν_n.

The (θ/º, θ_p/º, R/au) values for S–S in **3-1a** and **3-4** are (189.4, 197.5, 0.072) and (189.9, 197.6, 0.076), respectively. While the values for S–Se in **3-2a** and **3-5** are (184.4, 188.0, 0.053) and (185.0, 188.6, 0.055), respectively, those for Se–Se in **3-3a** and **3-6** are (185.6, 188.9, 0.043) and (186.4, 189.1, 0.045), respectively. The results show that all E–E´ in **3-1**–**3-6** are classified as the weak covalent bonds, since $\theta >$ 180º with $R < 0.15$ au.[26] The nature of E–E´ in **3-1a**–**3-3a** is predicted to be very close to that of **3-4**–**3-6**, respectively. The strength of E–E´ is reconfirmed in the order of Se–Se ≤ S–Se < S–S. All data of Se–Se, S–Se and S–S in **3-1**–**3-6** appear in the SS region. However, those of Se–Se and S–Se are closer to the *regular* CS region ($\theta_p \approx$ 189º), relative to the case of S–S ($\theta_p \approx$ 198º). Whereas values of R for **3-1a**–**3-3a** are less than those of **3-4**–**3-6**, respectively, the data for **3-1a**–**3-3a** seem to appear at the opposite side of the origin in the plots. The discrepancies must be the reflection of the complex contributions from $G_b(\boldsymbol{r}_c)$ and $V_b(\boldsymbol{r}_c)$ to $H_b(\boldsymbol{r}_c)$ and $H_b(\boldsymbol{r}_c) - V_b(\boldsymbol{r}_c)/2$ in E–E', according to eqs (2-1) and (2-2). It would be difficult to specify the reason for the characteristic behaviour in the plots, based on the data in Tables 3-2.

How are the E–E´ bonds affected by the formation of HBs? The formation of intramolecular HBs stabilizes **3-1**–**3-3**, relative to the conformers with no such interactions. The A–H---B angles are predicted to be around 130–150º for HBs in **3-1**–**3-3**, which must be the reflection of the restricted HBs in **3-1**–**3-3**. The results may suggest that the intramolecular HBs are formed under somewhat undesirable conditions (see Table 3-1). The HBs in **3-1**–**3-3** must affect on the stability and the strength of E–E' in **3-1**–**3-3**.

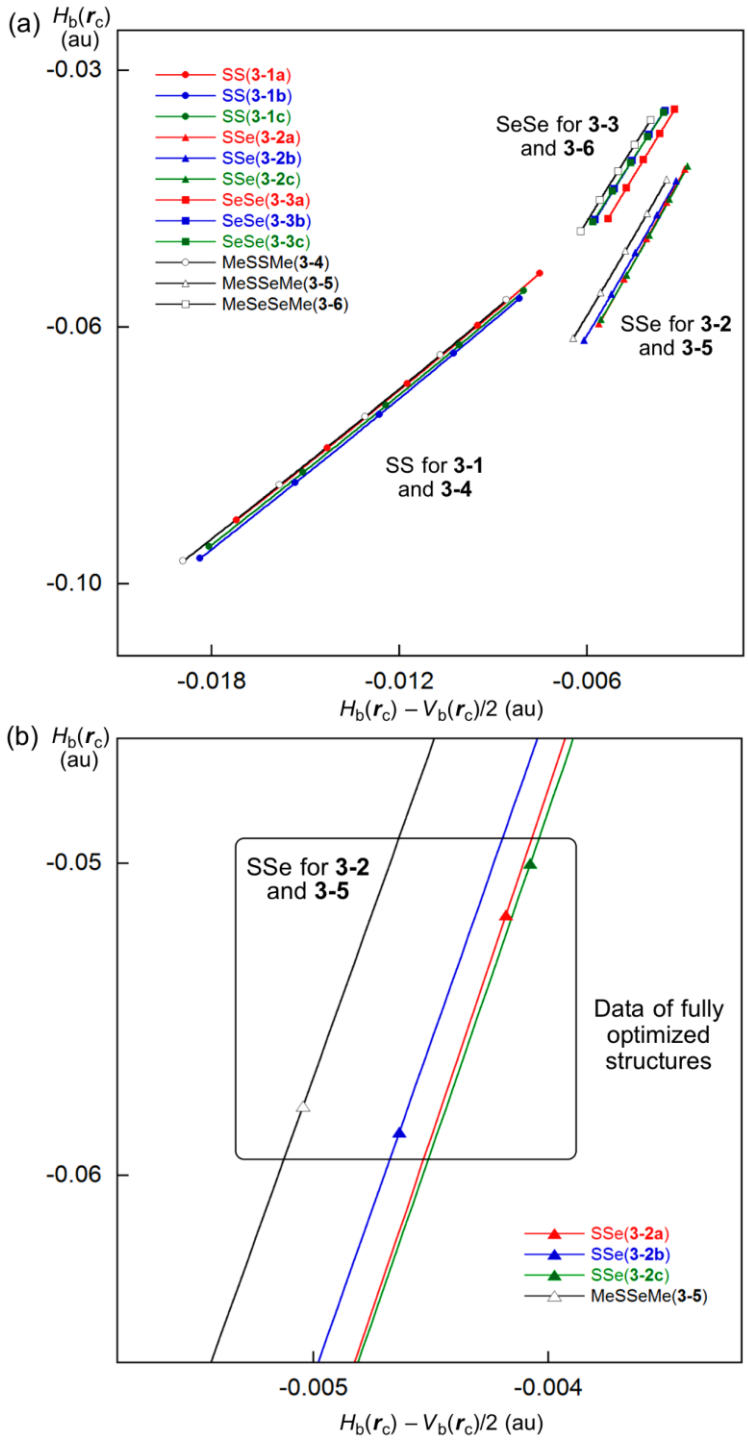

Figure 3-3. Plots of $H_b(r_c)$ versus $H_b(r_c) - V_b(r_c)/2$ for **3-1**–**3-6**. (a) Whole picture and (b) magnified one around data of fully optimized structures for **3-2a**–**3-2c** and **3-5**.

The variation of ϕ(CEE´C) in **3-1**–**3-3**, relative to the case of **3-4**–**3-6**, must be another evidence for the restricted HBs (Table 3-1). The conformation also affect on the strength of E–E´. In the case of **3-2**, the S–Se bond becomes stronger in the order of **3-2c** ≤ **3-2a** < **3-2b**, although very slightly (see Figure 3-3b). The strength of S–Se seems almost independent of the stability in **3-2a**–**3-2c**, for example. Namely, such molecules are stabilized through the formation of HBs, but the E–E' bonds could be sacrificed and somewhat weakened by the distortion.

The nature of the E–E´ bonds in **3-1**–**3-6** is well described with the dynamic nature of (θ_p, κ_p) and the static nature of (R, θ) by applying QTAIM-DFA.

Summary

QTAIM-DFA is applied to the E–E′ bonds (E, E′ = S and Se) in *R*-cystine (**3-1**) and the derivatives (**3-2** and **3-3** for the S–Se and Se–Se derivatives, respectively), together with those of MeEE'Me (**3-4**–**3-6**). The dynamic and static behavior is clarified for E–E′ in **3-4**–**3-6** by the application. The nature of E–E′ in **3-1**–**3-6** is further examined by comparing the (θ, θ_p, R) values with those of the standard ones. The (θ/º, θ_p/º, R/au) values for S–S in **3-1a** and **3-4** are (189.4, 197.5, 0.072) and (189.9, 197.6, 0.076), respectively. While the values for S–Se in **3-2a** and **3-5** are (184.4, 188.0, 0.053) and (185.0, 188.6, 0.055), respectively, those for Se–Se in **3-3a** and **3-6** are (185.6, 188.9, 0.043) and (186.4, 189.1, 0.045), respectively. All E–E′ in **3-4**–**3-6** are classified as the weak covalent bonds. The nature of E–E′ in **3-1a**–**3-3a** is very close to that in **3-4**–**3-6**, respectively. The strength of the bonds is predicted to be in the order of S–S > S–Se ≥ Se–Se. All data of E–E′ in **3-1**–**3-6** appear in the SS region. However, those of Se–Se and S–Se are closer to the *regular* CS region ($\theta_p \approx 189$º), relative to the case of S–S ($\theta_p \approx 198$º). The A–H---B angles in HBs of **3-1**–**3-3** are predicted to be around 130–150º, which must be the reflection of the restricted HBs in **3-1**–**3-3**. Indeed, **3-1**–**3-3** are stabilized by the formation of HBs, but the E–E′ bonds could be sacrificed and somewhat weakened by the distortion. The nature of the E–E′ bonds in **3-1**–**3-6** is well described by (θ_p, κ_p) of the dynamic nature and (R, θ) of the static nature obtained through QTAIM-DFA.

References

1 a) Their Chemistry and Biology, eds. D. L. Klayman and W. H. H. Günther, Wiley, New York, **1973**; b) The Chemistry of Organic Selenium and Tellurium Compounds, eds. S. Patai, Z. Rappoport, John-Wiley and Sons, New York, **1986**; Vols. 1 and 2; c) Organic Selenium Chemistry, ed. D. Liotta, Wiley-Interscience, New York, **1987**; d) Organoselenium Chemistry, A practical Approach, ed. T. G. Back, Oxford University Press, Oxford, **1999**; e) Organoselenium Chemistry Modern Developments in Organic Synthesis, Top. Curr. Chem., ed. T. Wirth, Springer, Berlin, Heidelberg, New York, London, Paris, Tokyo, **2000**.

2 Chemistry of Hypervalent Compounds, ed. K.-y. Akiba, Wiley-VCH, New York, **1999**.

3 a) W. Nakanishi, Hypervalent Chalcogen Compounds In Handbook of Chalcogen Chemistry: New Perspectives in Sulfur, Selenium and Tellurium, ed. F. A. Devillanova, Royal Society of Chemistry, Cambridge, **2006**, ch. 10.3, pp 644–668; b) W. Nakanishi and S. Hayashi, Hypervalent Chalcogen Compounds In Handbook of Chalcogen Chemistry: New Perspectives in Sulfur, Selenium and Tellurium, 2nd Edition, Vol. 2, eds. F. A. Devillanova, W.-W. du Mont, Royal Society of Chemistry, Cambridge, **2013**, ch. 12.3, pp 335–372.

4 A. J. Mukherjee, S. S. Zade, H. B. Singh, R. B. Sunoj, *Chem. Rev*. **2010**, *110*, 4357–416.

5 a) M. Kulcsar, A. Beleaga, C. Silvestru, A. Nicolescu, C. Deleanu, C. Todasca, A. Silvestru, Dalton Trans. **2007**, 2187–2196; b) A. Beleaga, M. Kulcsar, C. Deleanu, A. Nicolescu, C. Silvestru, A. Silvestru, *J. Organomet. Chem.* **2009**, *694*, 1308–1316.

6 a) S. Hayashi, W. Nakanishi, *J. Org. Chem.* **1999**, *64*, 6688–6696; b) W. Nakanishi, S. Hayashi, S. Toyota, *J. Org. Chem.* **1998**, *63*, 8790–8800; c) W. Nakanishi, S. Hayashi, S. Toyota, *Chem. Commun.* **1996**, *371*–372; d) W. Nakanishi, S. Hayashi and H. Yamaguchi, *Chem. Lett*. **1996**, 947–948; e) W. Nakanishi, *Chem. Lett*., **1993**, 2121.

7 W. Nakanishi, S. Hayashi, T. Arai, *Chem. Commun.* **2002**, 2416–2417.

8 W. Nakanishi, S. Hayashi, S. Morinaka, T. Sasamori, N. Tokitoh, *New J. Chem.* **2008**, *32*, 1881–1889.

9 a) W. Brandt, L. A. Wessjohann, *Chem. Bio. Chem*. **2005**, *6*, 386–394; b) S. Gromer, L. A. Wessjohann, J. Eubel, W. Brandt, *Chem. Bio. Chem.* **2006**, *7*, 1649–1652; c) L. A. Wessjohann, A. Schneider, M. Abbas, W. Brandt, *Biol. Chem.*, **2007**, *388*, 997–1006; d) B. M. Lacey, B. E. Eckenroth, S. Flemer, Jr., R. J. Hondal, *Biochemistry* **2008**, *47*, 12810–12821; e) L. A. Wessjohann, A. Schneider, *Chem. Biodiversity*, **2008**, *5*, 375–388.

10 B. Ren, W. Huang, B. Åkesson, R. Ladenstein, *J. Mol. Biol*. **1997**, *268*, 869–885.

11 W. A. Hendrickson, *Science* **1991**, *254*, 51–58.

12 A. Ishii, S. Matsubayashi, T. Takahashi, J. Nakayama, *J. Org. Chem.* **1999**, *64*, 1084–1085.

13 a) T. Saiki, K. Goto, R. Okazaki, *Angew. Chem., Int. Ed.* **1997**, *36*, 2223; b) K. Goto, D. Sonoda, K. Shimada, S. Sase, T. Kawashima, *Angew. Chem. Int. Ed.* **2010**, *49*, 545–547.

14 G. Mugesh, H. B. Singh, *Chem. Soc. Rev.* **2000**, *29*, 347–357.

15 a) K. P. Bhabak, G. Mugesh, *Chem. Asian J.* **2009**, *4*, 974–983; b) B. K. Sarma, G. Mugesh, *Chem. Eur. J.* **2008**, *14*, 10603–10614.

16 a) K. P. Bhabak, G. Mugesh, *Chem. Eur. J*. **2009**, *15*, 9846–9854; b) K. P. Bhabak, G. Mugesh, *Chem. Eur. J.* **2008**, *14*, 8640–8651; c) K. P. Bhabak, G. Mugesh, *Chem. Eur. J.* **2007**, *13*, 4594–4601; d) B. K. Sarma, G. Mugesh, *Inorg. Chem.* **2006**, *45*, 5307–5314; e) P. P. Phadnis, G. Mugesh, *Org. Biomol. Chem.* **2005**, *3*, 2476–2481.

17 M. Iwaoka, R. Ooka, T. Nakazato, S. Yoshida, S. Oishi, *Chem. Biodiv*. **2008**, *5*, 359–374.

18 F. Kumakura, B. Mishra, K. I. Priyadarsini, M. Iwaoka, *Eur. J. Org. Chem.* **2010**, 440–445.

19 K. Arai, K. Dedachi, M. Iwaoka, *Chem. Eur. J.* **2011**, *17*, 481–485.

20 S. Yoshida, F. Kumakura, I. Komatsu, K. Arai, Y. Onuma, H. Hojo, B. G. Singh, K. I. Priyadarsini, M. Iwaoka, *Angew. Chem. Int. Ed.* **2011**, *50*, 2125–2128.

21 D. Manna, G. Mugesh, *J. Am. Chem. Soc.* **2012**, *134*, 4269–4279.

22 L. Flohé, E. A. Günzler, H. H. Schock, *FEBS Lett.* **1973**, *32*, 132–134.

23 L. Flohé, Glutathione peroxidase brought into focus, In Free radicals in biology, ed. by, W. A. Pryor, Academic Press, New York, **1982**, Vol. 5, pp. 223–253.

24 a) V. S. Minkov, E. V. Boldyreva, *Acta Crystallogr*. *Sect. C*. *Cryst. Struct. Commun.* **2009**, *65*, o245; b) T. N. Drebushchak, S. V. Bizyaev, E. V. Boldyreva, *Acta Crystallogr., Sect. C: Cryst. Struct. Commun.* **2008**, *64*, o313; c) V. S. Minkov, E. V. Boldyreva, *Acta Crystallogr., Sect. C: Cryst. Struct. Commun*. **2008**, *64*, o344.

25 W. Nakanishi, S. Hayashi, K. Narahara, *J. Phys. Chem. A* **2008**, *112*, 13593–13599.

26 W. Nakanishi, S. Hayashi, K. Narahara, *J. Phys. Chem. A* **2009**, *113*, 10050–10057.

27 W. Nakanishi, S. Hayashi, *Current Organic Chemistry* **2010**, *14*, 181–197.

28 W. Nakanishi, S. Hayashi, *J. Phys. Chem. A* **2010**, *114*, 7423–7430.

29 W. Nakanishi, S. Hayashi, K. Matsuiwa and M. Kitamoto, *Bull. Chem. Soc. Jpn.* **2012**, *85*, 1293–1305.

30 R. F. W. Bader, *Atoms in Molecules. A Quantum Theory*; Oxford University Press: Oxford, U.K., **1990**.

31 *The Quantum Theory of Atoms in Molecules: From Solid State to DNA and Drug Design*, eds. by, C. F. Matta, R. J. Boyd, Wily-VCH, Weinheim, Germany, **2007**, ch. 1.

32 a) F. Biegler-König, J. Schönbohm, *J. Comput. Chem*. **2002**, *23*, 1489–1497; b) F. Biegler-König, J. Schönbohm, D. Bayles, *J. Comput. Chem.* **2001**, *22*, 545–559; c) R. F. W. Bader, *J. Phys. Chem. A* **1998**, *102*, 7314–7323; d) R. F. W. Bader, *Chem. Rev.*, **1991**, *91*, 893–926; e) R. F. W. Bader, *Acc. Chem. Res*. **1985**, *18*, 9–15; f) T. H. Tang, R. F. W. Bader, P. MacDougall, *Inorg. Chem.* **1985**, *24*, 2047–2053; g) R. F. W. Bader, T. S. Slee, D. Cremer, E. Kraka, *J. Am. Chem. Soc*. **1983**, *105*, 5061–5068; h) F. Biegler-König, R. F. W. Bader, T. H. Tang, *J. Comput. Chem.* **1982**, *3*, 317–328.

33 J. M. Molina, J. A. Dobado, *Theor. Chem. Acc.* **2001**, *105*, 328–337.

34 J. A. Dobado, H. Martînez-Garcîa, J. M. Molina, M. R. Sundberg, *J. Am. Chem. Soc*. **2000**, *122*, 1144–1149.

35 S. K. Ignatov, N. H. Rees, B. R. Tyrrell, S. R. Dubberley, A. G. Razuvaev, P. Mountford, G. I. Nikonov, *Chem. Eur. J.* **2004**, *10*, 4991.

36 S. K. Tripathi, U. Patel, D. Roy, R. B. Sunoj, H. B. Singh, G. Wolmershäuser, R. J. Butcher, *J. Org. Chem.* **2005**, *70*, 9237–9247.

37 R.J. Boyd, S.C. Choi, *Chem. Phys. Lett.* **1986**, *129*, 62–65.

38 Gaussian 09, Revision D.01, M. J. Frisch, G. W. Trucks, H. B. Schlegel, G. E. Scuseria, M. A. Robb, J. R. Cheeseman, G. Scalmani, V. Barone, B. Mennucci, G. A. Petersson, H. Nakatsuji, M. Caricato, X. Li, H. P. Hratchian, A. F. Izmaylov, J. Bloino, G. Zheng, J. L. Sonnenberg, M. Hada, M. Ehara, K. Toyota, R. Fukuda, J. Hasegawa, M. Ishida, T. Nakajima, Y. Honda, O. Kitao, H. Nakai, T. Vreven, J. A. Montgomery, Jr., J. E. Peralta, F. Ogliaro, M. Bearpark, J. J. Heyd, E. Brothers, K. N. Kudin, V. N. Staroverov, R. Kobayashi, J. Normand, K. Raghavachari, A. Rendell, J. C. Burant, S. S. Iyengar, J. Tomasi, M. Cossi, N. Rega, J. M. Millam, M. Klene, J. E. Knox, J. B. Cross, V. Bakken, C. Adamo, J. Jaramillo, R. Gomperts, R. E. Stratmann, O. Yazyev, A. J. Austin, R. Cammi, C. Pomelli, J. W. Ochterski, R. L. Martin, K. Morokuma, V. G. Zakrzewski, G. A. Voth, P. Salvador, J. J. Dannenberg, S. Dapprich, A. D. Daniels, Ö. Farkas, J. B. Foresman, J. V. Ortiz, J. Cioslowski, D. J. Fox, Gaussian, Inc., Wallingford CT, **2009**.

39 a) R. W. B. Ardill, K. J. M. Moriarty, M. Creutz, *Comput. Phys. Commun*. **1983**, *29*, 97–108; b) M. Creutz, *Phys. Rev. Lett.* **1983**, *50*, 1411, see also P. Bratley, B. L. Fox, L. E. Schrage. *A Guide to Simulation*, Springer-Verlag, New York, **1987**; c) G. M. Kalos, P. A. Whitlock, Monte Carlo Methods,

John Wiley, Sons, New York, **1986**; d) A. R. Leach. Molecular Modelling. Principles, *Applications, Addison Wesley Longman*, Essex, England, **1996**.

40 Spartan '02 for Windows, Wavefunction, Inc., Irvine, CA; Spartan '02 Windows, Tutorial and User's Guide, Wavefunction, Inc., Irvine CA, **2001**.

41 J. J. P. Stewart, *J. Comp. Chem*. **1989**, *10*, 209–220.

42 In our experience, the 6-311+G(d) basis sets or higher ones are recommended, when usual organic selenium compounds are calculated. For the 6-311+G(3d) basis sets, see: a) R. C. Binning, L. A. Curtiss, *J. Comput. Chem.* **1990**, *11*, 1206–1216; b) L. A. Curtiss, M. P. McGrath, J.-P. Blaudeau, N. E. Davis, R. C. Binning, Jr., L. Radom, *J. Chem. Phys.* **1995**, *103*, 6104–6113; c) M. P. McGrath, L. Radom, *J. Chem. Phys*. **1991**, *94*, 511–516; d) for the diffuse functions (+ and ++), see T. Clark, J. Chandrasekhar, G. W. Spitznagel, P. v. R. Schleyer, *J. Comput. Chem.* **1983**, *4*, 294–301. See for example, W. Nakanishi, S. Hayashi, *J. Phys. Chem. A* **1999**, *103*, 6074–6081.

43 a) Y. Zhao, G. D. Truhlar, *Org. Lett.* **2006**, *8*, 5753–5755; b) E. S. Wheeler, N. K. Houk, *J. Chem. Theory Comput.* **2010**, *6*, 395–404; b) S. Rayne, K. Forest, *J. Mol. Struct. THEOCHEM*. **2010**, *948*, 102–107; c) S. Rayne, K. Forest, *Nature Precedings*, **2010**, doi:10.1038/npre.2010.4865.1.

44 The AIM2000 program (Version 2.0) is employed to analyze and visualize atoms in molecules: F. Biegler-König, *J. Comput. Chem*. **2000**, *21*, 1040–1048; see also ref. 31b.

45 The bond orders become 1.50 and 0.67 times larger than the initial value if they are calculated at $0.2a_o$ shorter and longer distances from the initial length, respectively.[46] The change in the length could be observed and seems to affect not so much on our discussion to classify the weak interactions.

46 a) L. Pauling, *The Nature of the Chemical Bond, 3rd*, Cornell University Press, Ithaca, New York, **1960**, Chap. 7, pp. 221–264; b) L. Pauling, *J. Am. Chem. Soc*. **1947**, *69*, 542–553.

Chapter 4

Behavior of the E–E′ Bonds (E, E′ = S and Se) in Glutathione Disulfide and Derivatives Elucidated by QC Calculations with QTAIM Approach

Abstract

The nature is elucidated for E–E′ (E, E′ = S and Se) in glutathione disulfide and derivatives (**4-1**–**4-3**, respectively) by applying QTAIM-DFA (QTAIM dual functional analysis), to examine the role of E–E′ in the biological redox process, such as detoxification of hydroperoxides in the glutathione peroxidase process. Five most stable conformers (**a**–**e**) were optimized, after conformation analysis by the Monte-Carlo method. Total electron energy densities $H_b(\boldsymbol{r}_c)$ are plotted versus $H_b(\boldsymbol{r}_c) - V_b(\boldsymbol{r}_c)/2$ at bond critical points (BCPs) of E-∗-E′, where $V_b(\boldsymbol{r}_c)$ are the potential energy densities at BCPs. Data for the fully-optimized structures in the plots are analyzed by the polar coordinate (R, θ) representation, which correspond to the static nature. Those containing the perturbed structures, around the fully optimized structure are described by the (θ_p, κ_p) parameters: θ_p corresponds to the tangent line of each plot and κ_p is the curvature. (θ_p, κ_p) represent the dynamic nature of interactions. The nature of the S–S bonds in **4-1** is shown to be divided into two types, depending on the conformational property, although E–E′ in **4-1a**–**4-3e** are all classified by the shared shell interactions and characterized as the week covalent nature. Contributions from the intramolecular non-covalent interactions are estimated to the stability of the conformers. The stability of a conformer and the strength of E–E′ in the conformer show the inverse trend, as a whole, of which reason is also considered.

Introduction

In this chapter, he further progress the discussion about the E–E′ bonds (E, E′ = S and Se) based on the chapter 3.

The E–E′ bonds play a crucial role in the redox process in the biological processes.[1] High energy levels of HOMO and low energy levels of LUMO of E–E′ must be the driving force for the high reactivity in the redox processes. HOMO and LUMO of E–E′ would correspond to n_p(E/E′) and σ*(E–E′), respectively, where n_p(E/E′) denote the p-type lone pair orbitals of E and/or E′, while σ*(E–E′) corresponds to the σ*-orbital of E–E′. Glutathione disulfide (GSSG: **4-1**) has been used widely as the redox reagent *in vitro*. For the protein folding process, a mixture of **4-1** and glutathione (GSH) is often confirmed as optimum conditions, if the concentrations, similar to those observed *in vivo*,[2] are employed.[3–6] Ribonuclease A of the reduced form will undergo disulfide-coupled folding and gain in structural stability in the presence of **4-1**, for example.[7] Among the biological redox process, detoxification of hydroperoxides in the glutathione peroxidase (GPx) process must be one of most important biological activities.[8–30] The catalytic mechanism proposed for the antioxidant activity of GPx, which is a typical example of the intervention of E–E′ (E, E′ = S, Se) in biological reactions. Two equivalents of GSH are oxidized to the corresponding oxidized disulfide in the overall process according to the mechanism, while the hydroperoxide is reduced to water.[31, 32] (see Scheme 3-1 in chapter 3)

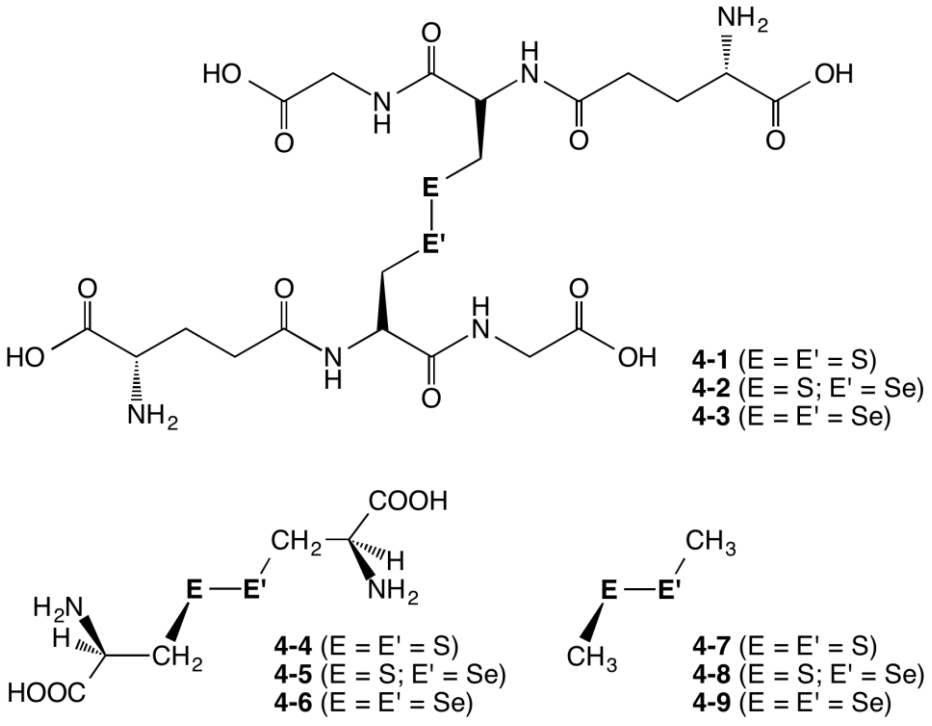

Chart 4-1. Structures of glutathione disulfide (**4-1**) and derivatives (**4-2** and **4-3**) and *R*-cystine (**4-4**) and derivatives (**4-5** and **4-6**), together with MeEE'Me (**4-7**–**4-9**).

The behavior of the S–S bond should be clarified, together the S–Se and Se–Se bonds, with the role of the bonds in the mechanism bearing in mind. The S–S bond in glutathione disulfide (**4-1**) must be a very important candidate for the behavior to be elucidated, together with S–Se and Se–Se in the derivatives of **4-1** (**4-2** and **4-3**, respectively). Chart 4-1 illustrates the structures of **4-1**–**4-3**. There are a lot of possibilities for the formation of intramolecular hydrogen bonds (HBs) in **4-1**–**4-3**, although the intermolecular HBs of the solute-solute and solute-solvent interactions must also be important in the real system. HBs in **4-1**–**4-3** must be considered, if the basic properties of **4-1**–**4-3** are discussed based on the calculated results, where the usual calculations correspond to the conditions for a single molecule in vacuum. Chart 4-1 also shows the structures of *R*-cystine and derivatives (**4-4**–**4-6**) and MeEE'Me (**4-7**–**4-9**).

The structures of **4-1** and **4-4** have been reported, determined by the X-ray crystallographic analysis, although **4-4** is in the di-protonated form. Figure 4-1 shows the structures. The structure of **4-1** was observed as the half-extended form close to the C_2 symmetry with the formation of zwitterions.[33] The structure of **4-4** was reported as the extended form.[34] The extended form in the observed structure of **4-4** may be the results from the electrostatic repulsion of the positive charges developed on **4-4**$^{2+}$. Lots of conformers must exist in such compounds, mainly due to the intramolecular HBs.[35]

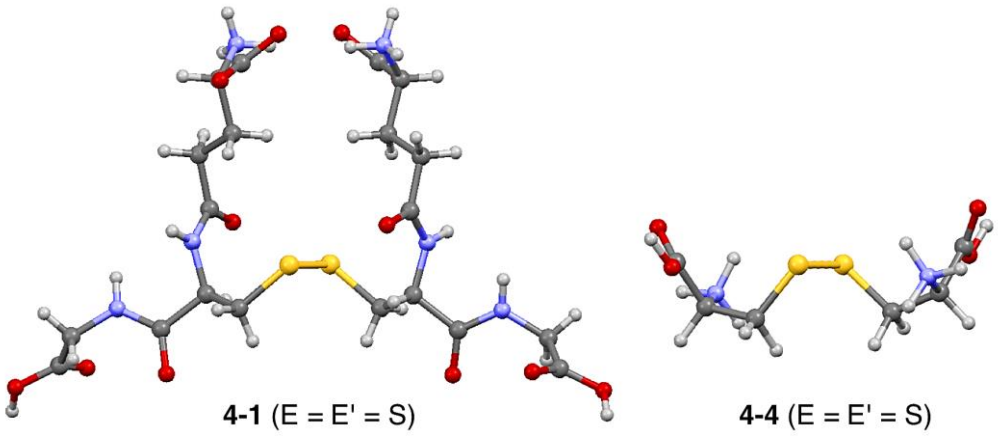

Figure 4-1. Structures of **4-1**[33] and di-protonated form of **4-4**,[34] determined by the X-ray analysis.

Reactions of **4-1** and/or **4-4** in *vivo* proceed under the conditions containing very huge and highly complex species. However, the essence of the elementary processes is expected to be close to that of usual chemical reactions. Therefore, it would be instructive to start with the less complex species, to clarify the behavior of the E–E′ bonds (E, E′ = S and Se). He reported the dynamic and static behavior of S–S in *R*-cystine (**4-4**) and S–Se and Se–Se in the derivatives of **4-4** (**4-5** and **4-6**, respectively), together with MeEE′Me (**4-7**–**4-9**), as references in Chapter 3.[35] It is challenging to clarify the nature of the E–E′ bonds

(E, E′ = S and Se) in glutathione disulfide and the derivatives (**4-1**–**4-3**), although the structures of **4-1**–**4-3** are much complex, relative to **4-4**–**4-6**, respectively. The numbers of HBs plausible for **4-1**–**4-3** will be much larger than those in **4-4**–**4-6**.

The behavior of E–E′ (E, E′ = S and Se) in **4-1**–**4-3** is expected to be related to that in the glutathione peroxidase (GPx) process. The dynamic and static nature of E–E′ in **4-1**–**4-3** is elucidated by applying QTAIM-DFA. The same method is applied to E–E′ in **4-4**–**4-6** and **4-7**–**4-9** to reexamine the nature. Herein, he presented the results of the theoretical elucidation of the nature of the E–E′ bonds in **4-1**–**4-6** with QTAIM-DFA, for the better understanding of the role of E–E′ in chemical sciences, containing the antioxidant activity of GPx. Quantum chemical (QC) calculations are also applied to examine the structural feature of **4-1**–**4-6**. The E–E′ bonds in **4-1**–**4-6** are classified and characterized by employing the criteria and the behavior of the bonds in **4-7**–**4-9**, as references. The details of QTAIM-DFA and the criteria are explained in the Chapter 2, employing Schemes 2-1 and 2-2, Figure 2-1 and eqs (2-1)–(2-7). The basic concept of the QTAIM approach is also surveyed in the Chapter 2.

Methodological Details

The structures were optimized employing the Gaussian 09 programs,[36] unless otherwise noted. Species **4-1**–**4-6** of five conformers for each were optimized with the 6-311+G(3d) basis sets for S and Se with the 6-311++G(d, p) basis sets for O, N, C and H. The basis set system is called BSS-A in this chapter.[37] The DFT level of M06-2X[38] is applied to the calculations. Before the final optimizations, the Monte-Carlo method in Spartan 02[39] was applied to each of **4-1**–**4-6**. At least six thousand and five hundred conformers were generated for each of **4-1**–**4-3** with the MMFF (Merck Molecular Force Field) method.[40] The most stable thirty independent conformers from the Monte-Carlo method were optimized using the 3-21G basis sets at the B3LYP level[41,42] for each of **4-1**–**4-3**. Then the most stable fifteen conformers were optimized with M062X/6-31G(d) for each, predicted with B3LYP/3-21G of Gaussian09 program. The most stable five conformers from M062X/6-31G(d) were further optimized with BSS-A at the M062X level (M062X/BSS-A). The finally optimized five conformers were confirmed by the frequency analysis for the each of **4-1**–**4-3**. We call the five conformers **a**, **b**, **c**, **d**, and **e**, where conformer **a** is most stable among the five, then **b**, then **c**, then **d**, and then **e**. Conformer **e** is most unstable among the five. In the case of **4-4**–**4-6**, seven hundred and twenty conformers were generated for each with the PM3 method.[43] Similarly to the case of **4-1**–**4-3**, the five most stable conformers (**a**-**e**) were determined for each of **4-4**–**4-6**. The structures of **4-7** and **4-9** are optimized retaining the C_2 symmetry, while that of **4-8** is retaining the C_1 symmetry. The population analysis has also been performed by the natural bond orbital method[44] at M06-2X/BSS-A level of theory using natural bond orbital (NBO) program.[45]

QTAIM functions were calculated using the Gaussian 09 program package at the same method of DFT theory (M06-2X/BSS-A), and the data were analyzed with the AIM2000 program.[46,47] Normal coordinates of internal vibrations (NIV) obtained by the frequency analysis were employed to generate the perturbed structures. The details of NIV and QTAIM-DFA is explained in Chapter 2.

Results and discussion

Optimized Structures for Conformers of 4-1–4-6 with M06-2X/BSS-A, Together with 4-7–4-9

The five conformers (**a**–**e**) for each of **4-1**–**4-6** are optimized with M06-2X/BSS-4-A, which are called **4-1a**–**4-1e**, **4-2a**–**4-2e**, **4-3a**–**4-3e**, **4-4a**–**4-4e**, **4-5a**–**4-5e**, and **4-6a**–**4-6e**, respectively. The whole species are also described by **4-1a**–**4-6e**, if necessary. Each conformer is optimized as a non-extended form. The total energies evaluated for ***nx*** (n = 1–6; ***x*** = **a**–**e**) (E(***nx***)) are defined to satisfy eq (4-1). The relative energies for the conformers of **4-1a**–**4-1e** [E_{rel}(**1*x***: ***x*** = **a**–**e**)] are evaluated from **4-1a** with M06-2X/BSS-4-A, so are E_{rel}(***nx***: n = 2–6; ***x*** = **a**–**e**). Structures of zwitterions are confirmed between the amino and carboxyl groups at the terminal positions of the main chains in **4-1a**–**4-3e**, except for **4-1b** and **4-1e**. Only one conformer was optimized for each of **4-7**–**4-9** with M06-2X/BSS-4-A, as expected. Table 4-1 collects the structural parameters of the r(E, E′) distances and torsional angles of ϕ(CEE′C) (= ϕ_A) for **4-1a**–**4-6a** and **4-7**–**4-9**, optimized with M06-2X/BSS-4-A, together with the relative energies, E_{rel} (= E(***nx***) – E(***n*****a**) (n = 1–6; ***x*** = **a**–**e**)).

$$E(\boldsymbol{n}\mathbf{a}) \le E(\boldsymbol{n}\mathbf{b}) \le E(\boldsymbol{n}\mathbf{c}) \le E(\boldsymbol{n}\mathbf{d}) \le E(\boldsymbol{n}\mathbf{e})\ (n = 1\text{–}6) \qquad (4\text{-}1)$$

The r(S, S) values for **4-1a**–**4-1e** are predicted to be longer than that of **4-7**. The differences in r(S, S) for **4-1a**–**4-1e** (Δr(S, S: **4-1*x***) = r(S, S: **4-1*x***) – r(S, S: **7**), where ***x*** = **a**–**e**) are 0.02 Å < Δr(S, S: **4-1*x***) < 0.03 Å for **4-1a**–**4-1c**, Δr(S, S: **4-1*x***) < 0.01 Å for **4-1d**, and Δr(S, S: **4-1*x***) ≈ 0.20 Å for **4-1e**. Similarly, the Δr(E, E') values are less than or very close to 0.01 Å for ***n*****a**–***n*****e** (n = 2–6), except for Δr(E, E') ≈ 0.015 Å for **4-2e**, **4-4a**, **4-5d**, and **4-5e** with Δr(E, E') ≈ 0.03 Å for **4-3d**. There must be a specific reason for the unexpectedly large value of 0.20 Å for Δr(E, E': **4-1e**). As shown in Figure 4-4, three S, S, O atoms align linearly in **4-1e**, which is well explained by assuming the formation of the hypervalent interactions of S_2O σ(3c–4e) of the n_p(O)→σ*(S–S) type. In this interaction, σ*(S–S) accepts electrons from the p-type lone pair orbital of O. As a result, the S–S bond must be unexpectedly elongated relative to the usual length and the O---S distance will be substantially shortened, relative to the sum of the vdW radii. The O---S distance is predicted to be 2.7714 Å, which is shorter than the sum of the vdW radii, by 0.55 Å. The S_2O σ(3c–4e) model explains reasonably the predicted result for **4-1e**.

In the case of the ϕ(CEE'C) (= ϕ_A), the values for **4-1a**–**4-6e** from the corresponding values of **4-7**–**4-9** are given by $\Delta\phi_A$(E, E′: **4-*nx***) = ϕ_A(E, E′: **4-*nx***) – ϕ_A(E, E': MeEE′Me), (where ***n*** = 1–6; ***x*** = **a**–**e**; E, E′ = S and Se). The absolute values of ϕ_A will be employed for the estimation of $\Delta\phi_A$. Magnitudes of the values are $\Delta\phi_A$(E, E′: **4-*nx***) ≈ 58° for **4-3d**, 31° < $\Delta\phi_A$(E, E': **4-*nx***) < 35° for **4-1a**–**4-1c** and **4-1e**, $\Delta\phi_A$(E, E': ***nx***) ≈ 25° for **4-2b**,

$10^{o} \leq \Delta\phi_A$(E, E': **4-*nx***) $\leq 20^{o}$ for **4-1d**, **4-3e**, **4-4e**, and **4-6d**. The magnitudes of $\Delta\phi_A$(E, E': ***nx***) are less than 10^{o} ($-10^{o} \leq \Delta\phi_A$(E, E': ***nx***) $\leq 10^{o}$) for others, except $\Delta\phi_A$(E, E': **4-*nx***) $\approx -12^{o}$ for **4-5d** and **4-6d** and $\Delta\phi_A$(E, E': ***nx***) $\approx -20^{o}$ for **4-2e**, **4-4a**, and **4-5e**. The results must be the reflection from the easy deformation in ϕ_A. To evaluate the energy for the deformation in ϕ_A, **4-7**–**4-9** were optimized assuming $\phi_A = 0°$ and 180°, in addition to the fully optimized structures ($85° \leq \phi_A \leq 86°$). They were optimized to be **4-7** (C_{2v}), **4-8** (C_s) and **4-9** (C_{2v}) at $\phi_A = 0°$ and **4-7** (C_{2h}), **4-8** (C_s) and **4-9** (C_{2h}) at $\phi_A = 180°$. In the case of **4-9**, the structures were further optimized with ϕ_A fixed every 15° for $0° \leq \phi_A \leq 180°$. The results are summarized in Table 4-A1 of the Appendix. Figure 4-2 shows the plot of the energies for the optimized structures versus ϕ_A. The energy seems less than 15 kJ mol^{-1} for $45° \leq \phi_A \leq 135°$ in **4-9**. The energy for the deformation of ϕ_A in **4-7** and **4-8** seems comparable to that in **4-9**. The very easy deformation in ϕ_A is well demonstrated, exemplified by **4-7**–**4-9**, which supports the results shown in Table 4-1. Such easy deformation in ϕ_A is also reported for some dichalcogenides.[48]

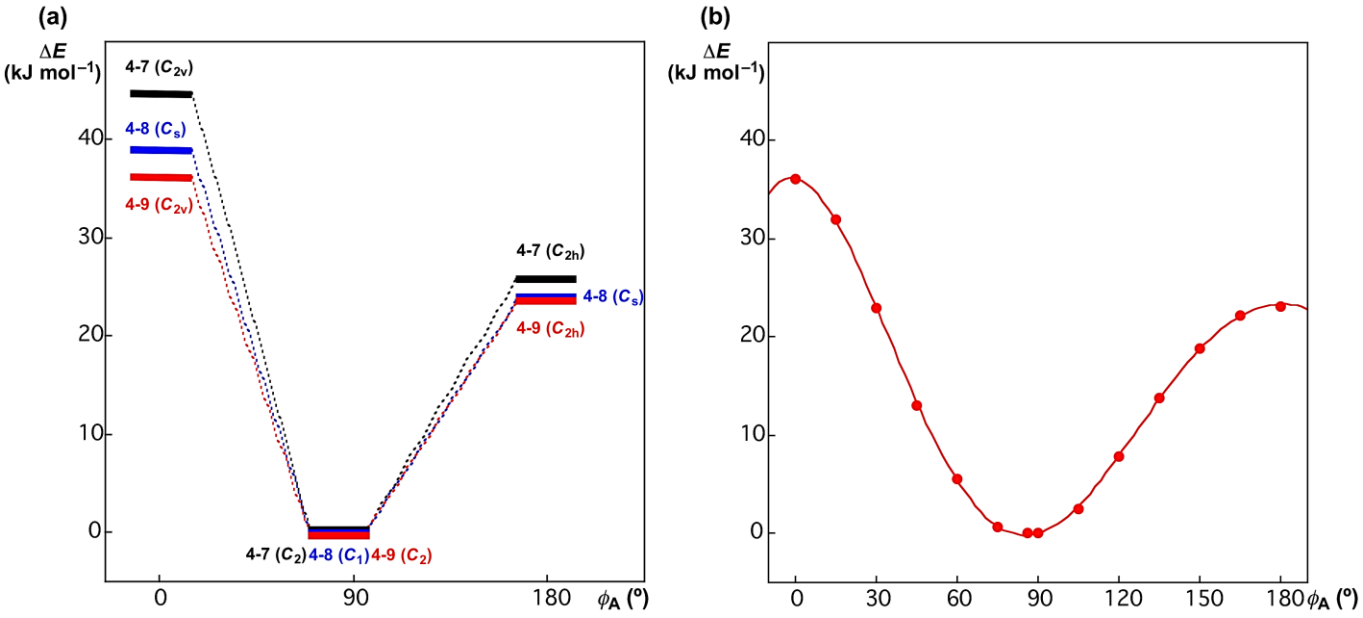

Figure 4-2. Plots of deformation energy (ΔE) versus ϕ_A. For **4-7**–**4-9** (**a**) and for **4-9** (**b**).

Table 4-1 Optimized r(E, E′) distances, torsional angles ϕ(CEE'C) (= ϕ_A), and E_{rel} values for **4-1a**–**4-6e** and **4-7**–**4-9**, evaluated with M06-2X/BSS-A[a]

Species	r_o(E, E′) (Å)	ϕ_A (°)	ΔE_{rel} (kJ mol^{-1})	Species	r_o(E, E′) (Å)	ϕ_A (°)	ΔE_{rel} (kJ mol^{-1})
4-1a	2.0736	–117.4	0.0	**4-4a**	2.0625	67.7	0.0
4-1b	2.0694	–116.4	8.6	**4-4b**	2.0471	–82.2	0.3
4-1c	2.0778	–119.3	14.1	**4-4c**	2.0529	88.5	0.7
4-1d	2.0561	100.3	29.3	**4-4d**	2.0541	–75.7	3.2
4-1e	2.2454	117.9	97.4	**4-4e**	2.0515	95.7	8.8
4-2a	2.2002	–85.6	0.0	**4-5a**	2.1984	–83.9	0.0
4-2b	2.1963	–110.1	1.0	**4-5b**	2.1890	84.3	5.7
4-2c	2.1982	–84.5	18.0	**4-5c**	2.2011	94.0	17.5
4-2d	2.1959	–78.4	23.1	**4-5d**	2.2070	72.9	19.6
4-2e	2.2079	–65.0	23.7	**4-5e**	2.2067	–66.9	27.4
4-3a	2.3252	–85.2	0.0	**4-6a**	2.3275	88.5	0.0
4-3b	2.3215	–82.5	13.6	**4-6b**	2.3303	93.4	1.4
4-3c	2.3138	–92.5	34.9	**4-6c**	2.3309	90.2	3.3
4-3d	2.3546	–144.5	47.9	**4-6d**	2.3351	74.9	3.6
4-3e	2.3320	105.2	58.8	**4-6e**	2.3286	93.1	3.7
4-7	2.0491	85.0	*b*	**4-8**	2.1923	85.6	*b*
4-9	2.3236	86.1	*b*				

[a] BSS-A: The 6-311+G(3d) basis sets for S and Se with the 6-311++G(d,p) basis sets for O, N, C and H.
[b] Not applicable

Structural Feature of 4-1a–4-6a and 4-7–4-9

Figure 4-3 illustrates the molecular graphs of **4-1a**–**4-3a**, drawn on the optimized structures, together with the optimized structures containing the non-covalent interactions. Figure 4-4 shows the molecular graphs of **4-1b**–**4-1e**, drawn on the optimized structures. Molecular graphs of **4-2b**–**4-2e** and **4-3b**–**4-3e** are drawn in Figures 4-A1 and 4-A2 of the Appendix, respectively. Figure 4-5 illustrates the molecular graphs of **4-4a**–**4-6a** and **4-4b**–**4-4e**, drawn on the optimized structures and the optimized structure. Molecular graphs of **4-5b**–**4-5e** and **4-6b**–**4-6e** are drawn in Figures 4-A3 and 4-A4 of the Appendix, respectively. The molecular graphs of **4-7**–**4-9** are shown in Figures 4-A5 of the Appendix.

The structural feature of **4-7**–**4-9** is described, first. Only classical chemical bonds are detected in the molecular graphs of **4-7**–**4-9**, as shown in Figure 4-A5 of the Appendix. Namely, no interactions other than the classical chemical bonds contribute to the interactions in **4-7**–**4-9**. The structural feature of **4-4**–**4-6** is examined, next. Various types of intramolecular interactions are detected in **4-4a**–**4-6e**, which are the HB type of O–H---O, O–H---N, N–H---O, N–H---N, O–H---E(E′), and N–H---E(E′), where E, E′ = S and Se. The E---π type of C=O---E(E′) and O=C---E(E′) are also detected. The conformers must be stabilized through the energy lowering effect by the formation of the intramolecular attractive interactions. The HB and E---π type interactions contribute to stabilize the conformers. The HB and E---π type interactions in the molecular graphs are drawn on the optimized structures, separately by the kind of the interactions, to realize them easily.

The interactions are drawn for O–H---O in red, O–H---N and N–H---O in pink, N–H---N in blue, O–H---E(E′), N–H---E(E′) and O=C---E(E′) in black, and C=O---E(E′) in gray, as shown in Figure 4-5. The stability of the conformers would be related to the number of the interactions. Therefore, the number is counted separately by the kind of interactions, differentiated by the colors. The results are collected in Table 4-2. The C–H---X interactions are also detected. However, they are neglected, since they would not contribute so much to stabilize the conformers.

The molecular graphs are very complex for **4-1a**–**4-3e**. Some efforts are made to classify the interactions in **4-1a**–**4-3e**, as in **4-4a**–**4-6e**. The interactions appeared in the molecular graphs of **4-1a**–**4-3e** are similarly drawn on the optimized structures, as shown in Figure 4-3. The numbers of the intramolecular non-covalent interactions in **4-1a**–**4-3e** are counted separately by the kind of interactions. Table 4-2 collects the results. The numbers of interactions seem to correlate to the stability of the conformers. However, the relation between the stability and the numbers seems not so clear. It must be very difficult to estimate the stability of the conformers numerically through the numbers of intramolecular interactions.

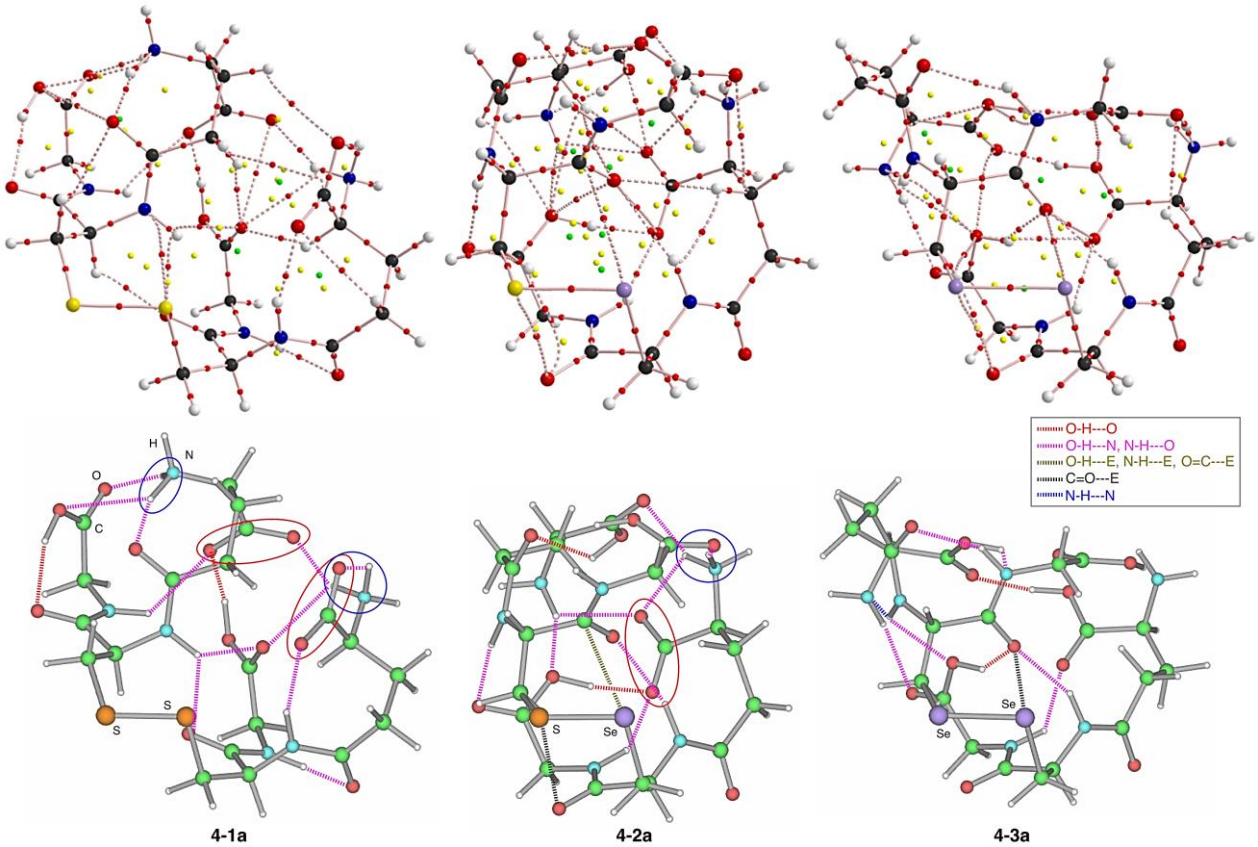

Figure 4-3. Molecular graphs of **4-1a**, **4-2a**, and **4-3a**, drawn on the optimized structures, and the optimized structures (top) and the intramolecular non-covalent interactions, corresponding to BPs in the molecular graphs, drawn on the optimized structures. The red and blue circles show the zwitter ionic -NH3+ and -COO– moieties, respectively (bottom). The energies of **4-1a**, **4-2a** and **4-3a** are employed as the standards for 1a–1e, 2a–2e and 3a–3e, respectively.

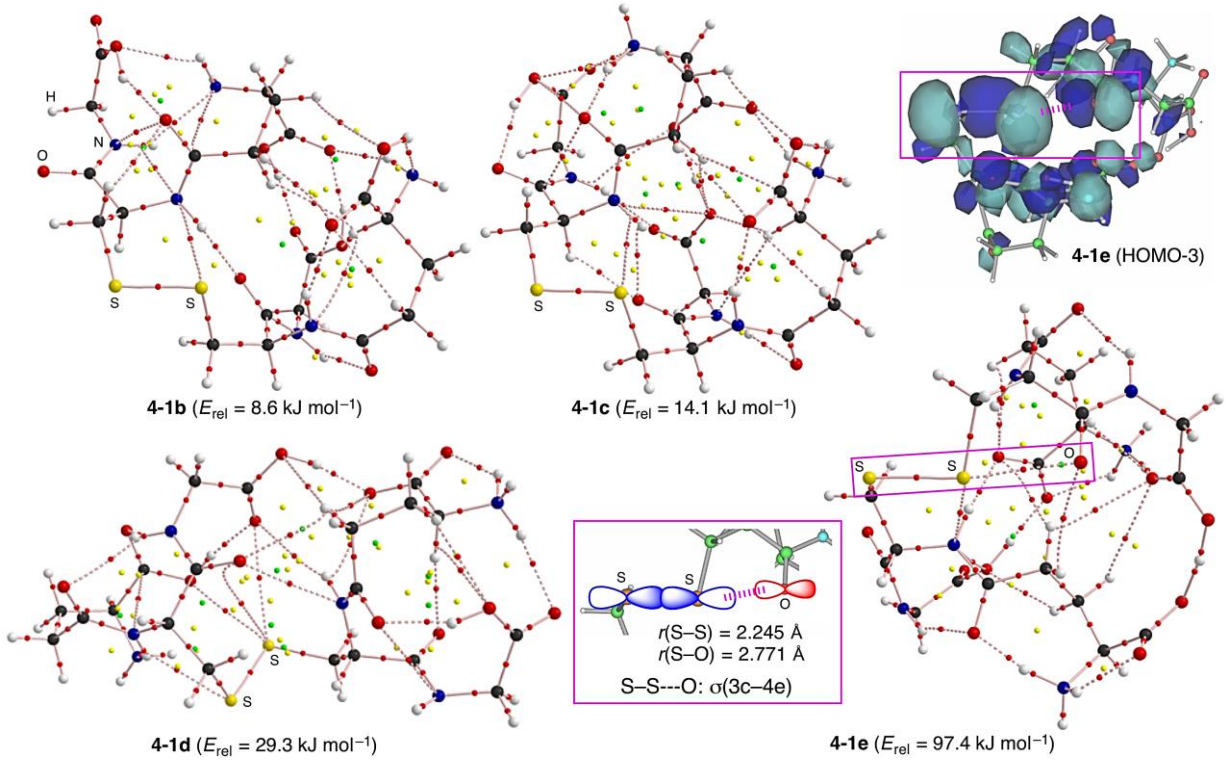

Figure 4-4. Molecular graphs of **4-1a**–**4-1e**, drawn on the optimized structures and the molecular orbital of HOMO-3 for **4-1e** with the orbital interaction map explaining the HOMO-3.

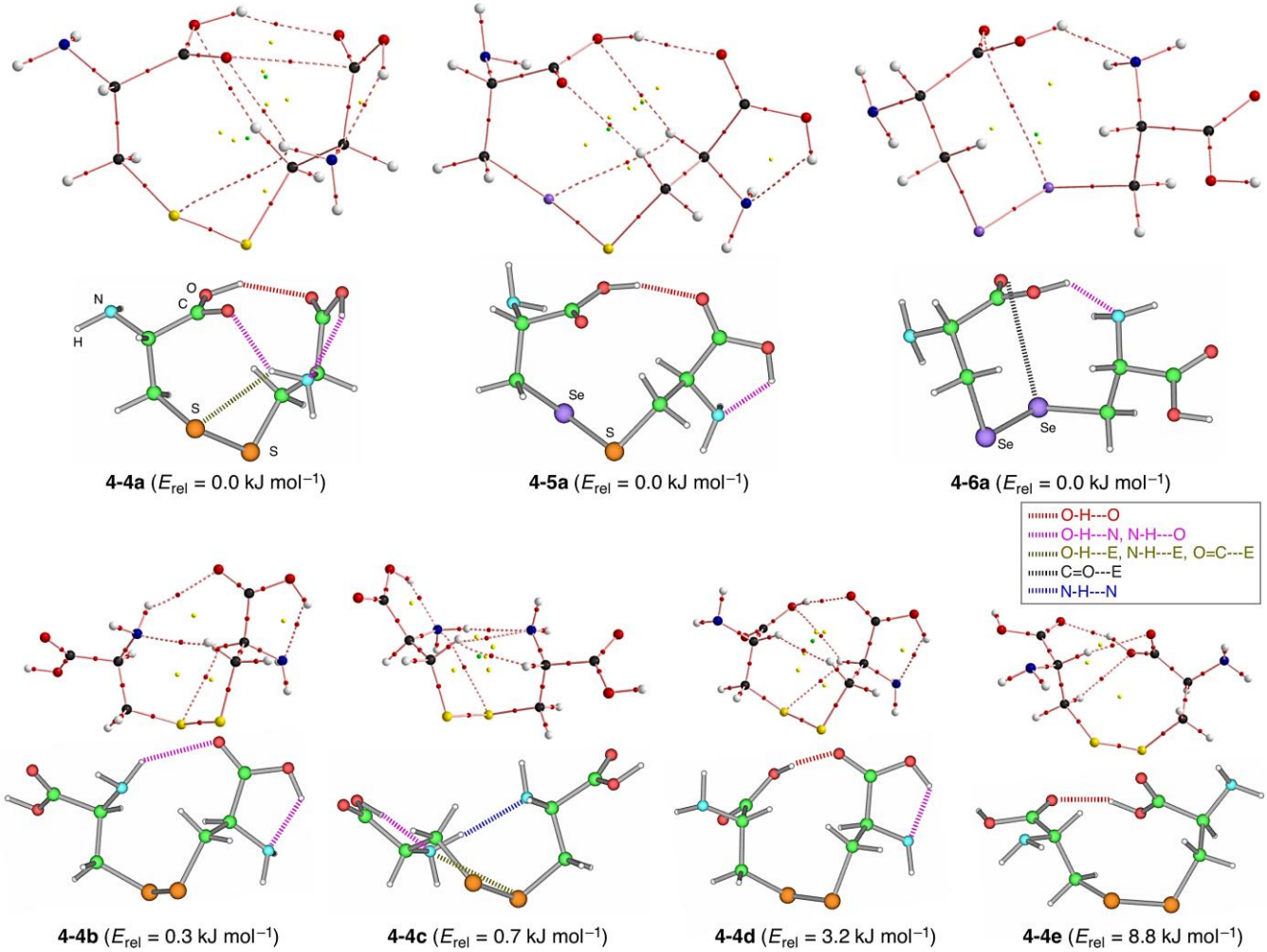

Figure 4-5. Molecular graphs of **4-4a**–**4-6a**, drawn on the optimized structures and the intramolecular non-covalent interactions, corresponding to BPs in the molecular graphs, drawn on the optimized structures (top two). Molecular graphs of **4-4b**–**4-4e**, drawn on the optimized structures and the intramolecular non-covalent interactions, corresponding to BPs in the molecular graphs, drawn on the optimized structures (bottom two).

Nevertheless, it would be important to understand how E_{rel} for the conformers are determined by the intramolecular non-covalent interactions in the conformers of **4-1a**–**4-3e**, as a whole. How can E_{rel} be evaluated based on contributions from the non-covalent interactions? He searched for such method that evaluates the stability of the conformers based on the intramolecular interactions, in total. Then, he devised a method to evaluate the contributions, which is discussed, next.

Table 4-2 Number of the O–H---O (Int A), O–H---N and N–H---O (Int B), N–H---N (Int C) HBs with the E (E′)---H–O(N), E(E′)---C=O (Int D), and E(E′)---O=C and E(E′)---NH–C=O (Int E) interactions in **4-1**–**4-6**, evaluated with M06-2X/BSS-A[a]

Species	Int A	Int B	Int C	Int D	Int E	Species	Int A	Int B	Int C	Int D	Int E
4-1a	2	10	0	0	1	**4-4a**	1	2	0	1	0
4-1b	3	6	1	0	1	**4-4b**	0	2	0	0	0
4-1c	2	7	0	0	1	**4-4c**	0	1	1	0	0
4-1d	3	6	1	1	3	**4-4d**	1	1	0	0	0
4-1e	2	8	0	0	2	**4-4e**	1	0	0	0	0
4-2a	2	9	0	1	1	**4-5a**	1	1	0	0	0
4-2b	2	9	0	0	1	**4-5b**	2	0	0	1	0
4-2c	2	7	0	0	1	**4-5c**	1	1	0	1	0
4-2d	2	6	0	1	1	**4-5d**	0	1	0	1	0
4-2e	2	8	0	0	1	**4-5e**	0	4	0	0	0
4-3a	3	6	1	0	2	**4-6a**	0	1	0	0	1
4-3b	3	6	1	0	2	**4-6b**	1	1	0	1	0
4-3c	4	4	1	1	3	**4-6c**	0	2	0	1	1
4-3d	1	9	0	1	2	**4-6d**	0	1	0	1	1
4-3e	2	9	0	1	4	**4-6e**	1	0	0	0	1

[a] BSS-A: The 6-311+G(3d) basis sets for S and Se with the 6-311++G(d,p) basis sets for O, N, C and H.

Factors to Determine Relative Energies of 4-1a–4-6a

The proposed method is explained in Scheme 4-2 with eqs (4-1)–(4-3). The process for the evaluation is as follows: (i) GEE'G is optimized. (ii) E and E′ in the optimized GEE′G are replaced by H and H. (iii) The structural parameters for the two H atoms replaced are optimized with other atoms being fixed at the fully optimized geometry. (iv) The structural parameters of CEE′C are fixed at the fully optimized positions and three H atoms are put on each of E and E′, in place of the organic ligands. (v) The structural parameters of the six H atoms are optimized.

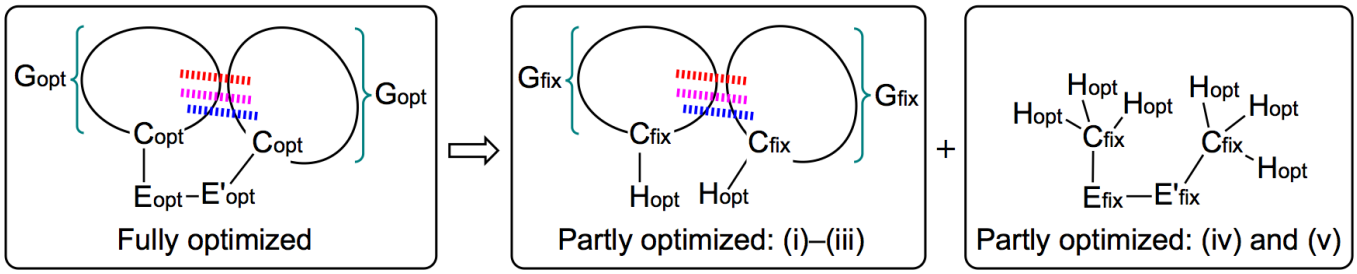

Scheme 4-2. Proposed method to evaluate the contributions from the G---G intramolecular interactions in GEE'G. The processes are given in the scheme, explained in the text.

$$E(\mathrm{GEE'G})_{opt} = 2E(\mathrm{G_{fix}C_{fix}–H_{opt}}) + E[(\mathrm{H_{opt}})_3\mathrm{C_{fix}E_{fix}–E'_{fix}C_{fix}}(\mathrm{H_{opt}})_3] - 2E(\mathrm{CH_4})_{opt} + \alpha \quad (4\text{-}1)$$

$$E_{rel}(\mathrm{GEE'G})_{opt} = 2E_{rel}(\mathrm{G_{fix}–H_{opt}}) + E_{rel}[(\mathrm{H_{opt}})_3\mathrm{C_{fix}E_{fix}–E'_{fix}C_{fix}}(\mathrm{H_{opt}})_3] + \alpha_{rel} \quad (4\text{-}2)$$

$$E_{rel}(\mathrm{GEE'G})_{opt} \approx 2E_{rel}(\mathrm{G_{fix}–H_{opt}}) + E_{rel}[(\mathrm{H_{opt}})_3\mathrm{C_{fix}E_{fix}–E'_{fix}C_{fix}}(\mathrm{H_{opt}})_3] \ (\alpha \text{ being almost constant}) \quad (4\text{-}3)$$

The method shown in Scheme 4-2 will evaluate the intramolecular G---G interactions and the deformation energies around CEE′C but not the steric factor around the E–E′ moiety. Eq (4-1) shows the relation between E(GEE′G) for the optimized structure and the energies evaluated by the proposed method, where α shows the errors in energy between E(GEE′G) and the components in energy, which contains the steric factor around the E–E' moiety. The relation for E_{rel}(GEE′G) is shown in eq (4-2), where $E(\mathrm{CH_4})$ disappears. As shown in eq (4-3), $E_{rel}(\mathrm{GEE'G})_{opt}$ could be approximated as $2E_{rel}(\mathrm{G_{fix}–H_{opt}})$ + $E_{rel}[(\mathrm{H_{opt}})_3\mathrm{C_{fix}E_{fix}–E'_{fix}C_{fix}}(\mathrm{H_{opt}})_3]$ if α is almost constant. The E_{rel} values are given from the value for the most stable conformers in **4-1a**–**4-6a**, if applied to **4-1a**–**4-6e**, respectively. The results of the calculations for **4-1a**–**4-3e** are collected in Table 4-3, where $2E_{rel}(\mathrm{G_{fix}–H_{opt}})$ and $E_{rel}[(\mathrm{H_{opt}})_3\mathrm{C_{fix}E_{fix}–E'_{fix}C_{fix}}(\mathrm{H_{opt}})_3]$ are abbreviated as $E_{rel}(\mathrm{2GH})_{p\text{-}opt}$ and $E_{rel}(\mathrm{MeSSMe})_{p\text{-}opt}$, respectively.

Figure 4-6 shows the plot of $E_{rel}(\mathrm{2GH+MeEE'Me})_{p\text{-}opt}$ for **4-1a**–**4-3e**, together with $E_{rel}(\mathrm{GSeSeG})_{opt}$. The $E_{rel}(\mathrm{2GH+MeEE'Me})_{p\text{-}opt}$ values seem to reproduce well $E_{rel}(\mathrm{GSeSeG})_{opt}$ for **4-1a**–**4-3e**, except for **4-2b** and **4-2d**.

Indeed, the relative stabilities of the conformers for the S–S and Se–Se species are well explained by the treatment, but they don't seem for the S–Se species, especially for **4-2b** and moderately for **4-2d**. Other factors, such as the steric factor around the S–Se moiety, would be important in this case. A very large magnitude of ϕ_A for **4-2b** (110.1º), relative to others (65.0º–85.6º), would be responsible for the results. The deviation in **4-2b**, due to $E_{rel}(2GH+MeEE'Me)_{p\text{-}opt}$ (–18.4 kJ mol^{-1}) versus $E_{rel}(GSeSeG)_{opt}$ (1.0 kJ mol^{-1}), is brought by the large stability of $E_{rel}(2GH)_{p\text{-}opt}$ (–22.7 kJ mol^{-1}), which would be the reflection of the C–H optimizations in 2GH from unstable position of C–H by ϕ_A for **4-2b** (110.1º). The smaller magnitudes in E_{rel} for **4-2a**–**4-2e** may make the deviations more vigorously. The results of calculations for **4a**–**6e** are given in Table 4-A2 of the Appendix. Similar plots for **4-4a**–**4-6e** is shown in Figure 4-A6 of the Appendix. The relationship between $E_{rel}(2CysH + MeEE'Me)_{p\text{-}opt}$ and $E_{rel}(CysEE'Cys)_{opt}$ seems not so clear for **4-4a**–**4-6e**.

After clarification of the structural feature of **4-1a**–**4-6e**, contour plots and negative Laplacians are examined, next.

Table 4-3 The relative energies (E_{rel}) of GEE'G, (G–H + G–H), and MeE–E'Me for **4-1a**–**4-3e**, evaluated with M06-2X/BSS-A[a]

Conformers	**a**	**b**	**c**	**d**	**e**
4-1 (E, E') = (S, S)					
$E_{rel}(GSSG)_{opt}$	0.0	8.6	14.1	29.3	97.4
$E_{rel}(2GH)_{p\text{-}opt}$	0.0	11.8	14.4	59.2	83.2
$E_{rel}(MeSSMe)_{p\text{-}opt}$	0.0[b]	-2.4	1.5	-9.9	27.1[c]
$E_{rel}(2GH+MeSSMe)_{p\text{-}opt}$	0.0	9.4	15.9	49.3	110.4[c]
4-2 (E, E') = (S, Se)					
$E_{rel}(GSSeG)_{opt}$	0.0	1.0	18.0	23.1	23.7
$E_{rel}(2GH)_{p\text{-}opt}$	0.0	-22.7	16.9	4.1	16.1
$E_{rel}(MeSSeMe)_{p\text{-}opt}$	0.0[d]	4.3	-0.5	4.3	2.2
$E_{rel}(2GH+MeSeSeMe)_{p\text{-}opt}$	0.0	-18.4	16.4	8.4	18.3
4-3 (E, E') = (Se, Se)					
$E_{rel}(GSeSeG)_{opt}$	0.0	13.6	34.9	47.9	58.8
$E_{rel}(2GH)_{p\text{-}opt}$	0.0	11.5	32.8	27.3	54.7
$E_{rel}(MeSeSeMe)_{p\text{-}opt}$	0.0[e]	-2.1	-2.4	15.2	3.5
$E_{rel}(2GH+MeSeSeMe)_{p\text{-}opt}$	0.0	9.3	30.4	42.4	58.1

[a] BSS-A: The 6-311+G(3d) basis sets for S and Se with the 6-311++G(d,p) basis sets for O, N, C and H. [b] Less stable than the fully optimized MeSSMe by 13.7 kJ mol^{-1}. [c] The n(O)→σ*(S–S) 3c–4e interaction being predicted to stabilize the system by 20.5 kJ mol^{-1}. [d] Less stable than the fully optimized MeSSeMe by 2.5 kJ mol^{-1}. [e] Less stable than the fully optimized MeSSMe by 4.2 kJ mol^{-1}.

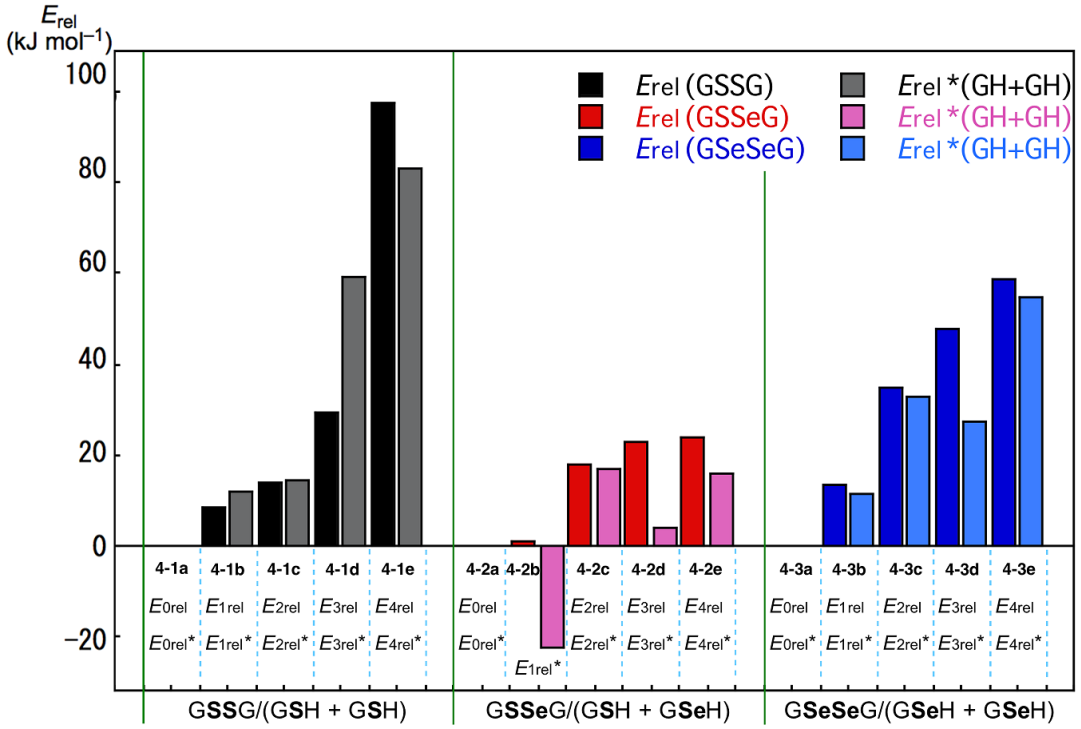

Figure 4-6. Plots of E_{rel} of GEE′G and (2G–H + MeE′′Me) for **4-1a**–**e** (GSSG), **4-2a**–**e** (GSSeG), and **4-3a**–**e** (GSeSeG), evaluated with M06-2X/BSS-A.

Contour Plots and Negative Laplacians around the E-∗-E′ Bonds in 4-1a–4-6e

Figure 4-7 shows the contour plots of $\rho(\boldsymbol{r})$, exemplified by **4-1a**–**4-1e**, which were drawn on an SSC plane of **4-1a**–**e**. The plots show that each BCP on E-∗-E′ exists at the three-dimensional saddle point of $\rho(\boldsymbol{r})$. Figure 4-8 illustrates the Negative Laplacian, exemplified by **4-1a**–**4-1e**, similarly drawn on an SSC plane. All BCPs on E-∗-E′ of **4-1a**–**4-1e** exist in the red area of the plots, which means that the BCPs are all in the range of $\nabla^2\rho_b(\boldsymbol{r}_c) < 0$, namely E-∗-E′ of **4-1a**–**4-1e** are classified by the SS (shared shell) interactions. The trajectory plots for **4-1a**–**4-1e** are similarly drawn in Figure 4-A7 of the Appendix. The plots imply that each space around **4-1a**–**4-1e** is reasonably fractionalized to the atoms in each species.

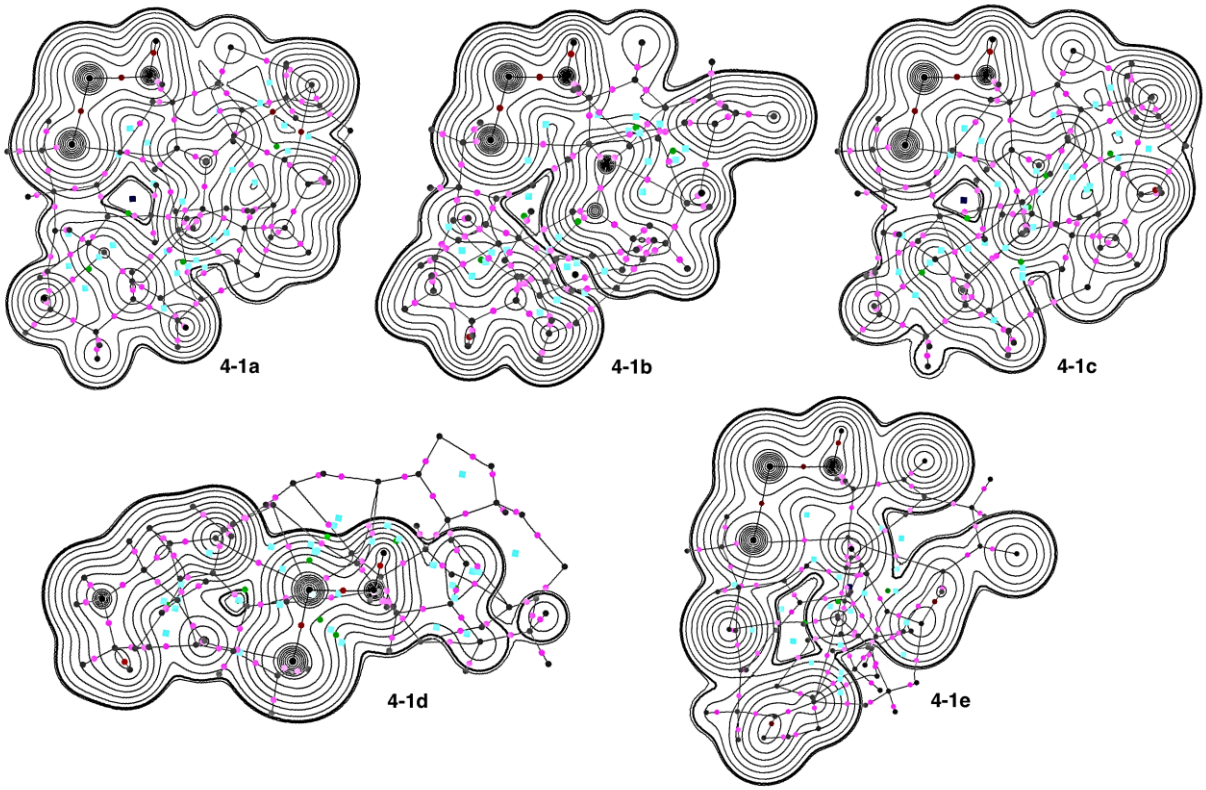

Figure 4-7. Counter maps of $\rho_b(r_c)$ drawn on the S–S–C planes of **4-1a**–**4-1e**, together with BCPs (red solid dots on the plane and pink solid out of the plane), RCPs (ring critical points: deep green solid squares on the plane and green solid squares out of the plane), CCPs (cage critical points: blue solid dots on the plane and cyan solid dots out of the plane), and bond paths (black solid lines). The counters (ea_o^{-3}) are at 2^l (l = ±8, ±7, …., 0) with the heavy line of 0.0047 for the molecular surface.

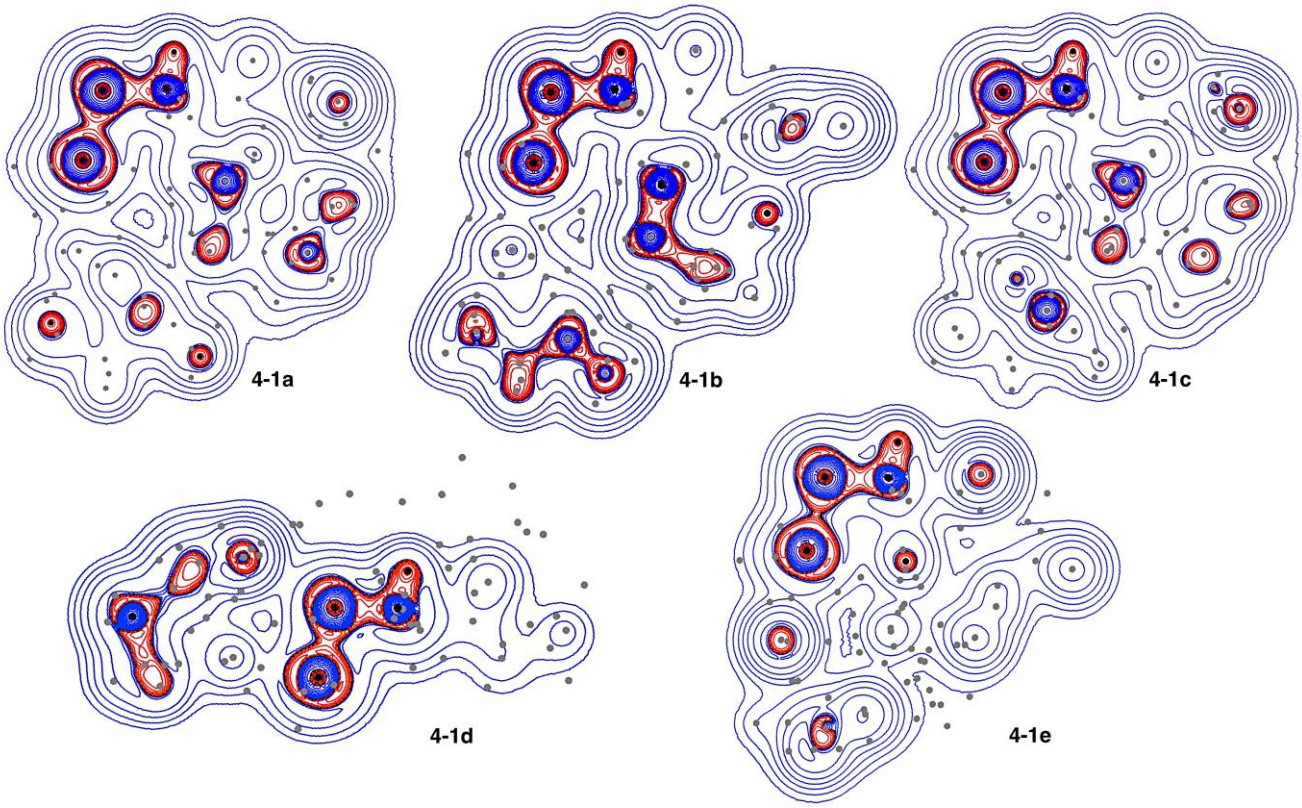

Figure 4-8. Negative Laplacians drawn on the S–S–C planes of **4-1a**–**4-1e**. While the negative areas are shown in red, the positive areas in blue.

Application of QTAIM-DFA to the E–E´ Bonds in 4-1a–4-6e

QTAIM functions are calculated for **4-1a**–**4-6e** and **4-7**–**4-9**. Table 4-4 collects those for **4-1a**–**4-3e** and **4-7**–**4-9**. Figure 4-9 shows the plots of $H_b(\boldsymbol{r}_c)$ versus $H_b(\boldsymbol{r}_c) - V_b(\boldsymbol{r}_c)/2$ for **4-1a**–**4-1d** and **4-7**, where the data for **4-1e** are not appeared in the plotted area. Figure 4-10 displays the plots of $H_b(\boldsymbol{r}_c)$ versus $H_b(\boldsymbol{r}_c) - V_b(\boldsymbol{r}_c)/2$ for **4-2a**–**4-3e**, **4-8**, and **4-9**. Figures 4-8 and 4-9 also contain the magnified pictures for the data around the fully optimized structures. All data in Table 4-4 and the perturbed structures of **4-1a**–**4-3e** and **4-7**–**4-9** are plotted in Figure 4-A8 of Appendix. All data for the fully optimized structures of **4-1a**–**4-6e** and **4-7**–**4-9** appear in the range of $H_b(\boldsymbol{r}_c) < 0$ and $H_b(\boldsymbol{r}_c) - V_b(\boldsymbol{r}_c)/2 < 0$. Therefore, the E–E´ interactions of **4-1a**–**4-6e** and **4-7**–**4-9** are all classified by the SS (shared shell) interactions, irrespective of the substantial elongation of the S-∗-S bond length by the perturbation occurred in the conformers, such as S–S in **4-1e**. The plots are analyzed, according to eqs (2-3)–(2-6) of the Chapter 2, by applying QTAIM-DFA. The QTAIM-DFA parameters of (R, θ) and (θ_p, κ_p) are also collected in Table 4-4, together with the frequencies (ν) and force constants (k_f), corresponding to the E-∗-E´ bonds in question. While the data for **4-4a**–**4-4e** are plotted in Figure 4-A9, those for **4-5a**–**4-6e** are in Figure 4-A10 of the Appendix, together with those for **4-7**–**4-9**. Similarly, the plots are analyzed to give the QTAIM-DFA parameters of (R, θ) and (θ_p, κ_p). The parameters are collected in Table 4-5 of the Appendix, together with the frequencies (ν) and force constants (k_f), corresponding to the E-∗-E´ bonds in question.

Table 4-4 QTAIM-DFA Parameters and QTAIM Functions at BCPs for the E-∗-E´ bonds in **4-1a**–**4-3e** and **4-7**–**4-9**,[a] together with the frequencies (ν) and force constants (k_f), corresponding to E-∗-E´ in question.

Compound (Symmetry: E-∗-E´)	$\rho_b(\boldsymbol{r}_c)$ (ea_o^{-3})	$c\nabla^2\rho_b(\boldsymbol{r}_c)^b$ (au)	$H_b(\boldsymbol{r}_c)$ (au)	R (au)	θ (°)	$k_b(\boldsymbol{r}_c)^c$
4-1a (C_1: S-∗-S)	0.1378	–0.0106	–0.0676	0.0684	188.9	–2.460
4-1b (C_1: S-∗-S)	0.1391	–0.0113	–0.0692	0.0701	189.2	–2.483
4-1c (C_1: S-∗-S)	0.1368	–0.0103	–0.0665	0.0673	188.8	–2.451
4-1d (C_1: S-∗-S)	0.1428	–0.0124	–0.0733	0.0744	189.6	–2.512
4-1e (C_1: S-∗-S)	0.1025	–0.0011	–0.0345	0.0345	181.9	–2.070
4-2a (C_1: S-∗-Se)	0.1169	–0.0043	–0.0528	0.0530	184.7	–2.195
4-2b (C_1: S-∗-Se)	0.1178	–0.0046	–0.0535	0.0537	184.9	–2.206
4-2c (C_1: S-∗-Se)	0.1174	–0.0045	–0.0532	0.0534	184.8	–2.203
4-2d (C_1: S-∗-Se)	0.1176	–0.0045	–0.0532	0.0534	184.8	–2.203
4-2e (C_1: S-∗-Se)	0.1158	–0.0043	–0.0520	0.0522	184.7	–2.198
4-3a (C_1: Se-∗-Se)	0.1027	–0.0046	–0.0437	0.0440	186.0	–2.265
4-3b (C_1: Se-∗-Se)	0.1035	–0.0048	–0.0444	0.0446	186.2	–2.275
4-3c (C_1: Se-∗-Se)	0.1048	–0.0050	–0.0458	0.0461	186.3	–2.282
4-3d (C_1: Se-∗-Se)	0.0988	–0.0046	–0.0406	0.0409	186.4	–2.291
4-3e (C_1: Se-∗-Se)	0.1022	–0.0045	–0.0435	0.0437	185.9	–2.259
4-7 (C_2: S-∗-S)	0.1446	–0.0131	–0.0751	0.0763	189.9	–2.535
4-8 (C_1: S-∗-Se)	0.1189	–0.0048	–0.0544	0.0547	185.0	–2.213
4-9 (C_2: Se-∗-Se)	0.1036	–0.0050	–0.0445	0.0448	186.4	–2.291

[a] BSS-A; the 6-311+G(3df) basis sets being employed for S and Se with the 6-311G(d) basis sets for C and H. [b] $c\nabla^2\rho_b(\boldsymbol{r}_c) = H_b(\boldsymbol{r}_c) - V_b(\boldsymbol{r}_c)/2$, where $c = \hbar^2/8m$. [c] $k_b(\boldsymbol{r}_c) = V_b(\boldsymbol{r}_c)/G_b(\boldsymbol{r}_c)$.

(Table 4-4 continued)

Compound (Symmetry: E-*-E´)	ν_n (n)[e] (cm^{-1})	k_f[e] (mDyn $Å^{-1}$)	θ_p (°)	κ_p (au^{-1})	Classification/ characterization
4-1a (C_1: S-*-S)	493.3(58)	0.928	197.3	0.82	SS/Cov-w
4-1b (C_1: S-*-S)	513.8(57)	1.718	197.3	0.78	SS/Cov-w
4-1c (C_1: S-*-S)	489.7(57)	0.910	197.2	0.84	SS/Cov-w
4-1d (C_1: S-*-S)	506.0(57)	0.917	197.6	0.70	SS/Cov-w
4-1e (C_1: S-*-S)	353.7(46)	0.447	193.8	3.62	SS/Cov-w
4-2a (C_1: S-*-Se)	418.7(53)	0.545	188.1	0.23	SS/Cov-w
4-2b (C_1: S-*-Se)	434.0(54)	0.955	188.4	0.15	SS/Cov-w
4-2c (C_1: S-*-Se)	421.5(54)	0.634	188.3	0.19	SS/Cov-w
4-2d (C_1: S-*-Se)	404.6(52)	0.684	188.7	0.21	SS/Cov-w
4-2e (C_1: S-*-Se)	415.9(54)	0.835	188.2	0.20	SS/Cov-w
4-3a (C_1: Se-*-Se)	302.0(42)	0.346	189.0	0.83	SS/Cov-w
4-3b (C_1: Se-*-Se)	310.2(42)	0.485	189.2	0.78	SS/Cov-w
4-3c (C_1: Se-*-Se)	316.0(43)	0.423	189.2	0.84	SS/Cov-w
4-3d (C_1: Se-*-Se)	304.2(41)	0.684	189.8	1.31	SS/Cov-w
4-3e (C_1: Se-*-Se)	300.6(42)	0.835	189.4	0.99	SS/Cov-w
4-7 (C_2: S-*-S)	513.7(6)	2.645	197.6	0.66	SS/Cov-w
4-8 (C_1: S-*-Se)	419.7(6)	2.072	188.6	0.38	SS/Cov-w
4-9 (C_2: Se-*-Se)	307.7(6)	2.730	189.1	0.77	SS/Cov-w

[e] Corresponding to the interaction in question. [f] Force constant for ν_n.

Table 4-5 QTAIM-DFA Parameters and QTAIM Functions at BCPs for the E–E' Bonds in **4-4a**–**4-6e** and **4-7**–**4-9**,[a] together with the frequencies (ν) and force constants (k_f), corresponding to the E-∗-E′ bonds in question.

Compound (Symmetry: E-∗-E´)	$\rho_b(\boldsymbol{r}_c)$ (ea_o^{-3})	$c\nabla^2\rho_b(\boldsymbol{r}_c)^b$ (au)	$H_b(\boldsymbol{r}_c)$ (au)	R (au)	θ (°)	$k_b(\boldsymbol{r}_c)^c$
4-4a (C_1: S-∗-S)	0.1409	–0.0117	–0.0710	0.0719	189.4	–2.495
4-4b (C_1: S-∗-S)	0.1443	–0.0126	–0.0749	0.0759	189.6	–2.509
4-4c (C_1: S-∗-S)	0.1432	–0.0124	–0.0737	0.0747	189.6	–2.508
4-4d (C_1: S-∗-S)	0.1431	–0.0124	–0.0735	0.0746	189.5	–2.506
4-4e (C_1: S-∗-S)	0.1430	–0.0122	–0.0734	0.0744	189.4	–2.495
4-5a (C_1: S-∗-Se)	0.1171	–0.0041	–0.0529	0.0531	184.4	–2.183
4-5b (C_1: S-∗-Se)	0.1188	–0.0045	–0.0547	0.0548	184.7	–2.195
4-5c (C_1: S-∗-Se)	0.1166	–0.0040	–0.0525	0.0527	184.4	–2.180
4-5d (C_1: S-∗-Se)	0.1157	–0.0036	–0.0524	0.0525	184.0	–2.161
4-5e (C_1: S-∗-Se)	0.1163	–0.0048	–0.0517	0.0519	185.3	–2.225
4-6a (C_1: Se-∗-Se)	0.1020	–0.0042	–0.0431	0.0433	185.6	–2.242
4-6b (C_1: Se-∗-Se)	0.1021	–0.0046	–0.0432	0.0434	186.0	–2.268
4-6c (C_1: Se-∗-Se)	0.1023	–0.0046	–0.0435	0.0437	186.1	–2.269
4-6d (C_1: Se-∗-Se)	0.1017	–0.0044	–0.0431	0.0433	185.9	–2.259
4-6e (C_1: Se-∗-Se)	0.1027	–0.0047	–0.0437	0.0439	186.1	–2.271
4-7 (C_2: S-∗-S)	0.1446	–0.0131	–0.0751	0.0763	189.9	–2.535
4-8 (C_1: S-∗-Se)	0.1189	–0.0048	–0.0544	0.0547	185.0	–2.213
4-9 (C_2: Se-∗-Se)	0.1036	–0.0050	–0.0445	0.0448	186.4	–2.291

[a] BSS-A; the 6-311+G(3df) basis sets being employed for S and Se with the 6-311G(d) basis sets for C and H. [b] $c\nabla^2\rho_b(\boldsymbol{r}_c) = H_b(\boldsymbol{r}_c) - V_b(\boldsymbol{r}_c)/2$, where $c = \hbar^2/8m$. [c] $k_b(\boldsymbol{r}_c) = V_b(\boldsymbol{r}_c)/G_b(\boldsymbol{r}_c)$.

(Table 4-5 continued)

Compound (Symmetry: E-∗-E´)	ν_n (n)[d] (cm^{-1})	k_f[e] (mDyn $Å^{-1}$)	θ_p (°)	κ_p (au^{-1})	Classification/ characterization
4-4a (C_1: S-∗-S)	511.3 (20)	2.060	197.5	0.75	SS/Cov-w
4-4b (C_1: S-∗-S)	522.5 (21)	1.118	197.4	0.67	SS/Cov-w
4-4c (C_1: S-∗-S)	506.8 (20)	1.947	197.5	0.69	SS/Cov-w
4-4d (C_1: S-∗-S)	514.1 (21)	2.089	197.4	0.71	SS/Cov-w
4-4e (C_1: S-∗-S)	519.5 (21)	1.508	197.4	0.70	SS/Cov-w
4-5a (C_1: S-∗-Se)	414.4 (18)	0.551	188.0	0.34	SS/Cov-w
4-5b (C_1: S-∗-Se)	423.6 (19)	1.896	188.4	0.33	SS/Cov-w
4-5c (C_1: S-∗Se)	414.7 (19)	1.440	188.2	0.40	SS/Cov-w
4-5d (C_1: S-∗Se)	413.8 (19)	1.996	187.5	0.34	SS/Cov-w
4-5e (C_1: S-∗-Se)	413.1 (18)	1.278	189.5	0.03	SS/Cov-w
4-6a (C_1: Se-∗-Se)	301.9 (15)	1.875	188.9	0.71	SS/Cov-w
4-6b (C_1: Se-∗-Se)	308.0 (16)	0.174	189.3	0.77	SS/Cov-w
4-6c (C_1: Se-∗-Se)	298.7 (13)	0.938	189.4	0.68	SS/Cov-w
4-6d (C_1: Se-∗-Se)	308.7 (16)	0.582	189.1	0.80	SS/Cov-w
4-6e (C_1: Se-∗-Se)	306.2 (16)	0.172	188.9	0.93	SS/Cov-w
4-7 (C_2: S-∗-S)	513.7 (6)	2.645	197.6	0.66	SS/Cov-w
4-8 (C_1: S-∗-Se)	419.7 (6)	2.072	188.6	0.38	SS/Cov-w
4-9 (C_2: Se-∗-Se)	307.7 (6)	2.730	189.1	0.77	SS/Cov-w

[d] Corresponding to the interaction in question. [e] Force constant for ν_n.

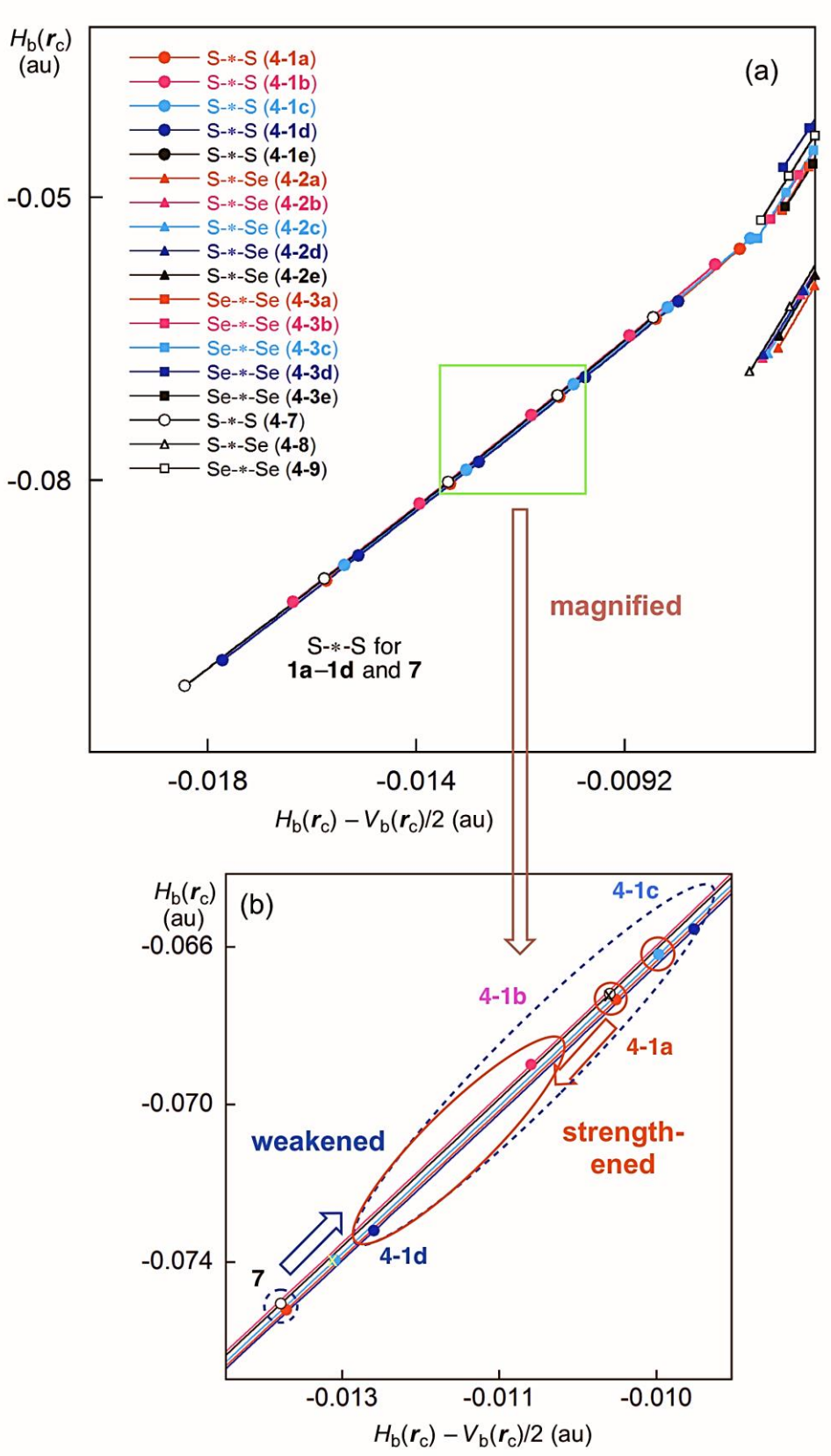

Figure 4-9. Plots of $H_b(r_c)$ versus $H_b(r_c) - V_b(r_c)/2$ for **4-1a**–**4-1e** and **4-7**. Whole picture (a) and the magnified one for the data around fully optimized structures (b)

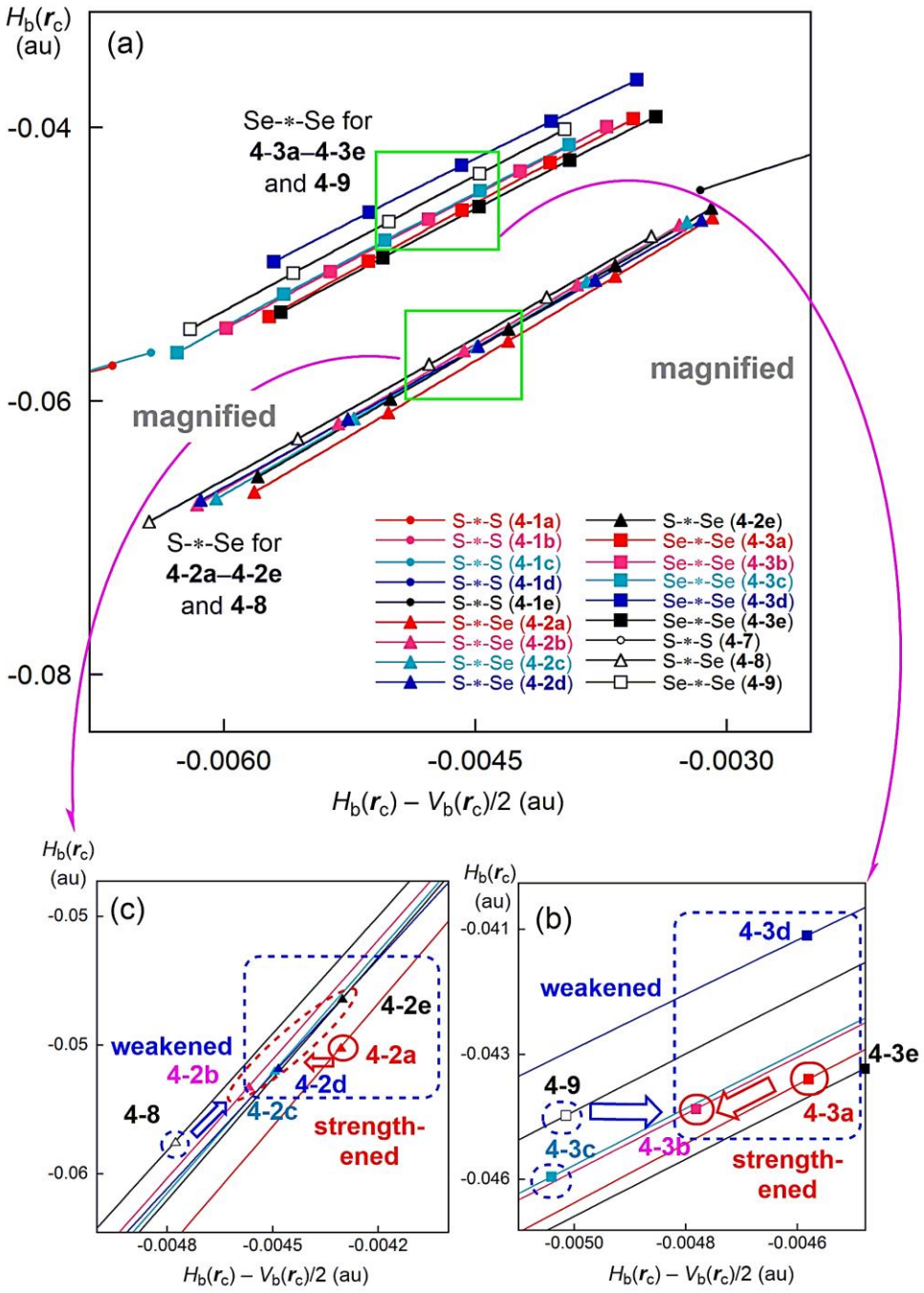

Figure 4-10. Plots of $H_b(r_c)$ versus $H_b(r_c) - V_b(r_c)/2$ for **4-2a**–**4-3e**, **4-8**, and **4-9**. Whole picture (a), the magnified one for the data around fully optimized structures of **4-2a**–**4-2e** and **4-9** (b), and the magnified one for the data around fully optimized structures of **4-3a**–**4-3e** and **4-9** (c).

Nature of the E–E´ Bonds in 4-1a–4-6e

The E-∗-E´ bonds in **4-1a**–**4-6e** are classified and characterized based on R, θ, and θ_p values, employing those of the standard interactions given in Scheme 4-3, as a reference. Before discussion of the nature of E-∗-E´ in **4-1a**–**4-6e** and **4-7**–**4-9**, it would be instructive to survey the criteria, related to the those in this paper. Interactions will be classified by the SS and CS interactions for $\theta > 180^o$ and $\theta < 180^o$, respectively, which correspond to $H_b(r_c) - V_b(r_c)/2 < 0$ and $H_b(r_c) - V_b(r_c)/2 > 0$, respectively. The θ_p values play an

important role to characterize the interactions. For the SS interactions with $\theta > 180^{\circ}$, $\theta_p > 190^{\circ}$ is given tentatively, where $\theta_p = 190^{\circ}$ corresponds to $\theta = 180^{\circ}$ for the typical interactions. The covalent interactions will be sub-divided depending on the values of R. The (classical) covalent interactions will be called strong (Cov-s) if $R > 0.15$ au, therefore, they should be weak (Cov-w) when $R < 0.15$ au.[36]

The R value of 0.076 au (< 0.15 au) is predicted for MeS-∗-SMe (**4-7**) and those for S-∗-S, S-∗-Se, and Se-∗-Se in **4-1a**–**4-6e**, **4-8**, and **4-9**, examined in this work, are less than 0.076 au. Therefore, the Cov-s interactions are not detected in this work. As shown in Scheme 4-3, the (θ, θ_p) values for S-∗-S in **4-1a**–**4-1e** are (188.8–189.6º, 197.2–197.6º) for **4-1a**–**4-1d** with (181.9º, 193.8º) for **4-1e**. The value for **4-1e** is apparently smaller than those for **4-1a**–**4-1d**, due to the elongation of S-∗-S by the formation of S–S---O σ(3c–4e) in **4-1e**. It means that S-∗-S in **4-1e** should be (much) weaker than those in **4-1a**–**4-1d**. Nevertheless, the S-∗-S interaction in **4-1e** is classified by the SS interaction and characterized to have the Cov-w nature (SS/Cov-w). All S-∗-S interactions in **4-1a**–**4-1d** are, of course, predicted to have the nature of (SS/Cov-w). The (θ, θ_p) values for S-∗-Se in **4-2a**–**4-2e** are (184.7–184.9º, 188.1–188.7º). Therefore, the S-∗-Se interactions are also classified by the SS interactions and characterized to have the Cov-w nature (SS/Cov-w), although the θ_p values are slightly less than 190º. In the case of Se-∗-Se in **4-3a**–**4-3e**, the (θ, θ_p) values are (185.9–186.4º, 189.0–189.8º). The Se-∗-Se interactions are predicted to have the nature of (SS/Cov-w), similarly to the cases of **4-1a**–**4-2e**. It is noteworthy that S-∗-S in **4-1e** is predicted to be weaker than S-∗-Se in **4-2a**–**4-2e** and Se-∗-Se in **4-3a**–**4-3e** by R and θ, although the inverse trend is by θ_p. Indeed, Se-∗-Se in **4-3a**–**4-3e** are predicted to be stronger than S-∗-Se in **4-2a**–**4-2e** by θ and θ_p, the inverse trend is by R. The E-**∗**-E´ bonds in **4-4a**–**4-6e** are all predicted to have the nature of (SS/Cov-w), so are the bonds in **4-7**–**4-9**, which are similar to the case of **4-1a**–**4-3e**.

Factor to Stabilize the E–E´ Bonds and the Conformers

The S–S bonds of **4-1a**–**4-1e** are predicted to be less stable than that of **4-7**. In the conformers in **4-1a**–**4-1e**, the S-∗-S bond is predicted to be weaker in the order shown in eq (4-4), where **4-1e** is much destabilized, due to the elongation by the formation of S–S---O σ(3c–4e). The order for the strength of S-∗-S seems to exhibit almost reverse trend of the stability of the conformers. Similar order is predicted for S-∗-Se of **4-2a**–**4-2e** with **4-8**. Eq (4-5) shows the order for S-∗-Se, where the S-∗-Se in **4-2a** seems to be substantially destabilized. On the other hand, the trend is not so clear for Se-∗-Se in **4-3a**–**4-3e**. The predicted order for Se-∗-Se is given in eq (4-6). The strength of E-∗-E' seems to show a trend almost inverse of the stability of the conformers containing the E-∗-E´, as mentioned above. While the trend seems rather clear for **4-1a**–**4-1e** with **4-7** and **4-2a**–**4-2e** with **4-8**, the trend seems unclear for **4-3a**–**4-3e** with **4-9**. The trend would be clear if the data were plotted in a narrow range, whereas it would not be clear if they were plotted in a wider range, although the mechanism is not clear.

S-∗-S in **4-7** > **4-1d** > **4-1b** > **4-1a** ≥ **4-1c** >> **4-1e** (4-4)

S-∗-Se in **4-8** > **4-2b** > **4-2c** ≈ **4-2d** > **4-2a** > **4-2e** (4-5)

Se-∗-Se in **4-3c** > **4-9** > **4-3b** > **4-3a** > **4-3e** > **4-3d** (4-6)

S-∗-S in **4-7** > **4-4b** > **4-4c** > **4-4d** > **4-4e** >> **4-4a** (4-7)

S-∗-Se in **4-8** ≈ **4-5b** > **4-5a** ≥ **4-5c** ≥ **4-5d** > **4-5e** (4-8)

Se-∗-Se in **4-9** > **4-6e** > **4-6c** > **4-6b** > **4-6d** > **4-6a** (4-9)

In the case of S–S in **4-4a**–**4-4e** with **4-7**, the S-∗-S bond becomes less stable in the order shown in eq (4-7). The order for the strength of S-∗-S is almost reverse of the stability of the conformers, with the species divided into four groups of **4-7**, **4-4b**–**4-4d**, **4-4e**, and **4-4a**. The order for the strength of Se-∗-Se is also almost inverse, with the species divided into four groups of **4-9**, **4-6b**–**4-6d**, **4-6e**, and **4-6a**, as shown in eq (4-9). However, the trend in S-∗-Se is not as clear for **5a**–**5e** with **8**, as predicted in eq (4-8). The data for **4a**–**4e** with **4-7** are plotted in a narrow range, as are those for **4-6a**–**4-6e** with **4-9**, which seems to exhibit a clear trends. However, the data for **4-5a**–**4-5e** with **4-8** are plotted over a wider range, and the trend seems unclear, similar to the cases of **4-1a**–**4-3e**, although the mechanism remains unclear.

The trends shown in eq (4-9) are also confirmed through the analysis of $\rho_b(\boldsymbol{r}_c)$ and bond orders evaluated based on the natural atomic orbitals, for E–E' in **4-1a**–**4-6e** and **4-7**–**4-9**. The plot of $\rho_b(\boldsymbol{r}_c)$ versus the bond orders is shown in Figure 4-A11 of the Appendix. See also Table 4-A3 of the Appendix for bond orders of

4-1a–**4-6e** and **4-7**–**4-9**.

While the results could be explained in a variety of way, his explanation is as follows: The intramolecular attractive interactions in **4-1a**–**4-6e** stabilize the species but the E–E′ bonds would be destabilized through distortion, where the E–E′ bonds operate to relax the excess deformation brought by the intramolecular attractive interactions, such as HBs. The destabilization would increase the stability of the species. As a result, the E–E′ bonds will be predicted to be less stable, if they exist in more stable species. The E–E′ bonds could be predicted to be rather stable, if the intramolecular attractive interactions do not affect the structures around the E–E′ bonds.

The nature of the E–E′ bonds in **4-1a**–**4-6e** is well described with dynamic nature of (θ_p, κ_p) and the static nature of (R, θ) by applying QTAIM-DFA.

Summary

The dynamic and static nature of E–E′ (E, E′ = S and Se) in glutathione disulfide and derivatives (**4-1**–**4-3**, respectively) is elucidated by applying QTAIM-DFA, together with *R*-cystine and derivatives (**4-4**–**4-6**) and MeEE′Me (**4-7**–**4-9**). Five conformers (**a**–**e**) for each of **4-1**–**4-6** are optimized with M06-2X/BSS-A. They are called **4-1a**–**4-1e**, which are defined to satisfy E(**1a**) < E(**1b**) < E(**1c**) < E(**1d**) < E(**1e**), for example. Indeed, no intramolecular non-covalent interactions are detected in **4-7**–**4-9**, a lot of such interactions operate to stabilize **4-1a**–**4-3e**. Among such interactions, the formation of S_2O σ(3c–4e) of the $n_p(O)\rightarrow\sigma^*(S–S)$ type detected in **1e** elongates r(S, S) by 0.20 Å. The contribution from the intramolecular non-covalent interactions to stabilize the conformers of GEE′G is estimated by calculating separately the G---G part as 2G–H and the E–E' part (as MeE–E′Me), under the suitable conditions. The E_{rel}(2GH + MeEE′Me) values explain well the E_{rel} values for **4-1a**–**4-1e** and **4-3a**–**4-3e**, but not so for **4-2a**–**4-2e**.

QTAIM-DFA is applied to E-∗-E′ in **4-1a**–**4-6e** and **4-7**–**4-9**, by plotting $H_b(\boldsymbol{r}_c)$ versus $H_b(\boldsymbol{r}_c) - V_b(\boldsymbol{r}_c)/2$ for the data of the fully optimized structures and the perturbed structures at BCPs. The QTAIM-DFA parameters of (R, θ) and (θ_p, κ_p) are obtained by analyzing the plots. The (θ, θ_p, and R) values for S-∗-S in **4-1a**–**4-1e** are (188.8–189.6º, 197.2–197.6º, 0.0673–0.0744 au) for **4-1a**–**4-1d** and (181.9º, 193.8º, 0.0343 au) for **4-1e**. The values for **4-1e** are apparently smaller than those for **4-1a**–**4-1d**, due to the elongation of S-∗-S by the formation of S_2O σ(3c–4e) in **4-1e**. Nevertheless, the S-∗-S interactions in **4-1a**–**4-1e** are all predicted to have the (SS/Cov-w) nature. Similarly, the E–E′ interactions in **4-2a**–**4-6e** and **4-7**–**4-9** are all predicted to have the (SS/Cov-w) nature. The S–S bonds of **4-1a**–**4-1e** are predicted to be less stable than that of **4-7** and the S-∗-S bond in **4-4a** becomes weaker than those in **4-4b**–**4-4e**, as a whole, although **4a** is most stable among **4-4a**–**4-4e**. Such an inverse trend between the stability of the conformers and the strength of E-∗-E′ is widely observed. The intramolecular attractive interactions in **4-1a**–**4-6c** stabilize the species but the E–E′ bonds would be destabilized through distortion, where the E–E′ bonds act to relax the excess deformation brought by the formation of the attractive interactions. The predicted behavior would give a hint to understand the reactivity of E–E′ in the chemical and biological processes.

Appendix

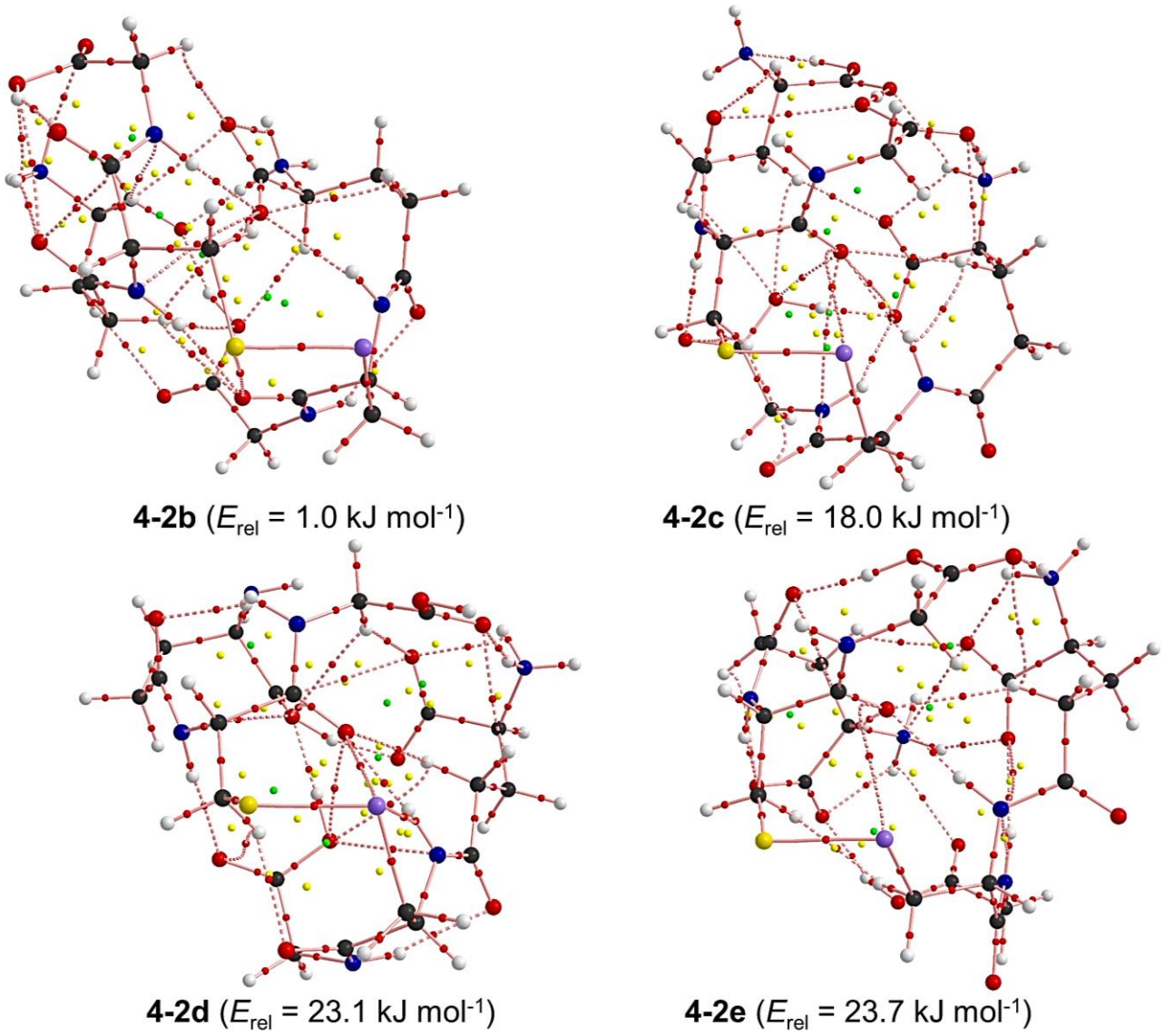

Figure 4-A1. Molecular graphs of **4-2b**–**4-2e**, drawn on the optimized structures.

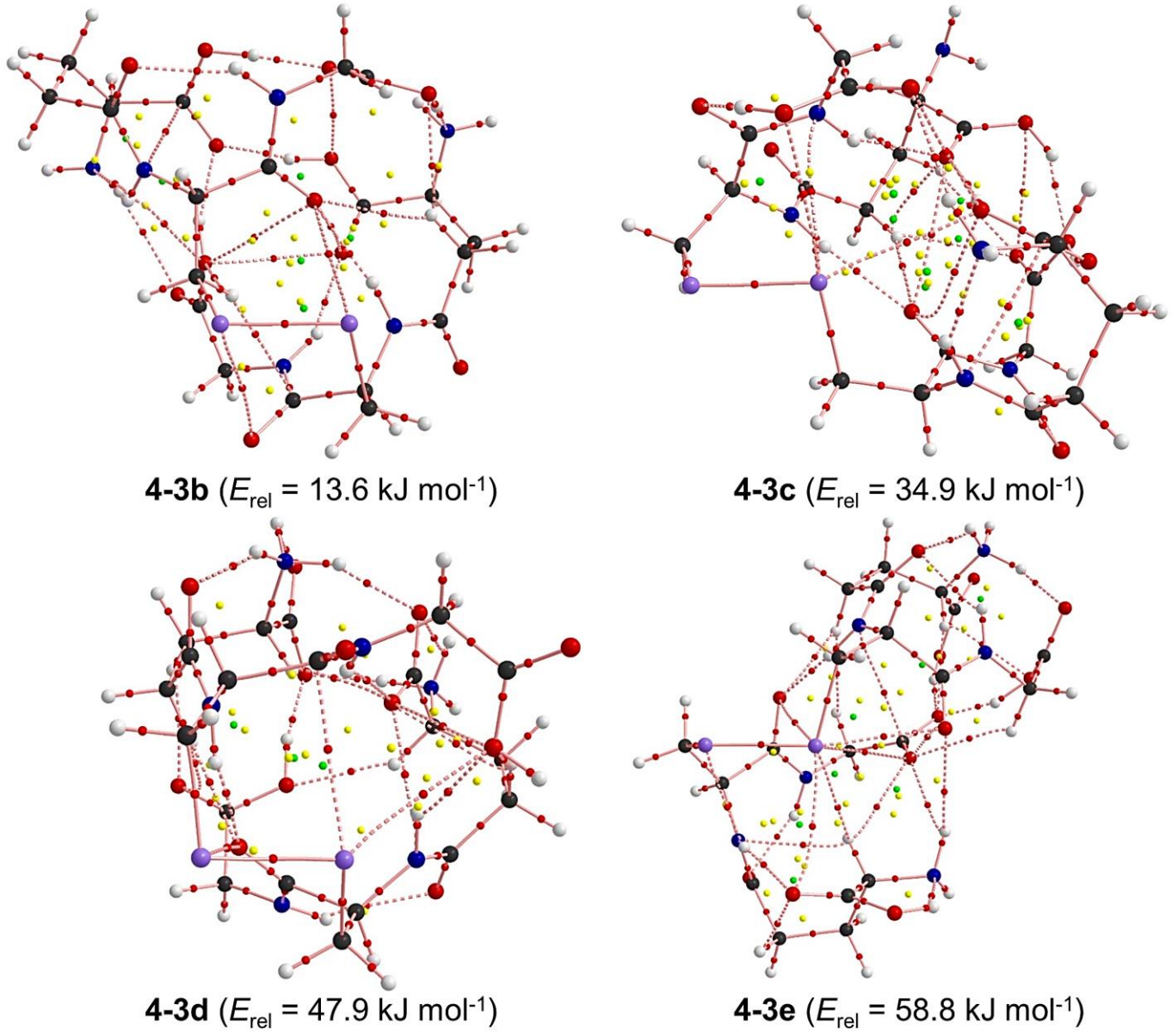

Figure 4-A2. Molecular graphs of **4-3b**–**4-3e**, drawn on the optimized structures.

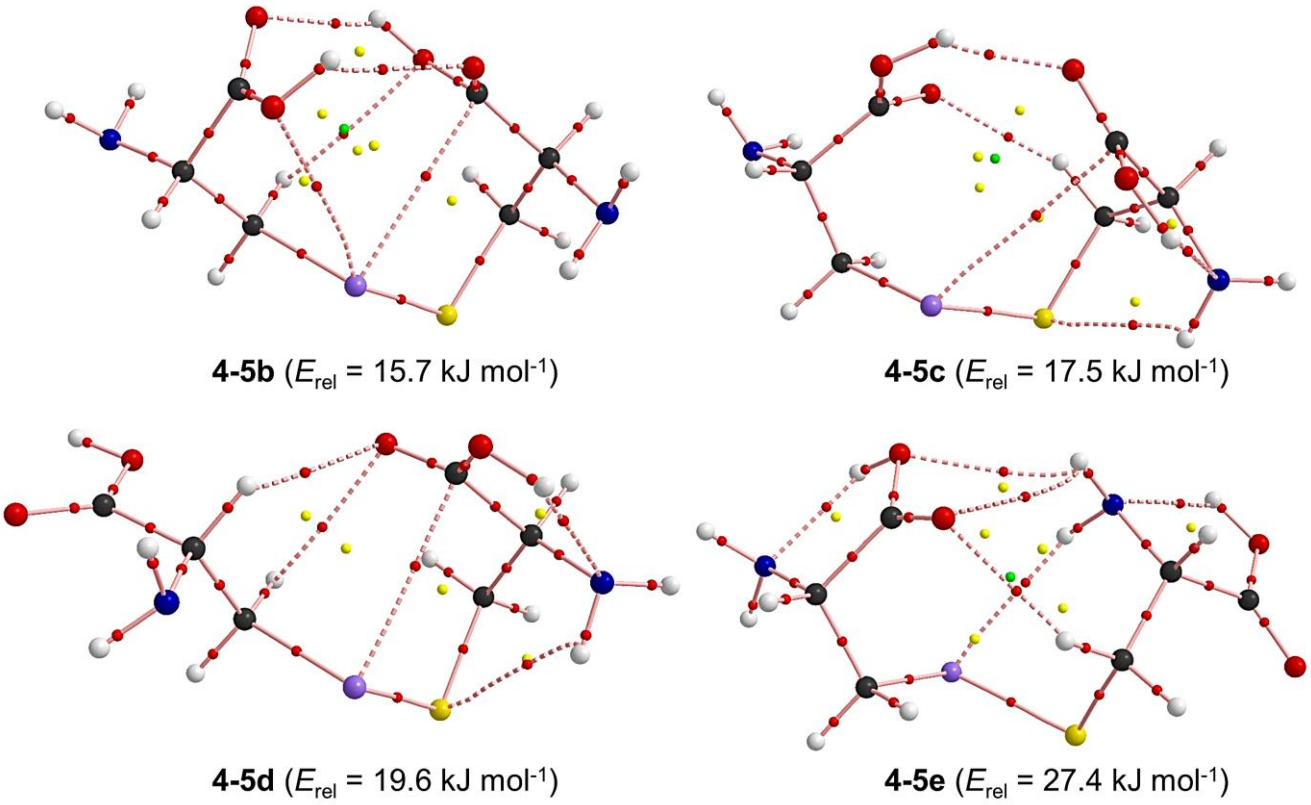

Figure 4-A3. Molecular graphs of **4-5b**–**4-5e**, drawn on the optimized structures.

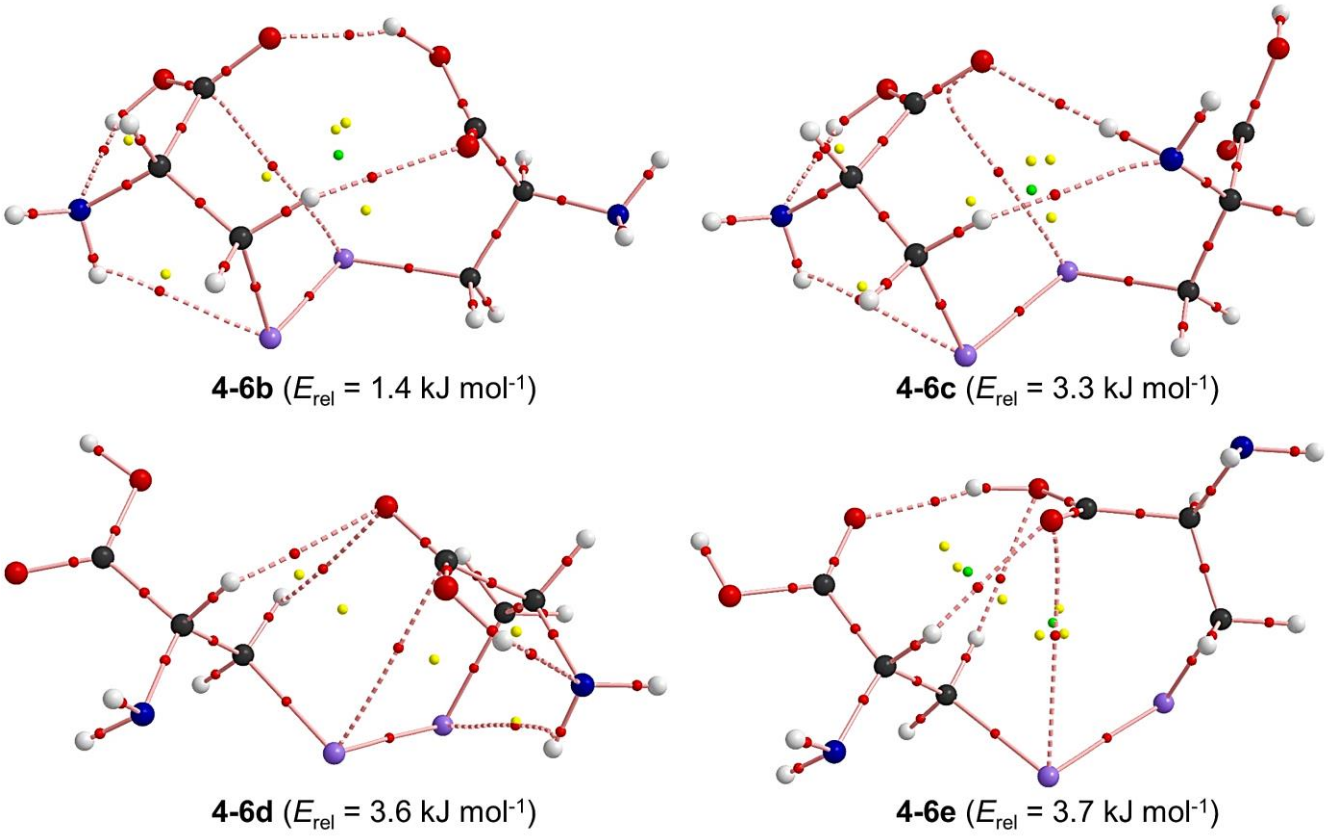

Figure 4-A4. Molecular graphs of **4-6b**–**4-6e**, drawn on the optimized structures.

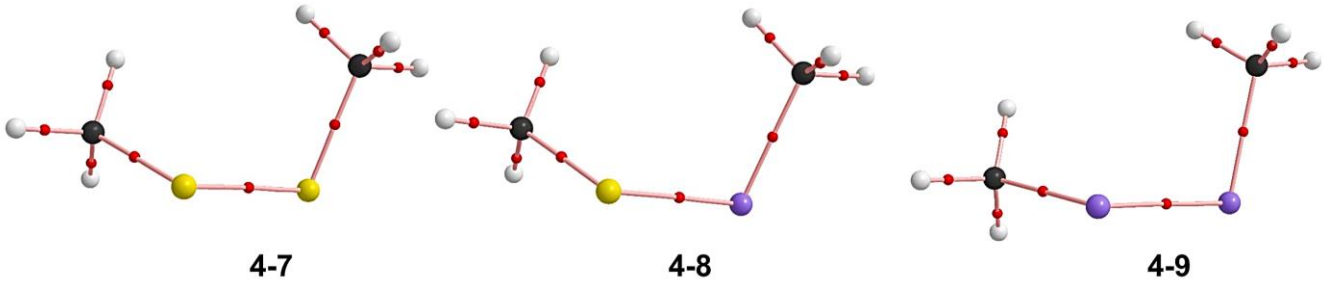

Figure 4-A5. Molecular graphs of **4-7**–**4-9**, drawn on the optimized structures.

Table 4-A1. The energies for **4-7**–**4-9** of the optimized structures and partially optimized structures with ϕ_A, fixed suitably, with M06-2X/BSS-A.

dihedral (°)	ΔE (kJ mol^{-1})	dihedral (°)	ΔE (kJ mol^{-1})
4-7		**4-9**	
0.00	44.72	0.00	35.96
84.96	0.00[a]	15.00	31.97
180.00	25.71	30.00	22.99
4-8		45.00	13.07
0.00	38.95	60.00	5.57
85.59	0.00[a]	75.00	0.62
180.00	23.62	86.08	0.00[a]
		90.00	0.10
		105.00	2.51
		120.00	7.86
		135.00	13.73
		150.00	18.80
		165.00	22.17
		180.00	23.11

[a] Taken as the reference (0.0 kJ mol^{-1}).

Table 4-A2. The relative energies (E_{rel}) of REE'R, (R–H + R–H), and MeE–E'Me for **4-4a**–**4-6e**, evaluated with M06-2X/BSS-A[a]

Conformers	**a**	**b**	**c**	**d**	**e**
4-4 (E, E´) = (S, S)					
$E_{rel}(RSSR)_{opt}$	0.0	0.3	0.7	3.2	8.8
$E_{rel}(2RH)_{p\text{-}opt}$	0.0	18.6	6.0	18.2	9.8
$E_{rel}(MeSSMe)_{p\text{-}opt}$	0.0[b]	-0.9	-2.0	–2.3	–0.6
$E_{rel}(2RH+MeSSMe)_{p\text{-}opt}$	0.0	17.7	4.0	15.8	9.2
4-5 (E, E´) = (S, Se)					
$E_{rel}(RSSeR)_{opt}$	0.0	15.7	17.5	19.6	27.4
$E_{rel}(2RH)_{p\text{-}opt}$	0.0	–3.3	11.7	24.4	12.5
$E_{rel}(MeSSeMe)_{p\text{-}opt}$	0.0[c]	0.7	0.8	0.7	3.2
$E_{rel}(2RH+MeSeSeMe)_{p\text{-}opt}$	0.0	–2.5	12.6	25.1	15.7
4-6 (E, E´) = (Se, Se)					
$E_{rel}(RSeSeR)_{opt}$	0.0	1.4	3.3	3.6	3.7
$E_{rel}(2RH)_{p\text{-}opt}$	0.0	25.5	20.6	22.6	3.7
$E_{rel}(MeSeSeMe)_{p\text{-}opt}$	0.0[d]	–2.9	–4.1	–3.3	–4.0
$E_{rel}(2RH+MeSeSeMe)_{p\text{-}opt}$	0.0	22.6	16.5	19.3	–0.3

[a] BSS-A: The 6-311+G(3d) basis sets for S and Se with the 6-311++G(d,p) basis sets for O, N, C and H. [b] Less stable than the fully optimized MeSSMe by 4.2 kJ mol^{-1}. [c] Less stable than the fully optimized MeSSeMe by 1.6 kJ mol^{-1}. [d] Less stable than the fully optimized MeSeSeMe by 5.5 kJ mol^{-1}.

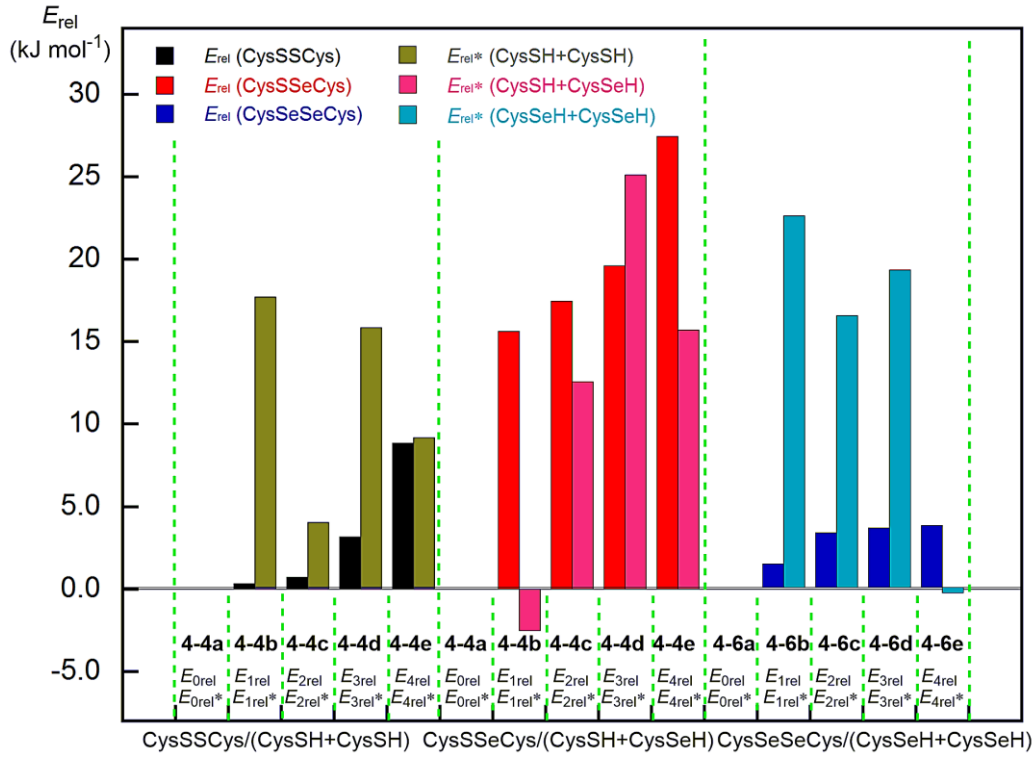

Figure 4-A6. Plots of E_{rel} of REE´R and (2R–H + MeEE´Me) for **4-4a**–**e** (RSSR), **4-5a**–**e** (RSSeR), and **4-6a**–**e** (RSeSeR), evaluated with M06-2X/BSS-A.

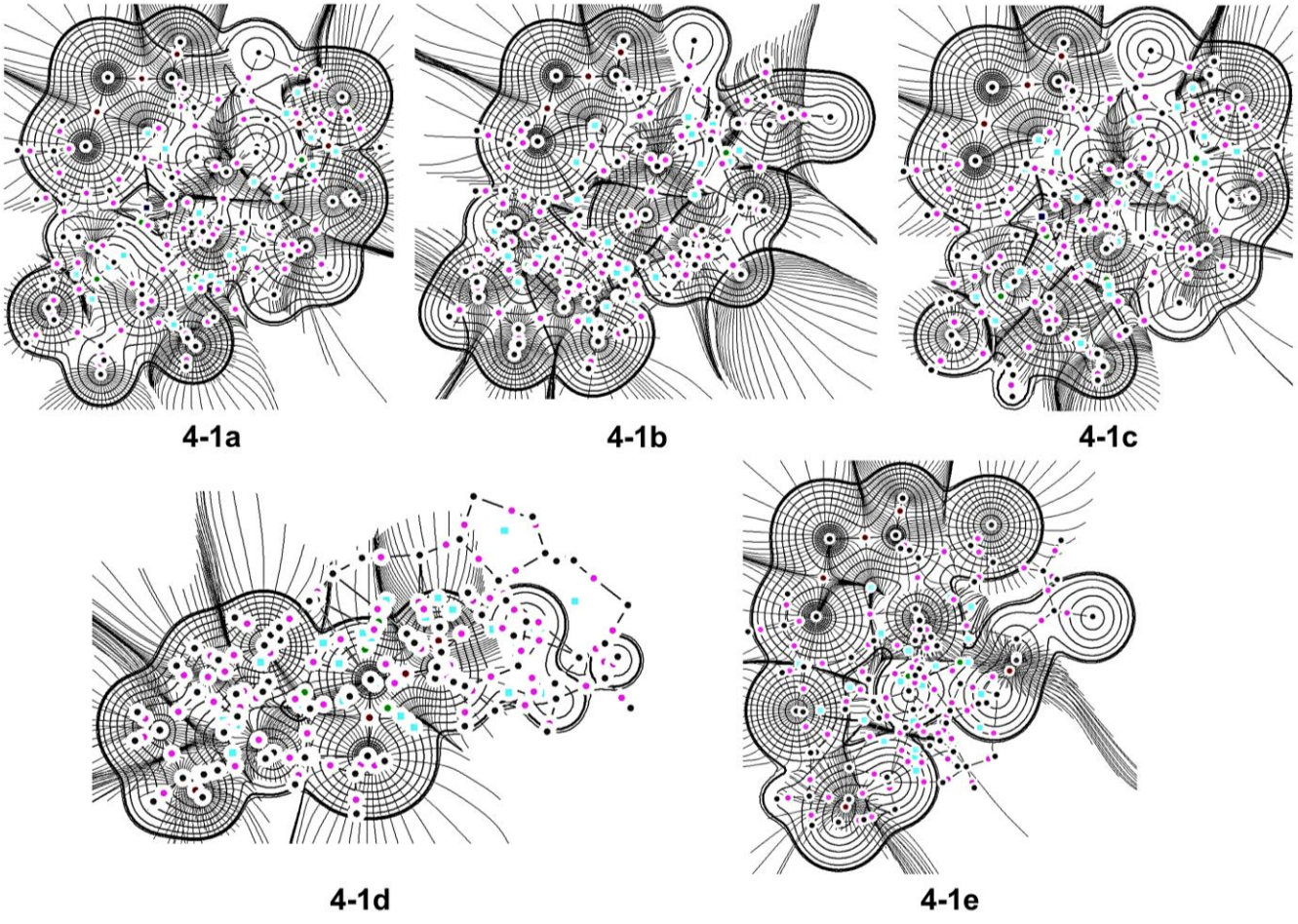

Figure 4-A7. Trajectory plots of ρ_b (r_c) drawn on the S–S–C planes of **4-1a**–**e**, similarly to the case of Figure 6 in the text. Color and marks are same as those in Figure 4-6.

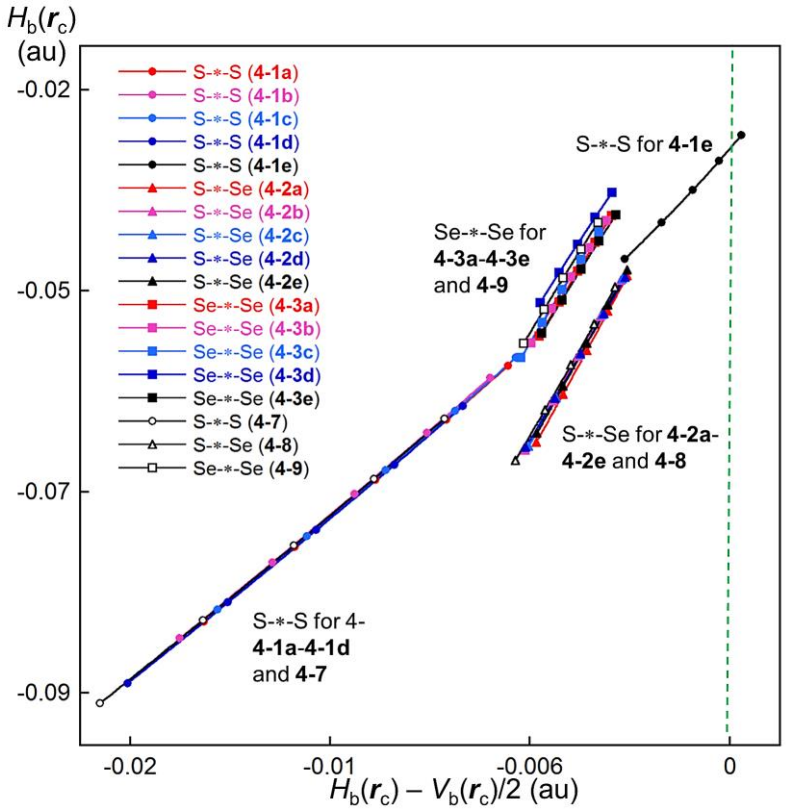

Figure 4-A8. Plots of $H_b(r_c)$ versus $H_b(r_c) - V_b(r_c)/2$ for **4-1a**–**4-3e** and **4-7**–**4-9**.

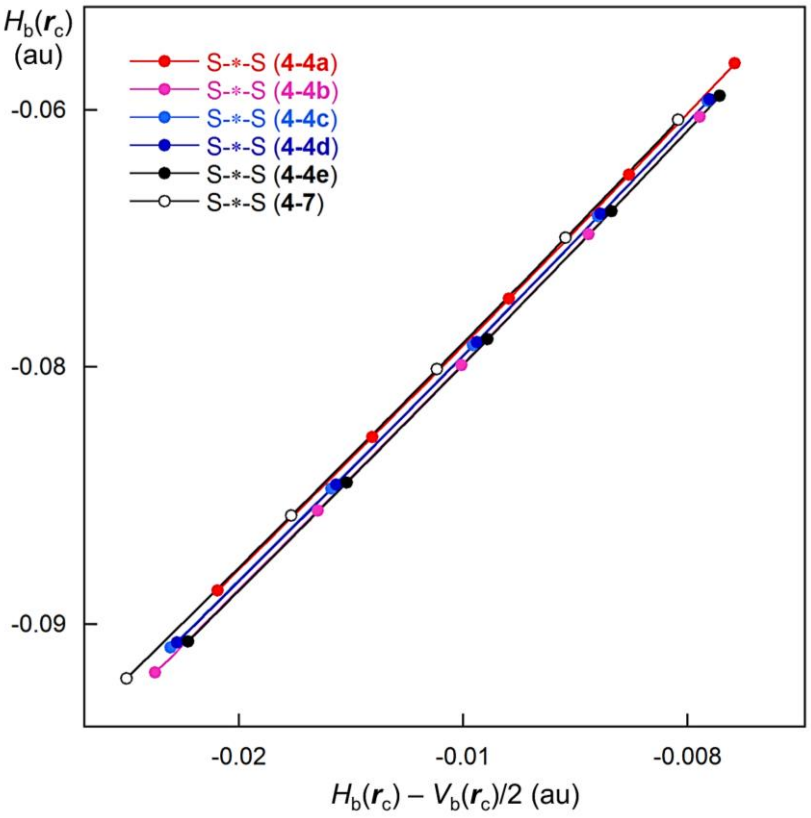

Figure 4-A9. Plots of $H_b(r_c)$ versus $H_b(r_c) - V_b(r_c)/2$ for **4-4a**–**4-4e** and **4-7**.

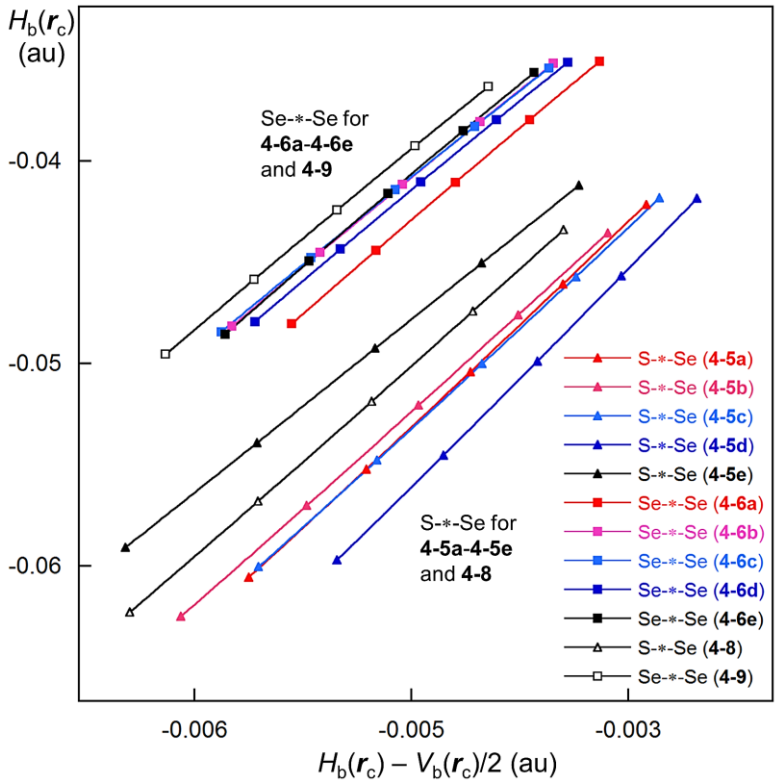

Figure 4-A10 Plots of $H_b(\boldsymbol{r}_c)$ versus $H_b(\boldsymbol{r}_c) - V_b(\boldsymbol{r}_c)/2$ for **4-5a**–**4-6e** and **4-7**–**4-8**.

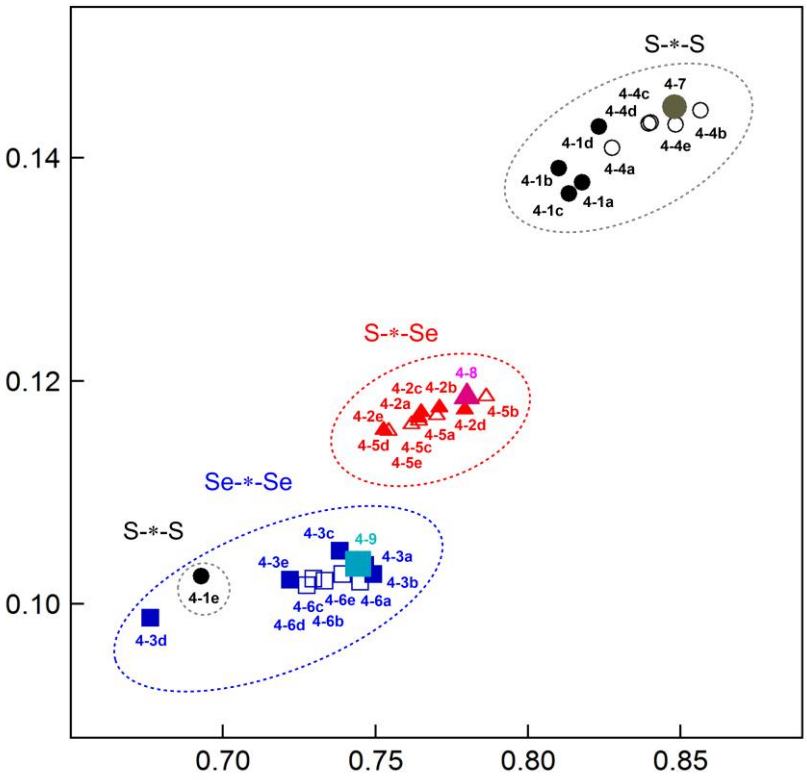

Figure 4-A11 Plots of $\rho_b(\boldsymbol{r}_c)$ versus NAO bond orders for **4-1a**–**4-6e** and **4-7**–**4-8**.

Table 4-A3 NAO bond orders for **4-1a**–**4-6e** and **4-7**–**4-8**.

Compound	NAO bond order[a,b]
4-1a	0.8177
4-1b	0.8101
4-1c	0.8134
4-1d	0.8233
4-1e	0.6928
4-2a	0.7641
4-2b	0.7709
4-2c	0.7650
4-2d	0.7792
4-2e	0.7526
4-3a	0.7493
4-3b	0.7465
4-3c	0.7383
4-3d	0.6762
4-3e	0.7219
4-4a	0.8275
4-4b	0.8565
4-4c	0.8402
4-4d	0.8395
4-4e	0.8484
4-5a	0.7701
4-5b	0.7863
4-5c	0.7642
4-5d	0.7543
4-5e	0.7618
4-6a	0.7450
4-6b	0.7333
4-6c	0.7296
4-6d	0.7275
4-6e	0.7391
4-7	0.8481
4-8	0.7799
4-9	0.7442

[a] Atom-atom overlap-weighted NAO bond order. [b] The orders evaluated based on the natural atomic orbitals using NBO 6.0 program.

References

1 W. Nakanishi, S. Hayashi, S. Morinaka, T. Sasamori, N. Tokitoh, *New J. Chem*. **2008**, *32*, 1881–1889.

2 C. Hwang, A. J. Sinskey, H. F. Lodish, *Science* **1992**, *257*, 1496–1502.

3 D. B. Wetlaufer, P. A. Branca, G. X. Chen, *Protein Eng. 1*. **1987**, 141–146.

4 H. F. Gilbert, *Methods Enzymol*. **1995**, *251*, 8–28.

5 M. M. Lyles, F. H. Gilbert, *Biochemistry* **1991**, *30*, 613–619.

6 J. Beld, W. J. Kenneth, D. Hilvert, *Biochemistry* **2007**, *46*, 5382−5390.

7 Y. Konishi, T. Ooi, A. H. Scheraga, *Biochemistry* **1982**, *21*, 4734–4740.

8 W. Brandt, L. A. Wessjohann, *Chem. Bio. Chem*. **2005**, *6*, 386–394.

9 S. Gromer, L. A. Wessjohann, J. Eubel, W. Brandt, *Chem. Bio. Chem*. **2006**, *7*, 1649–1652.

10 L. A. Wessjohann, A. Schneider, M. Abbas, W. Brandt, *Biol. Chem*. **2007**, *388*, 997–1006.

11 B. M. Lacey, B. E. Eckenroth, S. Flemer Jr, R. J. Hondal, *Biochemistry* **2008**, *47*, 12810–12821.

12 L. A. Wessjohann, A. Schneider, *Biodiversity* **2008**, *5*, 375–388.

13 B. Ren, W. Huang, B. Akesson, R. Ladenstein, *J. Mol. Biol*. **1997**, *268*, 869–885.

14 W. A. Hendrickson, *Science* **1991**, *254*, 51–58.

15 A. Ishii, S. Matsubayashi, T. Takahashi, J. Nakayama, *J. Org. Chem*. **1999**, *64*, 1084–1085.

16 T. Saiki, K. Goto, R. Okazaki, *Angew. Chem., Int. Ed*. **1997**, *36*, 2223–2224.

17 K. Goto, D. Sonoda, K. Shimada, S. Sase, T. Kawashima, *Angew. Chem. Int. Ed*. **2010**, *49*, 545–547.

18 G. Mugesh, H. B. Singh, *Chem. Soc. Rev.* **2000**, *29*, 347–357.

19 K. P. Bhabak, G. Mugesh, *Chem. Asian. J* **2009**, *4*, 974–983.

20 B. K. Sarma, and G. Mugesh, *Chem. Eur. J* **2008**, *14*, 10603–10614.

21 K. P. Bhabak, G. Mugesh, *Chem. Eur. J* **2009**, *15*, 9846–9854.

22 K. P. Bhabak, G. Mugesh, *Chem. Eur. J* **2008**, *14*, 8640–8651.

23 K. P. Bhabak, G. Mugesh, *Chem. Eur. J* **2007**, *13*, 4594–4601.

24 B. K. Sarma, G. Mugesh, *Inorg. Chem.* **2006**, *45*, 5307–5314.

25 P. P. Phadnis, G. Mugesh, *Org. Biomol. Chem*. **2005**, *3*, 2476–2481.

26 M. Iwaoka, R. Ooka, T. Nakazato, S. Yoshida, S. Oishi, *Chem. Biodiversity* **2008**, *5*, 359–374.

27 F. Kumakura, B. Mishra, K. I. Priyadarsini, M. A. Iwaoka, *Eur. J. Org. Chem*. **2010**, 440–445.

28 K. Arai, K. Dedachi, M. Iwaoka, *Chem. Eur. J.* **2011**, *17*, 481–485.

29 S. Yoshida, F, Kumakura, I. Komatsu, K. Arai, Y. Onuma, H. Hojo, B. G. Singh, *Angew. Chem. Int. Ed.* **2011**, *50*, 2125–2128.

30 D. Manna, G. Mugesh, *J. Am. Chem. Soc.* **2012**, *134*, 4269–4279.

31 L. Flohe, W. A. Günzler, H. H. Schock, *FEBS Lett*. **1973**, *32*, 132–134.

32 L. Flohé, *Glutathione peroxidase brought into focus, in Free radicals in biology*, ed. W. A. Pryor, Academic Press, New York, **1982**, vol. 5, pp. 223-253.

33 C. Jelsch, C. Didierjean, *Acta Cryst.C.* **1999**, *55*, 1538–1540.

34 Leela, S. and Ramamurthi, K. *Private Communication* **2007**.

35 Y. Tsubomoto, S. Hayashi, W. Nakanishi, *RSC Adv*. **2015**, *5*, 11534–11540.

36 M. J. Frisch, et al. Gaussian09, revision D.01; Gaussian, Inc.: Wallingford, CT, 2009. A complete list of authors is given in the Supporting Information.

37 In our experience, the 6-311+G(d) basis sets or higher ones are recommended, when usual organic selenium compounds are calculated. For the 6-311+G(3d) basis sets, see: a) R. C. Binning, L. A. Curtiss, *J. Comput. Chem.* **1990**, *11*, 1206–1216; b) L. A. Curtiss, M. P. McGrath, J.-P. Blaudeau, N. E. Davis, R. C. Binning, Jr., L. Radom, *J. Chem. Phys.* **1995**, *103*, 6104–6113; c) M. P. McGrath, L. Radom, *J. Chem. Phys*. **1991**, *94*, 511–516; d) for the diffuse functions (+ and ++), see T. Clark, J. Chandrasekhar, G. W. Spitznagel, P. v. R. Schleyer, *J. Comput. Chem.* **1983**, *4*, 294–301. See for example, W. Nakanishi, S. Hayashi, *J. Phys. Chem. A*, **1999**, *103*, 6074–6081.

38 Y. Zhao, D. G. Truhlar, *Theor. Chem. Acc*. **2008**, *120*, 215−241.

39 Spartan 02 for Windows, Wavefunction, Inc., Irvine, CA, Spartan '02 Windows, Tutorial and User's Guide, Wavefunction, Inc., Irvine, CA, **2001**.

40 T. A. Halgren, *J. Comput. Chem.* **1996**, *17*, 490–519.

41 A. D. Becke, *J. Chem. Phys*. **1993**, *98*, 5648−5652.

42 C. Lee, W. Yang, R. G. Parr, *Phys. Rev. B*: *Condens. Matter Mater. Phys*. **1988**, *37*, 785−789.

43 J. J. P. Stewart, *J. Comput. Chem*. **1989**, *10*, 209–220.

44 R. F. W. Bader, *Atoms in Molecules. A Quantum Theory*; Oxford University Press: Oxford, U.K., 1990.

45 The AIM2000 program (Version 2.0) is employed to analyze and visualize atoms-in-molecules: F.Biegler-König, *J. Comput. Chem*. **2000**, *21*, 1040−1048.

46 A. E. Reed, L.A. Curtiss, F. Weinhold, *Chem. Rev*. **1988**, *88*, 899–926.

47 E.D. Glendening, C.R. Landis, *J. Compt. Chem*. **2013**, *34*, 1429–1437.

48 W. Nakanishi, S. Hayashi, M. Hashimoto, M. Arca, M.C. Aragoni, V. Lippolis, Recent advances of structural chemistry of organoselenium and organotellurium compounds. In *The Chemistry of Organic Selenium and Tellurium Compounds*, eds. by, Z. Rappoport, Wiley: New York, NY, USA, **2013**, vol. 4, ch. 11, pp. 885–972.

Chapter 5

Nature of E_2X_2 σ(4c–6e) of the X---E–E---X Type at Naphthalene 1,8-Positions and Model, Elucidated by X-ray Crystallographic Analysis and QC Calculations with QTAIM Approach

Abstract

The nature of E_2X_2 (4c–6e) of the X-∗-E-∗-E-∗-X type is elucidated for 1-(8-$XC_{10}H_6$)E–E($C_{10}H_6$X-8')-1' (**5-1** (E, X) = (S, Cl), **5-2** (S, Br), **5-3** (Se, Cl), **5-4** (Se, Br)) after structural determination of **5-1**, **5-3** and **5-4**, together with model **5-A** (MeX--- E(H)–E(H)---XMe (E = S and Se; X = Cl and Br)). The quantum theory of atoms-in-molecules dual functional analysis (QTAIM-DFA) is applied. The total electron energy densities $H_b(\boldsymbol{r}_c)$ are plotted versus $H_b(\boldsymbol{r}_c) - V_b(\boldsymbol{r}_c)/2$ for the interactions at the bond critical points (BCPs; ∗), where $V_b(\boldsymbol{r}_c)$ show the potential energy densities at the BCPs. Data for the perturbed structures around the fully optimized structures are employed for the plots, in addition to those of the fully optimized structures. The plots were analysed using the polar coordinate (R, θ) representation of the data of the fully optimized structures. Data containing the perturbed structures were analyzed by (θ_p, κ_p), where p corresponds to the tangent line of the plot and p is the curvature. Whereas (R, θ) shows the static nature, (θ_p, κ_p) represents the dynamic nature of interactions. E-∗-E are all classified as shared shell (SS) interactions for **5-1**–**5-4** and as weak covalent (Cov-w) in nature (SS/Cov-w). The nature of *pure* CS (closed shell)/ *typical*-HB (hydrogen bond) with no covalency is predicted for E-∗-X in **5-1** and **5-3**, regular CS/*typical*-HB nature with covalency is predicted for **5-4**, and an intermediate nature is predicted for **5-2**. The NBO energies evaluated for E-∗-X in **5-1**–**5-4** are substantially larger than those in model **5-A** due the shortened length at the naphthalene 1,8-positions. The nature of E_2X_2 of (4c–6e) is well elucidated via QTAIM-DFA.

Introduction

Strong 2c–2e (two centre–two electron bonds) chemical bonds are formed if the orbital at each atom in question is filled with a single electron when the two atoms come approach to distance (much) less than the sum of the van der Waals (vdW) radii. The bonds will be moderately strong if the resulting orbitals are filled with one or three electrons, which are described as 2c–1e and 2c–3e, respectively. However, large repulsion will arise in 2c–4e due to the large disadvantageous exchange integrals if the original orbitals are both filled with two electrons. It is important to avoid such disadvantageous exchange integrals to control weak interactions. He has been interested in such weak interactions as a factor to control the fine details of structures and to create delicate properties in materials, in addition to the structural and energetic characteristics. How can the large repulsive interactions in 2c–4e be avoided? He hypothesized that they could be avoided and changed to weak attractive interactions if a low-lying vacant orbital is placed near the 2c–4e.

Figure 5-1 shows the formation of 2c–4e from ($1c_A$–2e + $1c_B$–2e) (a) and that of 3c–4e from ($1c_A$–2e + $1c_A$–0e + $1c_B$–2e), where $1c_A$–2e and $1c_A$–0e stand for filled and vacant orbitals, respectively, of atom A, while $1c_B$–2e stands for a filled orbital of atom B (b). The number of atoms is the same as that of the orbitals for 2c–2e, for example; however, $2c_A$ in $2c_A$–2e and 3c in 3c–4e do not represent the number of atoms but the number of orbitals, as shown in Figure 5-1b. In this case, $2c_A$–2e of atom A can be replaced by 2c–2e of molecule A, consisting of a σ-orbital filled with two electrons and a vacant σ*-orbital. While halogen molecules and dichalcogen bonds supply the typical 2c–2e of the σ- and σ*-orbitals (σ(2c–2e)), the p-type lone pair orbitals (n_p) of halogen and chalcogen atoms act as $1c_B$–2e at atom B, which are filled with two electrons. The large repulsive exchange integrals, due to 2c–4e, can be avoided through the formation of 3c–4e from ($1c_A$–2e + $1c_A$–0e + $1c_B$–2e) (σ($1c_A$–2e) + σ*($1c_A$–0e) + n_p($1c_B$–2e)). The CT interactions of the $n_p \rightarrow \sigma^*$ type stabilize the σ type linear 3c–4e (σ(3c–4e)), where the system is stabilized by the extension of electrons to a wider area than the original area, even if the energy level of the extended area is greater than the original energy level.

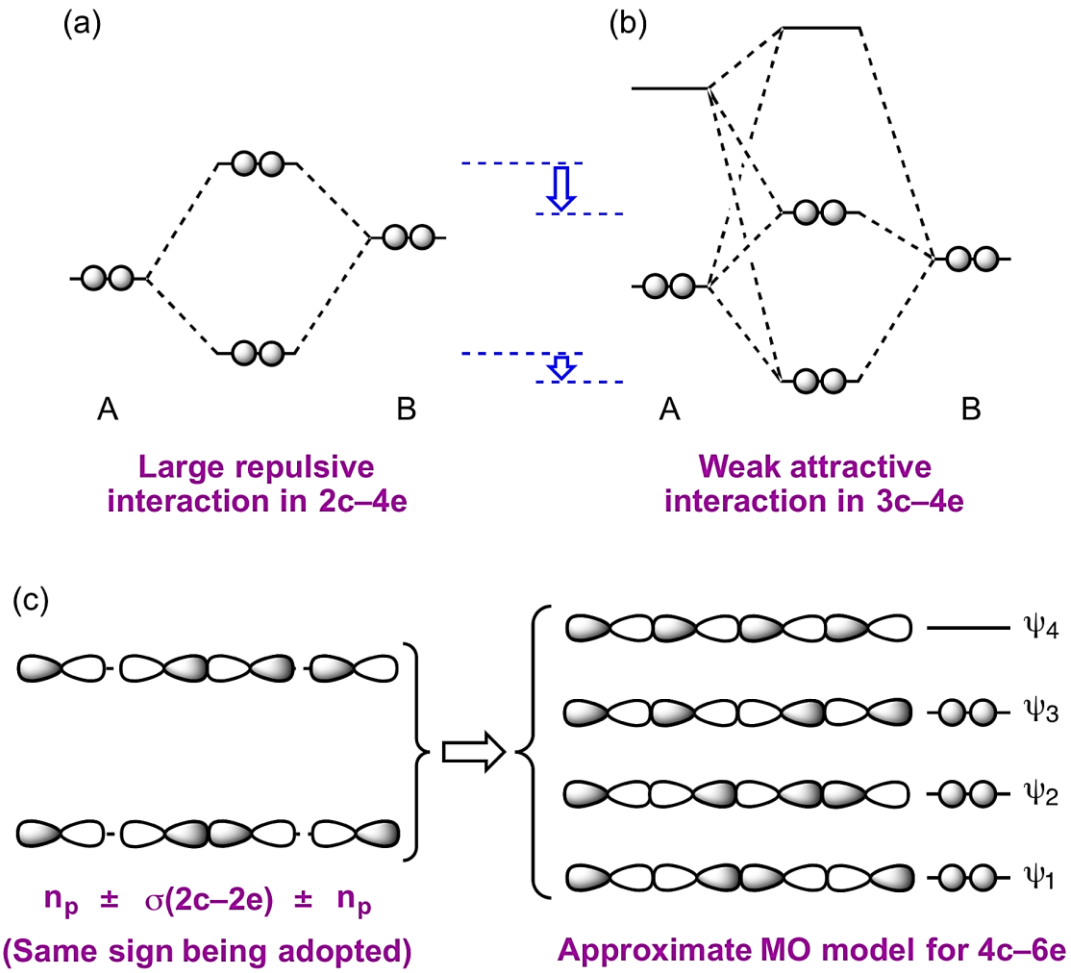

Figure 5-1. Large repulsive interaction due the formation of 2c–4e (a) and weak attractive interaction through the formation of 3c–4e (b), together with the approximate MO model for 4c–6e, formed from the n_p(1c–2e) ± σ(2c–2e) ± n_p(1c–2e) interactions (c).

What happens if σ(3c–4e) occur at both sides of σ(2c–2e) of the n_p(1c–2e)→σ(2c–2e)←n_p(1c–2e) form? Compounds containing linear interactions of four chalcogen atoms (E_4) of the n_p(1c–2e)→σ(2c–2e)←n_p(1c–2e) form were first prepared in a naphthalene system for 1-(8-Ph^{B}E$C_{10}H_6$)^{A}E–^{A}E($C_{10}H_6$^{B}EPh-8')-1' with (^{A}E, ^{B}E) = (Se, Se), and the structures were determined by X-ray crystallographic analysis.[1-3a] His research group proposed to analyse the linear E_4 interactions using the σ(4c–6e) model instead of the double σ(3c–4e) model. Figure 5-1c illustrates the approximate MO model for σ(4c–6e) formed from interactions of the n_p(1c–2e) ± σ(2c–2e) ± n_p(1c–2e) form, where the same sign should be adopted. His research group call such interactions extended hypervalent interactions, σ(*m*c–*n*e) ($4 \leq m$; $m < n < 2m$),[4,5a] after hypervalent σ(3c–4e) originally proposed by Pimentel and Musher.[6,7] A substantial number of compounds containing σ(4c–6e) have been reported.[4,5a] The σ(4c–6e) interactions are strongly suggested to play an important role in the development of high functionalities in materials and in the key processes of biological and/or pharmaceutical activities.[4,8-11]

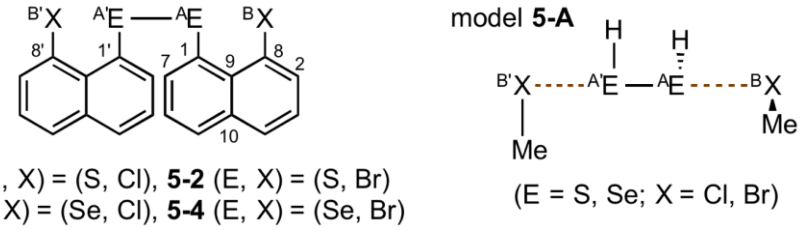

5-1 (E, X) = (S, Cl), **5-2** (E, X) = (S, Br)
5-3 (E, X) = (Se, Cl), **5-4** (E, X) = (Se, Br)

Scheme 5-1. Graphical representation of **5-1**–**5-4** and model **5-A**.

The E_2X_2 σ(4c–6e) of the $n_p(X)\rightarrow\sigma^*(E–E)\leftarrow n_p(X)$ type supplies important information for the chemical sciences, in addition to E_4 σ(4c–6e). It is challenging to elucidate the nature of E_2X_2 σ(4c–6e), which causes high functionality and reactivity in materials. Scheme 5-1 illustrates 1-(8-^{8}X$C_{10}H_6$)^{1}E–^{1}E($C_{10}H_6$^{8}X-8')-1' (**5-1** (^{1}E, ^{8}X) = (S, Cl); **5-2** (S, Br); **5-3** (Se, Cl); **5-4** (Se, Br)) in a naphthalene system and model **5-A** [Me^{B}X---^{A}E(H)–^{A}E(H)---^{B}XMe: ^{A}E = S and Se; ^{B}X = Cl and Br]. The ^{B}X---^{A}E–$^{A'}$E---$^{B'}$X notation is used for **5-1**–**5-4** and model **5-A** when it is necessary to distinguish $^{A'}$E---$^{B'}$X from ^{A}E---^{B}X, although ^{B}X---^{A}E–^{A}E---^{B}X is also used as the synonym, unless greater clarity is required. The former is typically applied to the angles, such as ∠^{B}X^{A}E$^{A'}$E, or the torsional angles, such as ϕ(^{B}X^{A}E$^{A'}$E$^{B'}$X). The nature of E_2X_2 σ(4c–6e) is elucidated for **5-1**–**5-4** and model **5-A** after determination of the structures of **5-1**, **5-3** and **5-4**, for a better understanding of the chemistry resulting from the interactions.

Theoretical investigations on the phenomena arising from σ(4c–6e) are increasing. However, it is still of high importance to clarify the causality of the phenomena arising from σ(4c–6e) with physical necessity. In this chapter, he discusses the nature of E_2X_2 σ(4c–6e) of the $n_p(X)\rightarrow\sigma^*(E–E)\leftarrow n_p(X)$ form in **5-1**–**5-4** and model **5-A**, elucidated via QTAIM-DFA. The interactions in question are classified and characterized by employing the criteria as a reference. The nature of E_2X_2 σ(4c–6e) in **5-1**, **5-3** and **5-4** are also discussed in relation to the observed structures determined by crystallographic analysis. The detail of QTAIM-DFA and the criteria are explained in the Chapter 2 using Schemes 2-1 and 2-2, Figure 2-1 and eqs (2-1)–(2-7). The basic concept of the QTAIM approach is also surveyed.

Methodological Details

Experimental

Bis(8-chloronaphthyl)-1,1'-disulfide (5-1)

1.00 g (5.14 mmol) of 8-chloro-1-naphthalenethiol in 3 ml of DMSO was stirring at 80–90 °C over 8 hrs.[12] The solution was poured into a iced-water. The white solid formed was filtered out and dried. The crude product was recrystallized from dichloromethane–hexane. **5-1** gave 91 % yield as pale yellow prisms: mp 183.2–183.8 °C, ^{1}H NMR (300 MHz, $CDCl_3$, δ, ppm, TMS): 7.34 (t, *J* = 7.9 Hz, 2H), 7.38 (t, *J* = 8.1 Hz, 2H), 7.62 (dd, *J* = 7.4 Hz and 1.4 Hz, 2H), 7.68 (dd, *J* = 8.3 Hz and 0.9 Hz, 2H), 7.79 (dd, *J* = 8.3 Hz and 1.1 Hz, 2H), 7.98 (dd, *J* = 7.7 Hz and 1.1 Hz, 2H); ^{13}C NMR (75.5 MHz, $CDCl_3$, δ, ppm, TMS): 125.7, 125.9, 126.3, 127.8, 128.6, 129.3, 129.5, 130.5, 133.1, 136.9; Anal. Calcd for **5-1** ($C_{20}H_{12}Cl_2S_2$): C, 62.02; H, 3.12%. Found: C, 61.74; H, 3.18%.

Bis(8-chloronaphthyl)-1,1'-diselenide (5-3)

1-chloro-8-iodonaphthalene (1.00 g, 3.47 mmol) with magnesium (0.08 g, 3.47 mmol) in dry diethyl ether (15 mL) and dry benzene (5 mL) was prepared Grignard reagent under an argon atmosphere.[13] Then, selenium powder (0.27 g, 3.47 mmol) was added to the solution. The reaction mixture was refluxed for 3 h. After usual workup, the solution was chromatographed on silica gel. **5-3** gave 72 % yield as yellow prisms: mp 199.0–200.5 °C, ^{1}H NMR (300 MHz, $CDCl_3$, δ, ppm, TMS): 7.25 (t, *J* = 7.8 Hz, 2H), 7.37 (t, *J* = 7.8 Hz, 2H), 7.60 (dd, *J* = 7.5 Hz and 1.4 Hz, 2H), 7.68 (dd, *J* = 8.2 Hz and 0.9 Hz, 2H), 7.77 (dd, *J* = 8.3 Hz and 1.0 Hz, 2H), 8.01 (dd, *J* = 7.6 Hz and 1.1 Hz, 2H); ^{13}C NMR (75.5 MHz, $CDCl_3$, δ, ppm, TMS): 125.8, 126.4, 127.0, 128.1, 128.6$_3$, 128.6$_4$, 130.3$_6$, 130.4$_0$, 131.3, 137.0; ^{77}Se NMR (57 MHz, $CDCl_3$, δ, ppm, Me_2Se): 479.8; Anal. Calcd for **5-3** ($C_{20}H_{12}Cl_2Se_2$): C, 49.93; H, 2.51%. Found: C, 49.95; H, 2.40%.

Bis(8-bromonaphthyl)-1,1'-diselenide (5-4)

Following the similar method to **5-3** starting from 1.00 g (3.00 mmol) of 1-bromo-8-iodonaphthalene,[13] **5-4** gave 64 % yield as yellow needles: mp 196.0–196.5 °C, ^{1}H NMR (300 MHz, $CDCl_3$, δ, ppm, TMS): 7.24 (t, *J* = 8.1 Hz, 2H), 7.31 (t, *J* = 7.9 Hz, 2H), 7.69 (dd, *J* = 8.1 Hz and 0.8 Hz, 2H), 7.81–7.86 (m, 4H), 8.08 (dd, *J* = 7.5 Hz and 1.1 Hz, 2H); ^{13}C NMR (75.5 MHz, $CDCl_3$/TMS) δ 120.3, 126.2, 126.9, 127.5, 128.4, 129.3, 131.1, 131.9, 132.9, 137.3; ^{77}Se NMR (57 MHz, $CDCl_3$, δ, ppm, Me_2Se): 489.4, Anal. Calcd for **5-4** ($C_{20}H_{12}Br_2Se_2$): C, 42.14; H, 2.12. Found: C, 42.39; H, 2.24%.

X-ray structure determination

Single crystals of **5-1**, **5-3** and **5-4** were obtained from solutions of *n*-hexane/dichloromethane (2/1, v/v). X-ray diffraction data for **5-1**, **5-3** and **5-4** were recorded on a Rigaku/MSC Mercury CCD diffractometer equipped with a graphite-monochromated MoKα radiation source. For **5-1**, the structure analysis was based on 5988 observed reflections with $I > 2\sigma(I)$ and 529 variable parameters; colourless prism, 103 K, orthorhombic, space group $Pca2_1$ (#29), a = 7.824(2) Å, b = 28.782(8) Å, c = 14.350(4) Å, V = 3231.7(15) Å^3, Z = 8, R = 0.0201, $_WR$ = 0.0520, GOF = 1.073. For **5-3**, the structure analysis was based on 6129 observed reflections with $I > 2\sigma(I)$ and 433 variable parameters; yellow prism, 103 K, orthorhombic, space group $Pca2_1$ (#29), a = 7.89330(10) Å, b = 29.1713(4) Å, c = 14.4594(2) Å, V = 3329.39(8) Å^3, Z = 8, R = 0.0243, R_W = 0.0592, GOF = 1.058. For **5-4** the structure analysis was based on 3813 observed reflections with $I > 2.00\sigma(I)$ and 217 variable parameters; light yellow plate, 103 K, triclinic, space group $P\bar{1}$ (#2), a = 7.83940(10) Å, b = 8.0986(2) Å, c = 15.0650(4) Å, α = 90.9410(10)°, β = 101.8880(10)°, γ = 111.0930(10)°, V = 868.92(3) Å^3, Z = 2, R = 0.0391, R_W = 0.0788, GOF = 1.198. Experimental details are summarized in Table 5-A1.

The structures were solved by SHELXS-97 for **5-1**, **5-3** and **5-4**, and refined by the full-matrix least squares on F^2 for all reflection.[14] CCDC-698897 for **5-1**, CCDC-1517582 for **5-3** and CCDC-698898 for **5-4** contain the supplementary crystallographic data for this paper. These data can be obtained free of charge from the Cambridge Crystallographic Data Centre via www.ccdc.cam.ac.uk/data request/cif.

Computational detail

Calculations were performed using the Gaussian 09 program package.[15] Compounds **5-1**–**5-4** were evaluated with the 6-311+G(3df) basis sets for S, Se, Cl and Br and the 6-311G(d) basis sets for C and H, which is called BSS-A (the basis set system A) in this chapter. BSS-B was also employed to optimize **5-1**–**5-4**, which consisted of the 6-311+G(3d) basis sets for S, Se, Cl and Br and the 6-311G(d) basis set for C and H. The results with BSS-A are mainly discussed in this paper. Model **5-A** was optimized with the 6-311+G(3df) basis sets for S, Se, Cl and Br and with the 6-311G(d, p) basis sets for C and H (BSS-C). The Møller-Plesset second-order energy correlation (MP2) level was applied to the calculations.[16] The DFT level of M06-2X was also applied when necessary.[17] Structures were confirmed by frequency analysis performed on the optimized structures using the same method.

QTAIM functions were calculated using the Gaussian 09 program package with the same method of the optimizations. The results were analysed with the AIM2000 program.[18] Normal coordinates of internal

vibrations (NIV) obtained by the frequency analysis were employed to generate the perturbed structures. The details of NIV and QTAIM-DFA are explained in Chapter 2.

Results and Discussion

Structural features of bis(8-halonaphthyl)-1,1'-diselenides and model A

The structures of **5-1**, **5- 3** and **5-4** were determined by X-ray crystallographic analysis at 103(2) K. Figure 5-2 shows the structure of **5-4**. The structures of **5-1** and **5-3** are essentially the same as that of **5-4** (Figures 5-A1, 5-A2 and Table 5-A1 of the Appendix). Selected structural parameters for the observed structures of **5-1**, **5-3** and **5-4** are collected in Table 5-1, together with the optimized structures of **5-1**–**5-4**. The averaged values are shown as the observed values if the same values are not obtained for the observed structural parameters. Selected structural parameters for model **5-A** are collected in Table 5-A2 of the Appendix. Optimized structures are not shown in the figures, but some can be found in the molecular graphs and contour plots of $\rho(\boldsymbol{r})$ drawn on the optimized structures (see, Figures 5-A3 and 5-A4 of the Appendix).

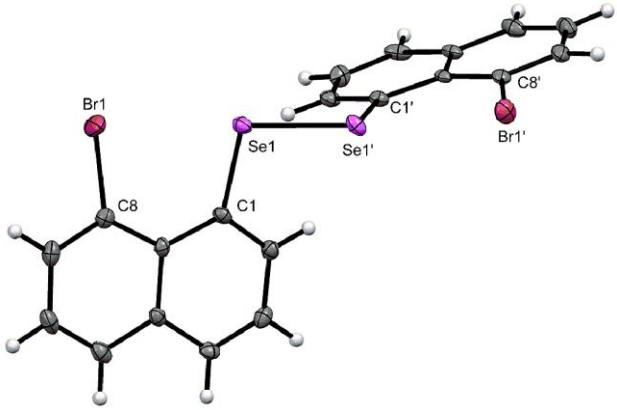

Figure 5-2. Structure of **5-4**, determined by the X-ray crystallographic analysis. Thermal ellipsoids are drawn at 50% probability.

The observed structures of **5-1**, **5-3** and **5-4** are reproduced well by the optimization with MP2/BSS-A overall, although the $\phi_1 = \phi(^1C^AE^{A'}E^{1'}C)$ values in the optimized structure of **5-1** (69.7º) are substantially smaller than those of **5-2**–**5-4** (84.2º–88.9º) (see also Figures 5-3 and 5-4). Re-optimizations of **5-1** converged to the structure shown in Table 5-1, even when the optimizations started with the structure of **5-2** with the Br atoms replaced by Cl. A magnitude of Δr (= $r_{calcd} - r_{obsd}$) less than 0.013 Å is very good for QTAIM-DFA if the predicted nature is discussed in relation to the observed structures. A magnitude of 0.026 Å would be acceptable for QTAIM-DFA (a magnitude of Δr of 0.013 Å corresponds to half of the intervals of adjacent (data) points in the plots of $H_b(\boldsymbol{r}_c)$ versus $H_b(\boldsymbol{r}_c) - V_b(\boldsymbol{r}_c)/2$ ($0.05a_o/2$ = 0.013 Å) and that of 0.026 Å corresponds to the intervals of adjacent (data) points in the plots (0.026 Å = $0.05a_o$)). The

r_o(E, E) values for **5-1**, **5-3** and **5-4** are predicted to be shorter than the observed values by 0.015, 0.024 and 0.028 Å, respectively, while the r_o(E, X) values are predicted to be longer than the observed values by 0.015, 0.007, and 0.011 Å, respectively, if optimized with MP2/BSS-A. While the predicted r_o(E, E) value is (very) good for **5-1**, the values are acceptable for **5-3** and **5-4**, although the magnitude of Δr(E, E) for **5-4** (0.028 Å) is slightly larger than the acceptable value of 0.026 Å. On the other hand, the predicted r_o(E, X) values are very good for **5-1**, **5-3** and **5-4**, although the magnitude of Δr(E, X) for **5-1** (0.015 Å) is slightly larger than 0.013 Å. The predicted distances are excellent for our purpose since the nature of the E-∗-X interactions are the main focus in E_2X_2 σ(4c–6e).

How are the energies in the formation of model **5-A** from the components? Table 5-A2 of the Appendix shows the values for model **5-A**, ΔE_{ESf} and ΔE_{ZP}, where ΔE_{ESf} stands for those on the energy surface and ΔE_{ZP} for those considering the zero-point energy corrections. The ΔE_{ESf} and ΔE_{ZP} values gradually decrease (become more stable) in the order shown in eq (5-1). The plot of ΔE_{ZP} versus ΔE_{ESf} showed a strong correlation ($\Delta E_{ZP} = 1.96\Delta E_{ESf} + 29.49$, $R_c^2 = 0.900$ (R_c^2: square of the correlation coefficient)).

(E, X) = (S, Br) ≥ (S, Cl) ≥ (Se, Cl) ≥ (Se, Br) (5-1)

Table 5-1 Structural parameters evaluated for **5-1**–**5-4** with MP2/BSS-A and those observed for **5-1**, **5-3** and **5-4**.[a]

Species (E, X) (Symmetry)	r_o(E, E) (Å)	r_o(E, X) (Å)	Δr_o(E, X)[b] (Å)	$\angle^1C^AE^{A'}E$ (º)	$\angle^8X^AE^{A'}E$ (º)
Optimized with MP2/BSS-A					
5-1 (S, Cl) (C_2)	2.0311	2.9340	–0.616	105.2	171.8
5-2 (S, Br) (C_2)	2.0330	3.0392	–0.611	104.6	170.0
5-3 (Se, Cl) (C_2)	2.3010	2.9774	–0.673	102.6	173.9
5-4 (Se, Br) (C_2)	2.3072	3.0837	–0.666	101.8	174.8
Determined by X-ray analysis					
5-1 (S, Cl)[c]	2.0461[d]	2.949[d]	–0.601	105.62[d]	170.87[d]
5-3 (Se, Cl)[c]	2.3249[d]	2.9708[d]	–0.679	103.61[d]	174.79[d]
5-4 (Se, Br)	2.3355(7)	3.0728[d]	–0.677	102.8[d]	170.67[d]

[a] With MP2/BSS-A. BSS-A: The 6-311+G(3df) basis set for S, Se, Cl and Br with the 6-311G(d) basis set for C and H. (b) $\Delta r_o(^AE, ^BX) = r_o(^AE, ^BX) - \Sigma r_{vdW}$(E, X), where r_{vdW}(S) = 1.80 Å, r_{vdW}(Se) = 1.90 Å, r_{vdW}(Cl) = 1.75 Å, and r_{vdW}(Br) = 1.85 Å.[19] [c] The crystals contain two independent molecules in a unit cell. [d] Averaged value.

(Table 5-1 continued)

Species (E, X) (Symmetry)	ϕ_1[e] (°)	ϕ_2[f] (°)	ϕ_3[g] (°)	$E(2)$[h] (kJ mol^{-1})
Optimized with MP2/BSS-A				
5-1 (S, Cl) (C_2)	69.7	–15.4	170.9	19.3
5-2 (S, Br) (C_2)	88.7	17.6	–171.2	18.5
5-3 (Se, Cl) (C_2)	84.2	10.6	–175.6	28.1
5-4 (Se, Br) (C_2)	88.9	20.2	–169.9	27.9
Determined by X-ray analysis				
5-1 (S, Cl)[c]	76.25[d]	8.64 [d]	176.0[d]	20.4[d]
5-3 (Se, Cl)[c]	74.2[d]	6.90 [d]	177.1[d]	29.4[d]
5-4 (Se, Br)	90.8(2)	13.2 [d]	173.2[d]	36.0[d]

[e] $\phi_1 = \phi(^1C^AE^{A'}E^{1'}C)$ [f] $\phi_2 = \phi(^AE^1C^8C^BX)$ [g] $\phi_3 = \phi(^{10}C^9C^8C^BX)$ [h] Evaluated based on the NBO analysis.

NBO analysis is also applied to ^AE---^BE in **5-1**–**5-4** and model **5-A** to evaluate the contributions from the CT interactions between $n_p(^BX)$ and $\sigma^*(^AE–^AE)$ to stabilize the interactions.[20-27] For each donor NBO (i) and acceptor NBO (j), the stabilization energy $E(2)$ is calculated based on the second-order perturbation theory in NBO, according to eq (5-2), where q_i is the donor orbital occupancy, ε_i and ε_j are diagonal elements (orbital energies) and $F(i,j)$ is the off-diagonal NBO Fock matrix element. The $E(2)$ values are evaluated at the M06-2X level using structures optimized at the MP2 level.

$$E(2) = q_i F(i,j)^2/(\varepsilon_j - \varepsilon_i) \qquad (5\text{-}2)$$

Table 5-1 shows the $E(2)$ values for **5-1**–**5-4**, while those for model **5-A** are in Table 5-A3 of the Appendix. The $E(2)$ values for **5-1**–**5-4** increase (become more stabilized) in the order shown in eq (5-3) if evaluated based on the optimized structures. The order is the opposite of that for Δr_o(E, X) given in Table 5-1. Similarly, the $E(2)$ values of model **5-A** increase (become more stabilized) in the order shown in eq (5-3). Eq (5-3) indicates that X-∗-E-∗-E-∗-X will become more stabilized if the accepting ability of σ^*(E–E) is increased relative to the case of an increase in the donating ability of n_p(X). Namely, σ^*(E–E) contributes much more than n_p(X) in $E(2)$. The trend is clearer when comparing $E(2)$ relative to the case of ΔE_{ESf}, where $2E(2)$ corresponds to ΔE_{ESf}.

$$(E, X) = (S, Cl) \approx (S, Br) << (Se, Cl) \approx (Se, Br) \qquad (5\text{-}3)$$

After clarification of the structural features, the next step is to elucidate the nature of E_2X_2 σ(4c–6e) in **5-1**–**5-4** and model **5-A**. Molecular graphs and contour plots are examined for **5-1**–**5-4** and model **5-A** before a discussion based on QTAIM-DFA.

Molecular graphs and contour plots around X-∗-E-∗-E-∗-X in 5-1–5-4 and model 5-A

Figures 5-3 and 5-4 show the molecular graphs and contour plots of $\rho(\boldsymbol{r})$, respectively, for **5-1**–**5-4**, for the optimized structures. Those for model **5-A** are illustrated in Figures 5-A3 and 5-A4 of the Appendix. All expected BCPs are detected, including those of the X-∗-E-∗-E-∗-X interactions (Dots are usually employed to show BCPs in molecular graphs. Therefore, A-•-B would be more suitable to describe BP with BCP. Nevertheless, A-∗-B is employed to emphasize the existence of BCP on BP in our case.) BCPs are located on the (three-dimensional) saddle points of $\rho(\boldsymbol{r})$. The contour plots of $\rho(\boldsymbol{r})$ for **5-1** in Figure 5-4 are somewhat different from those for **5-2**–**5-4**, possibly due to the smaller $\phi_1 = \phi(^1C^AE^{A'}E^{1'}C)$ value (69.7°) for the optimized structure of **5-1** relative to those for **5-2**–**5-4** (84.2°–88.9°). Re-optimizations of **5-1** converged to the structure shown in Figures 5-3 and 5-4, even if the optimizations started with the structure of **5-2**, with the Br atoms replaced by Cl, as mentioned above. Negative Laplacians and trajectory plots are illustrated for **5-1**–**5-4** and model **5-A** in Figures 5-A5 and 5-A6, respectively, of the Appendix. As shown in Figure 5-A5, the BCPs on E-∗-E are all placed in the negative area of $\nabla^2\rho_b(\boldsymbol{r}_c)$, whereas those on E-∗-X are in the positive area of $\nabla^2\rho_b(\boldsymbol{r}_c)$. The results show that E-∗-E and E-∗-X are classified by shared shell (SS) and closed shell (CS) interactions, respectively. The space around the species is reasonably divided into atoms of the species (see Figure 5-A6).

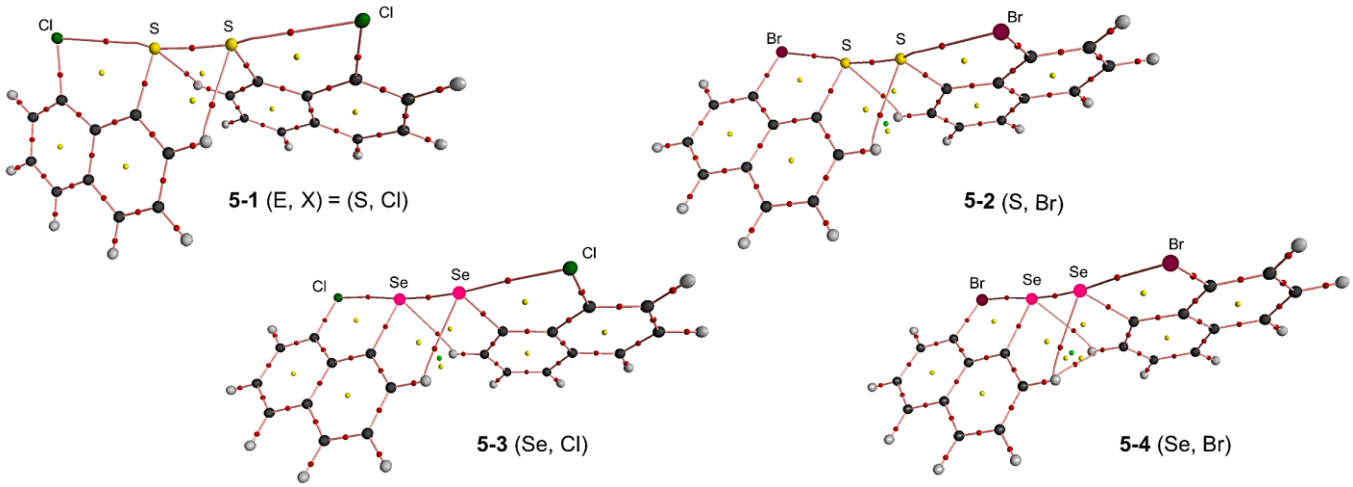

Figure 5-3. Molecular graphs for **5-1** (S, Cl)– **5-4** (Se, Br). BCPs (bond critical points) are denoted by red dots, RCPs (ring critical points) by yellow dots, CCPs (cage critical points) by green dots and BPs (bond paths) by pink lines. Carbon atoms are in black and hydrogen atoms are in grey, while sulfur, selenium, chlorine and bromine atoms are in yellow, pink, green and dark purple, respectively.

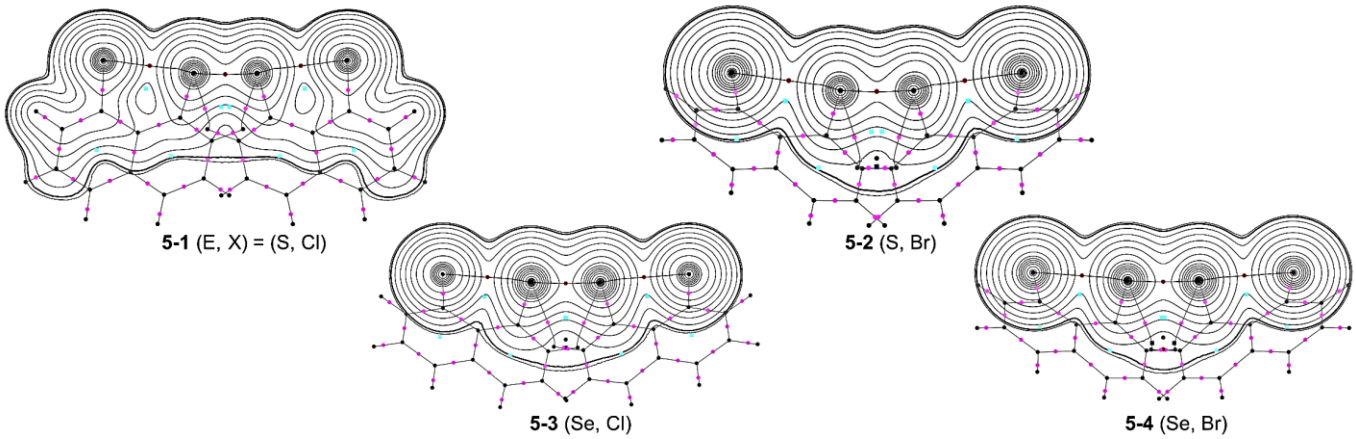

Figure 5-4. Contour plots of $\rho(\boldsymbol{r})$ for **5-1** (S, Cl)–**5-4** (Se, Br). BCPs on the plane are shown by red dots, those outside of the plane are shown as dark pink dots, and RCPs on and outside the plane are shown as blue squares and light blue squares, respectively. CCPs are shown as green squares and BPs on the plane as black lines and those outside of the plane as grey lines. Atoms on and outside the plane are shown as black dots and grey dots, respectively. The contours (ea_0^{-3}) are at 2^l (l = ±8, ±7, ..., 0) with 0.0047 (heavy line).

Survey of the X-∗-E-∗-E-∗-X interactions in 5-1–5-4 and model 5-A

Can the X-∗-E-∗-E-∗-X interactions of E_2X_2 σ(4c–6e) in **5-1**–**5-4** and model **5-A** really be approximated by straight lines? The lengths of BPs (r_{BP}), corresponding to E_2X_2 σ(4c–6e) in **5-1**–**5-4** and model **5-A**, are presented in Table 5-A4 of the Appendix, together with the straight-line distances (R_{SL}) and the differences between them ($\Delta r_{BP} = r_{BP} - R_{SL}$). The magnitudes of Δr_{BP} values are less than 0.014 Å for all BPs, which demonstrates that the interactions in E_2X_2 σ(4c–6e) can be described as straight lines for **5-1**–**5-4** and model **5-A**.

The QTAIM functions of $\rho_b(\boldsymbol{r}_c)$, $H_b(\boldsymbol{r}_c) - V_b(\boldsymbol{r}_c)/2$, $H_b(\boldsymbol{r}_c)$, and $k_b(\boldsymbol{r}_c)$ (= $V_b(\boldsymbol{r}_c)/G_b(\boldsymbol{r}_c)$) are calculated for E-∗-E and E-∗-X at BCPs for the fully optimized structures in **5-1**–**5-4** and model **5-A**, together with the observed structures in **5-1**, **5-3** and **5-4**. Table 5-2 reports the values. Figure 5-5 shows the plots of $H_b(\boldsymbol{r}_c)$ versus $H_b(\boldsymbol{r}_c) - V_b(\boldsymbol{r}_c)/2$ for the fully optimized structures for **5-1**–**5-4** and the observed structures for **5-1**, **5-3** and **5-4**, shown in Table 5-2. Data for the perturbed structures for **5-1**–**5-4**, around the fully optimized ones, are also included in the plots. The plots are analysed according to eqs (2-3)–(2-6) in the Chapter 2, and the QTAIM-DFA parameters of (R, θ) and (θ_p, κ_p) are obtained. Table 5-2 shows the (R, θ) and (θ_p, κ_p) values for **5-1**–**5-4** and model **5-A**. Table 5-2 also includes the frequencies (ν) and force constants (k_f) corresponding to the E-∗-E and E-∗-X in question.

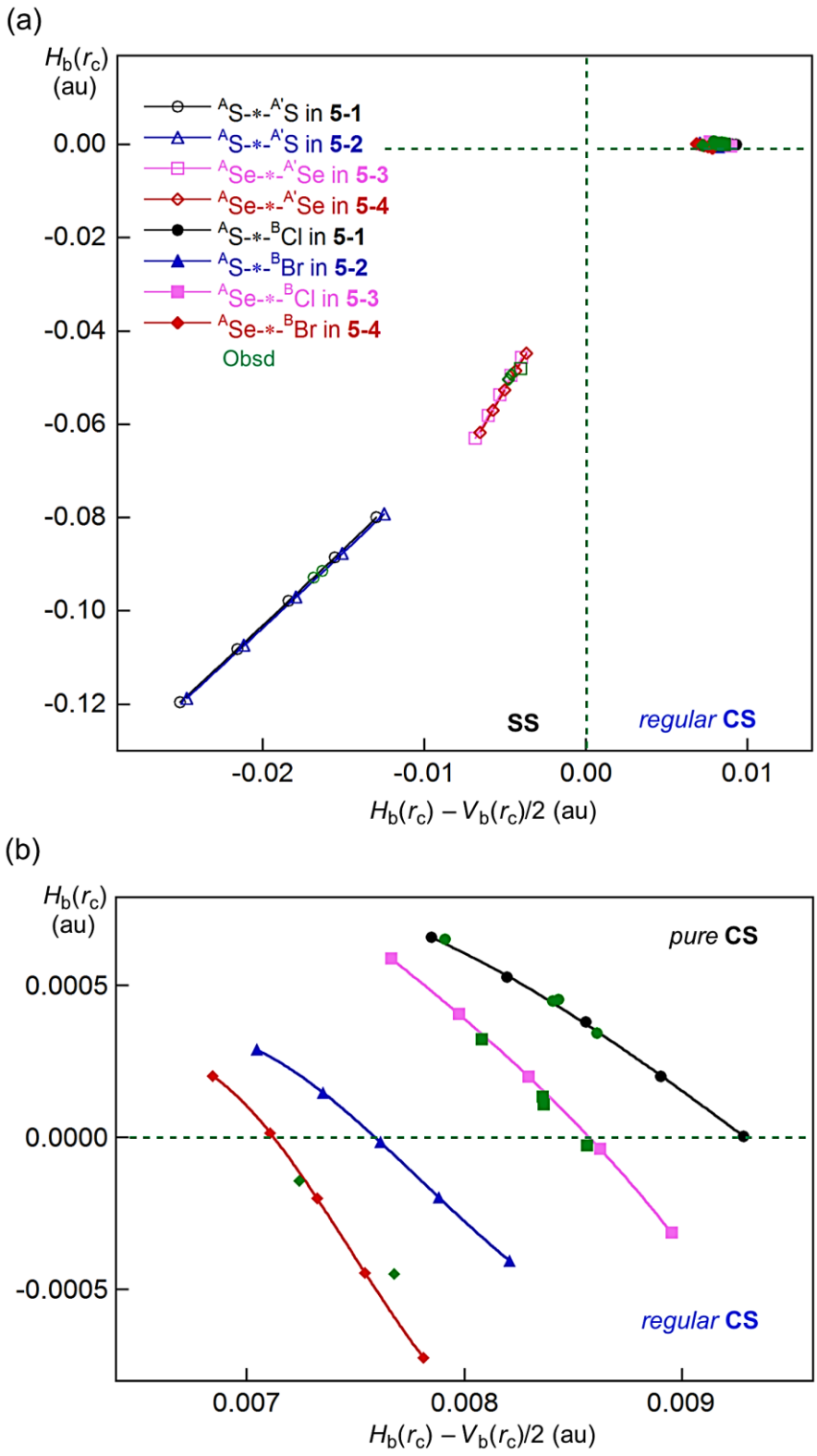

Figure 5-5. Plots of $H_b(\boldsymbol{r}_c)$ versus $H_b(\boldsymbol{r}_c) - V_b(\boldsymbol{r}_c)/2$ for E-∗-E and E-∗-X of **5-1**–**5-4**. Whole picture (a) and the magnified image (b) for E-∗-X. The marks and colours for the species are shown in the figure. The data for interactions in the observed structures of **5-1**, **5-3** and **5-4** are in green, where the marks for the interactions are the same as those in the optimized structures. Two (data) points for E-∗-X correspond to the slightly different interaction distances in a structure (*cf*: ^{8}Br---^{1}Se–$^{1'}$Se---$^{8'}$Br in **5-4**), while the four (data) points for E-∗-X arise from the two different types of observed structures (*cf*: **5-1** and **5-3**). (Table 5-2 shows the averaged values)

Table 5-2 QTAIM functions and QTAIM-DFA parameters for E-∗-E and E-∗-X at BCPs in the optimized structures of **5-1**–**5-4** and the observed structures of **5-1**, **5-3** and **5-4**, evaluated with MP2/BSS-A, together with model **5-A** evaluated with MP2/BSS-C.[a]

Species (Symmetry)	Interaction (E-∗-X)	$\rho_b(\boldsymbol{r}_c)$ (au)	$c\nabla^2\rho_b(\boldsymbol{r}_c)^b$ (au)	$H_b(\boldsymbol{r}_c)$ (au)	$k_b(\boldsymbol{r}_c)^c$	R (au)	θ (º)
The C_2 structures optimized for **5-1**–**5-4**							
5-1 (S, Cl)	(S-∗-S)	0.1553	–0.0184	–0.0978	–2.604	0.0995	190.7
5-2 (S, Br)	(S-∗-S)	0.1546	–0.0180	–0.0970	–2.589	0.0987	190.5
5-3 (Se, Cl)	(Se-∗-Se)	0.1103	–0.0053	–0.0536	–2.248	0.0539	185.7
5-4 (Se, Br)	(Se-∗-Se)	0.1091	–0.0050	–0.0525	–2.237	0.0528	185.5
5-1 (S, Cl)	(S-∗-Cl)	0.0223	0.0086	0.0004	–0.977	0.0086	87.5
5-2 (S, Br)	(S-∗-Br)	0.0220	0.0076	0.0000	–1.001	0.0076	90.1
5-3 (Se, Cl)	(Se-∗-Cl)	0.0228	0.0083	0.0002	–0.988	0.0083	88.6
5-4 (Se, Br)	(Se-∗-Br)	0.0225	0.0073	–0.0002	–1.013	0.0073	91.6
The C_1 structures for **5-1**, **5-3** and **5-4**, determined by X-ray analysis							
5-1 (S, Cl)	(S-∗-S)	0.1515	–0.0169	–0.0929	–2.570	0.0944	190.3
5-3 (Se, Cl)	(Se-∗-Se)	0.1066	–0.0048	–0.0503	–2.236	0.0505	185.5
5-4 (Se, Br)	(Se-∗-Se)	0.1041	–0.0041	–0.0480	–2.203	0.0482	184.8
5-1 (S, Cl)	(S-∗-Cl)	0.0226	0.0086	0.0003	–0.980	0.0086	87.7
5-3 (Se, Cl)	(Se-∗-Cl)	0.0231	0.0084	0.0001	–0.992	0.0084	89.1
5-4 (Se, Br)	(Se-∗-Br)	0.0223	0.0072	–0.0001	–1.010	0.0072	91.1
The C_2 structures for model **5-A** (E, X): ^{B}X---^{A}E(H)–^{A}E(H)---^{B}X							
5-A (S, Cl)	(S-∗-S)	0.1489	–0.0182	–0.0902	–2.675	0.0920	191.4
5-A (S, Br)	(S-∗-S)	0.1484	–0.0179	–0.0896	–2.667	0.0914	191.3
5-A (Se, Cl)	(Se-∗-Se)	0.1068	–0.0065	–0.0510	–2.340	0.0514	187.2
5-A (Se, Br)	(Se-∗-Se)	0.1063	–0.0064	–0.0506	–2.335	0.0510	187.2
5-A (S, Cl)	(S-∗-Cl)	0.0088	0.0038	0.0012	–0.812	0.0040	72.4
5-A (S, Br)	(S-∗-Br)	0.0088	0.0036	0.0010	–0.830	0.0037	73.8
5-A (Se, Cl)	(Se-∗-Cl)	0.0087	0.0036	0.0012	–0.795	0.0038	71.2
5-A (Se, Br)	(Se-∗-Br)	0.0087	0.0033	0.0010	–0.813	0.0035	72.5

[a] BSS-A: The 6-311+G(3df) basis set being employed for S and Se with the 6-311G(d) basis set for C and H and BSS-C: The 6-311+G(3df) basis set being employed for S and Se with the 6-311G(d, p) basis set for C and H. [b] $c\nabla^2\rho_b(\boldsymbol{r}_c) = H_b(\boldsymbol{r}_c) - V_b(\boldsymbol{r}_c)/2$, where $c = \hbar^2/8m$; [c] $k_b(\boldsymbol{r}_c) = V_b(\boldsymbol{r}_c)/G_b(\boldsymbol{r}_c)$.

(Table 5-2 continued)

Species (Symmetry)	Interaction (E-∗-X)	$\nu\,(n)^d$ (cm^{-1})	$k_f{}^e$ (f)	θ_p (º)	κ_p (au^{-1})	Classification /Character
The C_2 structures optimized for **5-1**–**5-4**						
5-1 (S, Cl)	(S-∗-S)	542.7	1.686	197.1	0.3	SS/Cov-w
5-2 (S, Br)	(S-∗-S)	536.3	1.996	197.2	0.3	SS/Cov-w
5-3 (Se, Cl)	(Se-∗-Se)	326.5	0.730	189.4	0.4	SS/Cov-w
5-4 (Se, Br)	(Se-∗-Se)	316.8	0.781	189.6	0.4	SS/Cov-w
5-1 (S, Cl)	(S-∗-Cl)	213.3	0.133	115.2	114	*p*-CS/*t*-HB-nc[g]
5-2 (S, Br)	(S-∗-Br)	149.2	0.369	123.5	128	*r*-CS/*t*-HB-wc[h]
5-3 (Se, Cl)	(Se-∗-Cl)	182.2	0.475	124.2	146	*p*-CS/*t*-HB-nc[g]
5-4 (Se, Br)	(Se-∗-Br)	132.8	0.083	137.3	152	*r*-CS/*t*-HB-wc[h]
The C_1 structures for **5-1**, **5-3** and **5-4**, determined by X-ray analysis						
5-1 (S, Cl)	(S-∗-S)	(i)	(i)	(i)	(i)	SS
5-3 (Se, Cl)	(Se-∗-Se)	(i)	(i)	(i)	(i)	SS
5-4 (Se, Br)	(Se-∗-Se)	(i)	(i)	(i)	(i)	SS
5-1 (S, Cl)	(S-∗-Cl)	(i)	(i)	(i)	(i)	*p*-CS
5-3 (Se, Cl)	(Se-∗-Cl)	(i)	(i)	(i)	(i)	*p*-CS
5-4 (Se, Br)	(Se-∗-Br)	(i)	(i)	(i)	(i)	*p*-CS
The C_2 structures for model **5-A** (E, X): ^{B}X---^{A}E(H)–^{A}E(H)---^{B}X						
5-A (S, Cl)	(S-∗-S)	533.6	4.703	197.6	0.4	SS/Cov-w
5-A (S, Br)	(S-∗-S)	530.8	4.629	197.6	0.4	SS/Cov-w
5-A (Se, Cl)	(Se-∗-Se)	305.8	3.707	190.5	0.3	SS/Cov-w
5-A (Se, Br)	(Se-∗-Se)	303.9	3.726	190.5	0.3	SS/Cov-w
5-A (S, Cl)	(S-∗-Cl)	77.2	0.022	85.1	112	*p*-CS/vdW
5-A (S, Br)	(S-∗-Br)	63.3	0.023	89.0	131	*p*-CS/vdW
5-A (Se, Cl)	(Se-∗-Cl)	65.0	0.040	82.5	128	*p*-CS/vdW
5-A (Se, Br)	(Se-∗-Br)	51.3	0.062	85.4	156	*p*-CS/vdW

[d] Corresponding to the interaction in question. Symmetric and anti-symmetric modes being employed for ^{A}E-∗-^{A}E and ^{A}E-∗-^{B}E, respectively. [e] Force constant for ν. [f] mdyn Å^{-1}. [g] *Typical*-HB nature with no covalency. [h] *Typical*-HB nature with covalency. [i] Not obtained.

Nature of E-∗-E and E-∗-X in 5-1–5-4 and model 5-A, elucidated by QTAIM-DFA

The nature of E-∗-E and E-∗-X in **5-1**–**5-4** and model **5-A** is examined based on the QTAIM-DFA parameters of (R, θ, θ_p). The standard values in Scheme 2-2 in the Chapter 2 are used as a reference. It is instructive to briefly survey the criteria related to those in this work. Interactions are called CS and SS interactions for 45º < θ < 180º ($0 < H_b(\boldsymbol{r}_c) - V_b(\boldsymbol{r}_c)/2$) and 180º < θ < 206.6º ($H_b(\boldsymbol{r}_c) - V_b(\boldsymbol{r}_c)/2 < 0$), respectively. The CS interactions are sub-divided into *pure* CS (*p*-CS) and *regular* CS (*r*-CS) for 45º < θ < 90º ($0 < H_b(\boldsymbol{r}_c)$) and 90º < θ < 180º ($H_b(\boldsymbol{r}_c) < 0$), respectively. The θ_p value plays an important role in characterizing the interactions. In the *p*-CS region of 45º < θ < 90º, the character of interactions is vdW type for 45º < θ_p < 90º and *typical*-hydrogen bond nature (*t*-HB) with no covalency (*t*-HB-nc) for 90º < θ_p < 125º, where θ_p of 125º is tentatively given corresponding to θ = 90º. CT interactions appear in the *r*-CS region of 90º < θ < 180º. *t*-HB interactions with covalency (*t*-HB-wc) appear in the range of 125º < θ_p < 150º (90º < θ < 115º), where (θ, θ_p) = (115º, 150º) is tentatively given for the borderline between *t*-HB-wc and CT-MC (molecular complex formation through CT). The borderline between CT-MC and CT-TBP (TBP adduct formation through CT) is defined by θ_p = 180º. Therefore, interactions of the CT-MC and CT-TBP types appear in the ranges of 150º < θ_p < 180º (115º < θ < 150º) and 180º < θ_p < 190º (150º < θ < 180º), respectively, where θ = 150º and θ_p = 190º are tentatively given for θ_p = 180º and θ = 180º, respectively. R helps to sub-characterize the classical covalent bonds (Cov). The classic chemical bonds of SS are strong covalent interactions (Cov-s) when R > 0.15 au, but they are weak covalent (Cov-w) when R < 0.15 au.

The nature of E_2X_2 σ(4c–6e) in model **5-A** is examined first and is classified and characterized based on the (R, θ, θ_p) values. The E-∗-E interactions in model **5-A** are all classified as SS interactions and have Cov-w nature (SS/Cov-w) (θ > 180º and θ_p > 190º with R < 0.09 au < 0.15 au). On the other hand, E-∗-X are all classified as *p*-CS interactions and are predicted to have vdW nature (*p*-CS/vdW) (θ < 90º and θ_p < 90º). The E-∗-X in model **5-A** become stronger in the order shown in eq (5-4), although only slightly, if estimated with (θ, θ_p).

(E, X) = (Se, Cl) < (S, Cl) ≈ (Se, Br) < (S, Br) (5-4)

The E_2X_2 σ(4c–6e) interactions in **5-1**–**5-4** are similarly classified and characterized based on the (R, θ, θ_p) values. The E-∗-E in **5-1**–**5-4** are all classified as SS interactions and have Cov-w nature (SS/Cov-w). On the other hand, the E-∗-X are classified as *pure* CS interactions and characterized as *t*-HB-nc (*p*-CS/*t*-

HB-nc) for **5-1** (θ = 87.5º < 90º; θ_p = 115.2º < 125º) and **5-3** (θ = 88.6º < 90º; θ_p = 124.2º < 125º). Additionally, the nature of E-∗-X in **5-3** is close to *t*-HB-wc. That of **5-4** is classified as *regular* CS interactions (θ = 91.6º > 90º) and characterized as *t*-HB-wc (θ_p = 137.3º > 125º) (*r*-CS/*t*-HB-wc). In the case of **5-2**, (θ, θ_p) = (90.1º, 123.5º), which are very close to (90.0º, 125º); therefore, the nature of E-∗-X in **5-2** is very close to the borderline between (*p*-CS/*t*-HB-nc) in **5-1** and **5-3** and (*r*-CS/*t*-HB-wc) in **5-4**, although θ_p = 123.5º seems to correspond to the *t*-HB-nc nature. The E-∗-X in **5-1**–**5-4** become slightly stronger in the order shown in eq (5-5) based on θ_p, although the order is the inverse for **5-2** and **5-3**, if estimated based on θ.

θ_p and θ: **5-1** (S, Cl) < **5-2** (S, Br) ≈ **5-3** (Se, Cl) < **5-4** (Se, Br) (5-5)

The static nature of E-∗-E and E-∗-X is evaluated for the observed structures of **5-1**, **5-3** and **5-4**, based on the optimized structures. The predicted nature of E-∗-E and E-∗-X evaluated for the optimized structures of **5-1**–**5-4** corresponds to that of the observed structures of **5-1**, **5-3** and **5-4**, respectively, although the dynamic nature is not obtained for the observed structures.

Nature of E-∗-H in 5-1–5-4 and model 5-A, elucidated by QTAIM-DFA

BPs are also detected between ^{A}E and $^{2'}$H ($^{A'}$E and ^{2}H), which are denoted BP (^{A}E-∗-^{2}H), in the optimized structures of **5-1**–**5-4** and the observed structures of **5-1**, **5-3** and **5-4**. BP (Se-∗-H_{Me}) is similarly observed for model **5-A** with (E, X) = (Se, Br), whereas no such BPs are detected for model **5-A** with (E, X) other than (Se, Br).

Highly theoretical treatment is necessary to clarify the cause of the appearance and disappearance of BPs. Pendâs and co-workers discussed BPs as privileged exchange channels using the interacting quantum atom (IQA) framework.[28] They investigated how the BPs between an atom A and atom B in its environment appear to be determined by competition among the A–B exchange-correlation energies, which always contribute to stabilize the A–B interactions. In addition, they predicted when a BP is found between two atoms by examining a number of archetypal simple systems: (1) there is no other competing atom in its vicinity, so there must be a direct exchange route between them or (2) the $\mathbf{V}_{xc}$ term is the largest among several possibilities, where $\mathbf{V}_{xc}$ stands for a quantum-mechanical correction coming from the exchange correlation second-order density.[28] Additionally, the interaction energies between atoms cannot be universally used to predict the existence of a BP between them.[29] Moreover, they are not correlated with

distances or with the density values at BCPs. In contrast, the exchange contribution is shown to be an appropriate descriptor.[29] Similarly, theoretical treatments are applied to various interactions using the QTAIM-defined atomic interaction line (AIL: presence or absence), the IQA-defined interaction energy and its components, the NCI (non-covalent interactions)-defined isosurfaces and the deformation density.[30] The reason for the appearance and disappearance of BPs/BCPs in **5-1**–**5-4** and model **5-A** is rationalized by applying this theory. However, the theoretical treatment is beyond the scope of this paper. The E-∗-H interactions verified by BPs are analysed by applying QTAIM-DFA before discussing the role in the species. The results are summarized in Table 5-3, together with the frequencies (ν) and force constants (k_f) corresponding to the E-∗-H interactions. The E-∗-^{2}H interactions in the optimized structures of **5-1**–**5-4** are characterized as *p*-CS/*t*-HB-nc in nature. The nature of the observed structures of **5-1**, **5-3** and **5-4** is expected to be similar to that of **5-1**–**5-4**, although the dynamic nature is not obtained for the observed structures. Indeed, the E-∗-^{2}H interactions in **5-1**–**5-4** are predicted to be somewhat weaker than the corresponding E-∗-X interactions, respectively, but they are substantially stronger than the vdW nature. The Se-∗-H_{Me} interaction in model **5-A** with (E, X) = (Se, Br) is predicted to have *p*-CS/vdW nature, which is the same as that predicted for Se-∗-X in the model. Compilation of these results suggests that the BPs of the E-∗-H type are substantially strong and are expected to play an important role in the stability of the linear E_2X_2 σ(4c–6e) interactions in the species through the exchange contribution, although theoretical treatment is necessary for the final conclusion.

Table 5-3 QTAIM functions and QTAIM-DFA parameters for E-∗-H at BCPs in optimized structures of **5-1**–**5-4** and the observed structures of **5-1**, **5-3** and **5-4**, evaluated with MP2/BSS-A, together with model **5-A** [(E, X) = (Se, Br)] with MP2/BSS-C.[a]

Species (Symmetry)	Interaction (E-∗-X)	$\rho_b(\boldsymbol{r}_c)$ (au)	$c\nabla^2\rho_b(\boldsymbol{r}_c)$[b] (au)	$H_b(\boldsymbol{r}_c)$ (au)	$k_b(\boldsymbol{r}_c)$[c]	R (au)	θ (°)
The C_2 structures optimized for **5-1**–**5-4**							
5-1 (S, Cl)	(S-∗-H)	0.0196	0.0076	0.0010	–0.927	0.0077	82.2
5-2 (S, Br)	(S-∗-H)	0.0187	0.0073	0.0011	-0.919	0.0074	81.4
5-3 (Se, Cl)	(Se-∗H)	0.0176	0.0062	0.0009	-0.918	0.0063	81.4
5-4 (Se, Br)	(Se-∗-H)	0.0168	0.0061	0.0010	-0.908	0.0062	80.4
The C_1 structures for **5-1**, **5-3** and **5-4**, determined by X-ray analysis							
5-1 (S, Cl)	(S-∗-H)	0.0169	0.0074	0.0017	–0.869	0.0076	77.0
5-3 (Se, Cl)	(Se-∗-H)	0.0150	0.0060	0.0015	–0.857	0.0062	75.9
5-4 (Se, Br)	(Se-∗-H)	0.0149	0.0060	0.0016	-0.849	0.0062	75.3
The C_2 structures for model **5-A** (Se, Br): ^{B}Br---^{A}Se(H)–^{A}Se(H)---^{B}Br							
5-A (Se, Br)	(Se-∗-H)	0.0059	0.0021	0.0007	-0.802	0.0022	71.7

[a] BSS-A: The 6-311+G(3df) basis set being employed for S and Se with the 6-311G(d) basis set for C and H and BSS-C. The 6-311+G(3df) basis set being employed for S and Se with the 6-311G(d, p) basis set for C and H. [b] $c\nabla^2\rho_b(\boldsymbol{r}_c) = H_b(\boldsymbol{r}_c) - V_b(\boldsymbol{r}_c)/2$, where $c = \hbar^2/8m$. [c] $k_b(\boldsymbol{r}_c) = V_b(\boldsymbol{r}_c)/G_b(\boldsymbol{r}_c)$.

(Table 5-3 continued)

Species (Symmetry)	Interaction (E-∗-X)	$\nu\,(n)$[d] (cm^{-1})	k_f[e] (f)	θ_p (°)	κ_p (au^{-1})	Classification /Character
The C_2 structures optimized for **5-1**–**5-4**						
5-1 (S, H)	(S-∗-H)	234.7	0.2639	101.4	100.7	*p*-CS/*t*-HB-nc[g]
5-2 (S, H)	(S-∗-H)	223.5	0.1840	98.6	73.9	*p*-CS/*t*-HB-nc[g]
5-3 (Se, H)	(Se-∗-H)	120.8	0.0721	98.4	102.9	*p*-CS/*t*-HB-nc[g]
5-4 (Se, H)	(Se-∗-H)	110.5	0.0819	96.0	86.4	*p*-CS/*t*-HB-nc[g]
The C_1 structures for **5-1**, **5-3** and **5-4**, determined by X-ray analysis						
5-1 (S, H)	(S-∗-H)	(h)	(h)	(h)	(h)	*p*-CS
5-3 (Se, H)	(Se-∗-H)	(h)	(h)	(h)	(h)	*p*-CS
5-4 (Se, H)	(Se-∗-H)	(h)	(h)	(h)	(h)	*p*-CS
The C_2 structures for model **5-A** (Se, Br): ^{B}Br---^{A}Se(H)–^{A}Se(H)---^{B}Br						
5-A (Se, Br)	(Se-∗-H)	79.6	0.0111	79.0	86.2	*p*-CS/vdW

[d] Corresponding to the interaction in question. Symmetric and anti-symmetric modes being employed for ^{A}E-∗-^{A}E and ^{A}E-∗-^{B}E, respectively. [e] Force constant for ν. [f] In mdyn Å^{-1}. [g] *Typical*-HB nature with no covalency. [h] Not obtained.

Summary

The nature of E_2X_2 σ(4c–6e) (E = S and Se; X = Cl and Br) of the X---E–E---X type was elucidated for the naphthalene system 1-(8-$XC_{10}H_6$)E–E($C_{10}H_6$X-8')-1' [**5-1** (E, X) = (S, Cl), **5-2** (S, Br), **5-3** (Se, Cl) and **5-4** (Se, Br)] and model **5-A**, MeX--E(H)–(H)E---XMe, after preparation and structural determination of **5-1**, **5-3** and **5-4**. Each interaction in the X---E–E---X of **5-1**–**5-4** and model **5-A** can be described as a straight line. The nature of X---E–E---X in **5-1**–**5-4** and model **5-A** is elucidated via QTAIM-DFA. The E-∗-E interactions in **5-1**–**5-4** and model **5-A** are all classified and characterized as SS/Cov-w. On the other hand, E-∗-X in model **5-A** are all classified and characterized as *p*-CS/vdW. In the case of E-∗-X in **5-1**–**5-4**, the interactions are predicted to be *p*-CS/*t*-HB-nc for **5-1** and **5-3**, and that for **5-4** is predicted as *r*-CS/*t*-HB-wc. In the case of **5-3**, E-∗-X is classified as borderline between *p*-CS and *r*-CS interactions since $\theta = 90.1^{o}$, very close to 90.0º. The E_2X_2 σ(4c–6e) interactions are accurately analyzed by applying QTAIM-DFA.

Appendix

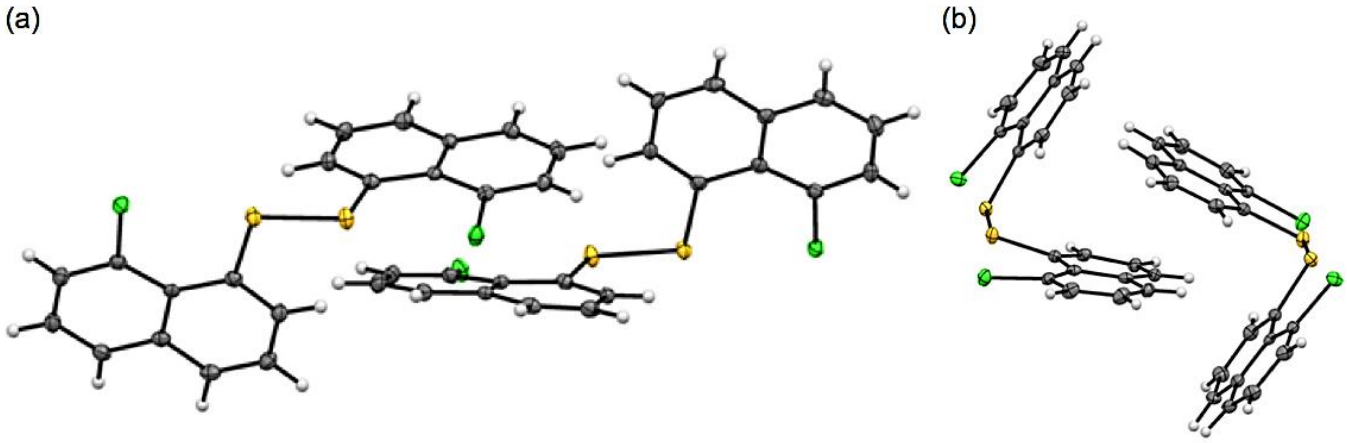

Figure 5-A1. Structure of **5-1**, determined by the X-ray crystallographic analysis. Thermal ellipsoids are drawn at 50% probability.

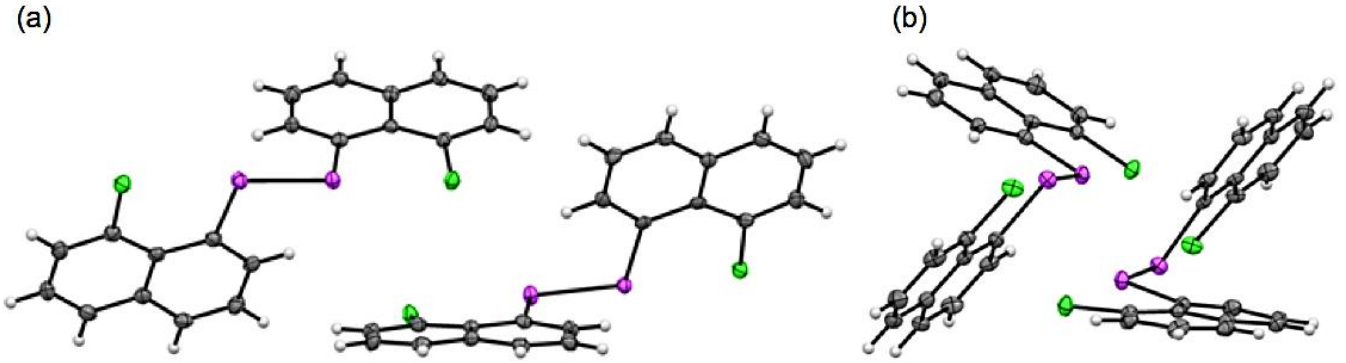

Figure 5-A2. Structure of **5-3**, determined by the X-ray crystallographic analysis. Thermal ellipsoids are drawn at 50% probability.

Table 5-A1. Crystallographic data for **5-1**, **5-3**, and **5-4**

	5-1	**5-3**	**5-4**
Empirical formula	$C_{20}H_{12}Cl_2S_2$	$C_{20}H_{12}Cl_2Se_2$	$C_{20}H_{12}Br_2Se_2$
Formula weight	387.32	481.12	570.04
Temperature (K)	103(2)	103(2)	103(2)
Crystal system	orthorhombic	orthorhombic	triclinic
Space group	*Pca*2$_1$ (#29)	*Pca*2$_1$ (#29)	$P\bar{1}$(#2)
Unit cell dimensions			
a (Å)	7.824(2)	7.89330(10)	7.83940(10)
b (Å)	28.782(8)	29.1713(4)	8.0986(2)
c (Å)	14.350(4)	14.4594(2)	15.0650(4)
α (deg)	90.00	90.00	90.9410(10)
β (deg)	90.00	90.00	101.8880(10)
γ (deg)	90.00	90.00	111.0930(10)
Volume (Å^3)	3231.7(15)	3329.39(8)	868.92(3)
Z	8	8	2
Dcalcd (g cm^{-3})	1.592	1.920	2.179
Theta range for data collection	2.70–25.50	2.09–25.50	2.86–27.10
F(000)	1584	1872	540
Reflections observed [I > 2σ(I)]	5988	6129	3813
R_1 [I > 2σ(I)]	0.020	0.024	0.0391
R_1 [all data]	0.020	0.026	0.0432
ωR_2 [I > 2σ(I)]	0.052	0.059	0.0788
ωR_2 [all data]	0.052	0.060	0.0805
Goodness-of-fit on F^2	1.073	1.058	1.198

Table 5-A2. Structural parameters evaluated for model **5-A** [(S, Cl), (S, Br), (Se, Cl), (Se, Br)] (C_2) with MP2/BSS-C.[a]

Species (E, X) (Symmetry)	r_o(E, E) (Å)	r_o(E, X) (Å)	Δr_o(E, X)[b] (Å)	$\angle^1C^AE^{A'}E$ (º)	$\angle^8X^AE^{A'}E$ (º)
Optimized with MP2/BSS-A					
5-A (S, Cl) (C_2)	2.0559	3.3838	–0.1662	98.9	170.4
5-A (S, Br) (C_2)	2.0572	3.4947	–0.1533	98.8	171.3
5-A (Se, Cl) (C_2)	2.3220	3.4617	–0.1883	96.7	161.4
5-A (Se, Br) (C_2)	2.3242	3.5805	–0.1695	96.6	160.9

[a] BSS-C: the 6-311+G(3df) basis sets being employed for S and Se with the 6-311G(d,p) basis sets for C and H. [b] $\Delta r_o(^AE, ^BX) = r_o(^AE, ^BX) - \Sigma r_{vdW}(^AE, ^BX)$, where r_{vdW}(S) = 1.80 Å, r_{vdW}(Se) = 1.90 Å, r_{vdW}(Cl) = 1.75 Å, and r_{vdW}(Br) = 1.85 Å.

(Table 5-A2 continued)

Species (E, X) (Symmetry)	ϕ_1[c] (º)	ϕ_2[d] (º)	ΔE_{ES} (kJ mol^{-1})	ΔE_{ZP} (kJ mol^{-1})
Optimized with MP2/BSS-C				
5-A (S, Cl) (C_2)	–101.8	–113.2	–26.5	–22.2
5-A (S, Br) (C_2)	–106.1	–121.7	–26.7	–22.6
5-A (Se, Cl) (C_2)	–130.2	–169.6	–26.9	–23.6
5-A (Se, Br) (C_2)	–135.6	179.6	–27.6	–24.3

[c] $\phi_1 = \phi(H^AE^{A'}EH)$. [d] $\phi_2 = \phi(H^AE^BXMe)$.

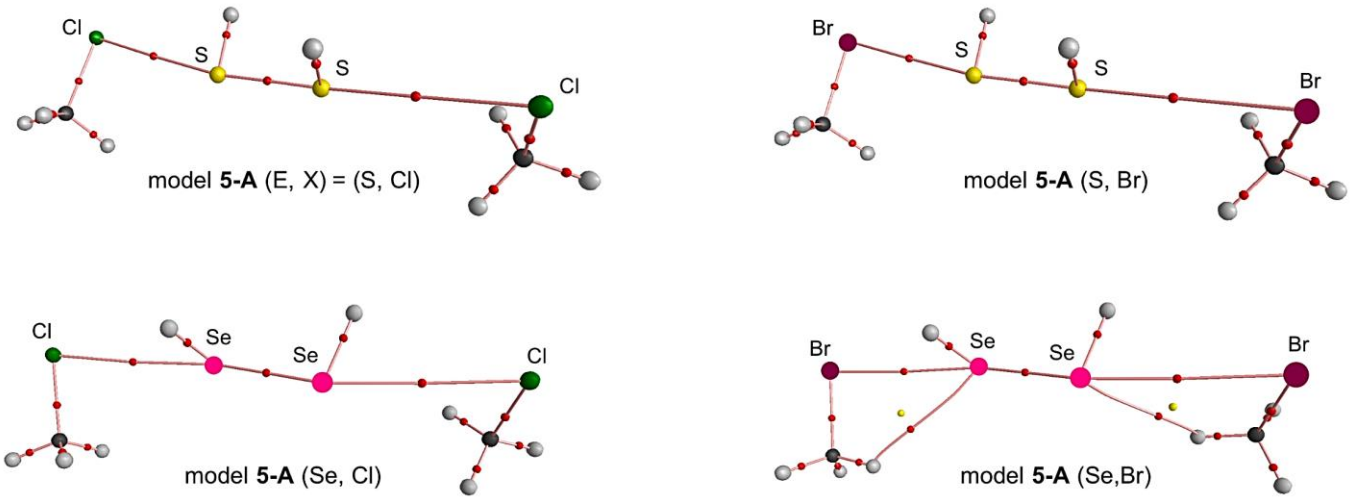

Figure 5-A3. Molecular graphs for models **5-A** [(E, X) = (S, Cl), (S, Br), (Se, Cl), (Se, Br)]. BCPs (bond critical points) are denoted by red dots, RCPs (ring critical points) by yellow dots, CCPs (cage critical points) by green dots, and BPs (bond paths) by pink lines. Carbon atoms are in black, hydrogen atoms are in gray, and selenium atoms in pink.

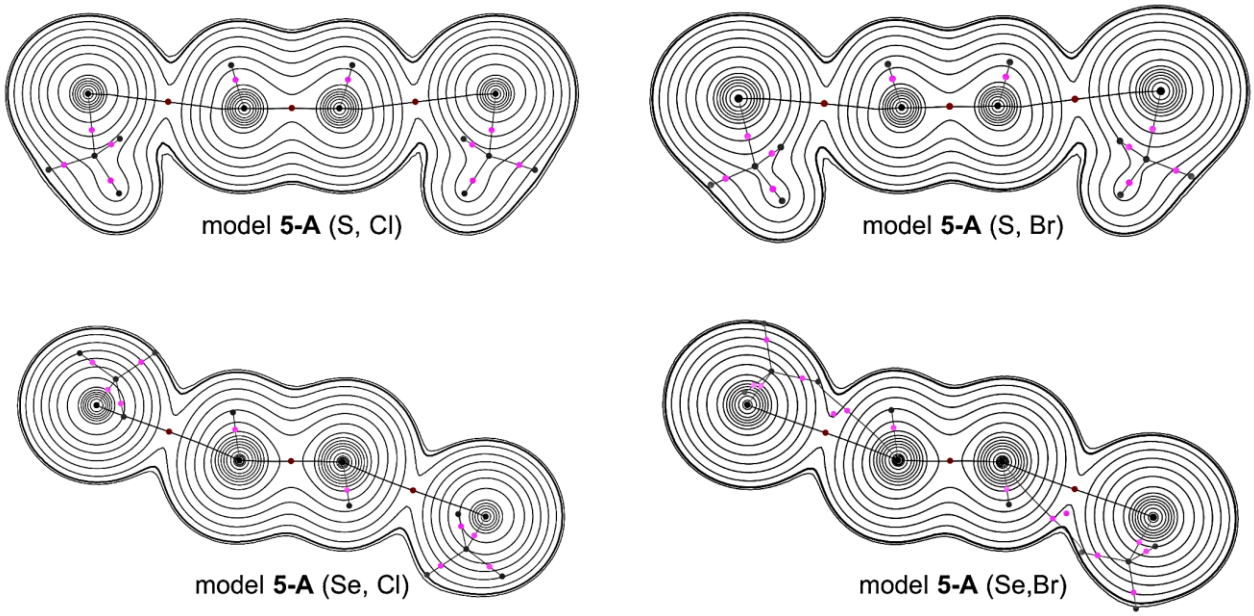

Figure 5-A4. Contour plots of $\rho_b(r_c)$ for models **5-A** [(E, X) = (S, Cl), (S, Br), (Se, Cl), (Se, Br)]. BCPs on the plane are shown by red dots, those outside of the plane in dark pink dots, RCPs on and outside the plane by blue squares and light blue ones, respectively. CCPs by green squares, and BPs on the plane by black lines and those outside of the plane are by gray lines. Atoms on and outside the plane are by black dots and gray ones, respectively. The contours (ea_0^{-3}) are at 2^l (l = ±8, ±7, ..., 0) with 0.0047 (heavy line).

Table 5-A3 Results of NBO analysis for the ^{1}E---^{8}X interactions in **5-1**–**5-4** with M06-2X/BSS-A//MP2/BSS-A and models **5-A** [(S, Cl), (S, Br), (Se, Cl), and (Se, Br)] with MP2/BSS-C//MP2/BSS-C.

Compound (^{A}E, ^{B}X)	$E(2)^{a,b}$ (kcal mol^{-1})	$E(2)^{a,b}$ (kJ mol^{-1})	[E(i) – E(j)]^c (au)	F(i,j)^d (au)
calculated				
5-1 (S, Cl) (C_2)	4.61	19.3	0.51	0.043
5-2 (S, Br) (C_2)	4.42	18.5	0.48	0.041
5-3 (Se, Cl) (C_2)	6.72	28.1	0.47	0.050
5-4 (Se, Br) (C_2)	6.66	27.9	0.42	0.047
observed				
5-1 (S, Cl)^e	4.88^f	20.4^f	0.51^f	0.044^f
5-3 (Se, Cl)^e	7.04^f	29.4^f	0.46^f	0.051^f
5-4 (Se, Br)^e	8.59^f	35.9^f	0.42^f	0.054^f
model **5-A**				
5-A (S, Cl) (C_2)	1.64	6.9	0.49	0.025
5-A (S, Br) (C_2)	1.88	7.9	0.46	0.026
5-A (Se, Cl) (C_2)	2.22	9.3	0.43	0.028
5-A (Se, Br) (C_2)	2.67	11.2	0.40	0.029

^{a} Second-order perturbation energy. ^{b} Only one side of energy is shown. ^{c} Donor orbital of NBO(i) is n_p(^{8}X or ^{B}X) and acceptor orbital of NBO (j) corresponds to σ∗(^{1}E–$^{1'}$E or ^{A}E–$^{A'}$E). ^{d} Fock matrix. ^{e} The crystals contain two independent molecules in a unit cell. ^{f} Averaged value.

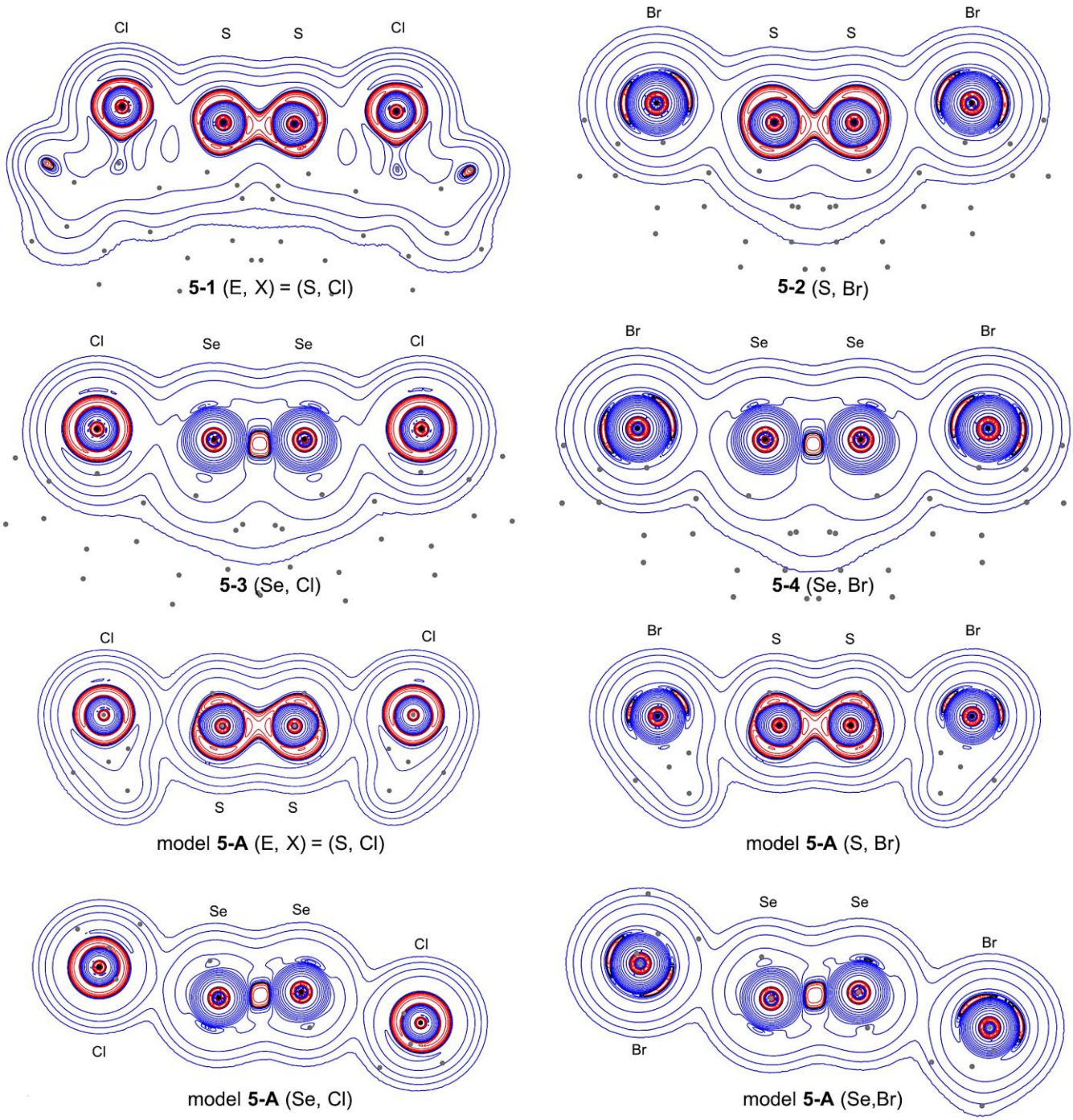

Figure 5-A5. Negative Laplacians for **5-1**–**5-5-4** drawn with M06-2X/BSS-A//MP2/BSS-A and model **5-A** (S, Cl)–(Se, Br) drawn with MP2/BSS-C//MP2/BSS-C, similarly to the case of Figure 5-4 in the text. Blue and red lines correspond to the positive and negative values, respectively.

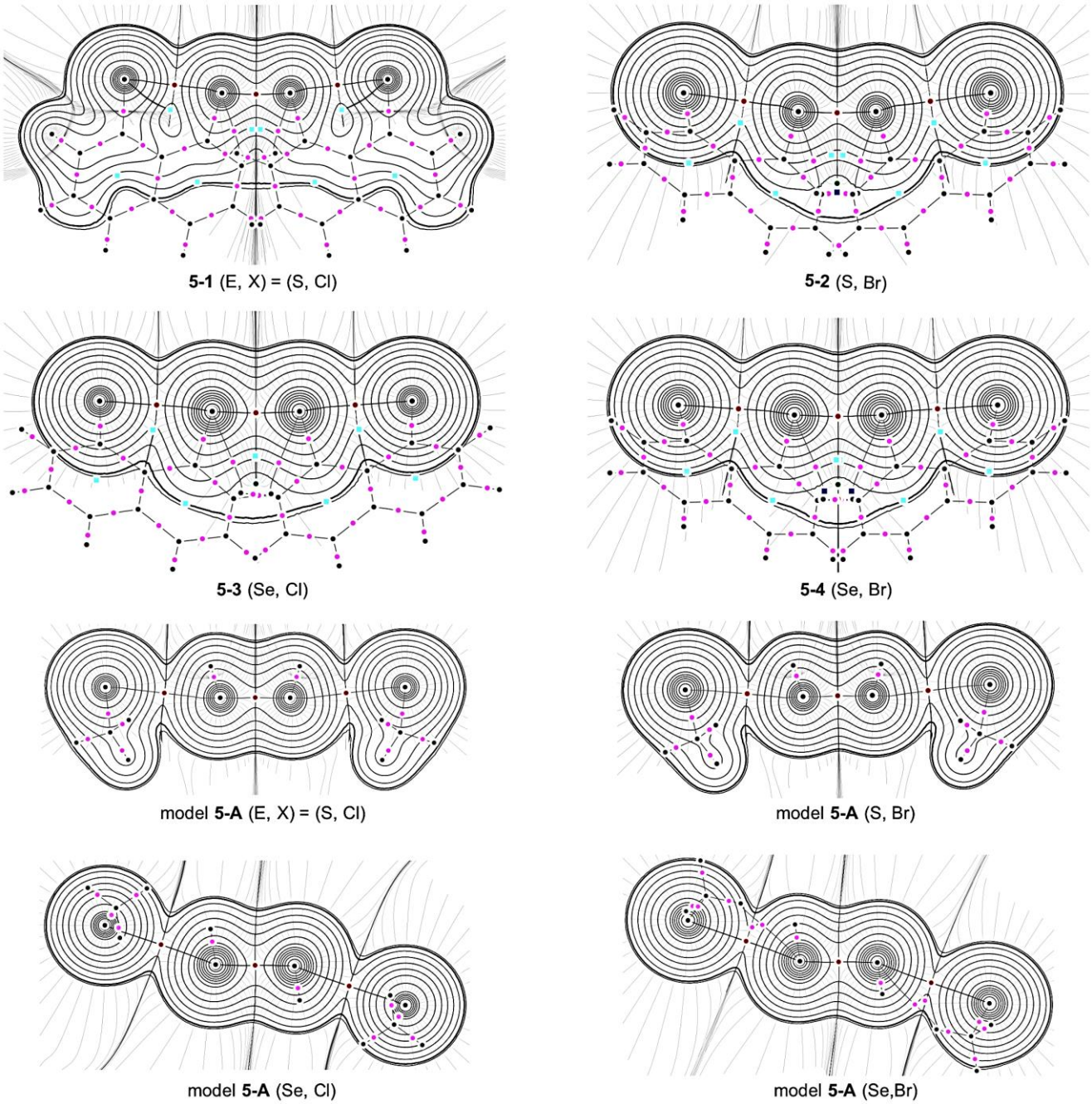

Figure 5-A6. Trajectory plots for **5-1**–**5-4** drawn with M06-2X/BSS-A//MP2/BSS-A and model **5-A** (S, Cl)–(Se, Br) drawn with MP2/BSS-C//MP2/BSS-C, similarly to the case of Figure 5-4 in the text. Colors and marks are the same as those in Figure 5-4.

Table 5-A4 r_{BP} and R_{SL} values for the ^{B}X---^{A}E–^{A}E---^{B}X interactions in compounds **5-1**–**5-4** with MP2/BSS-A and model **5-A** with MP2/BSS-C.[a]

Species (^{A}E, ^{B}X)	$R_{SL}(^{B}X, ^{A}E)$ (Å)	$R_{SL}(^{A}E, ^{A'}E)$ (Å)	$r_{BP}(^{B}X, ^{A}E)$ (Å)	$r_{BP}(^{A}E, ^{A'}E)$ (Å)	$\Delta r_{BP}(^{B}X, ^{A}E)^{b}$ (Å)	$\Delta r_{BP}(^{A}E, ^{A'}E)^{c}$ (Å)
The C_2 structures optimized for **5-1**–**5-4**						
5-1 (S, Cl) (C_2)	2.9340	2.0311	2.9481	2.0324	0.0142	0.0013
5-2 (S, Br) (C_2)	3.0392	2.0330	3.0526	2.0344	0.0134	0.0015
5-3 (Se, Cl) (C_2)	2.9774	2.3010	2.9824	2.3024	0.0050	0.0014
5-4 (Se, Br) (C_2)	3.0837	2.3072	3.0887	2.3085	0.0050	0.0013
The C_1 structures for **5-1**, **5-3** and **5-4**, determined by X-ray analysis						
5-1 (S, Cl)	2.9493	2.0461	2.9630	2.0474	0.0138	0.0013
5-3 (Se, Cl)	2.9708	2.3249	2.9754	2.3264	0.0046	0.0015
5-4 (Se, Br)	3.0740	2.3354	3.0791	2.3369	0.0051	0.0015
The C_2 structures for model **5-A**						
5-A (S, Cl) (C_2)	3.3838	2.0559	3.3943	2.0576	0.0105	0.0017
5-A (S, Br) (C_2)	3.4947	2.0572	3.5052	2.0589	0.0105	0.0017
5-A (Se, Cl) (C_2)	3.4617	2.3220	3.4682	2.3226	0.0065	0.0006
5-A (Se, Br) (C_2)	3.5805	2.3242	3.5871	2.3248	0.0066	0.0006

[a] BSS-A: the 6-311+G(3df) basis sets being employed for S and Se with the 6-311G(d) basis sets for C and H. BSS-C: the 6-311+G(3df) basis sets being employed for S and Se with the 6-311G(d,p) basis sets for C and H. [b] $\Delta r_{BP}(^{8}X, ^{1}E) = r_{BP}(^{8}X, ^{1}E) - R_{SL}(^{8}X, ^{1}E)$. [c] $\Delta r_{BP}(^{1}E, ^{1'}E) = r_{BP}(^{1}E, ^{1'}E) - R_{SL}(^{1}E, ^{1'}E)$.

References

1 W. Nakanishi, S. Hayashi, S. Toyota, *Chem. Commun.* **1996**, 371–372.

2 W. Nakanishi, S. Hayashi, S. Toyota, *J. Org. Chem.* **1998**, *63*, 8790–8800.

3 W. Nakanishi, S. Hayashi, S. Morinaka, T. Sasamori, N. Tokitoh, *New J. Chem.* **2008**, *32*, 1881–1889; b) W. Nakanishi, S. Hayashi, K. Narahara, *J. Phys. Chem. A* **2008**, *112*, 13593–13599.

4 W. Nakanishi, *Hypervalent Chalcogen Compounds*. In *Handbook of Chalcogen Chemistry: New Perspectives in Sulfur, Selenium and Tellurium*, ed. F. A. Devillanova, Royal Society of Chemistry: London, **2006**, Chapter 10.3, pp. 644–668.

5 a) W. Nakanishi, S. Hayashi, In *Handbook of Chalcogen Chemistry: New Perspectives in Sulfur, Selenium and Tellurium, 2nd ed.*, eds. F. A. Devillanova, W.-W. du Mont, Royal Society of Chemistry: Cambridge, U.K. **2013**, Vol. 2, Chapter 12.3, pp. 335−372. b) W. Nakanishi, S. Hayashi, *J. Phys. Chem. A* **2013**, *117*, 1795−1803.

6 G. C. Pimentel, *J. Chem. Phys.* **1951**, *19*, 446–448.

7 J. I. Musher, *Angew. Chem., Int. Ed. Engl.* **1969**, *8*, 54–68.

8 W. Nakanishi, S. Hayashi, T. Arai, *Chem. Commun.* **2002**, 2416–2417.

9 W. Nakanishi, S. Hayashi, N. Itoh, *Chem. Commun.* **2003**, 124–125.

10 a) W. Nakanishi, S. Hayashi, N. Itoh, *J. Org. Chem.* **2004**, *69*, 1676–1684; b) W. Nakanishi, S.Hayashi, S. Yamaguchi, K. Tamao, *Chem. Commun.* **2004**, 140–141.

11 *The Chemistry of Organic Selenium and Tellurium Compounds*, ed. Z. Rappoport, Wiley, New York, **2013**, Vol. 4, Chapters 13–16.

12 V. K. Dikshit, B. D. Tilak, *Proc. Indian Acad. Sci., Sect. A* **1951**, *33*, 78–82.

13 L. F. Fieser, A. M. Seligman, *J. Am. Chem. Soc.* **1939**, *61*, 136–140.

14 a) G. M. Sheldrick, SHELXS-97, Program for Crystal Structure Solution, Universität Göttingen, **1997**.; b) G. M. Sheldrick, SHELXL-97, Program for Crystal Structure Refinement, Universität Göttingen. **1997**.

15 *Gaussian 09 (Revision D.01)*, M. J. Frisch, G. W. Trucks, H. B. Schlegel, G. E. Scuseria, M. A. Robb, J. R. Cheeseman, G. Scalmani, V. Barone, B. Mennucci, G. A. Petersson, H. Nakatsuji, M. Caricato, X. Li, H. P. Hratchian, A. F. Izmaylov, J. Bloino, G. Zheng, J. L. Sonnenberg, M. Hada, M. Ehara, K. Toyota, R. Fukuda, J. Hasegawa, M. Ishida, T. Nakajima, Y. Honda, O. Kitao, H. Nakai, T. Vreven, J. A. Montgomery, Jr., J. E. Peralta, F. Ogliaro, M. Bearpark, J. J. Heyd, E.

Brothers, K. N. Kudin, V. N. Staroverov, R. Kobayashi, J. Normand, K. Raghavachari, A. Rendell, J. C. Burant, S. S. Iyengar, J. Tomasi, M. Cossi, N. Rega, J. M. Millam, M. Klene, J. E. Knox, J. B. Cross, V. Bakken, C. Adamo, J. Jaramillo, R. Gomperts, R. E. Stratmann, O. Yazyev, A. J. Austin, R. Cammi, C. Pomelli, J. W. Ochterski, R. L. Martin, K. Morokuma, V. G. Zakrzewski, G. A. Voth, P. Salvador, J. J. Dannenberg, S. Dapprich, A. D. Daniels, Ö. Farkas, J. B. Foresman, J. V. Ortiz, J. Cioslowski and D. J. Fox, Gaussian, Inc.: Wallingford CT, **2009**.

16 C. Møller, M. S. Plesset, *Phys. Rev.* **1934**, *46*, 618–622.

17 Y. Zhao, D. G. Truhlar, *Theor. Chem. Acc.* **2008**, *120*, 215−241.

18 The AIM2000 program (Version 2.0) is employed to analyze and visualize atoms-in-molecules: F. Biegler-König, *J. Comput. Chem.* **2000**, *21*, 1040–1048.

19 Bondi, A. *J. Phys. Chem.* **1964**, *68*, 441−451.

20 J. P. Foster, F. Weinhold, *J. Am. Chem. Soc.* **1980**, *102*, 7211–7218.

21 A. E. Reed, F. Weinhold, *J. Chem. Phys.* **1983**, *78*, 4066–4073.

22 a) A. E. Reed, R. B. Weinstock, F. Weinhold, *J. Chem. Phys.* **1985**, *83*, 735–746.; b) A. E. Reed, F. Weinhold, *J. Chem. Phys.* **1985**, *83*, 1736–1740.

23 A. E. Reed, L. A. Curtiss, F. Weinhold, *Chem. Rev.* **1988**, *88*, 899–926.

24 J. E. Carpenter, F. Weinhold, *J. Mol. Struct. (Theochem).* **1988**, *46*, 41–62. (Style: IUCr references)

25 F. Weinhold, C. R. Landis, *Chemistry Education: Research and Practice in Europe*, **2001**, *2*, 91–104.

26 F. Weinhold, C. R. Landis, *Discovering Chemistry with Natural Bond Orbitals*, Wiley, **2012**.

27 F. Weinhold, C. R. Landis, *Valency and Bonding: A Natural Bond Orbital Donor-Acceptor Perspective*, CUP. **2005**.

28 A. M. Pendâs, E. Francisco, M. A. Blanco, C. Gatti, *Chem. Eur. J.* **2007**, *13*, 9362–9371.

29 V. Tognetti, L. Joubert, *J. Chem. Phys.* **2013**, *138*, 024102-1–024102-8.

30 I. Cukrowski, J. H. de Lange, A. S. Adeyinka, P. Mangondo, *Comput. Theo. Chem.* **2015**, *1053*, 60−76.

Chapter 6

Nature of S_2Se_2 σ(4c–6e) at Naphthalene 1,8-Positions and Models, Elucidated by QTAIM Dual Functional Analysis

Abstract

The nature of extended hypervalent interactions of the ^{B}E-∗-^{A}E-∗-^{A}E-∗-^{B}E type is elucidated for 1-(8-Me^{B}E$C_{10}H_6$)^{A}E–^{A}E($C_{10}H_6$^{B}EMe-8')-1', (**6-1** (^{A}E, ^{B}E) = (S, S), **6-2** (S, Se), **6-3** (Se, S), **6-4** (Se, Se)), and models **6-A–6-D**, $^{B}R_2$^{B}E---(^{A}R)^{A}E–^{A}E(^{A}R)---^{B}E$^{B}R_2$ (^{A}R, ^{B}R = H and Me). QTAIM dual functional analysis, which his research group proposed recently, is applied to the analysis. Total electron energy densities $H_b(\boldsymbol{r}_c)$ are plotted versus $H_b(\boldsymbol{r}_c) - V_b(\boldsymbol{r}_c)/2$ for the interactions at bond critical points (BCPs; ∗), where $V_b(\boldsymbol{r}_c)$ show potential energy densities at BCPs. Data for the perturbed structures around the fully optimized structures are employed for the plots, in addition to those of the fully optimized ones. While the data for the fully optimized structures are analyzed by the polar coordinate (R, θ) representation, those containing the perturbed structures are by (θ_p, κ_p): θ_p corresponds to the tangent line for the plot and κ_p is the curvature. While (R, θ) show the static nature, (θ_p, κ_p) represent the dynamic nature of interactions. All ^{A}E-∗-^{A}E interactions in **6-1**–**6-4** and models **6-A**–**6-D** are classified by the shared shell interactions and have the character of the weak covalent nature. The ^{A}E-∗-^{B}E interactions in **6-1**–**6-4** are all classified by the *regular* closed shell interactions. They are predicted to have the *typical* HB (hydrogen bond) nature with covalency for **6-1** and **6-2** but the nature of the molecular complex formation through CT for **6-3** and **6-4**. The ^{A}E-∗-^{B}E interactions in models **6-A**–**6-D** are predicted to be weaker than those in **6-1**–**6-4**.

Introduction

In chapter 5, he discussed about the nature of the E_2X_2 σ(4c–6e) (E = S, Se; X = Cl, Br). In this chapter, he mainly discussed about the nature of $^{A}E_2{}^{B}E_2$ σ(4c–6e) ((^{A}E, ^{B}E) = (S, Se)).

Much attention has been paid to the linear σ-type interactions, constructed by the atoms of heavier main group elements. Three center–four electron interactions of the σ-type (σ(3c–4e)) are the *typical* example, originally proposed by Pimentel and Musher.[1] He have been much interested in such interactions higher than σ(3c–4e). Bis[8-(phenylselanyl)naphthyl]-1,1'-diselenide (1-(8-$Ph^{B}EC_{10}H_6$)^{A}E–$^{A}E(C_{10}H_6{}^{B}EPh$-8')-1': **6-I** (^{A}E, ^{B}E) = (Se, Se)) was first prepared and the structure was determined by the X-ray crystallographic analysis.[2] The four Se atoms are demonstrated to align linearly. Similar alignments of four $^{A}E_2{}^{B}E_2$ atoms were confirmed for with (^{A}E, ^{B}E) = (S, S),[3] (S, Se),[4] and (Se, S).[4] The linear alignments of the four $^{A}E_2{}^{B}E_2$ atoms are characterized by the $n_p(^{B}E)$---σ*(^{A}E–^{A}E)---$n_p(^{B}E)$ interactions, where $n_p(^{B}E)$ stands for the p-type lone pair orbital of ^{B}E and σ*(^{A}E–^{A}E) for the σ* orbital of ^{A}E–^{A}E. Figure 6-1 illustrates the structure of **6-I** (Se, S), determined by the X-ray analysis.

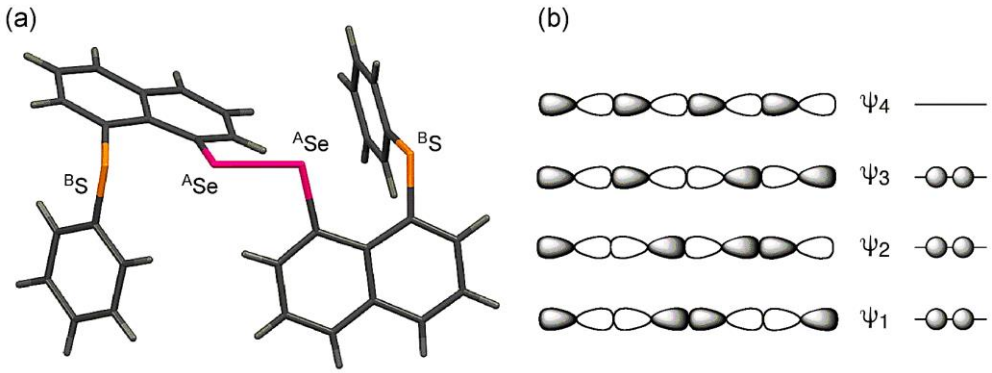

Figure 6-1. Structure of 1-(8-$Me^{B}EC_{10}H_6$)^{A}E–$^{A}E(C_{10}H_6{}^{B}EMe$-8')-1' (**6-I** (^{A}E, ^{B}E) = (Se, S)), determined by the X-ray analysis[4] (a) with approximate MO model for E_4 σ(4c–6e) (b).

His research group proposed to call the σ-type linear interactions higher than σ(3c–4e) "extended hypervalent interactions," named after hypervalent interactions.[2–6] Extended hypervalent interactions are characterized by *m* center–*n* electron interactions, σ(*m*c–*n*e) ($4 \leq m$; $m < n < 2m$).[2–6] σ(4c–6e) is the first member of σ(*m*c–*n*e) ($4 \leq m$). The linear ^{B}E---^{A}E–^{A}E---^{B}E interaction in **6-I** is analyzed by the σ(4c–6e) model, instead of double σ(3c–4e). The approximate MO model for E_4 σ(4c–6e) is shown in Figure 6-1. $^{A}E_2{}^{B}E_2$ σ(4c–6e) could be recognized as a chalcogen bonding.[7]

The high accepting ability of σ*(^{A}E–^{A}E) and the high donating ability of $n_p(^{B}E)$ must be the driving force for the linear alignment of ^{B}E---^{A}E–^{A}E---^{B}E. Namely, the charge transfer (CT) of the $n_p(^{B}E)$→σ*(^{A}E–

^{A}E)←σ_p(^{B}E) type plays an important role for the formation of $^{A}E_2{}^{B}E_2$ σ(4c–6e). Substantial number of compounds containing σ(4c–6e) are reported, so far, as reviewed recently.[6,8] Benzene 1,2-positions, naphthalene 1,8-positions and the related systems serve as good spacers to form σ(4c–6e) of the linear n(A)---σ*(E–E)---n(A) interactions, where A = N in the amino, imino, amido, and diazo groups,[9] A = O in the carbonyl, ether, hydroxyl, nitro and sulfonyl groups,[10] and A = X of halogen atoms,[11] together with A = E = S and/or Se.[2–4]

The σ(4c–6e) interactions are strongly suggested to play an important role in the development of high functionalities in materials and in the key processes of biological and/or pharmaceutical activities.[2–6,8–10] It must be challenging to elucidate the nature of σ(4c–6e), which causes high functionalities and reactivities in materials. How do the spacers operate in the formation and stability of σ(4c–6e)? Which is more important, σ*(^{A}E–^{A}E) or n_p(^{B}E), to stabilize the CT interactions of the n_p(^{B}E)→σ*(^{A}E–^{A}E)←n_p(^{B}E) type? It must be of highly productive to answer such questions with quantitative accuracy, which will promote to understand the nature of σ(4c–6e) and the behavior of usual interactions operating in chemical sciences, deeply. The nature of σ(4c–6e) will be elucidated, exemplified by 1-(8-Me^{B}E$C_{10}H_6$)^{A}E–^{A}E($C_{10}H_6{}^{B}$EMe-8')-1': **6-1** (^{A}E, ^{B}E) = (S, S), **6-2** (S, Se), **6-3** (Se, S), and **6-4** (Se, Se), after preparation and structural determination of **6-4** (Se, Se). The σ(4c–6e) nature is also elucidated for models **6-A**–**6-D** [$^{B}R_2{}^{B}$E---^{A}E(^{A}R)–(^{A}R)^{A}E---^{B}E$^{B}R_2$: **6-A** (^{A}R = ^{B}R = H), **6-B** (^{A}R = Me, ^{B}R = H), **6-C** (^{A}R = H, ^{B}R = Me), and **6-D** (^{A}R = ^{B}R = Me), where ^{A}E, ^{B}E = S and Se]. Chart 6-1 illustrates the structures of **6-1**–**6-4** and models **6-A**–**6-D**, together with **6-I**, for convenience of discussion, where (^{A}E, ^{B}E) = (S, S), (S, Se), (Se, S), and (Se, Se). The role of naphthalene 1,8-positions, as the spacer, will be clarified by comparing the behavior of σ(4c–6e) in **6-1**–**6-4** with that in models **6-A**–**6-D**.

His research group consider QTAIM-DFA to be well-suited to clarify the nature of $^{A}E_2{}^{B}E_2$ σ(4c–6e). Each interaction in $^{A}E_2{}^{B}E_2$ σ(4c–6e) of the ^{B}E-∗-^{A}E-∗-^{A}E-∗-^{B}E type in **6-1**–**6-4** and models **6-A**–**6-D** is classified and characterized with QTAIM-DFA. The criteria are employed to classify and characterize the interactions in question, as a reference. The criteria are surveyed in the text, although they are limited to those closely related to the interactions in ^{B}E-∗-^{A}E-∗-^{A}E-∗-^{B}E (see the section of "Nature of ^{A}E-∗-^{B}E and ^{A}E-∗-^{A}E in **6-1**–**6-4** and models **6-A**–**6-D**). An asterisk is employed for an interaction to emphasize the existence of a BCP on each BP, in question, in our case.[12] Here, he discusses the nature of $^{A}E_2{}^{B}E_2$ σ(4c–6e) in **6-1**–**6-4** and models **6-A**–**6-D**, together with the structural feature, to establish the firm basis for the nature of the extended hypervalent interactions.

QTAIM-DFA and the criteria are explained in the Chapter 2, employing Schemes 2-1 and 2-2, Figure

2-1, and eqs (2-1)–(2-7). The basic concept of the QTAIM approach is also surveyed.

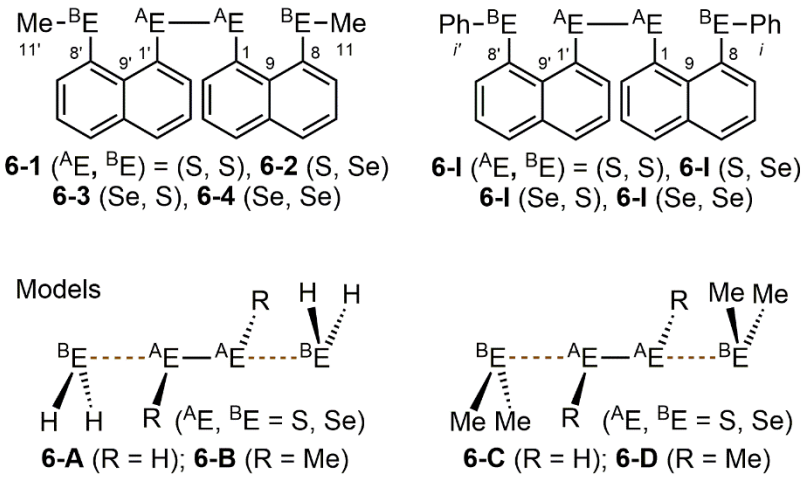

Chart 6-1. Graphical representation of **6-1**–**6-4** and models **6-A**–**6-D**, together with **6-I**.

Experimental

Bis[8-(methylselanyl)naphthyl]-1,1'-diselenide-(6-4)

To a solution of naphtho[1,8-*c*,*d*]-1,2-diselenole was added methyl lithium at 0 °C in diethyl ether. After a usual workup, the solution was chromatographed on silica gel containing acidic alumina. Recrystallization from hexane gave **6-4** as yellow prisms in 92% yield, mp 132.5–133.2 °C. ^{1}H NMR ($CDCl_3$/TMS, 300 MHz) δ 2.45 (s, 6H), 7.23 (t, J = 7.8 Hz, 2H), 7.36 (t, J = 7.8 Hz, 2H), 7.68 (dd, J = 0.9 and 7.8 Hz, 2H), 7.81 (dd, J = 1.1 and 8.1 Hz, 2H), 7.96 (dd, J = 1.3 and 7.2 Hz, 2H), 8.19 (dd, J = 1.2 and 7.8 Hz, 2H); ^{13}C NMR ($CDCl_3$/TMS, 75.5 MHz) δ 15.9 ($^{1}J_{Se,C}$ = 66 Hz), 125.7, 126.5, 128.2, 129.5, 130.1, 130.8, 132.2, 135.7, 136.0, and 136.7; ^{77}Se NMR ($CDCl_3$/Me_2Se, 57 MHz) δ 237.2 ($^{4}J_{Se,Se}$ = 357 Hz and $^{5}J_{Se,Se}$ = 14 Hz), 537.8 ($^{4}J_{Se,Se}$ = 357 Hz and $^{5}J_{Se,Se}$ = 14 Hz). Anal. Calcd for $C_{22}H_{18}Se_4$: C, 44.17; H, 3.03. Found: C, 44.02; H, 2.95.[13]

X-ray structure determination

Single crystals of **6-4** were obtained from a hexane solution. X-ray diffraction data for **6-4** were collected on a Bruker-Nonius FR591 rotating anode diffractometer using graphite-monochromated Mo$K\alpha$ radiation generated from a rotating anode (0.71073 Å) with ω and ϕ scans at 120 K.[14] Data were corrected for Multi-scan empirical absorption using the SADABS (v2) program[15] and structure solution and refinement were performed using SHELX-97 package.[16] Crystal data: monoclinic, space group $C2/c$ (No. 15), a = 24.6455(8) Å, b = 10.5901(4) Å, c = 7.9658(2) Å, β = 106.662(2)°, V = 1991.77(11) Å^3, Z = 4, Dc = 1.995 g cm^{-3}, Mo-Kα radiation, λ = 0.71073 Å, μ = 7.371 cm^{-1}, T = 120(2) K; 8215 reflections were collected, 2291 were unique, R_{int} 0.061; final refinement to convergence on F^2 with all non-H atoms anisotropic and all H atoms modelled isotropically gave R_1 = 0.0238 (F, 1144 obs. data only) and wR_2 = 0.0423 (F^2, all data), GOF = 1.080, 120 refined parameters; theta range for data collection: 0.3203–27.50°. CCDC-1489811 (**6-4**) contains the supplementary crystallographic data. These data can be obtained free of charge from the Cambridge Crystallographic Data Centre via www.ccdc.cam.ac.uk/data_request/cif.www.ccdc.cam.ac.uk/data_request/cif.www.ccdc.cam.ac.uk/data_request/cif.

Methodological details in calculations

Calculations are performed using the Gaussian 09 program package.[17] Compounds **6-1**–**6-4** were optimized with the 6-311+G(3df) basis sets for S and Se and the 6-311G(d) basis sets for C and H.[18] The basis set

system is called 6-A (BSS-A), in this paper. BSS-B was also employed to optimize **6-1**–**6-4**, which consisted of the 6-311+G(3d) basis sets for S and Se and the 6-311G(d) basis sets for C and H. Models **6-A**–**6-D** were optimized with the 6-311+G(3df) basis sets for S and Se with the 6-311G(d,p) basis sets for C and H (BSS-C). The Møller-Plesset second order energy correlation (MP2) level was applied to the calculations.[19] The DFT level of M06-2X[20] was also applied, when necessary (NBO analysis for **6-1**–**6-4**, for example). Structures were confirmed by the frequency analysis performed on the optimized structures with the same basis sets at the same level of the optimizations.

QTAIM functions were calculated using the Gaussian 09 program package with the same method of the optimizations. The results were analyzed with the AIM2000 program.[21] Normal coordinates of internal vibrations (NIV) obtained by the frequency analysis were employed to generate the perturbed structures. The details of QTAIM-DFA and NIV are explained in Chapter 2.

Results and Discussion

Structure of bis[8-(methylselanyl)naphthyl]-1,1'-diselenide (6-4)

Figure 6-2 displays the structure of **6-4**, determined by the X-ray crystallographic analysis. Table 6-1 collects the selected structural parameters of **6-4**, together with those for **6-I** ((^{A}E, ^{B}E) = (S, S), (S, Se), (Se, S), and (Se, Se)), reported earlier.[2–4] The structure of **6-4** is essentially the same as that of **6-I** (Se, Se), although the Se–Ph groups in **6-I** (Se, Se) are replaced by the Se–Me groups in **6-4**. One may image that the π-orbitals of the Se–Ph groups play an important role to stabilize the fine details in the structure of **6-I** (Se, Se) (see Figure 6-1). However, the structure of **6-4** seems well controlled without such interactions of the C–H(Nap)----π(C_6H_6) type. Namely, the fine detail in the structure of **6-4** must be determined through the contribution of the Se_4 σ(4c–6e) interaction, as shown in Figure. 6-2.

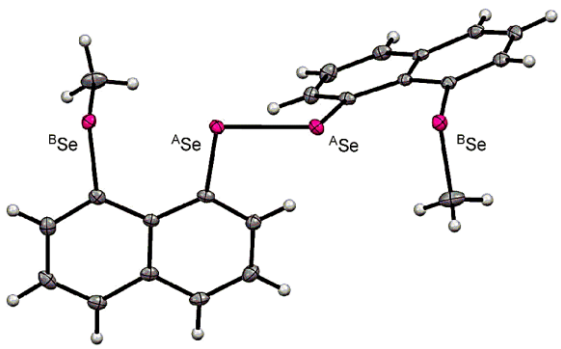

Figure 6-2. Structure of **6-4**, determined by the X-ray crystallographic analysis.

Optimizations of 6-1–6-4 and models 6-A–6-D

Table 6-1 collects the structural parameters around ^{B}E---^{A}E–^{A}E---^{B}E in **6-1**–**6-4** optimized with MP2/BSS-A, while those with MP2/BSS-B are collected in Table 6-A1 of the Appendix. The structural parameters for models **6-A**–**6-D** are summarized in Table 6-A2 of the Appendix, optimized with MP2/BSS-C. Optimized structures are not shown in figures but some are found in the molecular graphs, which are drawn on the optimized structures (see Figure 6-3).

The observed ^{A}E---^{B}E distances (r_o(^{A}E, ^{B}E)) of **6-4** (Se, Se) (3.030 Å) is very well reproduced by the optimization with MP2/BSS-A (3.035 Å), as shown in Table 6-1. The predicted r_o(^{A}E, ^{B}E) values for **6-2**–**6-4** are longer than the observed values for **6-I** (S, Se), **6-I** (Se, S), and **6-I** (Se, Se), by 0.031–0.018 Å, respectively. However, the observed r_o(^{A}E, ^{B}E) in **6-4** (Se, Se) is shorter than that in **6-I** (Se, Se) by 0.023 Å. Therefore, the differences are expected to be less than 0.01 Å, if r_o(^{A}E, ^{B}E) of **6-2**–**6-4** are assumed to be shorter than the observed values in **6-I** (S, Se), **6-I** (Se, S), and **6-I** (Se, Se), respectively, by 0.023 Å. In the case of r_o(^{A}S, ^{B}S) in **6-1** (S, S), the value is predicted to be shorter than that in **6-I** (S, S) by 0.046 Å, which could also be reduced to 0.024 Å after the correction by 0.023 Å.

The magnitude of Δr ($= r_{calcd} - r_{obsd}$) less than 0.013 Å is desirable for QTAIM-DFA, which corresponds to half of the intervals of adjacent data points in the plots of $H_b(\boldsymbol{r}_c)$ versus $H_b(\boldsymbol{r}_c) - V_b(\boldsymbol{r}_c)/2$ ($0.05a_o = 0.026$ Å) (*cf*: Figure 6-5). Therefore, the r_o(^{A}E, ^{B}E) values for **6-2**–**6-4** are desirable for QTAIM-DFA, if evaluated with MP2/BSS-A. The estimated magnitude for the calculation error of 0.024 Å for r_o(^{A}S, ^{B}S) in **6-1** (S, S) seems larger than the desirable value but less than the acceptable range of 0.026 Å ($0.05a_o$). Consequently, the predicted r_o(^{A}E, ^{B}E) values with MP2/BSS-A seem desirable for **6-2**–**6-4** and acceptable for **6-1** in the QTAIM-DFA treatment, although some crystal packing effect may affect on the observed structures.[2–4]

The predicted r_o(^{A}E, ^{A}E) value for **6-4** with MP2/BSS-A seems somewhat shorter than the observed value ($\Delta r = -0.033$ Å). However, the predicted r_o(^{A}E, ^{A}E) values for **6-1**–**6-4** seem to correspond very well to the observed values of **6-I** (S, S), **6-I** (S, Se), **6-I** (Se, S), and **6-I** (Se, Se), respectively, with MP2/BSS-A. On the other hand, the observed r_o(^{A}E, ^{A}E) value of **6-4** (2.386 Å) is very well reproduced with MP2/BSS-B (2.384 Å). Similarly, the observed r_o(^{A}E, ^{A}E) values of **6-1**–**6-3** could also be reproduced well with MP2/BSS-B, if the observed values of **6-1**–**6-4** are assumed to be longer than those of **6-I** (S, S), **6-I** (S, Se), **6-I** (Se, S), and **6-I** (Se, Se), respectively, by 0.021 Å, as observed in **6-4** versus **6-I** (Se, Se). In this case, the magnitudes of the differences will be less than 0.012 Å. The observed r_o(^{A}E, ^{A}E) and r_o(^{A}E, ^{B}E) values will be well reproduced, if MP2/BSS-A and/or MP2/BSS-B are suitably applied, although the predicted r_o(^{A}S, ^{B}S) values for **6-1** (S, S) with MP2/BSS-A and/or MP2/BSS-B seem somewhat shorter than

the observed value.

Table 6-1. Structural parameters evaluated for **6-1**–**6-4** with MP2/BSS-A, together with the observed values for **6-4** and **6-I** (^{A}E, ^{B}E)[a]

Species (^{A}E, ^{B}E) (symmetry)	r_o(^{A}E, ^{A}E) (Å)	r_o(^{A}E, ^{B}E) (Å)	Δr_o(^{A}E, ^{B}E)[b] (Å)	$\angle C_1{}^{A}E^{A}E$ (°)
MP2/BSS-A				
6-1 (S, S) (C_1)	2.0559	2.9418	–0.66	104.9
6-2 (S, Se) (C_2)	2.0603	3.0255	–0.67	104.6
6-3 (Se, S) (C_2)	2.3440	2.9556	–0.74	101.9
6-4 (Se, Se) (C_2)	2.3532	3.0353	–0.76	101.6
Observed				
6-4 (Se, Se)[c]	2.3864(4)	3.030	–0.77	102.64(6)
6-I (S, S)	2.055(2)	2.988(2)	–0.61	104.9[d]
6-I (S, Se)	2.0706	3.0560[d]	–0.64	104.2[d]
6-I (Se, S)	2.3561	2.9809[d]	–0.72	101.8[d]
6-I (Se, Se)	2.365(1)	3.053(1)[d]	–0.75	102.4[d]

[a] BSS-A; the 6-311+G(3df) basis sets being employed for S and Se with the 6-311G(d) basis sets for C and H. [b] $\Delta r_o(^{A}E, ^{B}E) = r_o(^{A}E, ^{B}E) - \Sigma r_{vdW}(^{A}E, ^{B}E)$, where r_{vdW}(S) = 1.80 Å and r_{vdW}(Se) = 1.90 Å (ref. 40). [c] Prepared and measured in this work. [d] Averaged value.

(Table 6-1 continued)

Species (^{A}E, ^{B}E) (symmetry)	$\angle C_8{}^{B}EC_{11}$ (°)	$\angle {}^{B}E^{A}E^{A}E$ (°)	ϕ_1[e] (°)	ϕ_2[f] (°)	E(2) kJ mol^{-1}
MP2/BSS-A					
6-1 (S, S) (C_1)	99.6	171.4	83.7	75.5	36.9
6-2 (S, Se) (C_2)	97.0	170.2	85.7	69.9	39.3
6-3 (Se, S) (C_2)	99.4	177.8	83.3	73.7	63.6
6-4 (Se, Se) (C_2)	96.6	176.9	85.1	68.3	71.0
Observed					
6-4 (Se, Se)[c]	96.98(9)[g]	173.3	79.1	78.7[h]	
6-I (S, S)	102.8[d,g]	167.3[d]	–89.0	76.4[d,h]	
6-I (S, Se)	99.2[d,g]	168.1[d]	–81.3	70.8[d,h]	
6-I (Se, S)	102.3[d,g]	174.4[d]	–91.5	76.6[d,h]	
6-I (Se, Se)	100.3[d,g]	173.8[d]	91.4(4)	73.1[d,h]	

[e] $\phi_1 = \phi(C_1{}^{A}E^{A}EC_{1'})$. [f] $\phi_2 = \phi(C_9C_8{}^{B}EC_{11})$. [g] $\angle C_8{}^{B}EC_i$. [h] $\phi_2 = \phi(C_9C_8{}^{B}EC_i)$.

How are the r_o(^{A}E, ^{B}E) values evaluated in the models? The Δr_o(^{A}E, ^{B}E) [= r_o(^{A}E, ^{B}E) – Σr_{vdW}(^{A}E, ^{B}E)] values become smaller (shorter) as shown in eq (6-1), where Σr_{vdW}(^{A}E, ^{B}E) are the sum of the van der Waals

radii[22] of ^{A}E and ^{B}E.

$\Delta r_o(^{A}E, ^{B}E)$:

model **6-B** > model **6-A** > model **6-D** > model **6-C** (>> **6-1**–**6-4**) (6-1)

ΔE_{ES} and ΔE_{ZP}:

model **6-A** > model **6-B** >> model **6-C** ≈ model **6-D** (6-2)

How are the energies in the formation of the models? Table 6-A2 of the Appendix contains the energies for the formation of the models from the components, ΔE_{ES} and ΔE_{ZP}, where ΔE_{ES} stands for those on the energy surface and ΔE_{ZP} for those considering the zero-point energy collections. The ΔE_{ES} and ΔE_{ZP} values become smaller (more stable) in the order shown in eq (6-2), if the same (^{A}E, ^{B}E) are compared. The plot of ΔE_{ZP} versus ΔE_{ES} gave an excellent correlation, although not shown ($\Delta E_{ZP} = 1.086\Delta E_{ES} + 6.88$, $R_c^2 = 0.999$ (R_c^2: square of correlation coefficient)). Therefore, ΔE_{ES} can be used to discuss the trend in the behavior of ΔE. Indeed, a very good correlation between ΔE_{ES} and $\Delta r_o(^{A}E, ^{B}E)$ is expected for the models, but the correlation seems not so good. Factors may operate to stabilize the models, other than those lead to a (very) good correlation between them.

The ΔE_{ES} and ΔE_{ZP} values are plotted to visualize the relative stability of models **6-A**–**6-D**. The plot is shown in Figure 6-A1 of the Appendix, which tells us that (a) ΔE_{ES} and ΔE_{ZP} are almost constant for models **6-A** and **6-B** and (b) ΔE_{ES} and ΔE_{ZP} become smaller (more stable) in the order of (^{A}E, ^{B}E) = (S, S) > (S, Se) > (Se, S) > (Se, Se) for models **6-C** and **6-D**. Eq (6-2) is completely confirmed and the methyl substitutions in $^{B}EH_2$ stabilize much the models, whereas the substitutions in $^{A}E_2H_2$ stabilize the models only slightly, judging from Figure 6-A1 of the Appendix, The accepting ability of $\sigma^*(^{A}E–^{A}E)$ seems more important than the donating ability of $n_p(^{B}E)$ to stabilize the models, especially in model **6-D**.

NBO analysis[23,24] is also applied to ^{A}E---^{B}E in models **6-A**–**6-D** and **6-1**–**6-4**, to evaluate the contributions from the CT interactions between $n_p(^{B}E)$ and $\sigma^*(^{A}E–^{A}E)$ to stabilize the interactions. For each donor NBO (i) and acceptor NBO (j), the stabilization energy $E(2)$ is calculated based on the second-order perturbation theory in NBO, according to eq (6-3), where q_i is the donor orbital occupancy, ε_i and ε_j are diagonal elements (orbital energies) and $F(i,j)$ is the off-diagonal NBO Fock matrix element. The $E(2)$ values of **6-1**–**6-4** are evaluated with M06-2X/BSS-A,[35] employing the structures optimized with MP2/BSS-A, since the evaluations were unsuccessful with MP2/BSS-A//MP2/BSS-A. Those with models **6-A**–**6-D** were performed with MP2/BSS-C//MP2/BSS-C.

$$E(2) = q_i\, F(i,j)^2/(\varepsilon_j - \varepsilon_i) \qquad (6\text{-}3)$$

Table 6-1 collects the $E(2)$ values for **6-1**–**6-4**, whereas those for models **6-A**–**6-D** are summarized in Table 6-A3 of the Appendix. The $E(2)$ values become larger (more stabilized) in the order shown in eq (6-4), if the values of the same (^{A}E, ^{B}E) are compared. The order is just the opposite to that for $\Delta r_o(^{A}E, ^{B}E)$ shown in eq (6-5), although the evaluation method for NBO of **6-1**–**6-4** are different from others. Similarly, the $E(2)$ values in models **6-A**–**6-D** increase (more stabilized) in the order shown in eq (6-5).

$E(2)$:

model **6-B** < model **6-A** < model **6-D** < model **6-C** << **6-1**–**6-4** (6-4)

$E(2)$:

(^{A}E, ^{B}E) = (S, S) ≈ (S, Se) << (Se, S) ≈ (Se, Se) (6-5)

The results show that the methyl substitutions in $^{B}EH_2$ much stabilize the ^{A}E---^{B}E interactions through the CT mechanism, whereas those in $^{A}E_2H_2$ seem to destabilize them. The trend is much clear in $E(2)$, relative to the case of ΔE_{ES}. $\sigma*(^{A}E–^{A}E)$ will be much more important, relative to the case of $n_p(^{B}E)$ in $E(2)$. The $2E(2)$ values should correspond to ΔE_{ES} for the models. Then, $2E(2)$ are plotted versus ΔE_{ES} for models **6-A**–**6-D**, which is shown in Figure 6-A2. The correlations are given in the figure. It is of interest, since the correlations are (very) good for modes **6-B**–**6-D**, whereas no reasonable correlation is predicted for model **6-A**. Very small differences in ΔE_{ES} (0.4 kJ mol^{-1}), versus those in $E(2)$ (5.2 kJ mol^{-1}), would be responsible for the observed results in model **6-A**.

After clarification of the structural feature for **6-1**–**6-4** and models **6-A**–**6-D**, next extension is to elucidate the nature of the $^{B'}$E---$^{A'}$E–^{A}E---^{B}E interactions. Molecular graphs and contour plots are examined, before detail discussion by employing QTAIM-DFA.

Molecular graphs and contour plots around $^{B'}$E-∗-$^{A'}$E-∗-^{A}E-∗-^{B}E in 6-1–6-4 and models 6-A–6-D

Figure 6-3 shows the molecular graphs, exemplified by **6-1** (S, S), **6-3** (Se, S), **6-4** (Se, Se), and model **6-A** (Se, Se)–model **6-D** (Se, Se) (see also Figure 6-A3 of the Appendix). All BCPs expected are detected, containing those between the chalcogen atoms. Figure 6-4 shows the contour plots of $\rho_b(\boldsymbol{r}_c)$ for **6-1** (S, S), **6-3** (Se, S), **6-4** (Se, Se), and model **6-A** (Se, Se)–**6-D** (Se, Se). BCPs are located on the three dimensional

saddle points of $\rho_b(\boldsymbol{r}_c)$, as illustrated in Figure 6-4. Negative Laplacians and trajectory plots are illustrated in Figures 6-A4 and 6-A5 of the Appendix, respectively, similarly to the case of Figure 6-4. BCPs on ^{A}E-∗-^{A}E are placed in the negative area of $\nabla^2\rho_b(\boldsymbol{r}_c)$, whereas those on ^{B}E-∗-^{A}E are in the positive area of $\nabla^2\rho_b(\boldsymbol{r}_c)$ as described in Figure 6-A4. The results show that ^{A}E-∗-^{A}E and ^{B}E-∗-^{A}E are classified by the sheared shell (SS) and closed shell (CS) interactions, respectively. The space around each species is divided reasonably into atoms in it, as shown in Figure 6-A5.

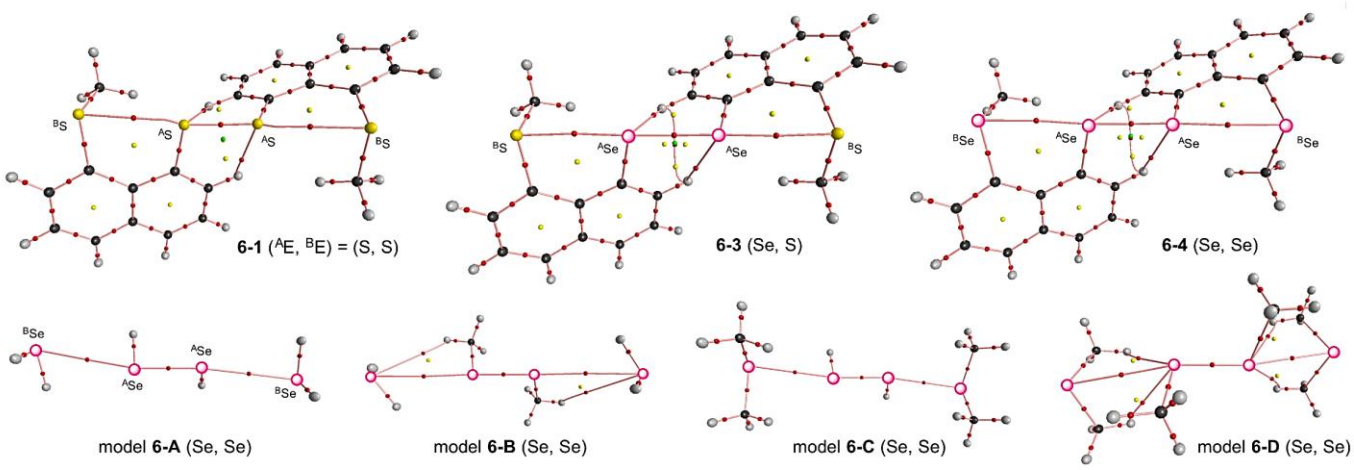

Figure 6-3. Molecular graphs for **6-1** (^{A}E, ^{B}E) = (S, S), **6-3** (Se, S), **6-4** (Se, Se), and models **6-A** (Se, Se)–**6-D** (Se, Se). BCPs (bond critical points) are denoted by red dots, RCPs (ring critical points) by yellow dots, CCPs (cage critical points) by green dots, and BPs (bond paths) by pink lines, accompanied by BCPs. Carbon atoms are in black, hydrogen atoms are in gray, sulfur atoms in yellow, and selenium atoms in pink.

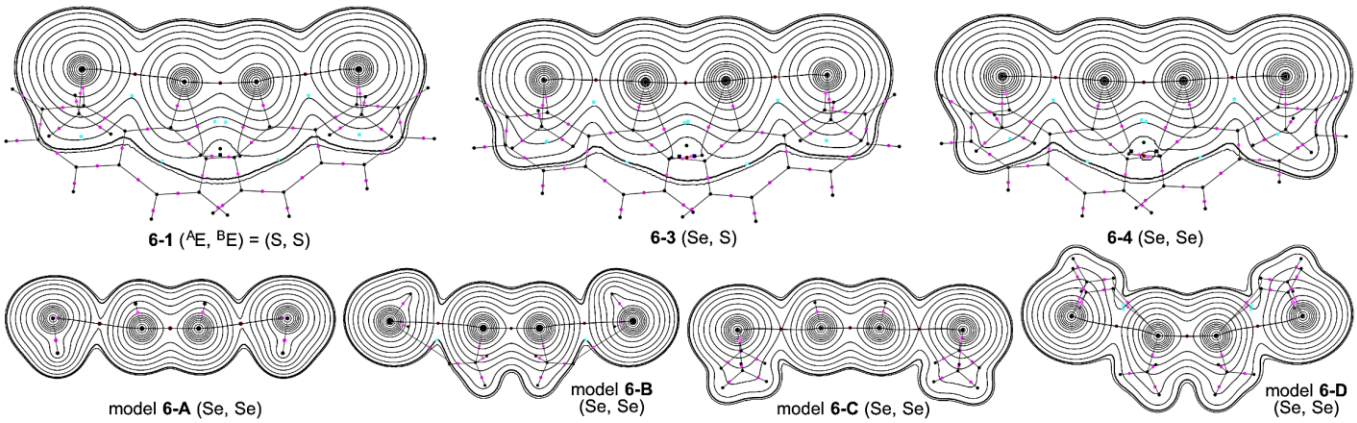

Figure 6-4. Contour plots of $\rho_b(\boldsymbol{r}_c)$ for **6-1** (^{A}E, ^{B}E) = (S, S), **6-3** (Se, S), **6-4** (Se, Se), and models **6-A** (Se, Se)–**6-D** (Se, Se). BCPs on the plane are shown by red dots, those outside of the plane in dark pink dots, RCPs on and outside the plane by blue squares, and light blue ones, respectively. CCPs by green dots, BPs on the plane by black lines, and those outside of the plane are by gray lines. Atoms on and outside the plane are by black dots and gray ones, respectively. The contours (ea_0^{-3}) are at 2^l (l = ±8, ±7, ..., 0) with 0.0047 (heavy line).

Survey of the ^{B}E-∗-^{A}E-∗-^{A}E-∗-^{B}E interactions in 6-1–6-4 and models 6-A–6-D

Bond paths (BPs) define the interactions, unambiguously. How can σ(4c–6e) of the ^{B}E-∗-^{A}E-∗-^{A}E-∗-^{B}E type in **6-1**–**6-4** and models **6-A**–**6-D** be described based on BPs? BPs in **6-1**–**6-4** and models **6-A**–**6-D** seem almost straight, as shown in Figures 6-3 and 6-4, together with Figure 6-A6 of the Appendix. Namely, σ(4c–6e) in **6-1**–**6-4** and models **6-A**–**6-D** can be approximated by the straight lines.

The lengths of BPs (r_{BP}) in question are collected in Table 6-A4 of the Appendix, together with the corresponding straight-line distances (R_{SL}). The differences between them ($\Delta r_{BP} = r_{BP} - R_{SL}$) are less than 0.022 Å with 0.048 Å for Δr_{BP} (^{A}S, ^{B}S) in model **6-B** (S, S). To confirm the linearity of the interactions, r_{BP} are plotted versus R_{SL}, which is shown in Figure 6-A6 of the Appendix. The plot gave an excellent correlation ($r_{BP} = 1.006R_{SL} + 0.0080$, $R_c^2 = 0.999$; $r_{BP} = 0.9996R_{SL} + 0.0129$, $R_c^2 = 0.9997$ without data for model **6-B** (S, S)). Consequently, σ(4c–6e) in **6-1** (S, S)–**6-4** (Se, Se) and models **6-A**–**6-D** can be substantially described by the straight lines, although ^{A}S-∗-^{B}S in model **6-B** (S, S) seems somewhat curved.

QTAIM functions of $\rho_b(\boldsymbol{r}_c)$, $H_b(\boldsymbol{r}_c) - V_b(\boldsymbol{r}_c)/2$, $H_b(\boldsymbol{r}_c)$, and $k_b(\boldsymbol{r}_c)$ (= $V_b(\boldsymbol{r}_c)/G_b(\boldsymbol{r}_c)$) are evaluated for ^{A}E-∗-^{B}E and ^{A}E-∗-^{A}E at BCPs in **6-1**–**6-4** and models **6-A**–**6-D**. Tables 6-2 and 6-3 collect the results for **6-1**–**6-4** and models **6-A**–**6-D**, respectively. Tables 6-2 and 6-3 also collect the frequencies (ν) and force constants (k_f), corresponding to ^{A}E-∗-^{B}E and ^{A}E-∗-$^{A'}$E. Figure 6-5 shows the plots of $H_b(\boldsymbol{r}_c)$ versus $H_b(\boldsymbol{r}_c) - V_b(\boldsymbol{r}_c)/2$ for the fully optimized data of **6-1**–**6-4** in Table 6-2, together with those from the perturbed structures around the fully optimized ones. The plots are analyzed according to eqs (2-3)–(2-6) in the Chapter 2 and the QTAIM-DFA parameters of (R, θ) and (θ_p, κ_p) are obtained. Tables 6-2 and 6-3 collect the (R, θ) and (θ_p, κ_p) values for ^{A}E-∗-^{B}E and ^{A}E-∗-^{A}E in **6-1**–**6-4** and models **6-A**–**6-D**, respectively.

Nature of ^{A}E-∗-^{B}E and ^{A}E-∗-^{A}E in 6-1–6-4 and models 6-A–6-D, elucidated by (R, θ) and (θ_p, κ_p)

The nature of ^{A}E-∗-^{B}E and ^{A}E-∗-^{A}E in **6-1**–**6-4** and models **6-A**–**6-D** is elucidated by employing (R, θ) and (θ_p, κ_p), with the standard values in Scheme 2-3, as a reference. It is instructive to survey the criteria briefly, closely related to those in this work. Interactions are called CS and SS interactions for $45° < \theta < 180°$ ($0 < H_b(\boldsymbol{r}_c) - V_b(\boldsymbol{r}_c)/2$) and $180° < \theta < 206.6°$ ($H_b(\boldsymbol{r}_c) - V_b(\boldsymbol{r}_c)/2 < 0$), respectively. The CS interactions are sub-divided into *pure* CS and *regular* CS for $45° < \theta < 90°$ ($0 < H_b(\boldsymbol{r}_c)$) and $90° < \theta < 180°$ ($H_b(\boldsymbol{r}_c) < 0$), respectively. The θ_p value plays an important role to characterize the interactions. In the *pure* CS region of $45° < \theta < 90°$, the character of interactions will be the vdW type for $45° < \theta_p < 90°$, whereas it will be the *typical* HB type without covalency for $90° < \theta_p \leq 125°$, although θ_p of 125° is tentatively given corresponding to $\theta = 90°$. The CT interactions will appear in the *regular* CS region of $90° < \theta < 180°$. The

typical HB interactions with some covalency appear in range of 125° < θ_p ≤ 150° (90° < θ ≤ 115°). Interactions of the CT-MC (molecular complex formation through CT) and CT-TBP (TBP adduct formation through CT) types will appear in the ranges of 150° < θ_p ≤ 180° (115° ≤ θ < 150°) and 180° < θ_p ≤ 190° (150° ≤ θ_p < 180°), respectively. Classical chemical bonds of SS should be called strong when R > 0.15 au, therefore, they will be weak when R < 0.15 au.

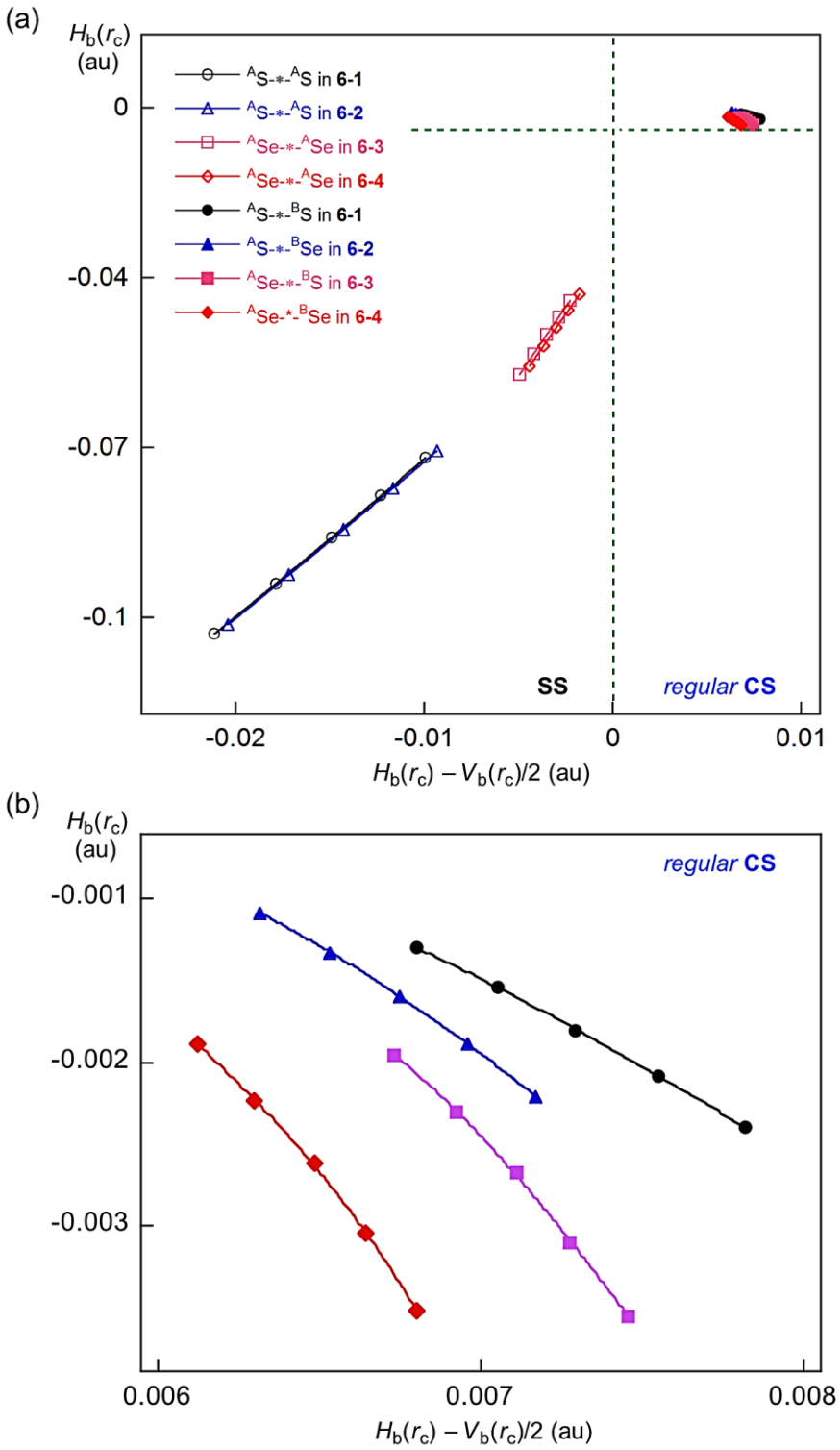

Figure 6-5. Plots of $H_b(\boldsymbol{r}_c)$ versus $H_b(\boldsymbol{r}_c) - V_b(\boldsymbol{r}_c)/2$ for ^{A}E-*-^{A}E and ^{A}E-*-^{B}E of **6-1**–**6-4**. (a) Whole picture and (b) magnified one for ^{A}E-*-^{B}E. Marks and colors for the species are shown in the figure.

Table 6-2 QTAIM functions and QTAIM-DFA parameters for ^{A}E-∗-$^{A'}$E and ^{A}E-∗-^{B}E at BCPs of **6-1**–**6-4**, 1-(8-Me^{B}EC$_{10}$H$_6$)^{A}E–$^{A'}$E(C$_{10}$H$_6$$^{B'}$EMe-8')-1', evaluated with MP2/BSS-A[a]

Species (^{A}E, ^{B}E) (symmetry)	Interactions (X-∗-Y)	$\rho_b(\boldsymbol{r}_c)$ (ea_o^{-3})	$c\nabla^2\rho_b(\boldsymbol{r}_c)$[b] (au)	$H_b(\boldsymbol{r}_c)$ (au)	$k_b(\boldsymbol{r}_c)$[c]	R (au)	θ (°)
6-1 (S, S) (C_1)	(^{A}S-∗-^{A}S)	0.1481	–0.0149	–0.0885	–2.509	0.0898	189.6
6-1 (S, S) (C_1)	(^{A}S-∗-^{B}S)	0.0267	0.0073	–0.0018	–1.110	0.0075	103.9
6-2 (S, Se) (C_2)	(^{A}S-∗-^{A}S)	0.1467	–0.0143	–0.0869	–2.490	0.0881	189.3
6-2 (S, Se) (C_2)	(^{A}S-∗-^{B}Se)	0.0258	0.0067	–0.0016	–1.106	0.0069	103.3
6-3 (Se, S) (C_2)	(^{A}Se-∗-^{A}Se)	0.1029	–0.0035	–0.0467	–2.177	0.0469	184.3
6-3 (Se, S) (C_2)	(^{A}Se-∗-^{B}S)	0.0292	0.0071	–0.0027	–1.160	0.0076	110.8
6-4 (Se, Se) (C_2)	(^{A}Se-∗-^{A}Se)	0.1011	–0.0030	–0.0452	–2.153	0.0453	183.8
6-4 (Se, Se) (C_2)	(^{A}Se-∗-^{B}Se)	0.0286	0.0064	–0.0026	–1.169	0.0070	112.2

[a] BSS-A; the 6-311+G(3df) basis sets being employed for S and Se with the 6-311G(d) basis sets for C and H. [b] $c\nabla^2\rho_b(\boldsymbol{r}_c) = H_b(\boldsymbol{r}_c) - V_b(\boldsymbol{r}_c)/2$, where $c = \hbar^2/8m$. [c] $k_b(\boldsymbol{r}_c) = V_b(\boldsymbol{r}_c)/G_b(\boldsymbol{r}_c)$.

(Table 6-2 continued)

Species (^{A}E, ^{B}E) (symmetry)	Interactions (X-∗-Y)	ν_n (n)[d] (cm^{-1})	k_f[e] (mDyn Å^{-1})	θ_p (°)	κ_p (au^{-1})	Classification/ characterization
6-1 (S, S) (C_1)	(^{A}S-∗-^{A}S)	508.6 (36)	2.016	197.1	0.4	SS/Cov-w
6-1 (S, S) (C_1)	(^{A}S-∗-^{B}S)	187.7 (15)	0.138	137.8	81.7	*p*-CS/*t*-HB[f]
6-2 (S, Se) (C_2)	(^{A}S-∗-^{A}S)	498.0 (36)	1.892	197.2	0.3	SS/Cov-w
6-2 (S, Se) (C_2)	(^{A}S-∗-^{B}Se)	152.6 (15)	0.130	142.6	102	*p*-CS/*t*-HB[f]
6-3 (Se, S) (C_2)	(^{A}Se-∗-^{A}Se)	281.6 (24)	0.822	190.0	0.3	SS/Cov-w
6-3 (Se, S) (C_2)	(^{A}Se-∗-^{B}S)	172.9 (17)	0.170	155.9	52.2	*p*-CS/CT-MC
6-4 (Se, Se) (C_2)	(^{A}Se-∗-^{A}Se)	270.0 (24)	1.076	190.2	0.3	SS/Cov-w
6-4 (Se, Se) (C_2)	(^{A}Se-∗-^{B}Se)	117.8 (11)	0.043	156.3	60.3	*p*-CS/CT-MC

[d] Corresponding to the interaction in question. Symmetric and anti-symmetric modes being employed for ^{A}E-∗-^{A}E and ^{A}E-∗-^{B}E, respectively. [e] Force constant for ν_n. [f] *Typical* HB nature with covalency

Table 6-3 QTAIM functions and QTAIM-DFA parameters for ^{A}E-∗-^{B}E at BCPs of models **6-A**–**6-D**, evaluated with MP2/BSS-C[a]

Species (^{A}E, ^{B}E) (symmetry)	Interactions (X-∗-Y)	$\rho_b(\boldsymbol{r}_c)$ (ea_o^{-3})	$c\nabla^2\rho_b(\boldsymbol{r}_c)$[b] (au)	$H_b(\boldsymbol{r}_c)$ (au)	$k_b(\boldsymbol{r}_c)$[c]	R (au)	θ (°)
Model **6-A**: $H_2{}^{B}E$---$^{A}E(H)$–$(H)^{A}E$---$^{B}EH_2$ (C_2)							
(S, S)	(^{A}S-∗-^{B}S)	0.0081	0.0031	0.0009	–0.839	0.0032	74.5
(S, Se)	(^{A}S-∗-^{B}Se)	0.0077	0.0028	0.0008	–0.831	0.0029	73.9
(Se, S)	(^{A}Se-∗-^{B}Se)	0.0085	0.0030	0.0009	–0.829	0.0031	73.7
(Se, Se)	(^{A}Se-∗-^{B}Se)	0.0082	0.0027	0.0008	–0.823	0.0028	73.2
Model **6-B**: $H_2{}^{B}E$---$^{A}E(Me)$–$(Me)^{A}E$---$^{B}EH_2$ (C_2)							
(S, S)	(^{A}S-∗-^{B}S)	0.0064	0.0027	0.0010	–0.766	0.0029	69.2
(S, Se)	(^{A}S-∗-^{B}Se)	0.0060	0.0025	0.0010	–0.754	0.0026	68.4
(Se, S)	(^{A}Se-∗-^{B}Se)	0.0065	0.0025	0.0009	–0.777	0.0027	70.0
(Se, Se)	(^{A}Se-∗-^{B}Se)	0.0063	0.0023	0.0009	–0.770	0.0025	69.5
Model **6-C**: $Me_2{}^{B}E$---$^{A}E(H)$–$(H)^{A}E$---$^{B}EMe_2$ (C_2)							
(S, S)	(^{A}S-∗-^{B}S)	0.0145	0.0047	0.0003	–0.971	0.0047	86.7
(S, Se)	(^{A}S-∗-^{B}Se)	0.0144	0.0044	0.0003	–0.963	0.0044	86.0
(Se, S)	(^{A}Se-∗-^{B}Se)	0.0161	0.0048	0.0001	–0.985	0.0048	88.3
(Se, Se)	(^{A}Se-∗-^{B}Se)	0.0155	0.0043	0.0002	–0.974	0.0043	87.1
Model **6-D**: $Me_2{}^{B}E$---$^{A}E(Me)$–$(Me)^{A}E$---$^{B}EMe_2$ (C_2)							
(S, S)	(^{A}S-∗-^{B}S)	0.0106	0.0036	0.0006	–0.909	0.0037	80.5
(S, Se)	(^{A}S-∗-^{B}Se)	0.0105	0.0034	0.0006	–0.906	0.0035	80.2
(Se, S)	(^{A}Se-∗-^{B}Se)	0.0128	0.0040	0.0005	–0.935	0.0040	83.0
(Se, Se)	(^{A}Se-∗-^{B}Se)	0.0121	0.0036	0.0005	–0.925	0.0036	82.1

[a] BSS-C; the 6-311+G(3df) basis sets being employed for S and Se with the 6-311G(d, p) basis sets for C and H. [b] $c\nabla^2\rho_b(\boldsymbol{r}_c) = H_b(\boldsymbol{r}_c) - V_b(\boldsymbol{r}_c)/2$, where $c = \hbar^2/8m$. [c] $k_b(\boldsymbol{r}_c) = V_b(\boldsymbol{r}_c)/G_b(\boldsymbol{r}_c)$.

(Table 6-3 continued)

Species (^{A}E, ^{B}E) (symmetry)	Interactions (X-∗-Y)	ν_n (n)[d] (cm^{-1})	k_f[e] (mDyn $Å^{-1}$)	θ_p (°)	κ_p (au^{-1})	Classification/ characterization
Model **6-A**: $H_2{}^{B}E$---$^{A}E(H)$–$(H)^{A}E$---$^{B}EH_2$ (C_2)						
(S, S)	(^{A}S-∗-^{B}S)	75.4 (7)	0.032	92.7	163	*p*-CS/*t*-HB[f]
(S, Se)	(^{A}S-∗-^{B}Se)	61.2 (6)	0.016	87.8	134	*p*-CS/vdW
(Se, S)	(^{A}Se-∗-^{B}Se)	59.6 (7)	0.062	91.2	238	*p*-CS/*t*-HB[f]
(Se, Se)	(^{A}Se-∗-^{B}Se)	45.5 (7)	0.053	86.9	214	*p*-CS/vdW
Model **6-B**: $H_2{}^{B}E$---$^{A}E(Me)$–$(Me)^{A}E$---$^{B}EH_2$ (C_2)						
(S, S)	(^{A}S-∗-^{B}S)	73.0 (8)	0.033	83.1	152	*p*-CS/vdW
(S, Se)	(^{A}S-∗-^{B}Se)	30.6 (3)[g]	0.006	80.1	735	*p*-CS/vdW
(Se, S)	(^{A}Se-∗-^{B}Se)	64.8 (6)	0.044	86.9	228	*p*-CS/vdW
(Se, Se)	(^{A}Se-∗-^{B}Se)	50.6 (6)	0.021	88.0	115	*p*-CS/vdW
Model **6-C**: $Me_2{}^{B}E$---$^{A}E(H)$–$(H)^{A}E$---$^{B}EMe_2$ (C_2)						
(S, S)	(^{A}S-∗-^{B}S)	90.5 (8)	0.042	114.5	146	*p*-CS/*t*-HB[f]
(S, Se)	(^{A}S-∗-^{B}Se)	76.0 (8)	0.037	113.8	207	*p*-CS/*t*-HB[f]
(Se, S)	(^{A}Se-∗-^{B}Se)	70.9 (8)	0.038	121.8	174	*p*-CS/*t*-HB[f]
(Se, Se)	(^{A}Se-∗-^{B}Se)	55.5 (7)	0.049	121.2	311	*p*-CS/*t*-HB[f]
Model **6-D**: $Me_2{}^{B}E$---$^{A}E(Me)$–$(Me)^{A}E$---$^{B}EMe_2$ (C_2)						
(S, S)	(^{A}S-∗-^{B}S)	81.9 (10)	0.020	103.4	170	*p*-CS/*t*-HB[f]
(S, Se)	(^{A}S-∗-^{B}Se)	58.9 (7)	0.030	100.0	247	*p*-CS/*t*-HB[f]
(Se, S)	(^{A}Se-∗-^{B}Se)	69.1 (8)	0.017	111.7	256	*p*-CS/*t*-HB[f]
(Se, Se)	(^{A}Se-∗-^{B}Se)	49.5 (7)	0.024	106.0	249	*p*-CS/*t*-HB[f]

[d] Corresponding to the interaction of the anti-symmetric mode in question. [e] Force constant for ν_n. [f] *Typical* HB nature without covalency. [g] Symmetric mode being employed.

The ^{A}E-∗-^{B}E and ^{A}E-∗-^{A}E interactions in **6-1**–**6-4** are classified and characterized based on the (R, θ, θ_p) values. The ^{A}E-∗-^{A}E interactions in **6-1**–**6-4** are all classified by the SS interactions and predicted to have the Cov-w (weak covalent) nature ($\theta > 180°$ and $\theta_p > 190°$ with $R < 0.15$ au). The ^{A}E-∗-^{B}E interactions in **6-1**–**6-4** are all classified by the regular CS interactions ($90° < \theta < 180°$). While ^{A}E-∗-^{B}E in **6-1** and **6-2** are characterized to have the *typical* HB nature with covalency ($125° < \theta_p < 150°$), those in **6-3** and **6-4** are predicted to have the CT-MC nature ($150° < \theta_p < 180°$). The results are also summarized in Table 6-2.

The nature of ^{A}E-∗-^{A}E and ^{A}E-∗-^{B}E in models **6-A**–**6-D** are classified and characterized based on the (θ, θ_p) values. The ^{A}E-∗-^{A}E interactions in models **6-A**–**6-D** are all classified by the SS interactions and have the Cov-w character nature ($\theta > 180°$ and $\theta_p > 190°$). On the other hand, ^{A}E-∗-^{B}E are all classified by

the *pure* CS interactions ($\theta < 90°$). They are predicted to have the character of the vdW nature for model **6-B** ($\theta_p < 90°$) but *typical* HB without covalency for models **6-A**, **6-C**, and **6-D** ($90° < \theta_p < 125°$), except for ^{A}Se-∗-^{B}Se in model **6-A** (Se, Se). The interaction is predicted to have the vdW nature. The ^{A}E-∗-^{B}E interactions in model **6-C** are predicted to be stronger than the case of model **6-D**, if the same ^{A}E-∗-^{B}E interactions are compared. The results are summarized in Table 6-3. The ^{A}E-∗-^{B}E interactions are predicted to be stronger in the order of model **6-B** < model **6-A** << model **6-D** < model **6-C** << **6-1**–**6-4**, based on QTAIM-DFA. The order is similar to those for $r_o(^{A}E, ^{B}E)$ (eq (6-1)), ΔE (eq (6-2)), and $E(2)$ (eq (6-5)), if the same ^{A}E-∗-^{B}E are compared. Much stronger ^{A}E-∗-^{B}E interactions predicted for **6-1**–**6-4**, relative to the case of the models, must be the reflection of the shorter $r_o(^{A}E, ^{B}E)$ for **6-1**–**6-4**, relative to the case of the models. The naphthalene 1,8-positions in **6-1**–**6-4** operate effectively as the spacer to shorten $r_o(^{A}E, ^{B}E)$, relative to the models, which have no spacers.

Summary

The nature of $^{A}E_2{}^{B}E_2$ σ(4c–6e) (^{A}E, ^{B}E = S and Se) of the ^{B}E---^{A}E–^{A}E---^{B}E type was elucidated for 1-(8-$Me^{B}EC_{10}H_6$)^{A}E–$^{A}E(C_{10}H_6{}^{B}EMe$-8')-1', (**6-1** (^{A}E, ^{B}E) = (S, S), **6-2** (S, Se), **6-3** (Se, S), and **6-4** (Se, Se)) and for models **6-A**–**6-D** [$^{B}R_2{}^{B}E$---$^{A}E(^{A}R)$–$(^{A}R)^{A}E$---$^{B}E^{B}R_2$: **6-A** (^{A}R = ^{B}R = H), **6-B** (^{A}R = Me, ^{B}R = H), **6-C** (^{A}R = H, ^{B}R = Me) and **6-D** (^{A}R = ^{B}R = Me), where ^{A}E, ^{B}E = S and Se]. The optimizations reproduced well the observed structures, containing the linear alignment of four ^{B}E---^{A}E–^{A}E---^{B}E atoms. Energies for the formation of model **6-A**–**6-D** changed depending on ^{A}R and ^{B}R. NBO analysis revealed that the ^{A}E---^{B}E interactions of the CT type are much stronger for **6-1**–**6-4**, relative to the case of model **6-A**–**6-D**, which shed light on the role of the naphthalene 1,8-positions as the spacer. The σ(4c–6e) interactions in **6-1**–**6-4** and model **6-A**–**6-D** can be approximated as the straight line, although that for ^{A}S-∗-^{B}S in model **6-B** (S, S) seem somewhat curved.

The nature of the ^{B}E-∗-^{A}E-∗-^{A}E-∗-^{B}E interactions in **6-1**–**6-4** and models **6-A**–**6-D** are elucidated by applying QTAIM-DFA, where $H_b(\boldsymbol{r}_c)$ are plotted versus $H_b(\boldsymbol{r}_c) - V_b(\boldsymbol{r}_c)/2$ for the interactions in question at BCPs. The nature of the interactions is examined employing QTAIM-DFA parameters of (R, θ) and (θ_p, κ_p). All ^{A}E-∗-^{A}E interactions in **6-1**–**6-4** and models **6-A**–**6-D** are classified by the SS interactions and have the Cov-w nature. On the other hand, the ^{A}E-∗-^{B}E interactions in **6-1**–**6-4** are all classified by the regular CS interactions. The interactions are characterized to have the *typical* HB nature with covalency for **6-1** and **6-2**, whereas they are predicted to have the CT-MC nature for **6-3** and **6-4**. The ^{A}E-∗-^{B}E interactions in models **6-A**–**6-D** are all classified by the *pure* CS interactions. While ^{A}E-∗-^{B}E in model **6-B** are predicted to have the vdW nature, they are characterized as the *typical* HB nature without covalency for models **6-A**, **6-C**, and **6-D**, except for ^{A}Se-∗-^{B}Se in model **6-A** (Se, Se). It is characterized as the vdW nature. The ^{A}E-∗-^{B}E interactions are predicted to be stronger in the order of model **6-B** < model **6-A** << model **6-D** < model **6-C** << **6-1**–**6-4**, judging from the QTAIM-DFA parameters.

Appendix

Table 6-A1. Structural parameters evaluated for **6-1**–**6-4** with MP2/BSS-A and MP2/BS-6-B, together with the observed values for **6-4** and **6-I**.[a,b]

Species (Symmetry)	r_o (^{A}E, ^{A}E) Å	r_o (^{A}E, ^{B}E) Å	Δr_o (^{A}E, ^{B}E)[c] Å
MP2/BSS-A			
6-1 (S, S) (C_1)	2.0559	2.9418	–0.66
6-2 (S, Se) (C_2)	2.0603	3.0255	–0.67
6-3 (Se, S) (C_2)	2.3440	2.9556	–0.74
6-4 (Se, Se) (C_2)	2.3532	3.0353	–0.76
MP2/BSS-B			
6-1 (S, S) (C_1)	2.0937	2.9419	–0.66
6-2 (S, Se) (C_2)	2.0990	3.0293	–0.67
6-3 (Se, S) (C_2)	2.3744	2.9682	–0.73
6-4 (Se, Se) (C_2)	2.3839	3.0540	–0.75
Observed Value			
6-4 (Se, Se)[d]	2.3864(4)	3.030	–0.77
6-I (S, S)	2.055(2)	2.988(2)	–0.61
6-I (S, Se)	2.0706	3.0560[e]	–0.64
6-I (Se, S)	2.3561	2.9809[e]	–0.72

[a] BSS-A: the 6-311+G(3df) basis sets being employed for S and Se with the 6-311G(d) basis sets for C and H. [b] BSS-B: the 6-311+G(3d) basis sets being employed for S and Se with the 6-311G(d) basis sets for C and H. [c] $\Delta r_o(^A\text{E}, ^B\text{E}) = r_o(^A\text{E}, ^B\text{E}) - \Sigma r_{vdW}(^A\text{E}, ^B\text{E})$, where r_{vdW}(S) = 1.80 Å and r_{vdW}(Se) = 1.90 Å (ref. 40 in the text). [d] Prepared and measured in this work. [e] Averaged value.

(Table 6-A1 continued)

Species (symmetry)	$\angle X_1{}^A E^A E$ (°)	$\angle X_8{}^B E C_{11}$ (°)	$\angle {}^B E^A E^A E$ (°)	$\phi_1{}^e$ (°)	$\phi_2{}^f$ (°)
MP2/BSS-A					
6-1 (S, S) (C_1)	104.9	99.6	171.4	83.7	75.5
6-2 (S, Se) (C_2)	104.6	97.0	170.2	85.7	69.9
6-3 (Se, S) (C_2)	101.9	99.4	177.8	83.3	73.7
6-4 (Se, Se) (C_2)	101.6	96.6	176.9	85.1	68.3
MP2/BSS-B					
6-1 (S, S) (C_1)	104.7	99.5	171.7	83.9	74.9
6-2 (S, Se) (C_2)	104.3	96.8	170.5	86.0	69.5
6-3 (Se, S) (C_2)	101.9	99.3	178.0	83.4	73.3
6-4 (Se, Se) (C_2)	101.6	96.5	177.1	84.9	67.9
Observed Value					
6-4 (Se, Se)[d]	102.64(6)	96.98(9)[g]	173.3	79.1	78.7[e]
6-I (S, S)	104.9[e]	102.8[e,h]	167.3 [i]	–89.0	76.4[e,i]
6-I (S, Se)	104.2 [e]	99.2[e,h]	168.1 [i]	–81.3	70.8 [e,i]
6-I (Se, S)	101.8 [e]	102.3 [e,h]	174.4[i]	–91.5	76.6 [e,i]

[f] $\phi_1 = \phi(C_1{}^A E^A EC_{1'})$. [g] $\phi_2 = \phi(C_9C_8{}^B EC_{11})$. [h] $\angle C_8{}^B EC_i$. [i] $\phi_2 = \phi(C_9C_8{}^B EC_i)$.

Table 6-A2 Structural parameters evaluated for models **6-A**–**6-D** with MP2/BSS-C.[a]

Species (symmetry)	$r_o(^AE, ^AE)$ (Å)	$r_o(^AE, ^BE)$ (Å)	$\Delta r_o(^AE, ^BE)$[b] (Å)	$\angle A^BE^AE^A$[c] (º)	$\angle ^BE^AE^AE$ (º)
model **6-A** (C_2)					
6-A (S, S) (C_2)	2.0590	3.5251	–0.07	74.2	167.9
6-A (S, Se) (C_2)	2.0601	3.6334	–0.07	74.1	167.9
6-A (Se, S) (C_2)	2.3408	3.5791	–0.12	80.7	169.2
6-A (Se, Se) (C_2)	2.3425	3.6894	–0.11	80.7	169.0
model **6-B** (C_2)					
6-B (S, S) (C_2)	2.0332	3.6907	0.09	55.1	171.0
6-B (S, Se) (C_2)	2.0336	3.7981	0.10	54.7	170.6
6-B (Se, S) (C_2)	2.3004	3.7302	0.03	60.6	176.1
6-B (Se, Se) (C_2)	2.3011	3.8281	0.03	58.5	175.7
model **6-C** (C_2)					
6-C (S, S) (C_2)	2.0695	3.2537	–0.35	85.4	173.7
6-C (S, Se) (C_2)	2.0720	3.3302	–0.37	83.7	175.5
6-C (Se, S) (C_2)	2.3412	3.2707	–0.43	87.9	174.4
6-C (Se, Se) (C_2)	2.3444	3.3654	–0.43	86.9	172.0
model **6-D** (C_2)					
6-D (S, S) (C_2)	2.0407	3.4434	–0.16	83.6	167.0
6-D (S, Se) (C_2)	2.0416	3.5215	–0.18	80.2	167.0
6-D (Se, S) (C_2)	2.3123	3.4081	–0.29	87.0	169.5
6-D (Se, Se) (C_2)	2.3127	3.5190	–0.28	82.5	164.4

[a] BSS-C: the 6-311+G(3df) basis sets being employed for S and Se with the 6-311G(d,p) basis sets for C and H. [b] $\Delta r_o(^AE, ^BE) = r_o(^AE, ^BE) - \Sigma r_{vdW}(^AE, ^BE)$, where r_{vdW}(S) = 1.80 Å and r_{vdW}(Se) = 1.90 Å.[37] [c] A = H or C_{Me}.

(Table 6-A2 continued)

Species (symmetry)	ϕ_1[d] (°)	ϕ_2[d] (°)	ΔE_{ES} (kJ mol^{-1})	ΔE_{ZP} (kJ mol^{-1})
model **6-A** (C_2)				
6-A (S, S) (C_2)	–90.5	–128.8	–21.7	–15.9
6-A (S, Se) (C_2)	–90.5	–129.4	–21.3	–16.1
6-A (Se, S) (C_2)	–90.3	–131.3	–21.6	–16.4
6-A (Se, Se) (C_2)	–90.3	–131.8	–21.3	–16.6
model **6-B** (C_2)				
6-B (S, S) (C_2)	–84.7	–116.9	–24.2	–18.4
6-B (S, Se) (C_2)	–84.8	–116.5	–24.4	–19.4
6-B (Se, S) (C_2)	–85.4	–122.1	–25.0	–19.2
6-B (Se, Se) (C_2)	–85.4	–120.9	–25.5	–20.6
model **6-C** (C_2)				
6-C (S, S) (C_2)	–90.5	–118.3	–41.4	–36.7
6-C (S, Se) (C_2)	–90.4	–130.8	–43.2	–39.0
6-C (Se, S) (C_2)	–90.4	–120.4	–45.0	–41.0
6-C (Se, Se) (C_2)	–90.4	–103.6	–46.2	–42.4
model **6-D** (C_2)				
6-D (S, S) (C_2)	–84.4	–107.4	–41.6	–37.8
6-D (S, Se) (C_2)	–84.4	–114.7	–43.4	–39.9
6-D (Se, S) (C_2)	–84.9	–94.7	–46.5	–42.9
6-D (Se, Se) (C_2)	–84.6	–82.6	–48.2	–45.0

[d] $\phi_2 = \phi$(H^{B}E^{A}EH, H^{B}E^{A}EC$_{Me}$, C$_{Me}$^{B}E^{A}EH, or C$_{Me}$^{B}E^{A}EC$_{Me}$).

Table 6-A3. Results of NBO analysis for the ^{A}E---^{B}E interactions in **6-1**–**6-4** with M06-2X/BSS-A//MP2/BSS-A and models **6-A**–**6-D** with MP2/BSS-C//MP2/BSS-C.[a]

Compound (^{A}E, ^{B}X)	$E(2)^{b,c}$ ([e])	$E(2)^{b,c}$ ([f])	$[E(i) - E(j)]^{d}$ (au)	$F(i,j)^{e}$ (au)
calculated/BSS-A				
6-1 (S, S) (C_1)	8.83	36.9	0.40	0.053
6-2 (S, Se) (C_2)	9.40	39.3	0.38	0.054
6-3 (Se, S) (C_2)	15.19	63.6	0.35	0.066
6-4 (Se, Se) (C_2)	16.97	71.0	0.33	0.067
model **6-A**				
6-A (S, S) (C_2)	1.88	7.9	0.43	0.025
6-A (S, Se) (C_2)	1.96	8.2	0.41	0.025
6-A (Se, S) (C_2)	2.99	12.5	0.37	0.030
6-A (Se, Se) (C_2)	3.12	13.1	0.36	0.030
model **6-B**				
6-B (S, S) (C_2)	0.52	2.2	0.45	0.014
6-B (S, Se) (C_2)	0.51	2.1	0.44	0.013
6-B (Se, S) (C_2)	2.22	9.3	0.43	0.028
6-B (Se, Se) (C_2)	2.67	11.2	0.40	0.029
model **6-C**				
6-C (S, S) (C_2)	4.30	18.0	0.39	0.037
6-C (S, Se) (C_2)	5.01	21.0	0.38	0.039
6-C (Se, S) (C_2)	6.73	28.2	0.34	0.043
6-C (Se, Se) (C_2)	7.32	30.6	0.33	0.044
model **6-D**				
6-D (S, S) (C_2)	1.88	7.9	0.41	0.025
6-D (S, Se) (C_2)	2.15	9.0	0.39	0.026
6-D (Se, S) (C_2)	3.68	15.4	0.36	0.032
6-D (Se, Se) (C_2)	3.61	15.1	0.34	0.031

[a] M06-2X/BSS-A//MP2/BSS-A was applied to **6-1**–**6-4**, since the calculations stopped before the end of the evaluations, if MP/BSS-A//MP2/BSS-A was employed. [b] Second-order perturbation energy. [c] Only one side of energy is shown. [d] Donor orbital of NBO(i) is $n_p(^{A}E)$ and acceptor orbital of NBO (j) corresponds to $\sigma^*(^{A}E–^{A}E)$. [e] Fock matrix. [f] In kcal mol^{-1}. [g] In kJ mol^{-1}.

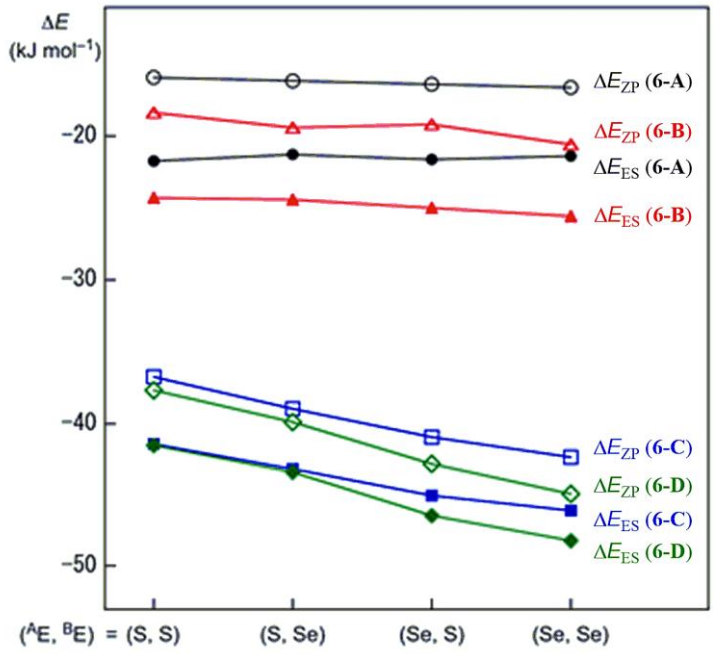

Figure 6-A1. Plots of ΔE_{ES} and ΔE_{ZP} for models **6-A**–**6-D**.

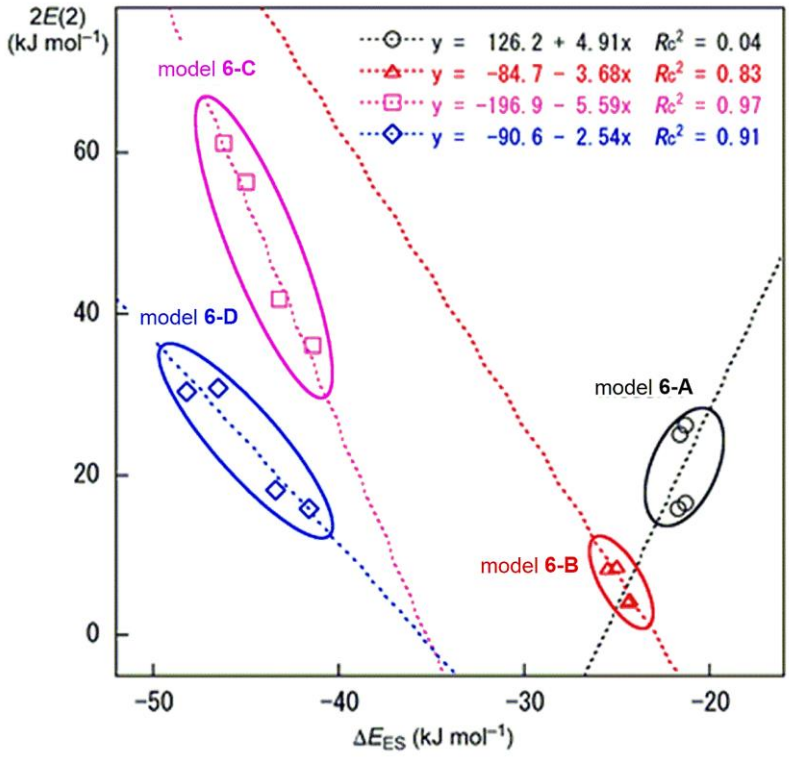

Figure 6-A2. Plots of ΔE_{ES} and ΔE_{ZP} for models **6-A**–**6-D**.

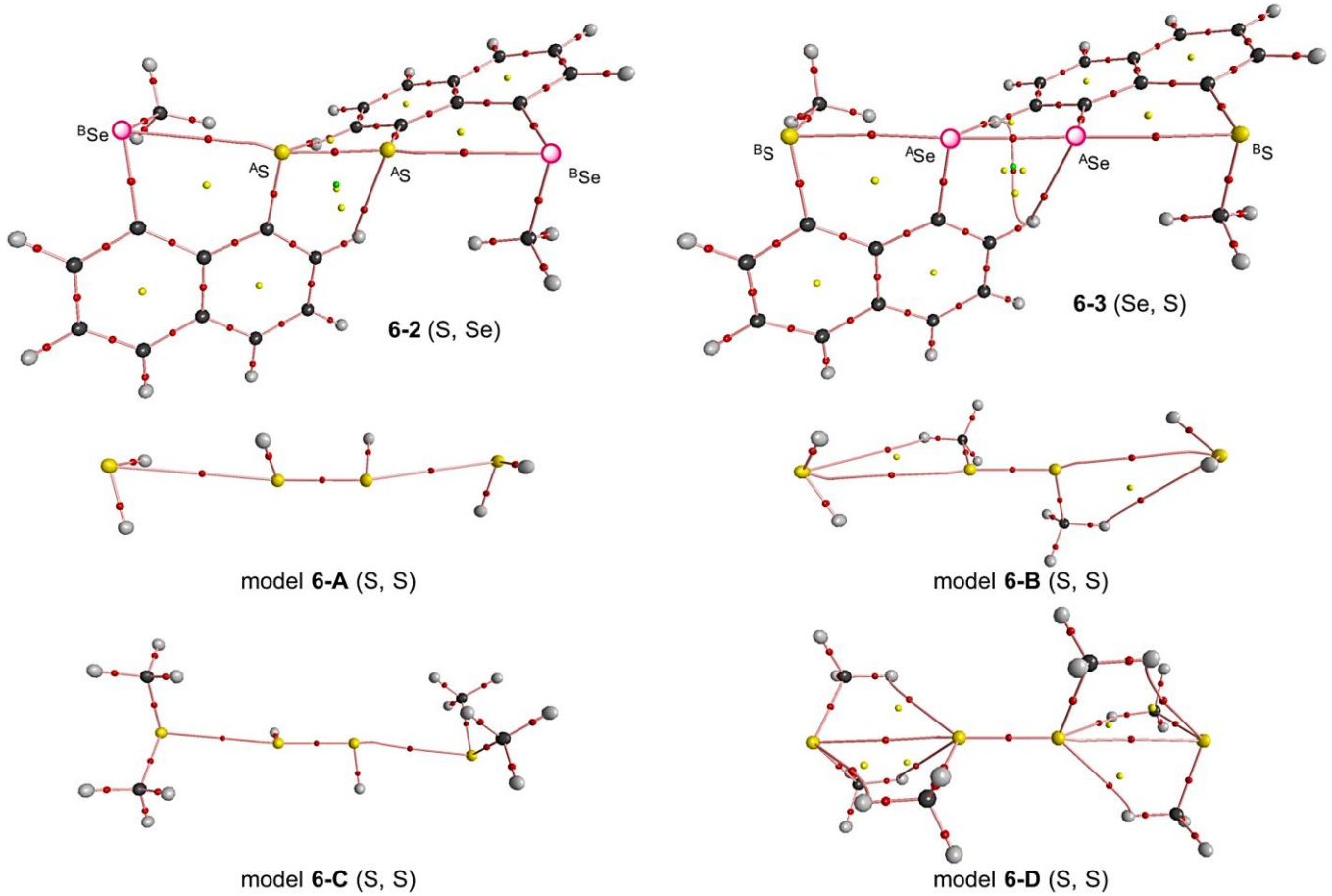

Figure 6-A3. Molecular graphs for **6-2**, **6-3**, and models **6-A** (S, S)–**6-D** (S, S), evaluated with MP2/6-311G(3d). BCPs are shown by red dots, RCPs by yellow dots, and CCPs by green dots, together with BPs by pink lines. Carbon atoms are drawn in black, hydrogen atoms in gray, sulfur atoms in yellow, and selenium atoms in pink.

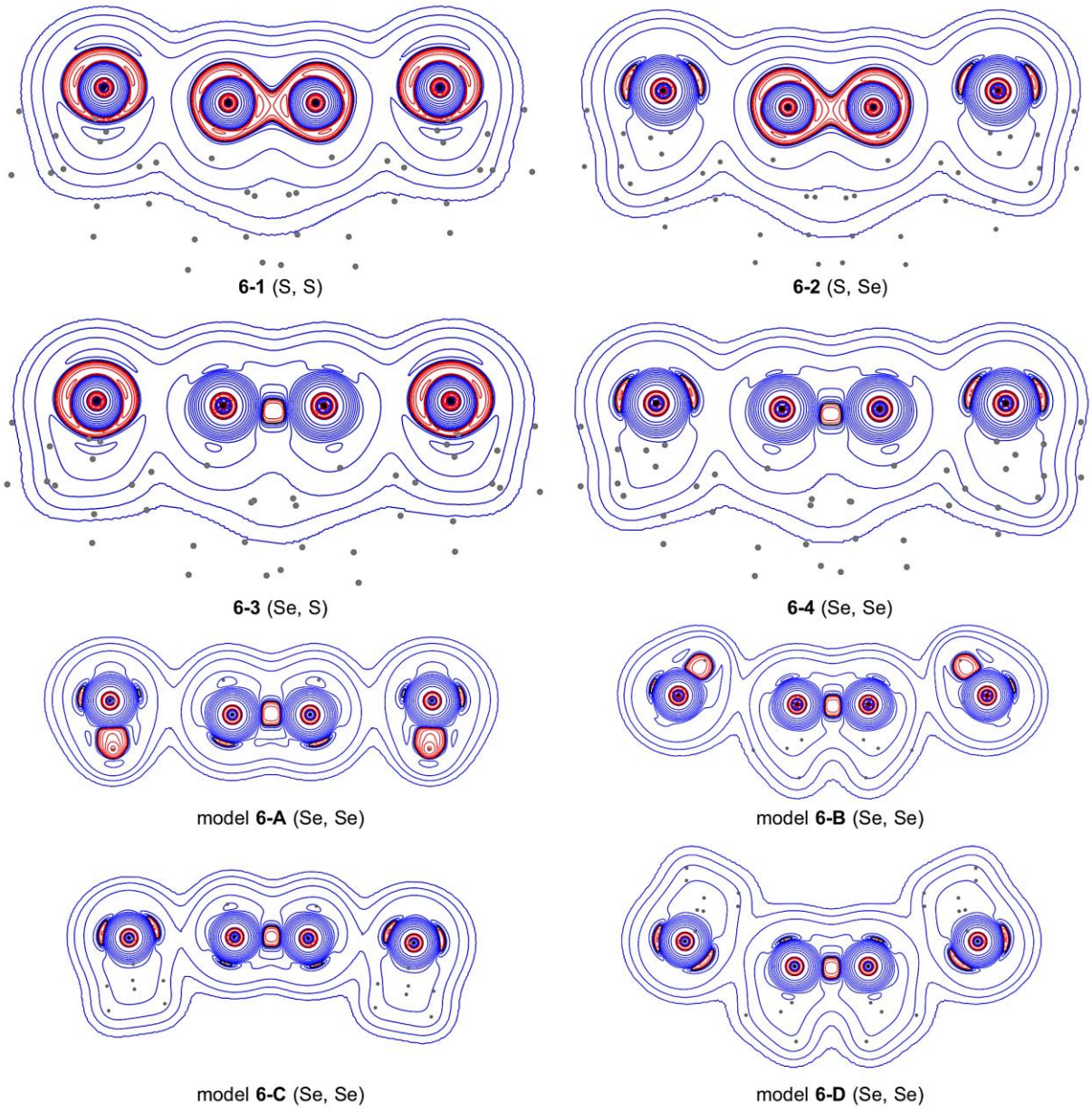

Figure 6-A4. Negative Laplacians for **6-1**–**6-4** and models **6-A** (Se, Se)– **6-D** (Se, Se) drawn with MP2/6-311G(d), similarly to the case of Figure 6-4 in the text. Blue and red lines correspond to the positive and negative values, respectively.

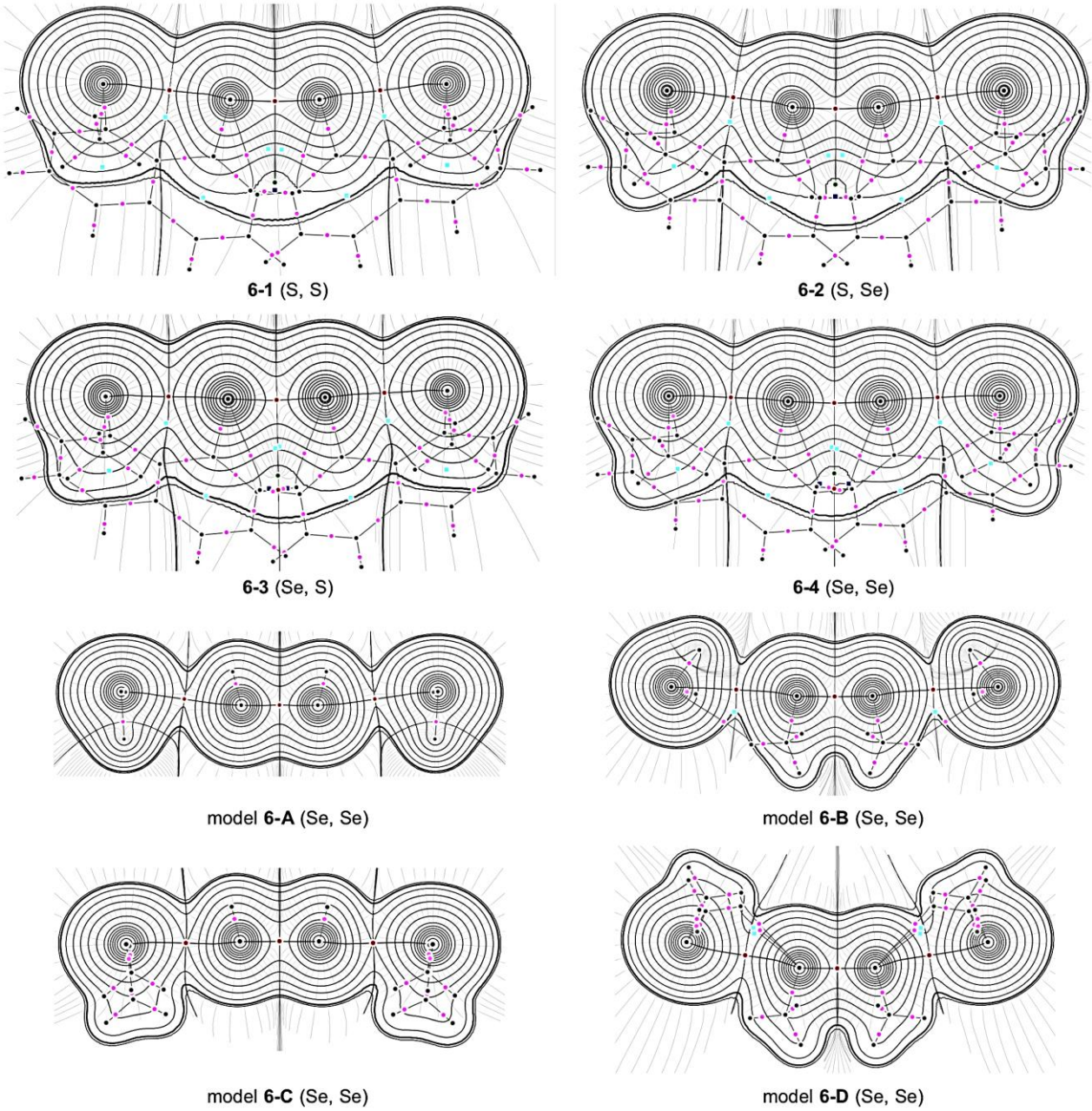

Figure 6-A5. Trajectory plots for **6-1**–**6-4** and models **6-A**–**6-D** (Se, Se) drawn with MP2/6-311G(d), similarly to the case of Figure 6-4 in the text. Colors and marks are the same as those in Figure 6-4.

Table 6-A4. r_{BP} and R_{SL} values for the ^{B}E ---^{A}E–^{A}E---^{B}E interactions in compounds **6-1**–**6-4** with MP2/BSS-A and models of **6-A**–**6-D** with MP2/BSS-C.[a]

Species (^{A}E, ^{B}E)	R_{SL}(^{B}E, ^{A}E) (Å)	R_{SL}(^{A}E, $^{A'}E$) (Å)	r_{BP}(^{B}E, ^{A}E) (Å)	r_{BP}(^{A}E, $^{A'}E$) (Å)	Δr_{BP}(^{B}E, ^{A}E)[b] (Å)	Δr_{BP}(^{A}E, $^{A'}E$)[c] (Å)
Calculated MP2/BSS-A						
6-1 (S, S) (C_1)	2.9418	2.0559	2.9577	2.0576	0.0159	0.0017
6-2 (S, Se) (C_2)	3.0255	2.0603	3.0396	2.0621	0.0141	0.0018
6-3 (Se, S) (C_2)	2.9556	2.3440	2.9625	2.3457	0.0069	0.0017
6-4 (Se, Se) (C_2)	3.0353	2.3532	3.0408	2.3549	0.0055	0.0017
model **6-A**						
6-A (S, S) (C_2)	3.5251	2.0590	3.5357	2.0607	0.0106	0.0017
6-A (S, Se) (C_2)	3.6334	2.0601	3.6404	2.0618	0.0070	0.0017
6-A (Se, S) (C_2)	3.5791	2.3408	3.5880	2.3415	0.0089	0.0007
6-A (Se, Se) (C_2)	3.6894	2.3425	3.6949	2.3432	0.0055	0.0007
model **6-B**						
6-B (S, S) (C_2)	3.6907	2.0332	3.7386	2.0342	0.0479	0.0010
6-B (S, Se) (C_2)	3.7981	2.0336	3.8191	2.0347	0.0210	0.0011
6-B (Se, S) (C_2)	3.7302	2.3004	3.7388	2.3009	0.0086	0.0005
6-B (Se, Se) (C_2)	3.8281	2.3011	3.8356	2.3015	0.0075	0.0004
model **6-C**						
6-C (S, S) (C_2)	3.2537	2.0695	3.2705	2.0712	0.0168	0.0017
6-C (S, Se) (C_2)	3.3302	2.0720	3.3448	2.0737	0.0146	0.0017
6-C (Se, S) (C_2)	3.2707	2.3412	3.2788	2.3418	0.0081	0.0006
6-C (Se, Se) (C_2)	3.3654	2.3444	3.3719	2.3450	0.0065	0.0006
model **6-D**						
6-D (S, S) (C_2)	3.4434	2.0407	3.4649	2.0418	0.0215	0.0011
6-D (S, Se) (C_2)	3.5215	2.0416	3.5391	2.0427	0.0176	0.0011
6-D (Se, S) (C_2)	3.4081	2.3123	3.4192	2.3127	0.0111	0.0004
6-D (Se, Se) (C_2)	3.5190	2.3127	3.5286	2.3132	0.0096	0.0005

[a] BSS-A: the 6-311+G(3df) basis sets being employed for S and Se with the 6-311G(d) basis sets for C and H. BSS-C: the 6-311+G(3df) basis sets being employed for S and Se with the 6-311G(d,p) basis sets for C and H. [b] $\Delta r_{BP}(^{8}X, ^{1}E) = r_{BP}(^{8}X, ^{1}E) - R_{SL}(^{8}X, ^{1}E)$. [c] $\Delta r_{BP}(^{1}E, ^{1'}E) = r_{BP}(^{1}E, ^{1'}E) - R_{SL}(^{1}E, ^{1'}E)$.

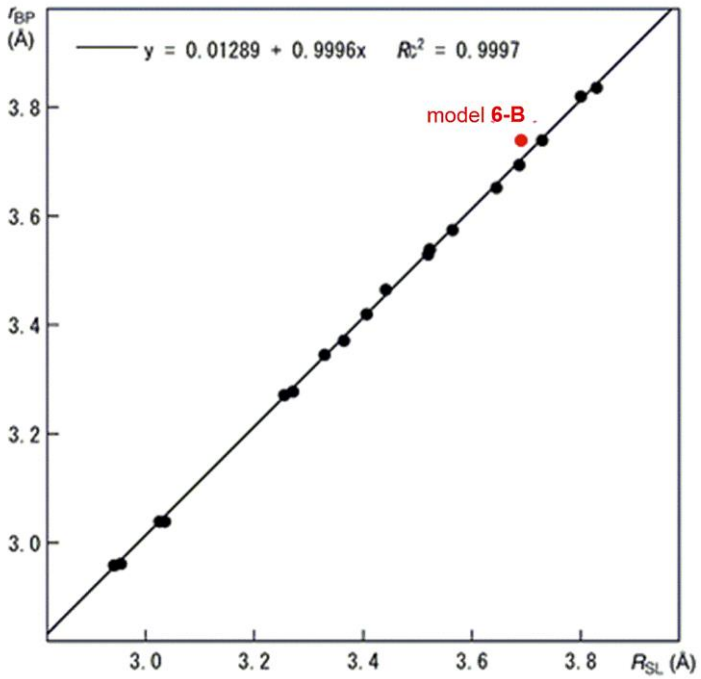

Figure 6-A6. Plot of r_{BP} versus R_{SL} for the interactions in models **6-A**–**6-D**. Correlation is very good, which are shown in the figure.

References

1 a) G. C. Pimentel, *J. Chem. Phys.* **1951**, *19*, 446–448; b) J. I. Musher, *Angew. Chem. Int. Ed. Engl.* **1969**, *8*, 54–68.

2 a) W. Nakanishi, S. Hayashi, S. Toyota, *Chem. Commun.* **1996**, 371–372; b) W. Nakanishi, S. Hayashi, S. Toyota, *J. Org. Chem.* **1998**, *63*, 8790–8800.

3 W. Nakanishi, S. Hayashi, T. Arai, *Chem. Commun.* **2002**, 2416–2417.

4 W. Nakanishi, S. Hayashi, S. Morinaka, T. Sasamori, N. Tokitoh, *New J. Chem.* **2008**, *32*, 1881–1889.

5 a) W. Nakanishi, S. Hayashi, N. Itoh, *Chem. Commun.* **2003**, 124–125; b) W. Nakanishi, S. Hayashi, N. Itoh, *J. Org. Chem.* **2004**, *69*, 1676–1684; c) W. Nakanishi, S. Hayashi, S. Yamaguchi, K. Tamao, *Chem. Commun.* **2004**, 140–141.

6 a) W. Nakanishi, *Hypervalent Chalcogen Compounds*. In *Handbook of Chalcogen Chemistry: New Perspectives in Sulfur, Selenium and Tellurium*; ed. F. A. Devillanova, Royal Society of Chemistry: London, **2006**; Chapter 10.3, pp. 644–668; b) W. Nakanishi, S. Hayashi, In *Handbook of Chalcogen Chemistry: New Perspectives in Sulfur, Selenium and Tellurium, 2nd ed.* eds. F. A. Devillanova, W.-W. du Mont, Royal Society of Chemistry: Cambridge, U.K., **2013**; Vol. 2, Chapter 12.3, pp. 335−372; c) W. Nakanishi, S. Hayashi, M. Hashimoto, M. Arca, M. C. Aragoni, V. Lippolis, In *The Chemistry of Organic Selenium and Tellurium Compounds* ed. Z. Rappoport, Wiley, New York, **2013**, Vol. 4, Chapter 11, pp. 885–972.

7 a) G. E. Garrett, G. L. Gibson, R. N. Straus, D. S. Seferos, M. S. Taylor, *J. Am. Chem. Soc.* **2015**, *137*, 4126–4133; b) M. E. Brezgunova, J. Lieffrig, E. Aubert, S. Dahaoui, P. Fertey, S. Lebègue, J. A. Ángyán, M. Fourmigué, E. Espinosa, *Cryst. Growth Des.* **2013**, *13*, 3283−3289; c) F. T. Burling, B. M. Goldstein, *J. Am. Chem. Soc.* **1992**, *114*, 2313−2320; d) Y. Nagao, T. Hirata, S. Goto, S. Sano, A. Kakehi, K. Iizuka, M. Shiro, *J. Am. Chem. Soc.* **1998**, *120*, 3104−3110; e) A. F. Cozzolino, P. J. W. Elder, I. Vargas-Baca, *Coord. Chem. Rev.* **2011**, *255*, 1426−1438; f) H. Zhao, F. Gabbaï, *Nat. Chem.* **2010**, *2*, 984−990; g) W. Wang, B. Ji, Y. Zhang, *J. Phys. Chem. A* **2009**, *113*, 8132–8135.

8 *The Chemistry of Organic Selenium and Tellurium Compounds*, ed. Z. Rappoport, Wiley, New York, **2013**, Vol. 4, Chapters 13–16, pp. 989–1236.

9 a) G. Mugesh, A. Panda, H. B. Singh, N. S. Punekar, R. J. Butcher, *Chem. Commun.* **1998**, 2227–2228; b) G. Mugesh, A. Panda, H. B. Singh, N. S. Punekar, R. J. Butcher, *J. Am. Chem. Soc.* **2001**, *123*, 839–850; c) G. Mugesh, A. Panda, S. Kumar, S. Apte, H. B. Singh, R. J. Butcher, *Organometallics,* **2002**, *21*, 884–892; d) S. Kumar, K. Kandasamy, H. B. Singh, R. J. Butcher, *New J. Chem.*, **2004**, *28*, 640–645; e) S. C. Menon, H. B. Singh, J. M. Jasinski, J. P. Jasinski, R.

J. Butcher, *Organometallics*, **1996**, *15*, 1707–1712; f) J. E. Drake, M. B. Hursthouse, M. Kulcsar, M. E. Light, A. Silvestru, Phosphorus, *Sulfur Silicon Relat. Elem.* **2001**, *169*, 293–296; g) J. E. Drake, M. B. Hursthouse, M. Kulcsar, M. E. Light, A. Silvestru, *J. Organomet. Chem.* **2001**, *623*, 153–160; h) J. R. Anacona, J. Gomez, D. Lorono, *Acta Crystallogr., Sect. C*, **2003**, *59*, o277–o280; i) G. Mugesh, H. B. Singh, R. J. Butcher, *Eur. J. Inorg. Chem.* **1999**, 1229–1236; j) G. Mugesh, H. B. Singh, R. J. Butcher, *J. Organomet. Chem.* **1999**, *577*, 243–248; k) D. Shimizu, N. Takeda, N. Tokitoh, *Chem. Commun.* **2006**, 177–178.

10 a) R.-F. Hu, Y.-H. Wen, J. Zhang, Z.-J. Li, Y.-G. Yao, *Acta Crystallogr. Sect. E: Struct. Rep. Online* **2004**, *60*, o2029–o2031; b) S. Wang, H. Mao-Lin, F. Chen, *Acta Crystallogr. Sect. E: Struct. Rep. Online* **2004**, *60*, m413–m415; c) X.-J. Wang, Z.-F. Chen, B.-S. Kang, H. Liang, H.-Q. Liu, K.-B. Yu, C.-Y. Su, Z.-N. Chen, *Polyhedron.* **1999**, *18*, 647–655.

11 *a*) J. R. Anacona, J. Gomez, D. Lorono, *Acta Crystallogr., Sect. C: Cryst. Struct. Commun.* **2003**, *59*, o277–o280; (*b*) T. C. W. Mak, W.-H. Yip, W.-H. Chan, G. Smith, C. H. L. Kennard, *Aust. J. Chem.*, **1989**, *42*, 1403–1406.

12 Dots are usually employed to show BCPs in molecular graphs. Therefore, A-•-B would be more suitable to describe BP with BCP. Nevertheless, A-∗-B is employed in our case.

13 ^{77}Se NMR spectra were analyzed for Se_4 σ(4c–6e) in **6-I** (^{A}E, ^{B}E) = (Se, Se) and the derivatives substituted at the *p,p'*-positions of both phenyl groups. The spectrum of **6-4** (Se, Se) is well explained based on the results. See, S. Hayashi, W. Nakanishi, *J. Org. Chem.*, **1999**, *64*, 6689–6696.

14 Bruker-Nonius. APEX v2.1, SAINT v7, and XPREP v6.14 (Bruker AXS Madison, **2003**).

15 G. M. Sheldrick, SADABS: Empirical Absorption and Correction Software (University of Göttingen, 1999–2006).

16 a) G. M. Sheldrick, SHELXS-97: Program for the Solution of Crystal Structures, (University of Göttingen, **1997**); b) G. M. Sheldrick, SHELXL-97: Programs for Crystal Structure Analysis (University of Göttingen, 1997).

17 *Gaussian 09 (Revision D.01)*, M. J. Frisch, G. W. Trucks, H. B. Schlegel, G. E. Scuseria, M. A. Robb, J. R. Cheeseman, G. Scalmani, V. Barone, B. Mennucci, G. A. Petersson, H. Nakatsuji, M. Caricato, X. Li, H. P. Hratchian, A. F. Izmaylov, J. Bloino, G. Zheng, J. L. Sonnenberg, M. Hada, M. Ehara, K. Toyota, R. Fukuda, J. Hasegawa, M. Ishida, T. Nakajima, Y. Honda, O. Kitao, H. Nakai, T. Vreven, J. A. Montgomery, Jr., J. E. Peralta, F. Ogliaro, M. Bearpark, J. J. Heyd, E. Brothers, K. N. Kudin, V. N. Staroverov, R. Kobayashi, J. Normand, K. Raghavachari, A. Rendell, J. C. Burant, S. S. Iyengar, J. Tomasi, M. Cossi, N. Rega, J. M. Millam, M. Klene, J. E. Knox, J. B. Cross, V. Bakken, C. Adamo, J. Jaramillo, R. Gomperts, R. E. Stratmann, O. Yazyev, A. J.

Austin, R. Cammi, C. Pomelli, J. W. Ochterski, R. L. Martin, K. Morokuma, V. G. Zakrzewski, G. A. Voth, P. Salvador, J. J. Dannenberg, S. Dapprich, A. D. Daniels, Ö. Farkas, J. B. Foresman, J. V. Ortiz, J. Cioslowski, D. J. Fox, Gaussian, Inc.: Wallingford CT, **2009**.

18 For the 6-311G basis sets, see: a) R. C. Binning Jr., L. A. Curtiss, *J. Comput. Chem.* **1990**, *11*, 1206–1216; b) L. A. Curtiss, M. P. McGrath, J.-P. Blaudeau, N. E. Davis, R. C. Binning Jr., L. Radom, *J. Chem. Phys.* **1995**, *103*, 6104–6113; c) M. P. McGrath, L. Radom, *J. Chem. Phys.* **1991**, *94*, 511–516. For the diffuse functions (+ and ++), see: T. Clark, J. Chandrasekhar, G. W. Spitznagel, P. v. R. Schleyer, *J. Comput. Chem.* **1983**, *4*, 294–301.

19 a) C. Møller, M. S. Plesset, *Phys. Rev.* **1934**, *46*, 618–622; b) J. Gauss, *J. Chem. Phys.* **1993**, *99*, 3629–3643; c) J. Gauss, *Ber. Bunsen-Ges. Phys. Chem.* **1995**, *99*, 1001–1008.

20 Y. Zhao, D. G. Truhlar, *Theor. Chem. Acc.* **2008**, *120*, 215−241.

21 The AIM2000 program (Version 2.0) is employed to analyze and visualize atoms-in-molecules: F. Biegler-König, *J. Comput. Chem.* **2000**, *21*, 1040–1048. See also ref. 14b.

22 A. Bondi, *J. Phys. Chem.* **1964**, *68*, 441–451.

23 a) J. P. Foster, F. Weinhold, *J. Am. Chem. Soc.* **1980**, *102*, 7211–7218; b) A. E. Reed, F. Weinhold, *J. Chem. Phys.*, **1983**, *78*, 4066–4073; c) A. E. Reed, R. B. Weinstock, F. Weinhold, *J. Chem. Phys.*, **1985**, 83, 735–746; d) A. E. Reed, F. Weinhold, *J. Chem. Phys.* **1985**, *83*, 1736–1740; e) J. E. Carpenter, F. Weinhold, *J. Mol. Struct. (Theochem)*, **1988**, *46*, 41–62; f) A. E. Reed, L. A. Curtiss, F. Weinhold, *Chem. Rev.* **1988**, *88*, 899–926.

24 a) F. Weinhold, C. R. Landis, *Chemistry Education: Research and Practice in Europe*, **2001**, *2*, 91–104; b) F. Weinhold, C. R. Landis, *Discovering Chemistry with Natural Bond Orbitals*, Wiley, **2012**; c) F. Weinhold, C. R. Landis, *Valency and Bonding: A Natural Bond Orbital Donor-Acceptor Perspective*, CUP, **2005**.

Chapter 7

High-Resolution X-ray Diffraction Determination of Electron Densities of 1-(8-PhSC$_{10}$H$_6$)SS(C$_{10}$H$_6$SPh-8')-1' with QTAIM Approach: Evidence for S$_4$ σ(4c–6e) at Naphthalene *Peri*-Positions

Abstract

An extended hypervalent S$_4$ σ(4c–6e) system is confirmed for the linear ^{B}S-∗-^{A}S-∗-^{A}S-∗-^{B}S interaction in 1-(8-Ph^{B}SC$_{10}$H$_6$)^{A}S–^{A}S(C$_{10}$H$_6$^{B}SPh-8')-1' (**7-1**) by high-resolution X-ray diffraction determination of electron densities. The presence of bond critical points (BCPs; ∗) on the bond paths confirms the nature and extent of the interaction. The recently developed QTAIM dual functional analysis (QTAIM-DFA) approach is also applied to elucidate the nature of the interaction. Total electron energy densities $H_b(\boldsymbol{r}_c)$ are plotted versus $H_b(\boldsymbol{r}_c) - V_b(\boldsymbol{r}_c)/2$ for the interaction at the BCPs [where $V_b(\boldsymbol{r}_c)$ is the potential energy densities at the BCP]. While data for an interaction in the fully optimized structure correspond to the static nature, those in the perturbed structures around it represent the dynamic nature of the interaction, in QTAIM-DFA. The former classifies the interaction and the latter characterises it. While ^{A}S-∗-^{A}S in **7-1** is classified by a shared shell interaction and exhibits weak covalent character, ^{A}S-∗-^{B}S is characterized as having *typical* hydrogen bond nature with covalency properties in the region of the *regular* closed shell interactions. Experimental results are supported by matching theoretical calculations throughout, particularly for the extended hypervalent ^{A}E$_2$^{B}E$_2$ σ(4c–6e) (E = S) interaction.

Introduction

He discussed about the background, importance and theoretical nature of σ(4c–6e) in Chapters 5 and 6.

The question arises as to how the nature of $^{A}E_2{}^{B}E_2$ σ(4c–6e) can be established experimentally. $^{A}E_2{}^{B}E_2$ σ(4c–6e) was first recognized for the linear alignments of four ^{B}E---^{A}E–$^{A'}E$---$^{B'}E$ atoms in the structures of bis[8-(phenylchalcogena)naphthyl]-1,1'-dichalcogenide, 1-(8-Ph$^{B}EC_{10}H_6$)-^{A}E–^{A}E($C_{10}H_6{}^{B'}$EPh-8')-1' [(^{A}E, ^{B}E) = (S, S: **7-1**),[1] (S, Se: **7-2**),[2] (Se, S: **7-3**)[2], and (Se, Se: **7-4**)[3]], determined by the X-ray crystallographic analysis. (See Figure 7-1 for the structure of **7-1** (S, S), determined by the high-resolution X-ray crystallographic analysis.) Chart 7-1 illustrates the structures of **7-1**–**7-4**.

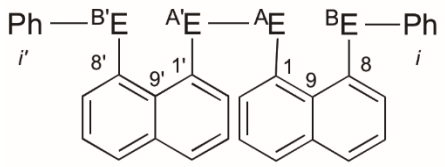

(^{A}E, ^{B}E) = **7-1** (S, S), **7-2** (S, Se)
7-3 (Se, S), **7-4** (Se, Se)

Chart 7-1. Graphical representation of **7-1**–**7-4**.

The high-resolution X-ray diffraction determination of electron densities of **7-1** (S, S) would provide a firm basis for the real existence of S_4 σ(4c–6e) in **7-1** (S, S). The quantum theory of atoms-in-molecules dual functional analysis (QTAIM-DFA), which we proposed recently,[4–8] will support the experimental results by elucidating the dynamic and static nature of S_4 σ(4c–6e) from the observed and/or optimized structures of **7-1** (S, S). It will be easily understood if the interactions can be defined by the corresponding bond paths (BPs) in QTAIM, but we must be careful to use the correct terminology with the concept.[9] A basis set system that reproduces the observed structural parameters, particularly for the ^{A}E---^{B}E distances, r(^{A}E---^{B}E), must be established.

This chapter is therefore concerned with the observation of the existence of S_4 σ(4c–6e) in **7-1** (S, S) based on the data obtained from high-resolution X-ray diffraction determination of electron densities. The real existence of S_4 σ(4c–6e) in **7-1** (S, S) is confirmed by theoretically elucidating the nature of S_4 σ(4c–6e) with QTAIM-DFA. QTAIM-DFA and the criteria are explained in the Chapter 2, employing Schemes 2-1 and 2-2, Figure 2-1, and eqs (2-1)–(2-7).

Experimental

Bis[8-(phenylthio)naphthyl]-1,1'-disulfide (7-1 (S, S))

7-1 (S, S) was obtained in the reaction of the naphtho[1,8-*c*,*d*]-1,2-dithiolate dianion[10] with excess benzenediazonium chloride in aqueous THF at 2–4 °C. After a usual workup, the solution was chromatographed on silica gel containing acidic alumina. Recrystallization from the solvent mixed with hexane and dichloromethane gave **7-1** (S, S) as yellow prisms in 68% yield, mp 169.8–170.6 °C. ^{1}H NMR ($CDCl_3$/TMS, 400 MHz) δ 7.02 (dd, J = 1.2 and 8.3 Hz, 4H), 7.12 (t, J = 7.7 Hz, 4H), 7.21 (t, J = 7.3 Hz, 4H), 7.45 (t, J = 7.6 Hz, 2H), 7.63 (dd, J = 1.0 and 8.1 Hz, 2H), 7.68 (dd, J = 1.1 and 7.6 Hz, 2H), 7.85 (dd, J = 1.4 and 7.2 Hz, 2H), 7.90 (dd, J = 1.3 and 8.2 Hz, 2H); ^{13}C NMR ($CDCl_3$/TMS, 75.5 MHz) δ 125.5, 125.8, 125.8, 126.2, 127.1, 127.4, 128.4, 128.9, 131.4, 133.8, 134.5, 136.4, 138.5 and 139.9. Anal. Calcd for $C_{32}H_{22}S_4$: C, 71.87; H, 4.15. Found: C, 71.58 H, 4.24.

High-resolution X-ray crystallographic measurement of 7-1 (S, S)

The single crystal high-resolution data ($\sin(\theta/\lambda_{max})$ = 1.08 Å^{-1}) were collected at 100(2) K on a Rigaku FRE+ equipped with VHF *Varimax* confocal mirrors, an AFC10 goniometer and an HG Saturn724+ detector using Mo-Kα radiation (λ = 0.71075 Å). Crystal Clear 3.1 software[11] was used for data collection and CrysAlisPro[12] for data reduction and Gaussian absorption correction. SORTAV[13] was used to average and merge the sets of intensities.

The crystal structure was resolved using direct methods, and a least-squares independent atom refinement (IAM) was carried out with the SHELXL-2014[14] software package. All the non-hydrogen atoms were refined with anisotropic displacement parameters, whereas all hydrogen atoms were calculated at theoretical positions with U_{iso} = 1.2 (See Figure 7-1 for the crystal structure of **7-1** (S, S) and the crystal data and refinement detailed in Table 7-A1 in the Appendix) This model served as the initial point for the aspherical atom refinement, using Hansen–Coppens formalism[15] as implemented in the XD2016 program.[16] According to this formalism, electron density in a crystal is divided into three components, as expressed in eq (7-1):

$$\rho(\mathbf{r}) = P_c\rho_{core}(\mathbf{r}) + P_v\kappa^3\rho_{valence}(\kappa r) + \sum_{l=0}^{l_{max}} \kappa'^3 R_l(\kappa'_l r) \sum_{m=0}^{l} P_{lm\pm} d_{lm\pm} \quad (7\text{-}1)$$

where the first term is a spherically averaged free-atom Hartree–Fock core contribution ρ_{core} with

population parameter P_c; the second term is a spherically averaged free atom Hartree–Fock normalized to one electron valence contribution $\rho_{valence}$ with population parameter P_v, modified by the expansion/contraction parameter κ. The third term represents the deviation of the valence density from spherical symmetry modified by the expansion/contraction parameter κ'. The deformation is expressed by a density normalized Slater-type radial function $R_l(\kappa'_l r)$ modulated by the density normalized, real spherical harmonics angular functions $d_{lm\pm}(\mathbf{r}/r)$ defined on local axes centered on the atoms and population parameters $P_{lm\pm}$.

$$R_I(\kappa'_I r) = (\kappa'_I a_I)^3 \frac{(\kappa'_I \alpha_I r)^{n(l)}}{n(l)+2} \exp(\kappa'_I a_I r) \quad (7\text{-}2)$$

$R_l(\kappa'_l r)$ is given by eq (7-2), where $n(l) \geq 1$ obey Poisson's electrostatic equation, and values for α_l are estimated from the Hartree–Fock optimized single-ξ exponents of the valence orbital wave function calculated for free atoms. Scattering factors for C, H, and S were derived from wave functions tabulated by Clementi and Roetti.[17] As shown in the literature, use of default values of $n(l)$ = (4,4,4,4) and α_l for second-row atom (S) may lead to ambiguous results.[15,18] For this reason, several models were tested previously,[19,20] and finally $n(l)$ = (4,4,6,8) values were used. An identical set of $n(l)$ was used to refine experimental data of another hypervalent sulfur-nitrogen species[21,22] as well as in experimental studies of L-cysteine.[23] The αl parameter was kept constant at 3.851 a_o^{-1}.[24] Initially, only the scale factor was refined on all data. Next, accurate positional and displacement parameters for all non-hydrogen atoms were obtained from the high order refinement ($\sin(\theta/\lambda) > 0.7$ Å^{-1}) whereas positional and isotropic displacements for hydrogen atoms were refined using low-angle data ($\sin(\theta/\lambda) < 0.7$ Å^{-1}). Due to unavailability of neutron data, all C–H distances were fixed to the averaged distances from neutron studies[25] (e.g., $d_{Carom–H}$ = 1.083 Å). During the next stages of refinement, monopole, dipole, quadrupole, octupole, and hexadecapole populations were refined with single expansion/contraction κ parameter in a stepwise manner. The expansions over the spherical harmonics were truncated at the hexadecapolar level [l_{max} = 4] for the sulfur-bonded atoms (^{A}S, ^{B}S, C_i, ---), and at the octupolar level [l_{max} = 3] for the remaining carbon. Hydrogen atoms were represented by the bond directed dipole. Finally, a single κ' parameter was refined for all non-hydrogen atoms. Chemically and symmetry related atoms were constrained to share the same expansion/contraction (κ/κ') parameters. Throughout the multipole refinement expansion/contraction parameters (κ/κ') of all hydrogen atoms were fixed to values κ = 1.20 and κ' = 1.20. This procedure was repeated several times in a block refinement until satisfactory convergence was achieved. Chemical constraints for similar atoms were applied at the initial stages of the refinements. These constraints were gradually released, and the final model was chemically unconstrained. The electron neutrality condition was imposed on the molecule for the entire refinement. Final multipole refinement led to a featureless residual density map (Figures 7-A1 and 7-A2 of the Appendix). The overall residual density after multipole refinement with all high order data

was $-0.24 \leq \nabla^2\rho \leq 0.25$ eÅ^{-3}. Multipolar refinement details are shown in Table 7-A1 in the Appendix.

Methodological details in calculation

Calculations are performed using the Gaussian 09 program package.[26] Compound **7-1** (S, S) was optimized with the 6-311+G(d) basis set for S and the 6-31G(d,p) basis sets for C and H.[27] The basis set system is called A (BSS-A), in this chapter. The Møller-Plesset second order energy correlation (MP2) level was applied to the calculations.[28] Structural parameters optimized with MP2/BSS-A (r(^{A}S, $^{A'}$S) = 2.0730 Å and r(^{A}S, ^{B}S) = 2.9874 Å) were very close to the observed values (r_{obsd}(^{A}S, $^{A'}$S) = 2.0559(5) Å and $r_{obsd:av}$(^{A}S, ^{B}S) = 2.9852 Å), respectively. Compounds **7-1**–**7-4** were similarly optimized with MP2/BSS-A, where the 6-311+G(d) basis sets were applied for S and/or Se with the 6-31G(d,p) basis sets for C and H. Deformation density map for **7-1** (S, S) was computed using Multiwfn program.[29]

QTAIM functions were calculated using the Gaussian 09 program package with MP2/BSS-A. The results were analyzed with the AIM2000 program.[30] Normal coordinates of internal vibrations (NIV) obtained by the frequency analysis were employed to generate the perturbed structures. The detail of OTAIM-DFA and NIV is explained in Chapter 2.

Results and Discussion

High-resolution X-ray diffraction determination of electron densities for 7-1 (S, S)

Figure 7-1 shows the crystal structure of **7-1** (S, S), determined by the high-resolution X-ray crystallographic analysis. Table 7-1 collects the selected bond distances, angles, and torsional angles of **7-1** (S, S), determined by the high-resolution X-ray crystallographic analysis. The $r_{obsd}(^{A}S, ^{A'}S)$ and $r_{obsd:av}(^{A}S, ^{B}S)$ values are determined to be 2.0559 Å(5) and 2.9852 Å, respectively, with $\angle ^{B}S^{A}S^{A'}S_{obsd:av}$ of 167.2° for **7-1** (S, S). The ^{B}S---^{A}S–$^{A'}S$---$^{B'}S$ interaction can be recognized as the linear interaction, since $\angle ^{B}S^{A}S^{A'}S$ is larger than the 150°, where $\angle ^{B}S^{A}S^{A'}S = 150°$ is tentatively proposed to determine the linearity of the interactions. As a result, the ^{B}S---^{A}S–$^{A'}S$---$^{B'}S$ interaction in **7-1** (S, S) can be well analyzed by the S_4 σ(4c–6e) model. Figure 7-2 depicts the valence electron density map drawn on the $^{A'}S^{A}SC_1$ plane for **7-1** (S, S) and the magnified map around the ^{B}S---^{A}S–$^{A'}S$---$^{B'}S$ interaction drawn on the $^{B}S^{A}S^{A'}S$ ($^{B'}S$) plane (Figures 7-2a and 7-2a', respectively). Figure 7-2 also depicts the deformation density map drawn on the $^{A'}S^{A}SC_1$ plane for **7-1** (S, S) and the magnified map around the ^{B}S---^{A}S–$^{A'}S$---$^{B'}S$ interaction drawn on the $^{B}S^{A}S^{A'}S$ ($^{B'}S$) plane (Figures 7-2b and 7-2b', respectively). Figure 7-3 shows the positive Laplacian map similarly drawn on the $^{A'}S^{A}SC_1$ plane for **7-1** (S, S) and the magnified map around the ^{B}E---^{A}E–^{A}E---^{B}E interaction drawn on the $^{B}S^{A}S^{A'}S$ ($^{B'}S$) plane (Figures 7-3a and 7-3a', respectively). BCPs around ^{B}S-∗-^{A}S-∗-$^{A'}S$-∗-$^{B'}S$ in **7-1** (S, S) are expected to locate in the negative area of $\nabla^2\rho_b(\boldsymbol{r}_c)$. Figure 7-4 illustrates the molecular graph of **7-1** (S, S), determined by high-resolution X-ray crystallographic analysis. All BCPs are detected as expected, including those around ^{B}S-∗-^{A}S-∗-$^{A'}S$-∗-$^{B'}S$ in **7-1** (S, S). Two pairs of BPs with BCPs are also detected for the weaker interactions, which are very close to those drawn theoretically and therefore discussed in the theoretical section.

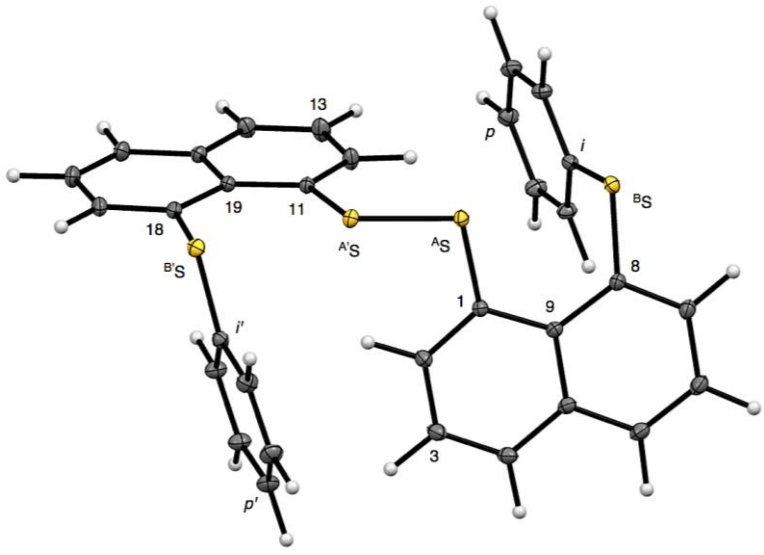

Figure 7-1. Structure of **7-1** (S, S) determined by the high-resolution X-ray crystallographic analysis.

Table 7-1 Selected structural parameters observed for **7-1** (S, S) and those evaluated with MP2/BSS-A[a]

Species (symmetry)	$r(^{A}S, ^{A'}S)$ (Å)	$\Delta r(^{A}S, ^{A'}S)^{b}$ (Å)	$r(^{A}S, ^{B}S)$ (Å)	$\Delta r(^{A}S, ^{B'}S)^{b}$ (Å)	$\Delta r_{van}(^{A}S, ^{B'}S)^{c}$ (Å)
7-1 (S, S) $(C_1)_{obsd}$	2.0559(5)	0.000	2.9852[d]	0.000	–0.615
7-1 (S, S) $(C_2)_{calcd}$	2.0730	0.017	2.9874	0.002	–0.613

[a] BSS-A; the 6-311+G(d) basis set for S with the 6-31G(d,p) basis sets for C and H. [b] $\Delta r(^{A}S, ^{X}S) = r_{calcd}(^{A}S, ^{X}S) - r_{obsd}(^{A}S, ^{X}S)$ where X = A' and B. [c] $\Delta r_{van}(^{A}S, ^{B}S) = r(^{A}S, ^{B}S) - \Sigma r_{vdW}(^{A}S, ^{B}S)$, where $r_{vdW}(S)$ = 1.80 Å (ref. 31) [d] Averaged value: $r_{obsd:av}(^{A}S, ^{B}S)$ = 2.9879(4) Å and 2.9825(5) Å.

(Table 7-1 continued)

Species (symmetry)	$\angle ^{A'}S^{A}SC_1$ (°)	$\angle C_8{}^{B}SC_i$ (°)	$\angle ^{B}S^{A}S^{A'}S$ (°)	$\phi_1{}^{d}$ (°)	$\phi_2{}^{e}$ (°)
7-1 (S, S) $(C_1)_{obsd}$	105.0[g]	102.5[h]	167.2[i]	–89.5	–75.6[j]
7-1 (S, S) $(C_2)_{calcd}$	104.0	100.6	169.4	–78.2	–64.2

[d] $\phi_1 = \phi(C_1{}^{A}S^{A'}SC_{1'})$. [e] $\phi_2 = \phi(C_9C_8{}^{B}SC_i)$ and/or $\phi(C_{19}C_{18}{}^{B'}SC_{i'})$. [g] Averaged value: $\angle C_1{}^{A}S^{A'}S_{obsd:av}$ = 105.54(2)° and 104.48(2)°. [h] Averaged value: $\angle C_8{}^{B}SC_{i\text{-}obsd:av}$ = 101.94(1)° and 102.99(2)°. [i] Averaged value: $\angle ^{B}S^{A}S^{A'}S_{obsd:av}$ = 168.68(2)° and 165.70(2)°. [j] Averaged value: $\phi_{2\text{-}obsd:av}$ = –70.22(2)° and –80.98(2)°.

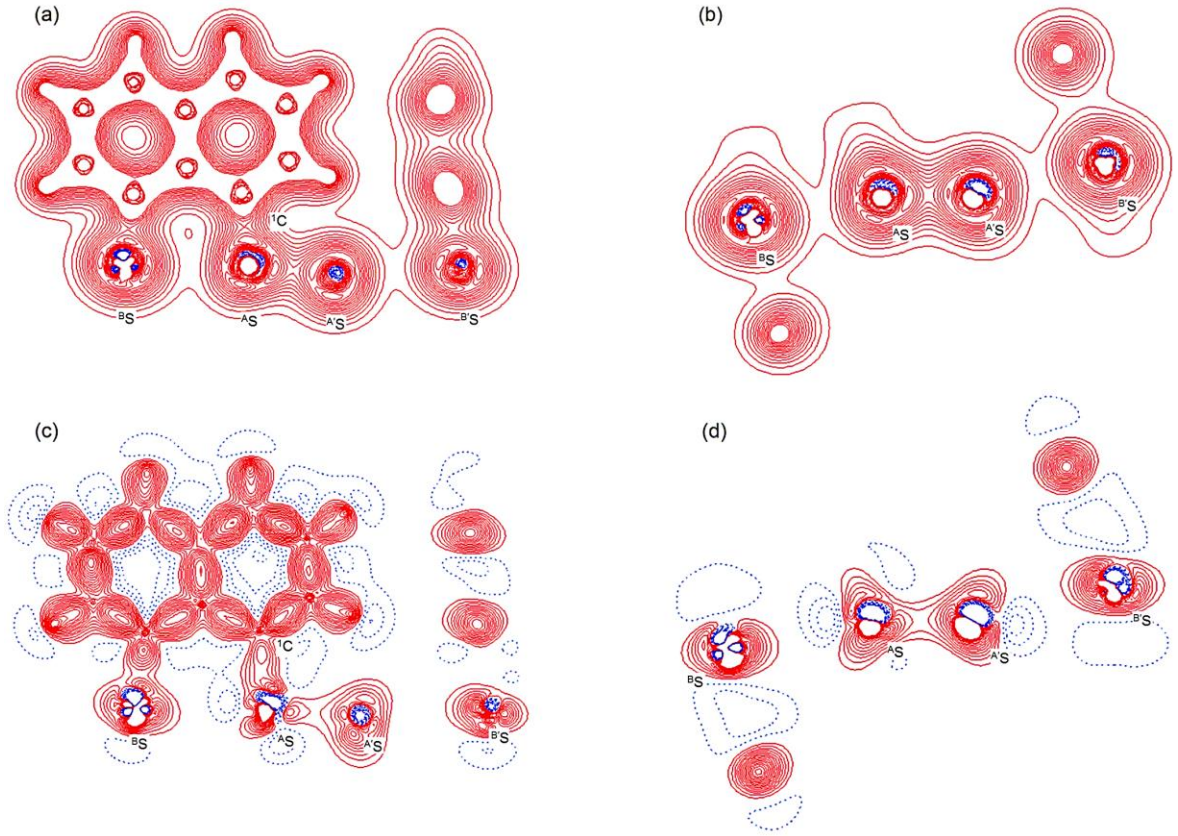

Figure 7-2. Valence electron density map drawn on the $^{B}S^{A}SC_1$ plane of **7-1** (S, S) and the magnified map for the ^{B}S---^{A}S–$^{A'}S$---$^{B'}S$ interaction drawn on the $^{B}S^{A}S^{A'}S$ plane ((a) and (b), respectively), which contour level is 0.1 eÅ^{-3}. Deformation density map drawn on the $^{B}S^{A}SC_1$ plane of **7-1** (S, S) and the magnified map for the ^{B}S---^{A}S–$^{A'}S$---$^{B'}S$ interaction drawn on the $^{B}S^{A}S^{A'}S$ plane ((c) and(d), respectively), which contour level is 0.05 eÅ^{-3}. The red and blue lines correspond to the increased and decreased electron densities, respectively, in the formation of the chemical bonds or interactions.

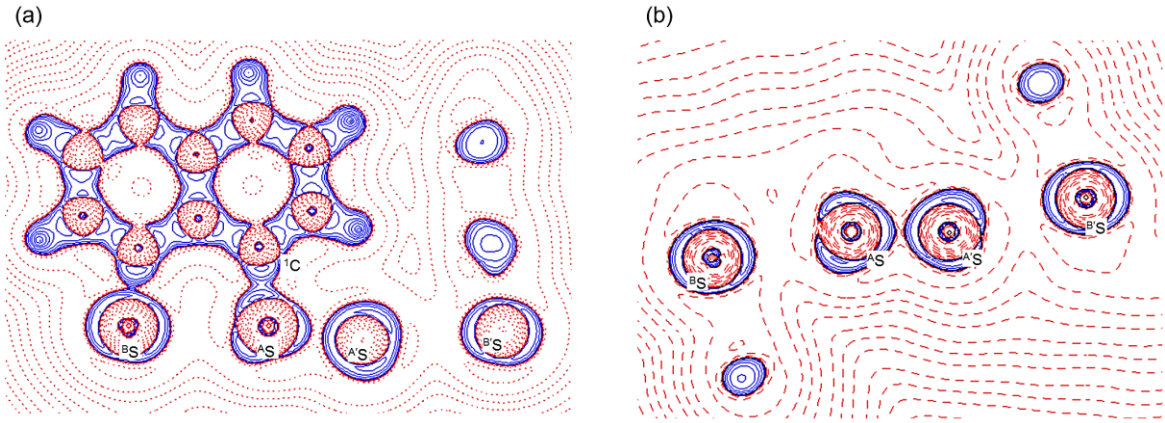

Figure 7-3. Positive Laplacian map in the $^{B}S^{A}SC_{1}$ plane of **7-1** (S, S) (a) and a magnification of the ^{B}S---^{A}S–$^{A'}S$---$^{B'}S$ interaction region in the $^{B}S^{A}S^{A'}S$ plane (b). Positive and negative areas are shown by red and blue lines respectively and each contour level is 0.05 eÅ^{-3}.

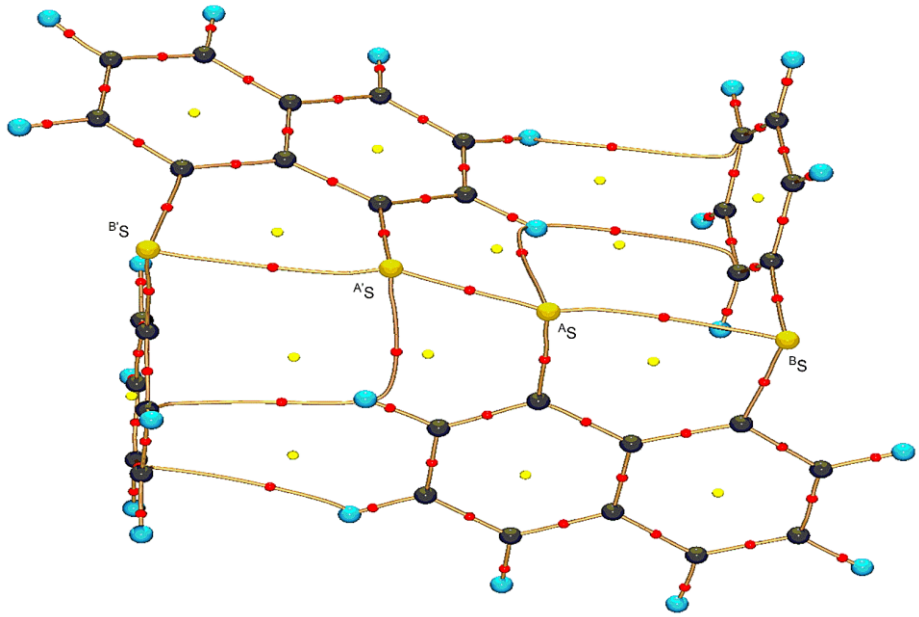

Figure 7-4. Molecular graph of **7-1** (S, S), determined by high-resolution X-ray crystallographic analysis.

Formation of S_4 σ(4c–6e) in 7-1 (S, S), confirmed based on experimental background

The electron distributions can be well overviewed by those illustrated in Figure 7-2. The valence electron density map of **7-1** (S, S) seems to define (three-dimensional) saddle points of $\rho(\boldsymbol{r})$ between ^{A}S and ^{B}S and between $^{A'}$S and $^{B'}$S of **7-1** (S, S), so is the typical one between ^{A}S and $^{A'}$S (see Figures 7-2a or 7-2b). Each saddle point of $\rho(\boldsymbol{r})$ between the adjacent S atoms in ^{B}S---^{A}S–$^{A'}$S---$^{B'}$S should correspond to a BCP on a BP in **7-1** (S, S) (see also Figure 7-4). The enhanced charge density at ^{B}S directs toward to the depleted area at ^{A}S extending over the backside of the ^{A}S–$^{A'}$S bond, as shown in Figures 7-2c or 7-2d. This must show the contribution of the CT interaction of the $n_p(^{B}S)\rightarrow\sigma^*(^{A}S–^{A'}S)$ form. Similar phenomena can be found between $^{B'}$S and $^{A'}$S–^{A}S, showing the CT interaction of the $n_p(^{B'}S)\rightarrow\sigma^*(^{A'}S–^{A}S)$ form. Such degenerated CT

interactions should be analyzed as S_4 σ(4c–6e) of the $n_p(^{B}S)\rightarrow\sigma^*(^{A}S–^{A'}S)\leftarrow n_p(^{B'}S)$ type, which must be the driving force for the formation of S_4 σ(4c–6e), as proposed by us. The valence electron density maps and the deformation density maps around the ^{B}S---^{A}S–$^{A'}S$---$^{B'}S$ interaction in Figure 7-2 strongly support the formation of linear S_4 σ(4c–6e) of the $n_p(^{B}S)\rightarrow\sigma^*(^{A}S–^{A'}S)\leftarrow n_p(^{B'}S)$ type in **7-1** (S, S), based on the experimental treatment.

As shown in Figure 7-3, three VSCCs (valence shell charge concentrations) appear at each S atom in the $^{B}S^{A}S^{A'}S$ ($^{B'}S$) plane of **7-1** (S, S). A pair of VSCCs on ^{A}S and ^{B}S is going to merge with each other, which confirms the presence of the ^{A}S---^{B}S interaction. The $^{A'}S$---$^{B'}S$ interaction is similarly confirmed through almost merging between the VSCCs on $^{A'}S$ and $^{B'}S$. The results, together with the original ^{A}S–$^{A'}S$ bond, also confirms the formation of S_4 σ(4c–6e) in **7-1** (S, S). The linearity of the VSCCs seems not so well, which would affect on BPs between the atoms. The differences between the lengths of BPs (r_{BP}) and the straight-line distances (R_{SL}) ($\Delta r_{BP} = r_{BP} - R_{SL}$) are less than 0.0010 Å and 0.012–0.013 Å for ^{A}S–$^{A'}S$ and ^{A}S---^{B}S (and $^{A'}S$---$^{B'}S$), respectively, in **7-1** (S, S). Therefore, each of the ^{B}S---^{A}S–$^{A'}S$---$^{B'}S$ interaction in **7-1** (S, S) can be approximated as the linear one.

The BCPs on BPs around ^{B}S---^{A}S–$^{A'}S$---$^{B'}S$ in **7-1** (S, S) are clearly specified in the molecular graph drawn experimentally in Figure 7-4, together with those expected for **7-1** (S, S). Some QTAIM parameters were experimentally determined at the BCPs around ^{B}S---^{A}S–$^{A'}S$---$^{B'}S$ in **7-1** (S, S) see the observed values for QTAIM parameters and those evaluated theoretically with MP2/BSS-A, employing the observed structure of **7-1** (S, S) in Table 7-2). While the ^{A}S–$^{A'}S$ bond in **7-1** (S, S) is experimentally classified by the regular CS (*r*-CS) interactions, the ^{A}S---^{B}S and $^{A'}S$---$^{B'}S$ interactions are shown to exist just on the border area between the pure CS (*p*-CS) and *r*-CS interactions (see, Figure 7-4 and Table 7-2). The values evaluated theoretically, employing the observed structure of **7-1** (S, S), reproduced very well the experimentally obtained values, except for $(\hbar^2/8m)\nabla^2\rho_b(\boldsymbol{r}_c)$ ($= H_b(\boldsymbol{r}_c) - V_b(\boldsymbol{r}_c)/2$), $H_b(\boldsymbol{r}_c)$, and $k_b(\boldsymbol{r}_c)$ ($= V_b(\boldsymbol{r}_c)/G_b(\boldsymbol{r}_c)$) at BCP of the ^{A}S–$^{A'}S$ bond, although the deviation seem not so severe. However, the difference in $(\hbar^2/8m)\nabla^2\rho_b(\boldsymbol{r}_c)$ ($= H_b(\boldsymbol{r}_c) - V_b(\boldsymbol{r}_c)/2$) affects much on the classification of ^{A}S–$^{A'}S$, since the signs are just the opposite between the values are predicted by experimentally and the value calculated employing the observed structure of **7-1** (S, S).

Theoretical basis for the nature of S_4 σ(4c–6e) in 7-1 (S, S)

Structure of 7-1 (S, S) optimized at the MP2 level

Compound **7-1** (S, S) was optimized, retaining the C_2 symmetry with MP2/BSS-A. Table 7-1 also shows the selected bond distances, angles, and torsional angles of **7-1** (S, S), predicted with MP2/BSS-A. The predicted

structural parameters are (very) close to the corresponding observed ones, respectively, as a whole. The $r_{calcd}(^{A}E, ^{A'}E)$ and $r_{calcd}(^{A}E, ^{B}E)$ values are 2.0730 and 2.9874 Å, respectively. The differences between the calculated and observed distances for $^{A}E–^{A'}E$ and $^{A}E---^{B}E$ are also given in Table 7-1, which are defined by $\Delta r(^{A}E, ^{A'}E) = r_{calcd}(^{A}E, ^{A'}E) - r_{obsd}(^{A}E, ^{A'}E)$ and $\Delta r(^{A}E, ^{B}E) = r_{calcd}(^{A}E, ^{B}E) - r_{obsd}(^{A}E, ^{B}E)$, respectively. The $\Delta r(^{A}E, ^{A'}E)$ and $\Delta r(^{A}E, ^{B}E)$ values are 0.017 and 0.002 Å, respectively. The magnitude of Δr less than 0.013 Å is desirable for QTAIM-DFA, since 0.013 Å corresponds to a half of each interval of adjacent two data points in the plots of $H_b(\boldsymbol{r}_c)$ versus $H_b(\boldsymbol{r}_c) - V_b(\boldsymbol{r}_c)/2$ in QTAIM-DFA (= $0.05a_o/2$ = 0.026 Å/2). The $\Delta r(^{A}E---^{B}E)$ value of 0.002 Å completely satisfies this criterion, while the $\Delta r(^{A}E–^{A'}E)$ value of 0.017 Å seems slightly larger than 0.013 Å. Irrespective of the slightly larger magnitude for $\Delta r(^{A}E–^{A'}E)$, the optimized structure of **7-1** (S, S) with MP2/BSS-A can be recognized to satisfy the desirable conditions to clarify the nature of S_4 σ(4c–6e), since the $^{A}E---^{B}E$ interactions should be mainly discussed for S_4 σ(4c–6e) in **7-1** (S, S) and $r_{calcd}(^{A}E–^{A'}E)$ is only slightly larger than $r_{obsd}(^{A}E–^{A'}E)$ (0.017 Å versus 0.013 Å). The $r_{calcd}(^{A}E–^{A'}E)$ value may correspond to the nature of its weaker limit. Figure 7-5a shows the molecular graph of optimized **7-1** (S, S).

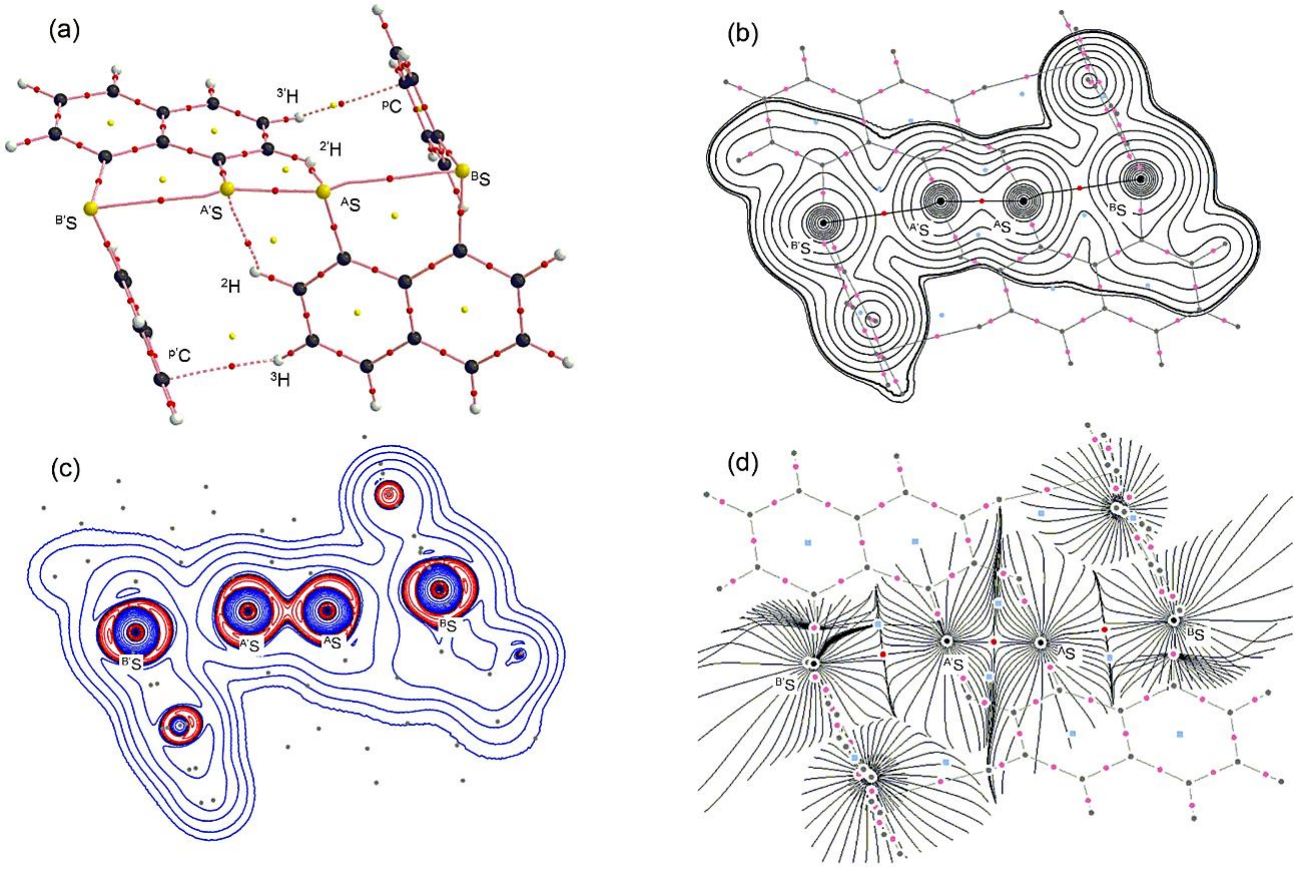

Figure 7-5. Molecular graph (a), contour plot (b), negative Laplacian map (c), and trajectory plot (d) for **7-1** (S, S), calculated with MP2/BSS-A. BCPs (bond critical points) are denoted by red dots, RCPs (ring critical points) by yellow dots, CCPs (cage critical points) by green dots, and BPs (bond paths) by pink lines, accompanied by BCPs. Carbon, hydrogen, and sulfur atoms are in black, gray, and yellow, respectively. The contours (ea_0^{-3}) for (b) are at 2^l (l = ±8, ±7 ..., and 0) with 0.0047 (heavy line)). Positive and negative areas in (c) are shown by blue and red lines, respectively.

Deformation density map around ^{B}S-∗-^{A}S-∗-^{A}S-∗-^{B}S of 7-1 (S, S)

Deformation density map was drawn theoretically on the ^{B}S^{A}S$^{A'}$S plane around the ^{B}S-∗-^{A}S-∗-$^{A'}$S-∗-$^{B'}$S interaction of **7-1** (S, S), although it retains the C_2 symmetry, similarly to the case of experimental approach. Figure 7-6 shows the map. The deformation density map shown in Figure 7-6 is (very) similar to that in Figure 7-2d. The enhanced charge density at ^{B}S also directs toward to the depleted area at ^{A}S extending over the backside of the ^{A}S–$^{A'}$S bond, as shown in Figure 7-6. Namely, the CT interaction of the $n_p(^{B}S)\rightarrow\sigma^*(^{A}S–^{A'}S)\leftarrow n_p(^{B'}S)$ type is also demonstrated theoretically by the deformation density map, which should be analyzed as linear S_4 σ(4c–6e), as discussed above. The contribution of the CT interaction of the $n_p(^{B}E)\rightarrow\sigma^*(^{A}E–^{A}E)\leftarrow n_p(^{B}E)$ type in **7-1** (S, S) was evaluated by the second order perturbation of Fock matrix (E (2))[32] with MP2/BSS-A, so were those for **7-2**–**7-4** (^{A}E, ^{B}E = S and/or Se). The results are shown in Table 7-A3 of Appendix.

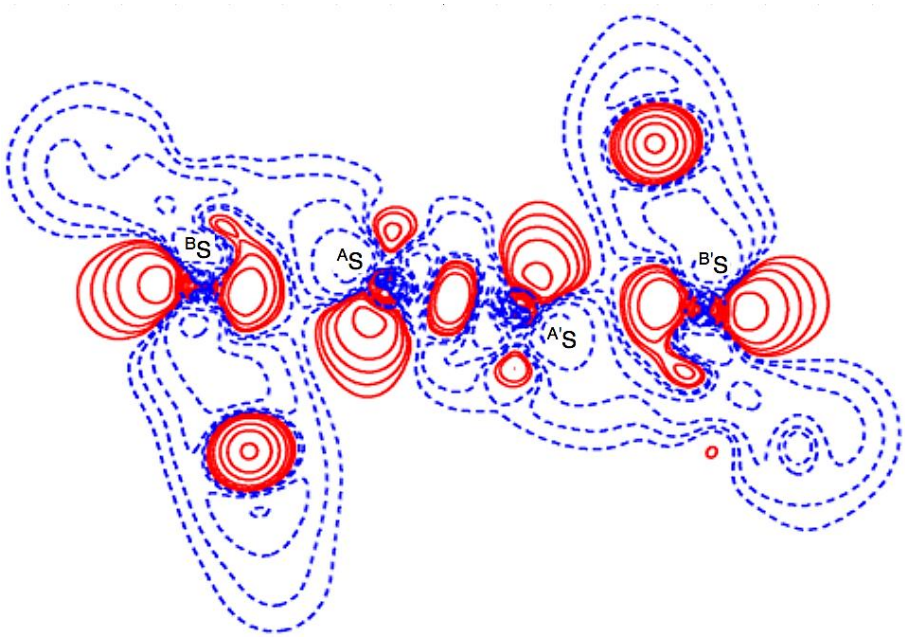

Figure 7-6. Deformation density map for the ^{B}S---^{A}S–$^{A'}$S---$^{B'}$S interaction drawn on the ^{B}S^{A}S$^{A'}$S plane of **7-1** (S, S) which contour level is 0.05 eÅ^{-3}. The red and blue lines correspond to the increased and decreased electron densities, respectively, in the formation of the chemical bonds or interactions.

Molecular graph, contour plot, negative Laplacian, and trajectory plots around ^{B}S-∗-^{A}S-∗-$^{A'}$S-∗-$^{B'}$S in 7-1 (S, S)

Figure 7-5 shows the molecular graph, contour plot, negative Laplacian, and trajectory plot for **7-1** (S, S), calculated with MP2/BSS-A. All BCPs are detected as expected, containing those around ^{B}S-∗-^{A}S-∗-$^{A'}$S-∗-$^{B'}$S in **7-1** (S, S). BCPs are also detected on the weaker interactions of ^{A}S-∗-$^{2'}$H with $^{A'}$S-∗-^{2}H and ^{3}H-∗-$^{p'}$C with $^{3'}$H-∗-^{p}C. The ^{A}S-∗-$^{2'}$H with $^{A'}$S-∗-^{2}H interactions may play an additional role to stabilize the linear ^{B}S-∗-^{A}S-∗-$^{A'}$S-∗-$^{B'}$S interaction, while ^{3}H-∗-$^{p'}$C with $^{3'}$H-∗-^{p}C may support the specific positions of the phenyl groups in the structure of **7-1** (S, S) through the C_{Nap}–H---π(C_6H_5S) interactions. As shown in Figure 7-5c, the BCP on ^{A}S-∗-$^{A'}$S is located in a negative area of $\nabla^2\rho_b(\boldsymbol{r}_c)$, while those on ^{A}S-∗-^{B}S are in a positive region. The results show that ^{A}S-∗-$^{A'}$S and ^{A}S-∗-^{B}S are classified by shared shell (SS) and closed shell (CS) interactions, respectively. The space around the space seems well fractionalized to the atoms in **7-1** (S, S), as shown in Figure 7-5d. The results clearly demonstrate the formation of S_4 σ(4c–6e) in **7-1** (S, S). As shown in Figure 7-5d, BPs (^{A}S-∗-^{B}S) seem somewhat bend just around ^{A}S. The differences between r_{BP} in question and the corresponding R_{SL} ($\Delta r_{BP} = r_{BP} - R_{SL}$) are 0.001 Å and 0.021 Å for Δr_{BP} (^{A}S, $^{A'}$S) and Δr_{BP} (^{A}S, ^{B}S), respectively, in **7-1** (S, S) (Table 7-A2 of the Appendix). The results show that each of the ^{B}S---^{A}S–$^{A'}$S---$^{B'}$S interaction in **7-1** (S, S) can also be approximated as the linear one, theoretically.

The nature of the non-covalent E---E interaction was established for E = S in **7-1** (S, S), experimentally and theoretically, in this work. The interaction becomes much stronger for E = Se in **7-4** (Se, Se) based on the theoretical investigations. The results are in accordance to those reported in chapter 6, although the strength of S---S seems to change widely, as the structure changes.

Application of QTAIM-DFA to $^{A}E_2{}^{B}E_2$ σ(4c–6e) (^{A}E, ^{B}E = S, Se)

QTAIM functions of $\rho_b(\boldsymbol{r}_c)$, $H_b(\boldsymbol{r}_c) - V_b(\boldsymbol{r}_c)/2$, $H_b(\boldsymbol{r}_c)$, and $k_b(\boldsymbol{r}_c)$ (= $V_b(\boldsymbol{r}_c)/G_b(\boldsymbol{r}_c)$) are evaluated for ^{A}E-∗-$^{A'}$E and ^{A}E-∗-^{B}E at BCPs of **7-1** (S, S). Table 7-2 collects the values. Table 7-2 contains the frequencies (ν) and force constants (k_f), corresponding to ^{A}E-∗-$^{A'}$E and ^{A}E-∗-^{B}E. Figure 7-7 shows the plots of $H_b(\boldsymbol{r}_c)$ versus $H_b(\boldsymbol{r}_c) - V_b(\boldsymbol{r}_c)/2$ for the fully optimized data of **7-1** (S, S) given in Table 7-2, together with those from the perturbed structures around the fully optimized ones, where the perturbed structures are generated with NIV, according to eqns (2-9) and (2-10) in chapter 2. The plots are analyzed according to eqs (2-3) – (2-6) in chapter 2 and the QTAIM-DFA parameters of (R, θ) and (θ_p, κ_p) are obtained. Table 7-2 collects the (R, θ) and (θ_p, κ_p) values for ^{A}E-∗-$^{A'}$E and ^{A}E-∗-^{B}E in **7-1**–**7-4**.

Table 7-2 QTAIM functions and QTAIM-DFA parameters for ^{A}E-∗-$^{A'}$E and ^{A}E-∗-^{B}E at BCPs of 1-(8-Ph^{B}EC$_{10}$H$_6$)^{A}E–$^{A'}$E(C$_{10}$H$_6$^{B}EPh-8')-1' (**7-1**–**7-4**)[a]

Species (symmetry)	Interactions (X-∗-Y)	$\rho_b(\boldsymbol{r}_c)$ (ea_o^{-3})	$c\nabla^2\rho_b(\boldsymbol{r}_c)$[b] (au)	$H_b(\boldsymbol{r}_c)$ (au)	$k_b(\boldsymbol{r}_c)$[c]	R (au)	θ (°)
7-1 $(C_1)_{obsd}$[d]	(^{A}S-∗-$^{A'}$S)	0.141	0.004	–0.11	–1.92		
	(^{A}S-∗-^{B}S)	0.020	0.008	0.00	–1.00		
	($^{A'}$S-∗-$^{B'}$S)	0.021	0.008	–0.00	–1.00		
7-1 $(C_1)_{obsd}$[e]	(^{A}S-∗-^{A}S)	0.1418	–0.0111	–0.0748	–2.424	0.0757	188.5
	(^{A}S-∗-^{B}S)	0.0229	0.0075	–0.0004	–1.027	0.0075	93.1
	($^{A'}$S-∗-$^{B'}$S)	0.0234	0.0076	–0.0005	–1.031	0.0076	93.7
7-1 $(C_2)_{calcd}$	(^{A}S-∗-$^{A'}$S)	0.1373	–0.0097	–0.0697	–2.383	0.0704	187.9
	(^{A}S-∗-^{B}S)	0.0227	0.0075	–0.0004	–1.026	0.0075	93.1
7-2 $(C_2)_{calcd}$	(^{A}S-∗-$^{A'}$S)	0.1356	–0.0089	–0.0677	–2.354	0.0683	187.5
	(^{A}S-∗-^{B}Se)	0.0225	0.0068	–0.0006	–1.042	0.0069	95.1
7-3 $(C_2)_{calcd}$	(^{A}Se-∗-$^{A'}$Se)	0.0970	–0.0018	–0.0403	–2.095	0.0404	182.5
	(^{A}Se-∗-^{B}S)	0.0246	0.0070	–0.0011	–1.071	0.0070	93.7
7-4 $(C_2)_{calcd}$	(^{A}Se-∗-$^{A'}$Se)	0.0948	–0.0013	–0.0387	–2.070	0.0387	181.9
	(^{A}Se-∗-^{B}Se)	0.0250	0.0064	–0.0014	–1.098	0.0066	102.3

[a] The 6-311+G(d) basis set is employed for S and Se with the 6-31G(d,p) basis set for C and H. [b] $c\nabla^2\rho_b(\boldsymbol{r}_c) = H_b(\boldsymbol{r}_c) - V_b(\boldsymbol{r}_c)/2$, where $c = \hbar^2/8m$. [c] $k_b(\boldsymbol{r}_c) = V_b(\boldsymbol{r}_c)/G_b(\boldsymbol{r}_c)$. [d] Observed QTAIM parameters. [e] QTAIM parameters evaluated employing the observed structure.

(Table 7-2 continued)

Species (symmetry)	Interactions (X-∗-Y)	ν_n (n)[f] (cm^{-1})	k_f[g] (mDyn $Å^{-1}$)	θ_p (°)	κ_p (au^{-1})	Classification/ characterization
7-1 $(C_1)_{obsd}$[d]	(^{A}S-∗-$^{A'}$S)					*r*-CS
	(^{A}S-∗-^{B}S)					*p*-CS/*r*-CS
	($^{A'}$S-∗-$^{B'}$S)					*p*-CS/*r*-CS
7-1 $(C_1)_{obsd}$[e]	(^{A}S-∗-^{A}S)					SS
	(^{A}S-∗-^{B}S)					*r*-CS
	($^{A'}$S-∗-$^{B'}$S)					*r*-CS
7-1 $(C_2)_{calcd}$	(^{A}S-∗-$^{A'}$S)	518.7 (48)	1.701	197.5	0.5	SS/Cov-w
	(^{A}S-∗-^{B}S)	181.1 (17)	0.209	117.8	68.9	*r*-CS/*t*-HB-wc[h]
7-2 $(C_2)_{calcd}$	(^{A}S-∗-$^{A'}$S)	502.9 (48)	1.698	197.5	0.6	SS/Cov-w
	(^{A}S-∗-^{B}Se)	152.0 (16)	0.154	128.1	133.3	*r*-CS/*t*-HB-wc[h]
7-3 $(C_2)_{calcd}$	(^{A}Se-∗-$^{A'}$Se)	288.9 (28)	0.442	186.6	2.5	SS/Cov-w
	(^{A}Se-∗-^{B}S)	150.9 (15)	0.086	140.1	126.4	*r*-CS/*t*-HB-wc[h]
7-4 $(C_2)_{calcd}$	(^{A}Se-∗-$^{A'}$Se)	275.5 (28)	0.664	187.1	2.4	SS/Cov-w
	(^{A}Se-∗-^{B}Se)	126.0 (15)	0.105	150.5	141.8	*r*-CS/CT-MC

[f] Corresponding to the interaction in question. Symmetric and anti-symmetric modes being employed for ^{A}E-∗-$^{A'}$E and ^{A}E-∗-^{B}E, respectively. [g] Force constant for ν_n. [h] *Typical* HB nature with covalency.

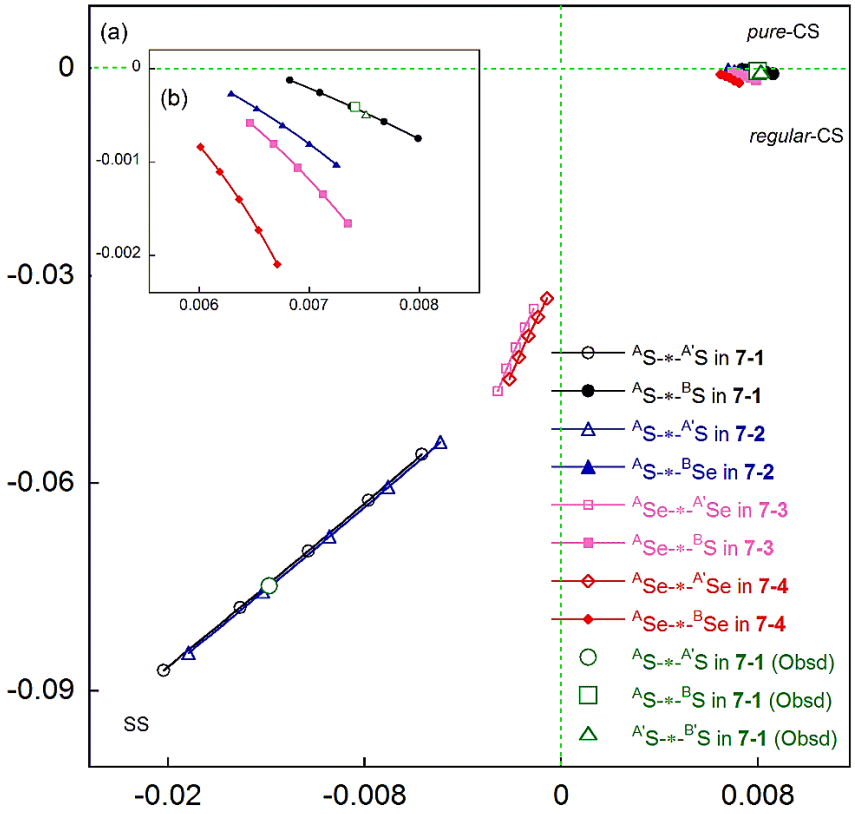

Figure 7-7. Plots of $H_b(\boldsymbol{r}_c)$ versus $H_b(\boldsymbol{r}_c) - V_b(\boldsymbol{r}_c)/2$ for ^{A}E-∗-^{A}E and ^{A}E-∗-^{B}E of **7-1**–**7-4**. (a) Whole picture and (b) magnified one for ^{A}E-∗-^{B}E. Marks and colors for the species are shown in the figure.

Nature of ^{A}S-∗-$^{A'}$S and ^{A}S-∗-^{B}S in 7-1 (S, S), elucidated by θ and θ_p

The nature of ^{A}S-∗-$^{A'}$S and ^{A}S-∗-^{B}S in **7-1** (S, S) is elucidated by employing the QTAIM-DFA parameters of (R, θ) and (θ_p, κ_p), with the standard values in Scheme 2-2 of Chapter 2 as a reference. The θ values are mainly employed for the classifications of interactions, while the interactions are characterized by the θ_p values with R to sub-divide the covalent interactions. It is instructive to survey the criteria briefly, closely related to those in this work. Interactions are called CS (closed shell) and SS (sheared shell) interactions for 45° < θ < 180° (0 < $H_b(\boldsymbol{r}_c) - V_b(\boldsymbol{r}_c)/2$) and 180° < θ < 206.6° ($H_b(\boldsymbol{r}_c) - V_b(\boldsymbol{r}_c)/2 < 0$), respectively. The CS interactions are sub-divided into *pure* CS and *regular* CS for 45° < θ < 90° (0 < $H_b(\boldsymbol{r}_c)$) and 90° < θ < 180° ($H_b(\boldsymbol{r}_c) < 0$), respectively. The θ_p value plays an important role to characterize the interactions. In the *pure* CS region of 45° < θ < 90°, the character of interactions will be the vdW type for 45° < θ_p < 90°, whereas it will be the *typical* HB type without covalency for 90° < θ_p ≤ 125°, although θ_p of 125° is tentatively given corresponding to θ = 90°.[4–7] The CT interactions will appear in the *regular* CS region of 90° < θ < 180°. The *typical* HB interactions with covalency appear in range of 125° < θ_p ≤ 150° (90° < θ ≤ 115°). Interactions of the CT-MC and CT-TBP types will appear in the ranges of 150° < θ_p ≤ 180° (115° ≤ θ < 150°) and 180° < θ_p ≤ 190° (150° ≤ θ_p < 180°), respectively. R contributes to sub-classify the SS interactions. Classical chemical bonds of SS should be called strong when R > 0.15 au, therefore, they will be weak when R < 0.15 au.

The (R, θ, θ_p) values for ^{A}S-∗-$^{A'}$S in **7-1** (S, S) are (0.0704 au, 187.9°, 197.5°). Therefore, ^{A}S-∗-$^{A'}$S in **7-1** (S, S) is classified by SS and predicted to have the Cov-w nature (SS/Cov-w). The predicted nature would correspond to the weak limit for ^{A}S-∗-$^{A'}$S in **7-1** (S, S). Similarly, the (R, θ, θ_p) values for ^{A}S-∗-^{B}S in **7-1** (S, S) are (0.0075 au, 93.1°, 117.8°). Therefore, ^{A}S-∗-^{B}S in **7-1** (S, S) is classified by *regular* -CS. The interaction is predicted to have the HB-wc (HB with covalency) nature, irrespective of the θ_p value of 117.8° (less than 125°), since the θ value of 93.1° (larger than 90°) is superior to θ_p = 117.8° (< 125°), where θ_p = 125° is tentatively given corresponding to θ = 90° for the typical interactions (see Scheme 2-2 of Chapter 2). Namely, ^{A}S-∗-^{B}S in **7-1** (S, S) is predicted to have the *r*-CS/HB-wc nature. The nature of ^{A}E-∗-$^{A'}$E and ^{A}E-∗-^{B}E is also predicted for **7-2** (S, Se), **7-3** (Se, S) and **7-4** (Se, Se). The ^{A}E-∗-$^{A'}$E interactions in **7-2**–**7-4** are concluded to have the nature of SS/Cov-w, irrespective of the θ_p values of about 187° for **7-3** (Se, S) and **7-4** (Se, Se), since the θ values larger than 180° should be superior to the θ_p values in the classification. While the ^{A}E-∗-^{B}E interactions in **7-2**–**7-4** are classified by the *r*-CS interactions based on 93° < θ < 102°, they are predicted to have the *t*-HB-wc, *t*-HB-wc, and CT-MC nature, respectively, based on the θ_p values. The results are summarized in Table 7-2.

Summary

The high-resolution X-ray diffraction determination of electron densities, supported by a rigorous theoretical treatment, was performed for **7-1** (S, S). The valence electron density map exhibits (three-dimensional) saddle points of $\rho(\boldsymbol{r})$ between ^{A}S and ^{B}S and between $^{A'}$S and $^{B'}$S. Enhanced charge densities at ^{B}S and $^{B'}$S direct toward to the depleted area around ^{A}S and $^{A'}$S respectively and extend over the backside of the ^{A}S–$^{A'}$S bond. The results demonstrate the formation of S_4 σ(4c–6e) of the $n_p(^{B}S)\rightarrow\sigma^*(^{A}S–^{A'}S)\leftarrow n_p(^{B'}S)$ type. This is supported by the valence electron density map(s) and the deformation density maps in the region around the ^{B}S---^{A}S–$^{A'}$S---$^{B'}$S interaction. A pair of VSCCs originating from ^{A}S and ^{B}S merge with each other confirming the presence of the ^{A}S---^{B}S interaction, as well as those on $^{A'}$S and $^{B'}$S which form the $^{A'}$S---$^{B'}$S interaction. These results, together with the conventional ^{A}S–$^{A'}$S bond, confirm the formation of S_4 σ(4c–6e) in **7-1** (S, S). The formation of S_4 σ(4c–6e) is experimentally demonstrated clearly by BPs with BCPs in the molecular graph for ^{B}S---^{A}S–$^{A'}$S---$^{B'}$S. The ^{A}S---^{B}S and $^{A'}$S---$^{B'}$S interactions are observed on the border area between the *p*-CS and *r*-CS interactions. These experimental results are well supported and rationalised by the complementary theoretical calculations.

The dual experimental-theoretical approach provides a solid basis for understanding the behavior of ^{B}E---^{A}E–$^{A'}$E---$^{B'}$E of E_4 σ(4c–6e) not only in **7-1** (S, S) but also in **7-2**–**7-4**. This methodology has previously been applied to 2-(2-pyridylimino)-2*H*-1,2,4-thiadiazolo[2,3-*a*]pyridine[33] where the behavior of N–E–N σ(3c–4e) (E = S, Se, and Te) was clarified. Compilation of these results makes it possible to confirm the real existence and chemistry of hypervalent and extended hypervalent interactions.

Appendix

Table 7-A1 Crystallographic data for **7-1** (S, S)

Empirical formula	$C_{32}H_{22}S_4$
Formula weight	534.73
Temperature (K)	100(2)
Crystal system	monoclinic
Space group	$P2_1/c$ (#14)
Unit cell dimensions	
a (Å)	10.4959(5)
b (Å)	23.8566(11)
c (Å)	10.3499(5)
β (°)	106.471(5)
Volume (Å^3)	2485.2(2)
Z	4
Theta range for data collection [θ]	1.71–60.09
D_{calcd} (g cm^{-3})	1.429
Reflections observed [$I > 2\sigma(I)$]	37520
Spherical refinement	
R [F] and *R [F^2]*	0.0252, 0.0423
R_{all} *[F]* and R_{all} *[F^2]*	0.0283, 0.0424
R_w *[F]*and R_w *[F^2]*	0.0334, 0.0623
Goodness of fit	1.9487
Nref/Nv	85.2
Multipole refinement	
R [F] and *R [F^2]*	0.0165, 0.0205
R_{all} *[F]* and R_{all} *[F^2]*	0.0197, 0.0206
R_w *[F]*and R_w *[F^2]*	0.0235, 0.0412
Goodness of fit	1.3814
Nref/Nv	32.7
Residual density (e Å^{-3})	-0.24 to 0.25

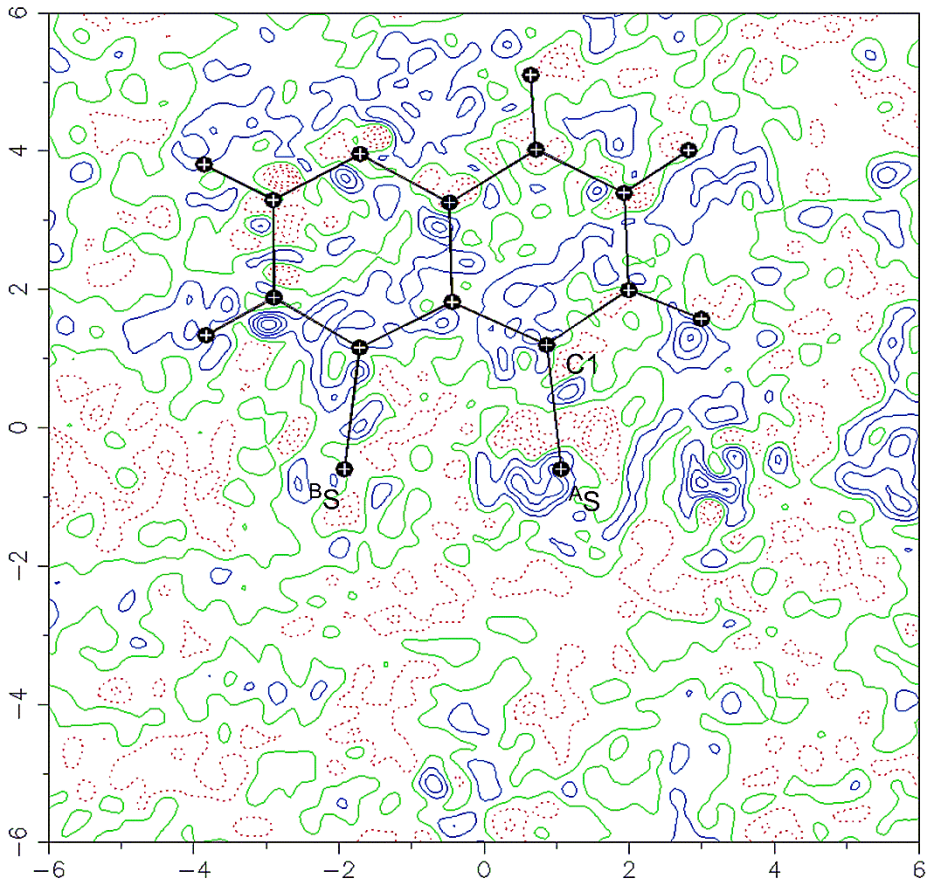

Figure 7-A1. Residual electron density map for final structure of **7-1** (S, S) on the $^{B}S^{A}SC_{1}$ plain. (contour 0.05 e Å^{-3}). Positive and negative areas are shown by red and blue lines, respectively.

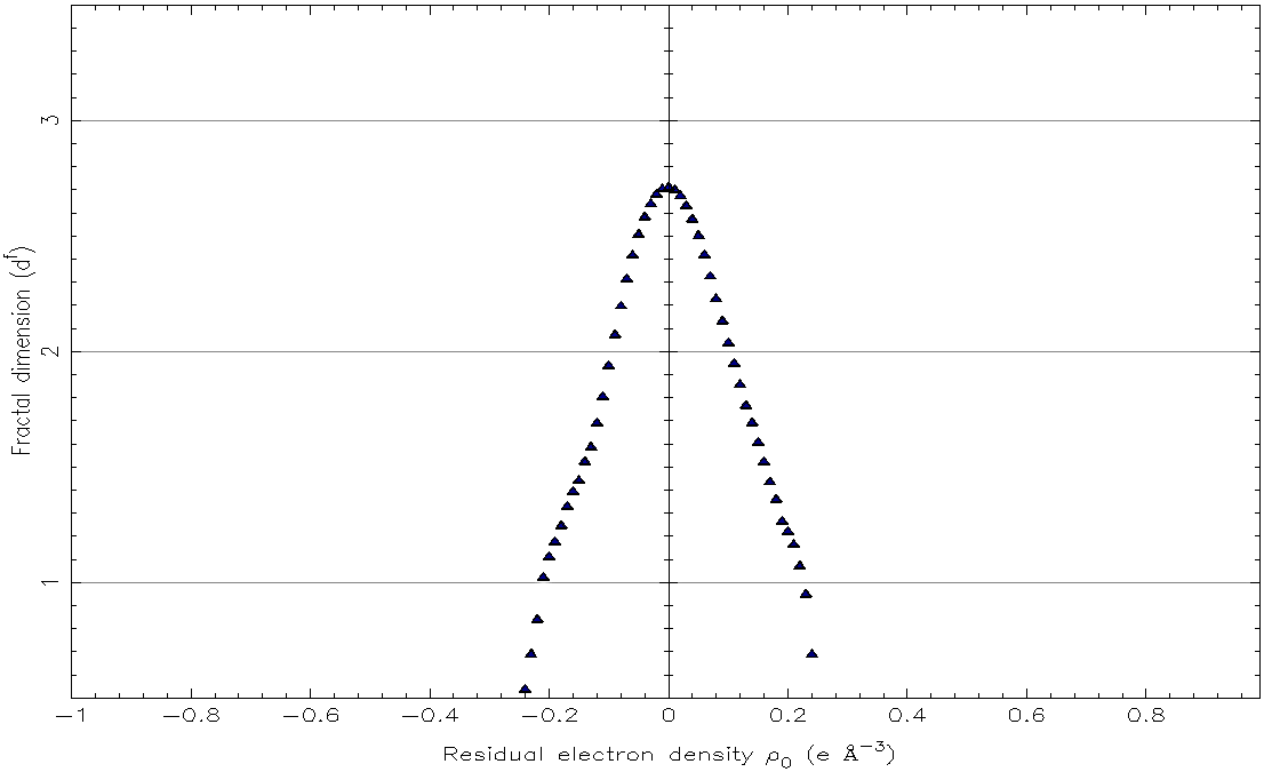

Figure 7-A2. Residual electron density fractal dimension plots for final structure of **7-1** (S, S).

Table 7-A2 R_{BP} and r_{SL} values for the ^{B}E ---^{A}E–^{A}E---^{B}E interactions in compounds **7-1**–**7-4**[a]

Species	$R_{SL}(^{A}E, ^{B}E)$ (Å)	$R_{SL}(^{A}E, ^{A}E)$ (Å)	$r_{BP}(^{A}E, ^{B}E)$ (Å)	$r_{BP}(^{A}E, ^{A}E)$ (Å)	$\Delta r_{BP}(^{A}E, ^{B}E)$[b] (Å)	$\Delta r_{BP}(^{A}E, ^{A}E)$[c] (Å)
7-1 (S, S) (C_2)	2.9874	2.0730	3.0083	2.0742	0.0208	0.0012
7-2 (S, Se) (C_2)	3.0673	2.0801	3.0842	2.0814	0.0170	0.0013
7-3 (Se, S) (C_2)	3.0188	2.3512	3.0281	2.3524	0.0093	0.0012
7-4 (Se, Se) (C_2)	3.0884	2.3642	3.0957	2.3655	0.0072	0.0013
7-1 $(S, S)_{obsd}$ (C_1)	2.9879[d]	2.0559	3.0055[e,f]	2.0569[e]	0.0176	0.0010

[a] The 6-311+G(d) basis sets being employed for S and Se with the 6-31G(d,p) basis sets for H and C. [b] $\Delta r_{BP}(^{A}E, ^{B}E) = r_{BP}(^{A}E, ^{B}E) - R_{SL}(^{A}E, ^{B}E)$. [c] $\Delta r_{BP}(^{A}E, ^{A}E) = r_{BP}(^{A}E, ^{A}E) - R_{SL}(^{A}E, ^{A}E)$. [d] Averaged value: $r_{obsd}(^{A}E, ^{B}E)$ = 2.9879(4) and 2.9825(5) Å. [e] r_{BP} value evaluated employing the observed structure. [f] Averaged value: $r_{BP:obsd}(^{A}E, ^{B}E)$ = 3.0037 and 3.0073 Å.

Table 7-A3 Contributions from the CT interactions for the $n_p(^{B}E)\rightarrow\sigma^*(^{A}E–^{A}E)\leftarrow n_p(^{B}E)$ type (^{A}E, ^{B}E = S and Se) for **7-1**–**7-4**, evaluated with MP2/BSS-A[a,b]

Species ***n*** (^{A}E, ^{B}E)	NBO (*i*)[c]	NBO (*j*)[d]	*E*(2) (kcal mol^{-1})	*E*(*j*)–*E*(*i*) (au)	F(*i*,*j*) (au)
7-1 (S, S)	n_p(S)	σ*(S–S)	6.58	0.38	0.045
7-2 (S, Se)[e]	n_p(Se)	σ*(S–S)	7.36	0.37	0.046
7-3 (Se, S)	n_p(S)	σ*(Se–Se)	10.81	0.34	0.054
7-4 (Se, Se)[f]	n_p(Se)	σ*(Se–Se)	13.03	0.32	0.058

[a] BSS-A: the 6-311+G(d) basis set for S and Se with the 6-31G(d,p) basis sets for C and H. [b] Second order perturbation of Fock matrix (threshold being 0.50 kcal mol^{-1}). Only one side of the interaction is evaluated [c] Donor orbitals. [d] Acceptor orbitals. [e] *E*(2: n_s(Se)→σ*(S–S)) = 1.07 kcal mol^{-1}. [f] *E*(2: n_s(Se)→σ*(Se–Se)) = 1.09 kcal mol^{-1}.

References

1 W. Nakanishi, S. Hayashi, T. Arai, *Chem. Commun.* **2002**, 2416–2417.

2 W. Nakanishi, S. Hayashi, S. Morinaka, T. Sasamori, N. Tokitoh, *New J. Chem.* **2008**, *32*, 1881–1889.

3 a) W. Nakanishi, S. Hayashi, S. Toyota, *Chem. Commun.* **1996**, 371–372; b) W. Nakanishi, S. Hayashi, S. Toyota, *J. Org. Chem.* **1998**, *63*, 8790–8800.

4 W. Nakanishi, S. Hayashi, *Curr. Org. Chem.* **2010**, *14*, 181–197.

5 W. Nakanishi, S. Hayashi, *J. Phys. Chem. A* **2010**, *114*, 7423–7430.

6 W. Nakanishi, S. Hayashi, K. Matsuiwa, M. Kitamoto, *Bull. Chem. Soc. Jpn.* **2012**, *85*, 1293–1305.

7 a) S. Hayashi, K. Matsuiwa, M. Kitamoto, W. Nakanishi, *J. Phys. Chem. A* **2013**, *117*, 1804–1816; b) Y. Sugibayashi, S. Hayashi, W. Nakanishi, *Phys. Chem. Chem. Phys.* **2015**, *17*, 28879–28891; c) S. Hayashi, Y. Sugibayashi, W. Nakanishi, *Phys. Chem. Chem. Phys.* **2016**, *18*, 9948–9960; d) S. Hayashi, K. Matsuiwa, N. Nishizawa, W. Nakanishi, *J. Org. Chem.* **2015**, *80*, 11963–11976; e) Y. Sugibayashi, S. Hayashi, W. Nakanishi, *Chem. Phys. Chem.* **2016**, doi: 10.1002/cphc.201600227.

8 *Atoms in Molecules. A Quantum Theory*, ed. R. F. W. Bader, Oxford University Press, Oxford, UK, **1990**.

9 (a) F. Biegler-König, J. Schönbohm, *J. Comput. Chem*. **2002**, *23*, 1489–1494; (b) F. Biegler-König, J. Schönbohm, D. Bayles, *J. Comput. Chem*., **2001**, *22*, 545–559; (c) R. F. W. Bader, *J. Phys. Chem. A*, **1998**, *102*, 7314–7323; (d) R. F. W. Bader, *Chem. Res*., **1991**, *91*, 893–926; (e) R. F. W. Bader, *Acc. Chem. Res.*, **1985**, *18*, 9–15; (f) T. H. Tang, R. F. W. Bader, P. MacDougall, *Inorg. Chem.*, **1985**, *24*, 2047–2053; (g) R. F. W. Bader, T. S. Slee, D. Cremer, E. Kraka, *J. Am. Chem. Soc.*, **1983**, *105*, 5061–5068; (h) F. Biegler-König, R. F. W. Bader, T. H. Tang, *J. Comput. Chem.*, **1982**, *3*, 317–328.

10 (a) W. Nakanishi, S. Hayashi, T. Arai, *Chem. Commun*. **2002**, 2416–2417; (b) W. Nakanishi, S. Hayashi, S. Morinaka, T. Sasamori, N. Tokitoh, *J. New J. Chem*. **2008**, *32*, 1881–1889.

11 CrystalClear, Rigaku Corporation, Tokyo, Japan, **2009**

12 CrysAlis^{Pro}, Agilent Technologies, Oxfordshire, **2013**.

13 R. H. Blessing, *J. Appl. Crystallogr*. **1997**, *30*, 421–426.

14 G. M. Sheldrick, *Acta Crystallogr*. **2015**, *C71*, 3–8.

15 N. K. Hansen, P. Coppens, *Acta Crystallogr.* 1978, **A34**, 909–921.

16 A. Volkov, P. Macchi, L. J. Farrugia, C. Gatti, P. Mallinson, T. Richter, T. Koritsanszky, XD2016, A Computer Program Package for Multipole Refinement, Topological Analysis of Charge Densities and Evaluation of Intermolecular Energies from Experimental and Theoretical Structure Factors, **2016**.

17 E. Clementi, C. Roetti, *At. Data Nucl. Data Tables* **1974**, *14*, 177–478.

18 J. Overgaard, D. E. Hibbs, *Acta Crystallogr*. **2004**, *A60*, 480–487.

19 E. Espinosa, E. Molins, C. Lecomte, *Phys. Rev. B* **1997**, *56*, 1820–1833.

20 P. M. Dominiak, P. Coppens, *Acta Crystallogr*. **2006**, *A62*, 224–227.

21 S. Pillet, M. Souhassou, Y. Pontillon, A. Caneschi, D. Gatteschi, C. Lecomte, *New J. Chem.* **2001**, *25*, 131–143.

22 D. Leusser, J. Henn, N. Kocher, B. Engels, D. J. Stalke, *Am. Chem. Soc.* **2004**, *126*, 1781–1793.

23 S. Dahaoui, V. Pichon-Pesme, J. A. K. Howard, C. J. Lecomte, *Phys. Chem. A*, **1999**, *103*, 6240–6250.

24 E. Clementi, D. L. J. Raimondi, *Chem. Phys*. **1963**, *38*, 2686–2689.

25 International Union of Crystallography (IUCr). *International Tables for Crystallography*, Kluwer Academic, Norwell, MA, **2004**; vol. C, pp. 796–811.

26 *Gaussian 09 (Revision D.01)*, M. J. Frisch, G. W. Trucks, H. B. Schlegel, G. E. Scuseria, M. A. Robb, J. R. Cheeseman, G. Scalmani, V. Barone, B. Mennucci, G. A. Petersson, H. Nakatsuji, M. Caricato, X. Li, H. P. Hratchian, A. F. Izmaylov, J. Bloino, G. Zheng, J. L. Sonnenberg, M. Hada, M. Ehara, K. Toyota, R. Fukuda, J. Hasegawa, M. Ishida, T. Nakajima, Y. Honda, O. Kitao, H. Nakai, T. Vreven, J. A. Montgomery, Jr., J. E. Peralta, F. Ogliaro, M. Bearpark, J. J. Heyd, E. Brothers, K. N. Kudin, V. N. Staroverov, R. Kobayashi, J. Normand, K. Raghavachari, A. Rendell, J. C. Burant, S. S. Iyengar, J. Tomasi, M. Cossi, N. Rega, J. M. Millam, M. Klene, J. E. Knox, J. B. Cross, V. Bakken, C. Adamo, J. Jaramillo, R. Gomperts, R. E. Stratmann, O. Yazyev, A. J. Austin, R. Cammi, C. Pomelli, J. W. Ochterski, R. L. Martin, K. Morokuma, V. G. Zakrzewski, G. A. Voth, P. Salvador, J. J. Dannenberg, S. Dapprich, A. D. Daniels, Ö. Farkas, J. B. Foresman, J. V. Ortiz, J. Cioslowski, D. J. Fox, Gaussian, Inc.: Wallingford CT, **2009**.

27 For the 6-311G basis sets, see: a) R. C. Binning, Jr., L. A. Curtiss, *J. Comput. Chem.* **1990**, *11*, 1206–1216; b) L. A. Curtiss, M. P. McGrath, J.-P. Blaudeau, N. E. Davis, R. C. Binning Jr, L. Radom, *J. Chem.*

Phys. **1995**, *103*, 6104–6113; c) M. P. McGrath, L. Radom, *J. Chem. Phys.* **1991**, *94*, 511–516. For the diffuse functions (+ and ++), see: T. Clark, J. Chandrasekhar, G. W. Spitznagel, P. v. R. Schleyer, *J. Comput. Chem.* **1983**, *4*, 294–301.

28 a) C. Møller, M. S. Plesset, *Phys. Rev.* **1934**, *46*, 618–622; b) J. Gauss, *J. Chem. Phys.* **1993**, *99*, 3629–3643; c) J. Gauss, *Ber. Bunsen-Ges. Phys. Chem.* **1995**, *99*, 1001–1008.

29 T. Lu, 'Multiwfn: Multifunctional wavefunction analyzer', http://Multiwfn.codeplex.com.

30 The AIM2000 program (Version 2.0) is employed to analyze and visualize atoms-in-molecules: F. Biegler-König, *J. Comput. Chem.* **2000**, *21*, 1040–1048.

31 A. Bondi, *J. Phys. Chem.* **1964**, *68*, 441–451.

32 E. D. Glendening, C. R. Landis, F. Weinhold, *J. Comput. Chem.* **2013**, *34*, 1429–1437.

33 W. Nakanishi, S. Hayashi, M. B. Pitak, M. B. Hursthouse, S. J. Coles, *J. Phys. Chem. A* **2011**, *115*, 11775–11787.

Conclusions

The structure of every molecule and compound is constructed by the strong and weak interaction in chemistry. Strong interaction is usually called classical covalent bonds, and constructs framework of molecules. In contrast, weak interaction is the collective term for van der Waals interactions (vdW), hydrogen bonds (HB), and/or charge-transfer interactions (CT), must be the driving force for the aggregation. A weak interaction plays a crucial role in physical, chemical, and biological properties of materials, since they control fine details of the structures of molecules and create delicate properties of materials. The property of materials is related with the structure. 00Therefore, it is necessary to understand details of the nature of such interaction for more efficient development and research. If we understand detail of such interactions, it enables to control such interaction and design new materials with high functionalities. Therefore, it is very important to investigate such interaction and clarify the quiddity of phenomena arising from such interactions.

It is also necessary to search the theoretical method to evaluate and classify these interactions for achievement of the aim. QTAIM approach, introduced by Bader, enables us to analyze the nature of chemical bonds and interactions. Such the topological analysis method has been promoted to understand the nature of interactions. QTAIM dual functional analysis (QTAIM-DFA), proposed recently, will be confirmed as an excellent method to elucidate the nature of weak to strong interactions if the calculated results are demonstrated to be equal to those obtained experimentally. It should be necessary to realize the approximate expression of some QTAIM functions, together with the definition, which connect calculated and experimentally observed values.

The E–E´ bonds are of current and continuous interest due to the indispensable role in biological, chemical and physical sciences. The E–E´ bonds in chalcogenides are characterized by the high-energy levels of HOMO and low energy levels of LUMO. HOMO and LUMO of E–E´ would correspond to np(E/E´) and σ*(E–E´), respectively, where np(E/E´) denote the p-type lone pair orbitals of E and/or E´, while σ*(E–E´) corresponds to the σ*-orbital of E–E´. The energy profile of E–E´ must be the driving force for the high reactivity in the redox processes and the E–E´ bonds play a crucial role in the redox process in

the biological processes. It was worth challenging to clarify the nature of the E–E´ bonds and the related interactions, in greater detail. As mentioned above, the σ*-orbitals of E–E´ (E, E´ = S and Se) are able to accept rather easily electron pairs of atoms belonging to the group 15–17 elements (A), due to the low energy levels of σ*(E–E´) with the reasonably high energy levels of n_p(A). If the interaction occurs at one side of E–E´, the interaction can be described by the CT (charge-transfer) interactions of the n_p(A)→σ*(E–E') form. The interaction can be analyzed by the σ(3c-4e) model (the three center-four electron model of the σ bond). If the CT interactions occur at both sides of E–E´, the process can be described by CT of the n_p(A)→σ*(E–E´)←n_p(A) form. The CT interaction could be described by the double σ(3c-4e) occurred at the both sides of σ*(E–E´). However, the CT interaction was analyzed by the extended hypervalent interactions of the E_2A_2 σ(4c-6e) model. The σ(4c-6e) interactions are strongly suggested to play an important role in the development of high functionalities in materials and in the key processes of biological and/or pharmaceutical activities.

The dynamic and static nature of E–E´ (E, E´ = S and Se) in glutathione disulfide and derivatives (GEE´G) is elucidated by applying QTAIM-DFA, together with *R*-cystine and their derivatives (CysEE´Cys) and MeEE´Me. The all E–E´ interactions are predicted to have the (SS/Cov-w) nature. The S–S bonds of GSSG are predicted to be less stable than that of MeSSMe. The intramolecular attractive interactions in GEE´G and CysEE´Cys stabilize the species but the E–E´ bonds would be destabilized through distortion, where the E–E´ bonds act to relax the excess deformation brought by the formation of the attractive interactions. The predicted behavior would give a hint to understand the reactivity of E–E´ in the chemical and biological processes.

The nature of E_2X_2 σ(4c–6e) (E = S and Se; X = Cl and Br) of the X---E–E---X type was elucidated. Each interaction in the X---E–E---X of 1-(8-X$C_{10}H_6$)E–E($C_{10}H_6$X-8')-1' [**8-1** (E, X) = (S, Cl), **8-2** (S, Br), **8-3** (Se, Cl), **8-4** (Se, Br)] and models **8-A** (MeX--E(H)–(H)E---XMe; E = S and Se; X = Cl and Br) could be described as a straight line. The nature of E–E and E---X in X---E–E---X was elucidated via QTAIM-DFA. The E-∗-E interactions in **8-1**–**8-4** and model **8-A** are all classified and characterized as SS/Cov-w. On the other hand, E-∗-X in model **8-A** are all classified and characterized as *p*-CS/vdW. In the case of **8-1**–**8-4**, the interactions are predicted to be *p*-CS/*t*-HB-nc for **8-1**–**8-3**, and that for (E, X = Se, Br) is predicted as *r*-CS/*t*-HB-wc. S-∗-Br in **8-2** is classified as borderline between *p*-CS and *r*-CS interactions since θ =

90.1º, very close to 90.0º. The E_2X_2 σ(4c–6e) interactions are accurately analysed by applying QTAIM-DFA.

The nature of $^{A}E_2{}^{B}E_2$ σ(4c–6e) (^{A}E, ^{B}E = S and Se) of the ^{B}E---^{A}E–^{A}E---^{B}E type were also elucidated for 1-(8-Me$^{B}EC_{10}H_6$)^{A}E–^{A}E($C_{10}H_6{}^{B}E$Me-8')-1' [**8-5** (^{A}E, ^{B}E) = (S, S), **8-6** (S, Se), **8-7** (Se, S), **8-8** (Se, Se)], and for models [$^{B}R_2{}^{B}E$---^{A}E(^{A}R)–(^{A}R)^{A}E---$^{B}E{}^{B}R_2$: **8-B** (^{A}R = ^{B}R = H), **8-C** (^{A}R = Me, ^{B}R = H), **8-D** (^{A}R = H, ^{B}R = Me) and **8-E** (^{A}R = ^{B}R = Me), where ^{A}E, ^{B}E = S and Se]. NBO analysis revealed that the ^{A}E---^{B}E interactions of the CT type are much stronger for **8-5**–**8-8**, relative to the case of model **8-B**–**8-E**, which shed light on the role of the naphthalene 1,8-positions as the spacer. The σ(4c–6e) interactions in **8-5**–**8-8** and model **8-B**–**8-E** can be approximated as the straight line, although that for ^{A}S-∗-^{B}S in model **8-C** (S, S) seem somewhat curved. The nature of the ^{B}E-∗-^{A}E-∗-^{A}E-∗-^{B}E interactions in **8-5**–**8-8** and models **8-B**–**8-E** are elucidated by applying QTAIM-DFA. All ^{A}E-∗-^{A}E interactions in **8-5**–**8-8** and models **8-B**–**8-E** are classified by the SS interactions and have the Cov-w nature. On the other hand, the ^{A}E-∗-^{B}E interactions in **8-5**–**8-8** are all classified by the regular CS interactions. The interactions are characterized to have the *typical* HB nature with covalency for **8-5** and **8-6**, whereas they are predicted to have the CT-MC nature for **8-7** and **8-8**. The ^{A}E-∗-^{B}E interactions in models **8-B**–**8-E** are all classified by the *pure* CS interactions. While ^{A}E-∗-^{B}E in model **8-C** are predicted to have the vdW nature, they are characterized as the *typical* HB nature without covalency for models **8-B**, **8-D** and **8-E**, except for ^{A}Se-∗-^{B}Se in model **8-B** (Se, Se). It is characterized as the vdW nature. The ^{A}E-∗-^{B}E interactions are predicted to be stronger in the order of model **8-C** < model **8-B** << model **8-E** < model **8-D** << **8-5**–**8-8**, judging from the QTAIM-DFA parameters.

The extended hypervalent S_4 σ(4c–6e) interaction is confirmed for the linear ^{B}S-∗-^{A}S-∗-^{A}S-∗-^{B}S interaction in 1-(8-Ph$^{B}SC_{10}H_6$)^{A}S–^{A}S($C_{10}H_6{}^{B}S$Ph-8')-1' (**8-9**) by the high-resolution X-ray diffraction determination of electron densities. The experimental results are thoroughly supported by the theoretical ones. The extended hypervalent E_4 σ(4c–6e) (E = S) interaction is demonstrated both by the experimental and theoretical treatments of the interaction, exemplified by **8-9**.

These results must be very important key to develop of chalcogen chemistry. For instance, it would enable us to clarify the E−E and E---E in transition state on reaction. At that time, these results in his thesis must be basis for estimation the nature of such the interactions. He has been confident that chalcogen chemistry is progress rapidly if we achieve deductively the analysis of the interactions in transition state.

List of Publications

1. Dynamic and static behavior of the E−E′ bonds (E, E′ = S and Se) in cystine and derivatives, elucidated by AIM dual functional analysis, Y. Tsubomoto, S. Hayashi, W. Nakanishi, *RSC Adv.*, **5**, 11534–11540 (2015) (Chapter 3).

2. Behavior of the E–E' Bonds (E, E' = S and Se) in Glutathione Disulfide and Derivatives Elucidated by Quantum Chemical Calculations with the Quantum Theory of Atoms-in-Molecules Approach, S. Hayashi, Y. Tsubomoto, W. Nakanishi, *Molecules*, **23**, 443-1−443-19 (2018) (Chapter 4).

3. Nature of E_2X_2 σ(4c-6e) of the X---E−E---X type at naphthalene 1,8-positions and model, elucidated by X-ray crystallographic analysis and QC calculations with the QTAIM approach, Y. Tsubomoto, S. Hayashi, W. Nakanishi, *Acta Cryst*, **B73**, 265−275 (2017) (Chapter 5).

4. Nature of S_2Se_2 σ(4c-6e) at naphthalene 1,8-positions and models, elucidated by QTAIM dual functional analysis, W. Nakanishi, Y. Tsubomoto, S. Hayashi, *RSC Adv.*, **6**, 93195−93204 (2016) (Chapter 6).

5. High-resolution X-ray diffraction determination of electron density of 1-(8-$PhSC_{10}H_6$)SS($C_{10}H_6$SPh-8')-1' with QTAIM approach: Evidence for S_4 σ(4c–6e) at naphthalene peri-positions, Y. Tsubomoto, S. Hayashi, W. Nakanishi, L. K. Mapp, S. J. Coles, *RSC Adv.*, **8**, 9651–9660 (2018) (Chapter 7).

Other Publications

1. Behavior of Intramolecular π–π Interactions with Doubly Degenerated Bond Paths Between Carbon Atoms in Opposite Benzene Rings of Diethenodihydronaphthalenes by QTAIM Approach, K. Matsuiwa, Y. Sugibayashi, Y. Tsubomoto, S. Hayashi, and W. Nakanishi, *Chemistry Select*, **2**, 90–100 (2017).

List of International Conferences

1. Halogen Bonding in Neutral Polybromine Clusters, Elucidated by QTAIM Dual Function Analysis, Y. Tsubomoto, S. Hayashi, W. Nakanishi, *8th International Meeting on Halogen Chemistry* (HALCHEM VIII), September 12–15, 2017, Inuyamashi (Japan), P-2.

2. Nature of E_2X_2 σ(4c–6e) at Naphthalene 1,8-Positions and Models, Elucidated by QTAIM Dual Functional Analysis, S. Hayashi, Y. Tsubomoto, W. Nakanishi, *The 12th International Conference on Heteroatom Chemistry* (ICHAC-12), June 11–17, 2017, Vancouver (Canada), P-11.

3. Behavior of Extended Hypervalent σ(4c–6e) Interactions Containing Halogen Atoms, Elucidated with QTAIM Dual Functional Analysis, W. Nakanishi, S. Hayashi, Y. Tsubomoto, *2nd International Symposium on Halogen Bonding* (ISXB2), June 6–10, 2016, Gothenburg (Sweden), OC21.

4. Behavior of the E–E′ Bonds (E, E' = S and Se) in Cystine, Glutathione, and the Derivatives, Elucidated by AIM Dual Functional Analysis, W. Nakanishi, S. Hayashi, Y. Tsubomoto, *5th Workshop of Selenium and Sulfur Redox and Catalysis* (WSeS-5), May 21, 2016, Tokai University (Hiratsuka, Japan), LO4.

5. Extended Hypervalent Se_4 4c–6e Interactions in Benzene and Naphthalene Systems, Y. Tsubomoto, Y. Nagano, S. Hayashi, W. Nakanishi, *The 11th International Conference on Heteroatom Chemistry* (ICHAC-11), June 14–19, 2015, Caen (France), P25.

Acknowledgement

The author would like to express his deepest gratitude to Emeritus Professor Waro Nakanishi and Associate Professor Satoko Hayashi at Wakayama University for their valuable and helpful suggestions, discussion, and encouragement during this work.

Furthermore, this work is supported by Professor Simon. J. Coles in Southampton University. So the author also would like to show his appreciation for his support and kindness.

Acknowledgements are also extended to the members of Hayashi Laboratory for their kindness support for his research work.

Finally, the author would like to thank his family and grandparents for their continuous support and warm encouragement.

March 2018

Yutaka Tsubomoto
Graduate School of Systems Engineering
Wakayama University